

On-Chip Broadband Magnetic Resonance Spectroscopy Down to Ultralow Temperatures

Von der Fakultät Mathematik und Physik
der Universität Stuttgart zur Erlangung der Würde eines Doktors
der Naturwissenschaften (Dr. rer. nat.) genehmigte Abhandlung

vorgelegt von
Conrad Clauß
aus Leipzig

Hauptberichter:	Prof. Dr. Martin Dressel
Mitberichter:	Prof. Dr. Jörg Wrachtrup
Prüfungsvorsitzender:	Prof. Dr. Günter Wunner

Tag der mündlichen Prüfung: 03.12.2014



Kurzfassung

Die Wechselwirkung von Licht und Materie ist seit jeher Bestand wissenschaftlicher Überlegungen und Nachforschungen und kann zurück bis zu den jungen Tagen der Naturphilosophie verfolgt werden. Eine aus heutiger Sicht komplette Beschreibung dieser Wechselwirkung und der damit einhergehenden beobachtbaren Phänomene kann allerdings nur im Rahmen der Quantenmechanik erfolgen [1]. Die Entwicklung der modernen Quanten-Elektrodynamik [3] in den 1940er Jahren ermöglichte es schließlich, diese Wechselwirkungen mittels einer relativistischen Quanten-Feldtheorie voll zu beschreiben.

Das Konzept der magnetischen Resonanz verkörpert einen Aspekt dieser Wechselwirkung insofern, dass quantenmechanische Objekte (Atome, Spin Systeme) mittels eines Lichtfeldes zu Übergängen zwischen ihren verschiedenen energetischen Zuständen angeregt werden und diese Anregungen als Absorptionslinien sichtbar gemacht werden können. Auf diese Weise können wertvolle Informationen über die (quantenmechanischen) Eigenschaften der untersuchten Materialien gewonnen werden.

Seit der ersten erfolgreichen experimentellen Messung der Elektronenspinresonanz (ESR) im Jahre 1945 [19] hat sich nicht nur ein sich dieser Technik widmentes eigenständiges Forschungsfeld etabliert, auch die Einsatzgebiete dieser Messmethode umfassen heutzutage viele verschiedene Bereiche (Grundlagenforschung, Chemie, Biologie, Medizin und Materialforschung) und machen ESR damit zu einem interdisziplinären Forschungsinstrument.

Obwohl die Technik von ESR Spektrometern in den letzten Jahrzehnten ständig verbessert werden konnte (hierbei sind viele Neuerungen und Weiterentwicklungen der stetig wachsenden Bedeutung der Mikrowellentechnik für die moderne Telekommunikation aber auch der militärischen Forschung (Radar etc.) zu zollen) basieren alle gängigen Geräte unverändert auf dem selben Grundprinzip. Die zu untersuchende Probe wird in einen Hohlraumresonator wohldefinierter Eigenfrequenz eingebracht und die reflektierte Mikrowellenleistung als Funktion eines externen Magnetfeldes detektiert. Entspricht die magnetfeldabhängige Aufspaltung der Spin-Zustände gerade der Frequenz der Mikrowellenstrahlung (Eigenfrequenz des Resonators), so werden Übergänge im Material angeregt und die reflektierte Leistung verzeichnet eine Änderung. Der Effekt der Absorption ist allerdings ganz grundlegender Natur und benötigt keinen Resonator; der Resonator dient lediglich zur Steigerung der Empfindlichkeit. Diese typische Bauweise birgt jedoch den entscheidenden Nachteil, dass die Spektrometer die untersuchten Materialien nur bei einer bestimmten Frequenz analysieren können. Für viele Fragestellungen – wie z.B. der Unterscheidung zwischen feldabhängigen und feldunabhängigen Prozessen, der genaueren Bestimmung der Parameter des Spin-Hamiltonoperators, der Messung von Spin-Spin Abständen mittels dipolarer Kopplung oder aber der Identifizierung von Relaxationsmechanismen – ist es allerdings von Vorteil oder sogar zwingend notwendig, die Spektren bei unterschiedlichen Frequenzen zu analysieren [30]. Eine Apparatur welche die Möglichkeit bietet, die Probe bei vielen verschiedenen Frequen-

zen zu untersuchen, ist also wünschenswert.

Die vorliegende Arbeit widmet sich der Realisierung einer solchen Messapparatur unter Verwendung von supraleitenden koplanaren Wellenleitern und supraleitenden koplanaren Wellenleiter Resonatoren. Es wird hierbei gezeigt, dass Messungen der Elektronenspinresonanz über einen weiten Frequenzbereich (bis hin zu ~ 40 GHz) möglich sind und dass die vorgestellte Technik zudem sehr flexibel in ihrer Handhabung ist und dadurch Untersuchungen unter Bedingungen zulässt, welche für konventionelle ESR Spektrometer bislang unzugänglich waren (freie Wahl der Frequenz, ultrakalte Temperaturen).

Der erste Teil der Arbeit beschäftigt sich mit dem konzeptionellen Aufbau von koplanaren Wellenleitern und koplanaren Wellenleiter Resonatoren und diskutiert deren Eigenschaften als Mikrowellen-Wellenleiter in Abhängigkeit von geometrischen Parametern. Zum Ende dieses Abschnittes werden die Fabrikationsschritte vorgestellt und ein zusätzlicher Herstellungsschritt, welcher die Ausbildung eines großflächigen regelmäßigen Gitters von Löchern (sogenannten Antidots) mit submikrometer Abmessungen ermöglicht, wird dargelegt. Die Erzeugung solcher Antidot-Gitter basiert auf Photolithographie mittels selbstorganisierter Filme von Mikrokügelchen. Die damit erzeugten supraleitenden koplanaren Resonatoren weisen deutlich verbesserte Resonatoreigenschaften in Anwesenheit externer Magnetfelder auf. Diese Steigerung ist darauf zurückzuführen, dass die Mikrolöcher die magnetischen Flussschläuche wirkungsvoll in ihrer Bewegungsfreiheit einschränken und damit die Verluste, hervorgerufen durch Vortex-Bewegung, signifikant reduzieren. Die verbesserten Eigenschaften in mäßig starken Magnetfeldern von bis zu mehreren 100 mT ist nicht nur für ESR Messungen mit supraleitenden koplanaren Wellenleiter Resonatoren von Bedeutung sondern auch für die Quanteninformationsverarbeitung, im Speziellen für das Feld der “Schaltkreis” -Quantenelektrodynamik mit Spin-Systemen, in welchem supraleitende koplanare Resonatoren als Quantenbus, zum Transfer quantenmechanischer Zustände fungieren.

Im folgenden Kapitel wird die elektrische und magnetische Mikrowellenfeldverteilung von koplanaren Wellenleitern beschrieben. Die Felder wurden hierbei mittels analytischer Berechnungen basierend auf der Summation der propagierenden TE und TM Schwingungsmoden und mittels 3D elektromagnetischer (EM) Simulationen (mit CST Microwave Studio) bestimmt. Im Besonderen wird anhand von EM Simulationen gezeigt, dass für einen koplanaren Wellenleiter Resonator mit einer metallischen Probe im Abstand d oberhalb der Resonatorstruktur ein Idealabstand existiert für welchen die magnetischen Wechselfelder an der Probenoberfläche maximal werden.

Der Machbarkeitsnachweis für die beschriebene Technik wird im Folgenden durch die Messung an zwei unterschiedlichen Proben erbracht. Eine dieser Proben ist das sogenannte NITPhOMe, ein organisches Radikal aus der Familie der Nitronyl-Nitroxide, welche häufig als Spin-Labels zur Untersuchung der Struktur und Bewegung in biologischen und medizinischen Studien verwendet werden [18, 30]. Es konnte dabei gezeigt werden, dass ESR Absorptionslinien über einen weiten Frequenzbereich bis zu ~ 40 GHz und Magnetfeldern von bis zu 1.4 T deutlich sichtbar sind. In diesem

Kapitel werden auch mögliche Methoden zur Auswertung der Rohdaten vorgestellt und verglichen. Dieser Punkt ist von Bedeutung, da die ESR Absorptionen aufgrund des starken Hintergrundes der frequenzabhängigen Dämpfung der Koaxialkabel und sich langsam entfaltender feldabhängiger Artefakte häufig nicht direkt in den Frequenzspektren sichtbar sind.

Nachdem die Funktion der Apparatur anhand des Spin $1/2$ Systems nachgewiesen werden konnte, wurden weitere Tests der Technik mit dem etwas komplexeren Spin $3/2$ Material Rubin durchgeführt. Rubin wurde im Rahmen der Entwicklung der ersten Maser und Laser eingehendst studiert [65–72] und eignet sich aufgrund seiner Spin-Niveaustuktur (da Spin $S > 1/2$, kommt es zu einer Nullfeldaufspaltung, welche für Rubin mit 11.4 GHz ideal in den zugänglichen Frequenzbereich fällt) und der Fülle an Literatur zur Verifizierung der Ergebnisse damit perfekt als Testobjekt für den Messaufbau.

Es kann gezeigt werden, dass alle theoretisch erwarteten Übergänge sichtbar sind und dass die Position der Absorptionen als Funktion der Frequenz und des äußeren Magnetfeldes die Ermittlung der Winkelausrichtung der kristallographischen Hauptachse in Bezug auf die Magnetfeldorientierung zulässt.

Im darauffolgenden Abschnitt wird ein Einkristall eines jüngst synthetisierten, auf Gadolinium basierenden Einzelionmagneten mittels breitbandiger ESR bei ultrakalten Temperaturen untersucht. Bei der niedrigsten erreichbaren Temperatur von ca. 60 mK konnte eine Vielzahl von Übergängen beobachtet werden. Die hohe Anzahl der Absorptionslinien liegt in der starken Anisotropie des $S = 7/2$ Spin-Systems begründet. Aufgrund der niedrigen Symmetrie (C_2) müssen Anisotropieterme höherer Ordnung berücksichtigt werden und der Hamiltonoperator beinhaltet somit zehn unbekannte Parameter (neun Stevens-Operator Koeffizienten und einen Winkel). Die Anisotropieterme bewirken ein starkes Mischen der Spin-Zustände und man kann nicht mehr zwischen erlaubten und verbotenen Übergängen unterscheiden. Tatsächlich können bei solchen Systemen alle nur denkbaren Übergänge zwischen den Zuständen $|m_i\rangle$ und $|m_f\rangle$ ($i, f = -7/2, -5/2, \dots, +5/2, +7/2$,) mit einer bestimmten Wahrscheinlichkeit P_{if} auftreten. Da die beobachteten Absorptionslinien nicht eindeutig zu Übergängen zwischen bestimmten Eigenfunktionen des Hamiltonoperators zugeordnet werden können, lassen sich die zehn unbekannt Parameter nicht zweifelsfrei bestimmen (zumindest nicht ohne weitere Information zu dem System oder einer Eingrenzung der Anisotropieterme).

Obwohl die Systemparameter aus den Messdaten nicht ermittelt werden konnten, so veranschaulicht die Messung doch auf eindrucksvolle Weise das Potential der Messmethode (in Anbetracht der erreichbaren Temperaturen und des Informationsgehalts der Spektren).

Das zuletzt in dieser Arbeit behandelte Material ist das schwere-Fermionen System YbRh_2Si_2 . Dieses Material zeigt bei ultratiefen Temperaturen von $T \lesssim 70$ mK eine antiferromagnetische Ordnung, welche sich mit einem geringen Magnetfeld von nur ca. 60 mT (für $H \perp c$ -Achse) bis auf $T = 0$ unterdrücken lässt und an dieser Stelle einen Quantenphasenübergang aufweist. Das quantenkritische Verhalten beeinflusst

dabei die Eigenschaften des Materials in einem Bereich oberhalb des quantenkritischen Punktes (im durch Magnetfeld und Temperatur aufgespannten Phasendiagramm) maßgeblich. Auf diese Weise zeigt YbRh_2Si_2 auch bei endlichen Temperaturen (in einem trichterförmigen Gebiet oberhalb des Quantenphasenüberganges) ein Verhalten, welches sich nicht durch das typische Fermi-Flüssigkeitsmodell beschreiben lässt. YbRh_2Si_2 kann hierbei stellvertretend für eine ganze Klasse an Systemen, welche die gleichen oder ähnliche Eigenschaften aufweisen, betrachtet werden. Da diese Systeme bis heute nicht vollständig verstanden sind, können ESR Messungen auch mit dazu beitragen das Wissen um diese Materialien zu erweitern.

Im Rahmen dieser Arbeit wurde YbRh_2Si_2 sowohl mit der breitbandigen- als auch der resonanten Technik untersucht. Die Resultate der breitbandigen Messungen zeigen ein sehr schwaches Signal außerhalb der antiferromagnetischen Phase (innerhalb konnte kein Signal detektiert werden). Durch Filtern und diskrete Differenzierung der Daten konnte das Signal deutlicher vom Rauschen abgehoben werden und ein linearer Zusammenhang zwischen Absorptionsfrequenz und -Feld festgestellt werden. Wird der g -Faktor aus dem Differenzenquotienten dieser linearen Abhängigkeit gewonnen, so ergibt er sich zu ca. $g_{\text{Steigung}} \approx 3.4$. Wird der g -Faktor hingegen aus der Absolutposition der Absorption abgeleitet, so kann man eine starke Magnetfeldabhängigkeit beobachten, bei welcher g_{Abs} für kleine Felder (in der Nähe des quantenkritischen Punktes) deutlich erniedrigt ist ($g_{\text{Abs}} \approx 2.8$ bei $H_{\text{ext}} \lesssim 70$ mT) und sich mit steigendem Magnetfeld g_{Steigung} asymptotisch annähert. Es kann gezeigt werden, dass diese Diskrepanz durch ein noch unbekanntes Verhalten bei sehr niedrigen Feldern/Frequenzen hervorgerufen wird.

Mit der resonanten Methode konnte YbRh_2Si_2 bei insgesamt 19 verschiedenen Frequenzen im Bereich von 1.5 bis 13.4 GHz untersucht werden. Die Parameter (Resonanzfeld, Linienbreite) der Absorptionslinien zeigen unterschiedliches Verhalten in den drei verschiedenen “Grundzuständen” des Systems. In dem Nicht-Fermi-Flüssigkeitsbereich nimmt das Resonanzfeld mit sinkender Temperatur zu und die Linienbreite ab. Beim Übergang in die antiferromagnetische Phase (in niedrigen Feldern) ist dieses Verhalten gerade gegenläufig: das Resonanzfeld nimmt wieder ab und die Linienbreite mit sinkender Temperatur stark zu. In höheren Feldern geht das System in den Fermi-Flüssigkeitsbereich über und das Resonanzfeld bleibt konstant. Der temperaturabhängige Verlauf der Linienbreite kann, entsprechend den theoretischen Vorhersagen [95], durch einen quadratischen Zusammenhang einigermaßen beschrieben werden. Die zusätzliche quadratische Feldabhängigkeit kann allerdings nicht beobachtet werden.

Die in dieser Arbeit vorgestellten Ergebnisse basieren auf den ersten ESR Messungen, welche YbRh_2Si_2 bei niedrigen Temperaturen und Feldern in unmittelbarer Nähe des quantenkritischen Punktes untersuchen. Eine komplette, zweifelsfreie Auswertung und Interpretation der Daten steht allerdings noch aus. Insbesondere zeigt die Linienbreite als Funktion der Temperatur und des Magnetfeldes zum Teil starke Schwankungen, da sie sehr empfindlich auf die vorhergehende Subtraktion des Hintergrundes reagiert (siehe Hauptteil).

Das letzte Kapitel der Arbeit beschäftigt sich schließlich mit der Sensitivität, dem Signal/Rausch Verhältnis und der räumlichen Verteilung der magnetischen Wechselfelder für unterschiedliche Wellenleitergeometrien. Die kleinstmögliche detektierbare Anzahl an Spins sowie das Signal/Rausch Verhältnis werden hierbei anhand der Ergebnisse der NITPhOMe Probe hergeleitet.

Die mit der in dieser Arbeit vorgestellten Technik gewonnen Ergebnisse zeigen deutlich das Potential der breitbandigen Untersuchungsmethode. Durch die zusätzliche äußerst flexible Handhabung ist es daher möglich, neue, bislang unzugängliche Bereiche zu erschließen.

Contents

Kurzfassung	iii
1 Introduction	1
1.1 Electron Paramagnetic Resonance	5
1.2 EPR with Coplanar Waveguides	7
1.3 Coplanar Waveguide Resonators in Magnetic Fields	9
2 Superconducting Coplanar Waveguides and Resonators	11
2.1 Introduction	11
2.2 Superconductors in Magnetic Fields	14
2.2.1 Type-II Superconductors	15
2.2.2 Abrikosov Vortices	16
2.3 Superconducting Microwave Resonators in Magnetic Fields	18
2.3.1 Current and Flux Distribution	18
2.3.2 Flux Penetration in Thin Film Structures	19
3 Investigated Systems	25
3.1 Nitronyl-Nitroxide Radical NITPhOMe	25
3.2 Chromium III in Al_2O_3	26
3.3 Gadolinium III based Single Ion Magnet	27
3.4 Heavy Fermion Metal YbRh_2Si_2	31
4 Design and Fabrication	35
4.1 Characteristic Impedance	36
4.2 Minimal Distance of neighboring Lines	37
4.3 Modelling the Coupling Gaps	40
4.4 Field Simulation of Resonator Structures	40
4.5 Fabrication	44
5 Experimental Setup	49
5.1 Broadband ESR Sample Preparation	52
5.2 Resonant ESR Sample Preparation	54
6 Broadband Electron Spin Resonance	63
6.1 Broadband ESR on NITPhOMe	63
6.1.1 Frequency Sweep Spectroscopy	63
6.1.2 Field Sweep Spectroscopy	70
6.1.3 Temperature Dependence	71
6.2 Broadband ESR on Ruby Single Crystals	73
6.3 Broadband ESR on Gd-based Single Ion Magnets	77
6.4 Broadband ESR on the Heavy Fermion Metal YbRh_2Si_2	82
7 EPR on Heavy Fermions at mK Temperatures	95

8	Sensitivity or Why Size Does Matter	113
9	Summary and Outlook	129
	Appendix	135
A	Field Calculations for Coplanar Structures	135
B	AFM Phase Transition Spectra with adjusted Temperatures	139
	References	143
	Acknowledgements	xi

1 Introduction

The interaction of light and matter has been a field of interest dating even back to nature philosophy. Nevertheless, the first key concepts towards the development of a comprehensive description of this interaction started to emerge only within the framework of quantum mechanics, initiated by Dirac in the late 1920's [1, 2]. Though in this theory the quantized electromagnetic field was described by an ensemble of harmonic resonators and the interaction with charged particles was included to derive the coefficient of spontaneous emission by an atom, the modern concept of quantum electrodynamics (QED) was developed only 20 years later through the work of Richard Feynman, Freeman Dyson, Julian Schwinger and Sin-Itiro Tomonaga [3]. QED merged the hitherto separate fields of classical electrodynamics, quantum mechanics and special relativity to form a consistent relativistic quantum field theory (QFT), within which particles and fields are described as discrete excitations of quantized fields and the interaction between (charged) particles and light is given in terms of exchange of virtual photons.

A showcase example is given by the two-level system, which is extremely simple, yet comprehensively incorporates the fundamental hallmarks of light-matter interaction. Considering a quantum object (atom) comprised of two states, a low energetic ground state $|g\rangle$ and a high energetic excited state $|e\rangle$ which are separated by ΔE , then the most basic light-matter interactions can already be described in an illustrative manner using just this system. There are, basically, three possible scenarios (see Figure 1.1) – (i) the atom is initially in the excited state and spontaneously relaxes into its ground state by emitting a photon with the energy $E = \Delta E = h\nu$ (h : Planck's constant, ν : photon frequency). (ii) The atom is in the excited state and gets 'triggered' by a photon with frequency ν to demote to the ground state. Since energy is conserved, this stimulated emission creates another photon of frequency ν . In the last case (iii), the atom resides initially in its ground state $|g\rangle$ and gets promoted to the excited state by absorbing a photon with frequency ν .

It is of particular interest that the spontaneous decay rate of such a two-level system can be controlled by modifying the environment or, more precisely, by controlling the vacuum mode density. If, for example, an atom (two-level system) with a transition wavelength $\lambda = c/\nu$ (c : vacuum speed of light) is placed between two mirror planes with distance ℓ and $\ell < \lambda/2$, then the spontaneous emission rate is completely suppressed for a parallel alignment of the atomic transition dipole moment with respect to the mirror planes. For this configuration the atom simply cannot emit a photon

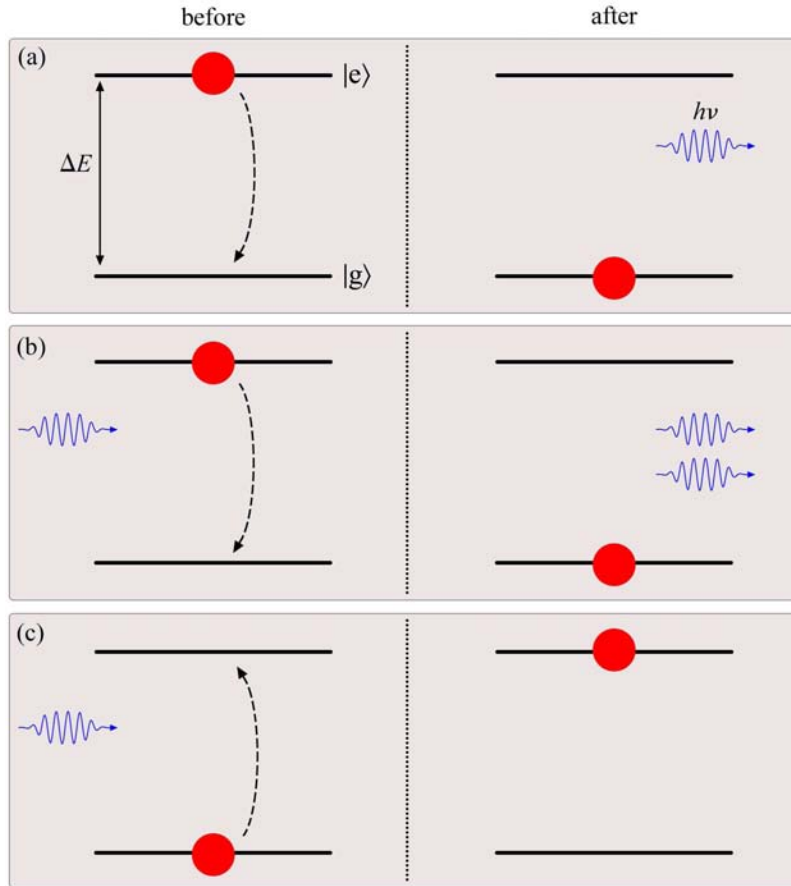


Figure 1.1: Schematics of an atom-like quantized two-level system and its interactions with light (photons). (a) Is the atom initially in the excited state it can decay into the ground state by spontaneous emission of a photon with frequency ν ($h\nu = \Delta E$). (b) The atom can also be stimulated to demote to the ground state under the emission of a photon. (c) Promotion of the atom into the excited state by absorption of a photon.

since the mode density vanishes for all modes with $\lambda \geq 2\ell$. Is the mirror distance, on the other hand, greater than $\lambda/2$, the spontaneous emission rate can even be enhanced compared to its free-space value. Both the suppression as well as the enhancement of the spontaneous emission rate can easily be explained in terms of image charges and the resulting electric fields at the atoms position [4, 5].

Microwave or optical resonant Fabry-Pérot cavities are real life examples of such mirror arrangements as described above. The distance between those (typically spherical) mirrors selects the modes (frequencies ν_i) that are supported by the cavity and the reflectivity of the mirrors determines the linewidth ($\delta\nu_i$) or finesse of the resonator spectrum. Remarkably, the modification of the linewidth $\delta\nu_i$ has severe consequences for the way the cavity light field interacts with an intracavity atom.

Is the linewidth large compared to the free-space atomic emission rate (low finesse, low mirror reflectivity) while the mirror distance is such that the cavity resonance is close to the transition frequency ν of the atomic states, then the mode density becomes a continuum from the atoms point of view and, as a result, the spontaneous emission rate is enhanced. This enhancement is known as the Purcell effect as it was pointed out by him in a note in 1946 [6]. On the other hand, if the cavity linewidth is small, meaning of the order of the free-space emission rate, the perturbative approach breaks down and the spontaneous emission rate becomes coherent. In this case, the atom emits and reabsorbs the photon (coherently!) many times before the photon eventually escapes the cavity and the system is in the so-called strong coupling regime. A clear signature of this behavior is given by the observation of Rabi oscillations between the atom's states [7–11].

The above made considerations clearly show the conceptual strength of the two-level model system, especially in combination with photons trapped inside a box (cavity). It is therefore not surprising that it were thought experiments like that which progressed into the establishment of individual fields of research such as cavity quantum electrodynamics (cavity QED) or superradiance and that have stimulated the development and constant advancement of masers and lasers.

Although the focus of this work is on a slightly different angle, the small discourse made above is helpful for the understanding of many key concepts and working principles of light-matter interaction.

As far as real systems are concerned, the spin $1/2$ system can be regarded as the archetypical two-level system. In the presence of an external magnetic field a quantization axis is introduced and the zero field energy degeneracy is lifted. As a consequence, the two states, spin-up (\uparrow) and spin-down (\downarrow), are then separated in energy by the Zeeman splitting $\Delta E = g\mu_B H_{\text{ext}}$ (with the g -factor g , the Bohr magneton μ_B and the external magnetic field H_{ext})*. Considering an ensemble of N_0 identical, non-interacting spin $1/2$ systems in a thermal bath of temperature T and at an external magnetic field H_{ext} , each state is populated by a number of spins according to the Boltzmann distribution (provided the system is in thermal equilibrium). Interacting with a light field with the transition frequency $\nu = g\mu_B H_{\text{ext}}/h$, absorption and stimulated emission of photons happen with equal probability. There will, however, be a net absorption since, in thermal equilibrium, the ground state is populated by more spins than the excited one. This light-matter interaction is illustrated schematically

*In fact, the external magnetic field should be given as B_{ext} . This work follows the common convention and the external field is called H_{ext} . However, it is still given in units of [T].

in Figure 1.2.

Magnetic resonance experiments are prime examples for the exploitation of this kind of light-matter interaction in order to gain knowledge about the magnetic properties, spin-spin and spin-lattice interaction and even the spin dynamics of the material under study. The standard generic working principle is similar to that of cavity QED with the difference that typically many photons are used to investigate an ensemble consisting of many magnetic particles. The quantification of ‘many’ can actually

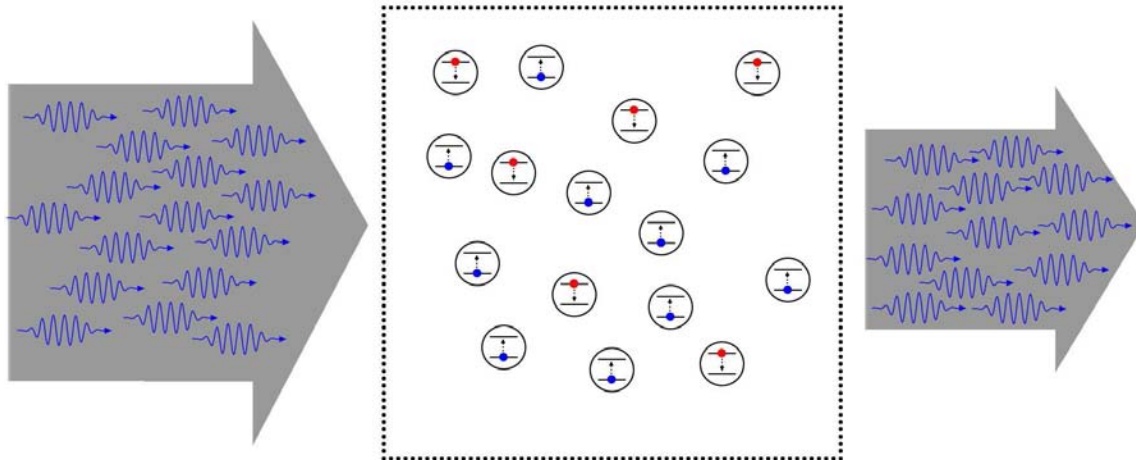


Figure 1.2: Schematic display of an ensemble of two-level systems interacting with a light field. In thermal equilibrium more systems are in the ground state and thus the absorption process dominates over the stimulated emission. As a result, the transmitted light gets attenuated.

vary over several orders of magnitude, depending on the sensitivity of the experimental apparatus. In fact, electron spin resonance was demonstrated in the strong coupling regime with only a single or very few photons within the resonator on a sample of nitrogen vacancies in diamond [12, 13] (in this case an ensemble of spins is needed to enhance the coupling strength which scales with the square root of the number of atoms/spins). Both concepts, that of cavity QED and that of magnetic resonance share a lot of common ground since both are based on the notion of having a quantized object (atom, spin system) interacting with photons trapped in a box. As a matter of fact, many theoretical tools used for cavity QED were borrowed from the theory of (nuclear) magnetic resonance [4].

1.1 Electron Paramagnetic Resonance

This work is about a novel technique to perform electron paramagnetic resonance (EPR). To classify this new technical approach the basic working principle of standard EPR devices will be briefly outlined in the following. Leaving the detection scheme aside for the moment and concentrating solely on the interaction of the magnetic moments with the microwave light field, three basic criteria can be set to achieve a large absorption signal:

1. The microwave magnetic field at the sample position should be as strong as possible without saturating the spectrum.
2. The filling factor η should be high.
3. The conversion efficiency should be maximized.

The first point is obvious since the absorption intensity scales with the square of the microwave magnetic field amplitude (H_{rf}) [14–18]. However, depending on the relaxation times T_1 and T_2 (spin-lattice and spin-spin relaxation time, respectively) there exists an optimum microwave magnetic field strength with regard to the signal intensity which is just below the saturation field strength. Stronger microwave fields drive the system out of equilibrium and the signal intensity does no longer increase linearly with incident microwave power ($P_{\text{in}} \propto H_{\text{rf}}^2$).

note

Care has to be taken regarding the notion of ‘signal intensity’ in textbooks. If ‘signal’ refers to a voltage then it typically scales with the square root of the incident microwave power since $H_{\text{rf}}^2 \propto P_{\text{in}} \propto U^2$ (U : signal voltage at the end of the transmission line/waveguide).

In this work the signal always denotes the power, and thus scales linearly with P_{in} .

In standard EPR devices these high microwave magnetic fields are realized utilizing cavity resonators which are coupled to (rectangular) waveguides. At a certain frequency, depending on the size of those cavities, the incident wave and those reflected at the cavity walls interfere constructively and the intracavity fields are substantially multiplied. A measure of the effectiveness of this interference, and therefore also for the resulting strength of the microwave magnetic fields, is given by the quality factor

Q of the resonator. It is defined as the ratio of energy stored in the resonator and energy dissipated per cycle. Experimentally the quality factor can be obtained as

$$Q = \frac{\nu_{\text{res}}}{\delta\nu_{\text{res}}} \quad (1.1)$$

with the cavity resonance frequency ν_{res} and the full width at half maximum $\delta\nu_{\text{res}}$ of the frequency-swept resonance curve. Due to the strong microwave field enhancement in high- Q cavities the EPR absorption becomes prominent as the frequency of the magnetic transition is swept (via H_{ext}) through the cavity resonance frequency.

The filling factor η is another important quantity for maximizing the absorption intensity. Basically, it describes the ratio between the sample volume V_s and the cavity volume V_c . However, since the absorption intensity scales with H_{rf}^2 and the microwave magnetic fields are not uniform within the cavity a more sensible definition can be given with [18]

$$\eta = \frac{\int_{V_s} H_{\text{rf}}^2 dV_s}{\int_{V_c} H_{\text{rf}}^2 dV_c}. \quad (1.2)$$

So, in order to obtain the strongest possible absorption signal one would need a filling factor of unity. This is, however, impractical for several reasons. In a cavity electric and magnetic fields are spatially separated, meaning, the standing wave patterns show a magnetic field antinode where the electric field features a node. Since all samples exhibit dielectric losses it is advantageous to place a sample at the magnetic field maximum position. In this way the sample only couples to the magnetic field component and the dielectric losses can be ignored. If the filling factor, however, is very large, then the sample also covers regions where the electric field strength is no longer negligible. The dielectric losses can no longer be discarded and the resulting reduction of Q for very large samples might already outweigh the benefits from the increase of the filling factor. In addition, one has to consider the actual size of a typical EPR cavity. The most common frequency band used for EPR spectrometers is the so-called X-band located around 9 GHz. At this frequency the volume of the cavity is in the order of $\sim 5 \text{ cm}^3$. In most of the cases the dimensions of available sample material never come even close to those sizes.

The standard filling factors in modern day EPR spectrometers (determined after Equation (1.2)) are in the range of $\eta \leq 10 \%$ [18].

The conversion efficiency, stated as the last point of the criteria given above, is

closely related to the quality factor mentioned earlier. Basically, it quantifies how well the incident microwave power is converted into microwave magnetic field inside the cavity. In a sense, a high conversion efficiency inevitably goes hand in hand with a high quality factor. In order to achieve a high conversion efficiency it is important to have the cavity perfectly matched to the $50\ \Omega$ impedance of the waveguide so that no microwave power is reflected before entering the cavity. In addition, the walls of the cavity should be made of highly conducting material and should have a smooth surface to reflect the microwaves most efficiently.

1.2 EPR with Coplanar Waveguides

Having laid the groundwork of what is essentially necessary to successfully perform EPR measurements one can now consider different ways of satisfying the three fundamental requirements stated above.

From a historical point of view, the development of radar during the second World War provided researchers with the appropriate tools to overcome previous technical issues. In particular the construction of high-power microwave sources and highly sensitive detection schemes (crystal detectors as well as narrow band amplifiers and lock-in detectors) paved the way for the advancement of EPR measurement techniques [15]. Finally, the usage of cavities to locally enhance the microwave magnetic fields allowed for the experimental realization of the first EPR studies [19–21].

The ever progressing development and improvement of microwave devices and electronics has not just revolutionized the way of modern telecommunication but also pushed the limits of EPR measurement hardware. Higher frequencies and constantly improving noise reduction schemes have led to a variety of EPR spectrometers with outstanding performance. The basic working principle, however, was kept unchanged throughout the years – meaning the spectrometers commercially available these days still operate in only a narrow frequency band predetermined by the cavity resonance frequency. Only in recent years new techniques were developed based on planar micro-resonators that work in the low GHz frequency range [22–24]. In addition, the new experimental branch of ‘circuit quantum electrodynamics’ emerged in recent years following a publication by the Schoelkopf group [25]. This novel field is conceptually identical to that of cavity QED but replaces the three-dimensional cavity by a superconducting coplanar waveguide resonator (CPW resonator) and the natural (Rydberg) atoms by mesoscopic artificial atoms (superconducting qubits). By doing so, the system parameters can be very well controlled and, even more

important, can be changed (switched) extremely fast. One of the key elements to circuit QED is the superconducting coplanar resonator, which can be fabricated in a way that it features very large local electric and magnetic microwave fields. It is this quality that renders CPW structures into particularly suitable devices to also perform EPR with.

In this work, it will be shown that superconducting CPW resonators indeed can be used for EPR studies. Even more, it will be shown that simple coplanar transmission lines allow for EPR experiments in a continuous broad frequency range up to 40 GHz. This is owed to the fact that the maximum microwave magnetic field in a microfabricated superconducting coplanar waveguide can already be stronger than the maximum field in standard EPR cavities for equal input powers [26, 27]. Previous broadband realizations in the low frequency range (≤ 50 GHz) were either based on coupled antennas (from 500 MHz to 9 GHz, see [28]) or on tunable cavities (4 to 40 GHz, see [29]). Both approaches lack the flexibility of the presented one, either in the achievable frequency range (antenna approach) or in handling (tunable cavity; to access the whole frequency range the cavity has to be (partially) filled with different dielectrics).

The ability of performing EPR at different frequencies widens the ‘spectrum’ of properties and processes that can be studied. A comprehensive discussion of observable effects and quantities in multi-frequency EPR is summarized by Misra [30]. Only a few of those points will be recapitulated here to give an idea of the versatility of the broadband technique.

– **Distinction between field-dependent and field-independent processes** –

If a material is studied only at a single frequency it is very hard to tell which lines stem from field-dependent (Zeeman interaction) and which from field-independent (e.g. hyperfine interaction) processes without a priori information about the system. For different frequencies, however, the Zeeman shifted levels produce absorption lines at different fields while the splitting caused by the hyperfine interaction remains the same.

– **More precise estimation of spin-Hamiltonian parameters** –

By fitting the spectra taken at different frequencies simultaneously the anisotropy terms and the hyperfine structure parameters can be estimated with higher precision from low-frequency data while the g -tensor is determined more accurately from higher frequency spectra.

– **Measurement of distances based on dipolar coupling** –

Since the dipolar spin-spin coupling scales with the inverse cube of the spin distance the resulting splitting of the lines can be used to estimate the distance and respective orientation of two spin labels by simultaneously fitting the spectra recorded at several different frequencies.

These are just a few examples to illustrate the potential of multi-frequency EPR. Therefore, a device that covers a broad frequency range can perform all those types of experiments using just a single instrument without the need to remount and re-orient the sample for a different spectrometer and risk sample contamination or degradation.

In addition, the presented very compact design can easily be cooled down to mK temperatures in a dilution refrigerator which pushes the range of applicability towards new limits and enables the investigation of materials at temperatures which were so far inaccessible to standard EPR techniques.

1.3 Coplanar Waveguide Resonators in Magnetic Fields

Although superconducting CPW resonators can produce extremely high local microwave magnetic fields, the utilization of those devices for EPR studies is not as straight forward as it may seem. To tune the transition frequencies between different spin states an external magnetic field has to be applied. The resulting Zeeman shift allows to tune the spin ensemble on or off resonance with the resonator. This ability, however, comes at a price since the magnetic field also indirectly introduces new loss channels for the resonator which, in turn, lower its quality factor.

Since the resonator structure is made of superconducting material (type II superconductor), magnetic fields cause the creation of vortices - thin channels into which the quantized flux penetrates and superconductivity breaks down. Due to the ever increasing range of applications for high-performance devices based on superconductors, the investigation of these magnetic flux lines (Abrikosov vortices) and in particular their interaction with natural and artificial defects still remains a topic of high interest.

Since any current in the vicinity of unpinned Abrikosov vortices leads to a dissipative motion caused by Lorentz force (see Figure 1.3 (a)), the operational behavior of superconducting electronics are often constrained by vortex losses (increased noise, lower quality factor, shortened coherence time). To decrease the motional freedom of vortices and therefore improve the performance of the device, the vortices can be

pinned to defects which act as local energy minima (pinning sites) [31–37].

In high- Q coplanar waveguide resonators any type of loss manifests itself in an undesired reduction of Q . So, in order to maintain high quality factors even in moderate magnetic fields it is stringently required to trap/pin the vortex lattice [38–40]. One way to do so is by introducing a regular array of microholes (antidots) into the thin-film structure. In this work it will be shown that by fabricating CPW resonators from films perforated with a lattice of sub- μm antidots it was possible to achieve high quality factors for external magnetic fields up to a few hundred mT.

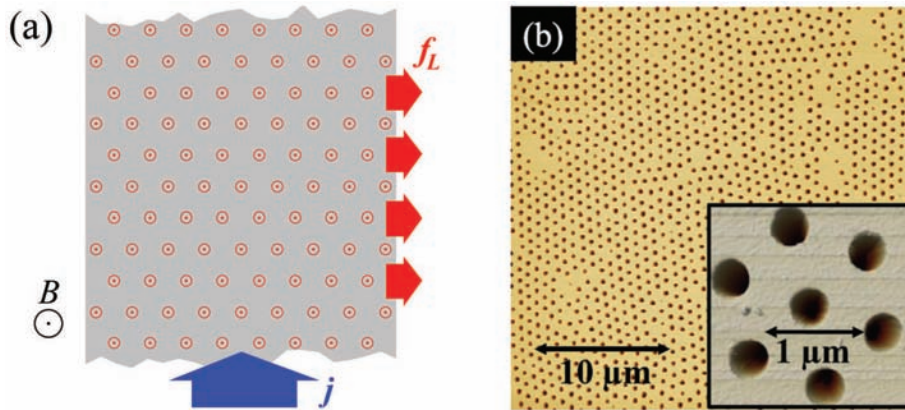


Figure 1.3: (a) Sketch of a type II superconductor in an external magnetic field. The magnetic vortices experience a displacing Lorentz force due to the applied current. (b) Superconducting thin film (thickness $\sim 150\ \text{nm}$) structured with many sub- μm microholes (antidots) to pin the flux vortices in magnetic fields.

2 Superconducting Coplanar Waveguides and Resonators

2.1 Introduction

The work presented in this thesis is centered around coplanar waveguides and resonators working in the microwave regime. Here, these devices are used as a toolset to investigate physical properties of various sample materials (mainly their magnetic transitions and interactions). In the fairly related field of circuit quantum electrodynamics, superconducting coplanar resonators play an essential role by mutually coupling quantum bits (qubits) and storing quantum information. It is therefore reasonable to have a closer look at these coplanar structures, or planar microwave structures in general, and work out their properties and respective advantages and disadvantages.

Planar waveguides typically come in three different designs. The stripline, the microstrip and the coplanar waveguide (see Figure 2.1). All three can be thought of transformations from the well-known coaxial line. A stripline consists of a center conductor strip which is immersed in some dielectric and shielded by ground planes at the top and bottom (see Figure 2.1 (b)). The microstrip geometry is very similar, only that the top part of the dielectric and the top ground plane are missing (see Figure 2.1 (c)). The coplanar waveguide is essentially a center conductor strip flanked by two ground planes at the same level, all on top of a dielectric substrate (see Figure 2.1 (d)). If one imagines a simple coaxial line, one can construct a coplanar waveguide by just taking a thin slice out of that coaxial line along its length (see Figure 2.2 (a) and (b)), extending the outer conductor parts to planes, removing the dielectric in between (Figure 2.2 (c) and (d)) and finally placing the whole assembly onto a substrate.

While the coaxial line is very well shielded from the environment (which also holds true for the stripline, as long as the center conductor width is small compared to the ground plane extensions), this is not the case for the microstrip geometry. This is why striplines and coplanar waveguides are typically used to transport signals, to act as band pass filters or to couple different lines laterally or vertically to each other while microstrip devices play an important role for antenna design in modern telecommunication devices. The great advantage of these planar designs over the conventional coaxial line, is that they can easily be printed on circuit boards, can be made very compact, and fabricated at low cost.

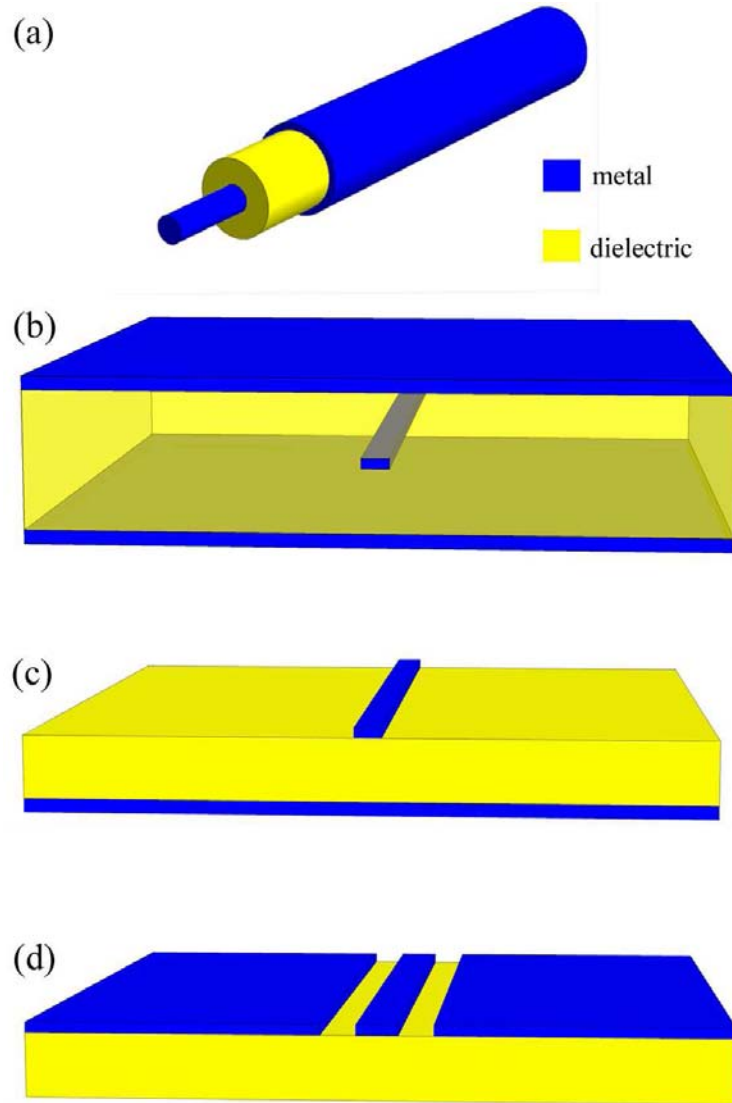


Figure 2.1: Typical microwave waveguides. (a) Coaxial line, (b) stripline, (c) microstrip and (d) coplanar waveguide.

The transport properties of planar waveguides depend on the characteristic impedance Z_0 which is determined by geometrical parameters like the ratio of center conductor width to the distance between center conductor and ground plane. In the cases of striplines and microstrips, any change of the center conductor width requires a change in the dielectric thickness. For a coplanar waveguide, however, this ratio can be kept constant without the need to change the substrate thickness. This feature enhances the flexibility and applicability of coplanar devices, as it is often needed to widen or to narrow the center conductor line.

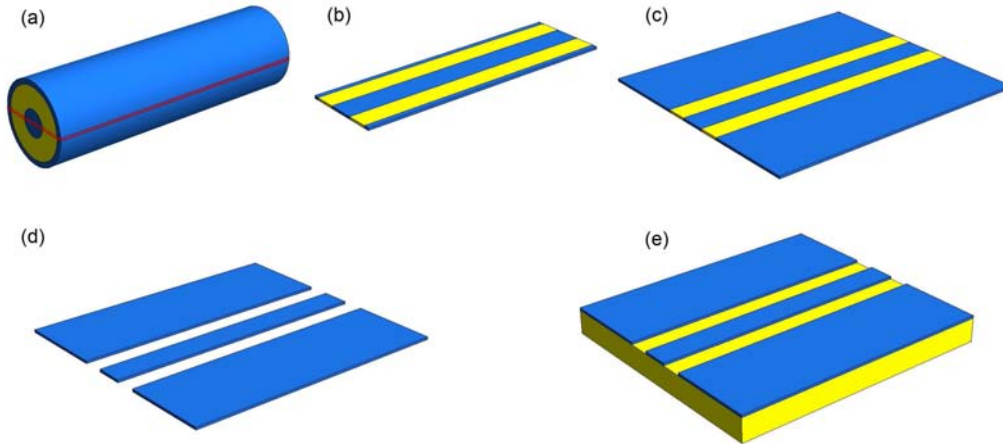


Figure 2.2: Transformation from a coaxial line to a coplanar waveguide (see text).

Coplanar waveguide (CPW) resonators can be realized by introducing two gaps into the center conductor (see Figure 2.3). The distance ℓ between those gaps determines the resonator fundamental frequency. The resonance condition is fulfilled if ℓ is an integer multiple of the half-wavelength of the incident microwave (hence the common notation ‘half-wavelength resonator’). The size of the gaps defines the strength of the capacitive coupling of the input (or output) feed to the resonator strip and can be tuned to some extent to either favor high power throughput or high quality factors. For many fields of application it is desirable to attain high quality factors. To achieve this, the whole system has to be optimized since the measured (‘loaded’) quality factor is dominated by the ‘weakest’ component (see section 4).

In this work, CPWs and CPW resonators are made from superconducting (niobium) thin films that will be exposed to external magnetic fields in the experiment. To optimize the structures in order to maintain high performance characteristics under those conditions it is important to understand the physics of superconducting thin-films carrying ac currents in the presence of magnetic fields.

Since this work is not primarily dedicated to the optimization of superconducting CPW resonators, just the main key points will be recapitulated in the following.

In fact, the historical advances in superconductivity, or better, our understanding thereof, are closely linked to the (fundamental) interplay of magnetism and superconductivity (since both phenomena are tightly interwoven). So, to work out the most important aspects of this interaction one can therefore simply follow along the historical path of superconductivity.

However, the following section makes no claims to completeness. It is merely intended

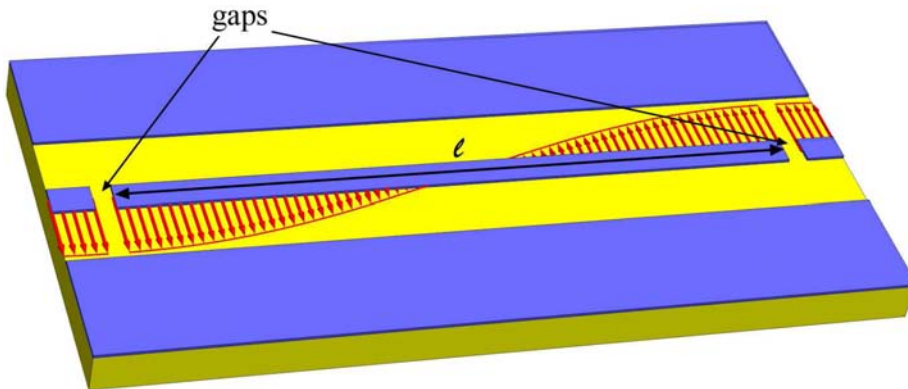


Figure 2.3: Generic layout of a coplanar waveguide resonator with the amplitude profile of the electric field of the fundamental mode.

to illustrate the basic characteristics and their consequential implications. A much more detailed and in-depth discussion, especially with respect to superconducting CPW resonators, can be found in the PhD thesis of D. Bothner [41].

2.2 Superconductors in Magnetic Fields

After the discovery of superconductivity in 1911 by H. K. Onnes, while studying the temperature dependence of the electrical resistance of mercury [42], W. Meissner and R. Ochsenfeld found in 1933 another characteristic effect of superconductors which settled the question whether the superconducting state can be regarded as a real thermodynamic phase or is merely a material ground state with vanishing electrical resistance [43]. Considering a material featuring a perfect conducting ground state for temperatures below a critical temperature T_c , the cooling below T_c can be done in two different ways – once in zero magnetic field and once with magnetic field already applied above T_c – leading to different final situations. If the material is cooled below T_c with $B = 0$ (zero-field-cooled) and the magnetic field is applied in the perfectly conducting state, eddy currents are induced in the sample (according to Lenz’s law) which generate a magnetic field opposing the external one and of the same magnitude, leading to a net field of zero within the sample. If, on the other hand, the field is applied in the normal state (field-cooled), the induced eddy currents vanish quickly after reaching a static field B due to ohmic losses in the material and the sample shows a non-vanishing net magnetization which remains also after cooling below T_c into the perfect conducting state.

The scenario found by W. Meissner and R. Ochsenfeld, however, was that the sample always behaves as an ideal diamagnet regardless of how the system enters the

superconducting state. In this way, the Meissner-Ochsenfeld effect proves that superconductivity has to be considered as a real thermodynamic phase and is not just characterized by perfect conductivity.

Shortly after its discovery, the effect could be explained by the London equations [44] which are based on the assumption that the magnetic field is expelled from the superconductor bulk by eddy currents forming in a thin sheet at the surface. Furthermore the electric field has to vanish in the superconductor due to perfect conductivity.

As a result, the spatial distribution of the magnetic field inside a superconductor can be given as

$$B(z) = B_{\text{ext}} e^{-\frac{z}{\lambda_L}}.$$

Here, z is the distance from the surface of the superconductor (into the bulk) and λ_L is the material specific London penetration depth. This result demonstrates that the magnetic field is not completely expelled from the superconductor but remains finite in a thin surface layer of the order of λ_L .

2.2.1 Type-II Superconductors

Although it was at that point possible to describe the Meissner effect by the London equations (at least phenomenologically) it became soon apparent that the interplay of superconductivity and magnetism still held further mysteries. In the following years, many materials were found (first 1937 by Shubnikov [45, 46] and later by Zavaritskii [47]) that showed a different behavior – above a certain threshold field magnetic flux obviously penetrated the superconductor while it still maintained perfect conductivity. Is the external field increased further, more and more flux penetrates the sample until superconductivity eventually breaks down. In that way, one can distinguish between two critical fields – a lower one (B_{c1}) at which the Meissner phase of perfect diamagnetism is broken and flux starts to penetrate the bulk, and an upper one (B_{c2}) at which superconductivity finally ceases to exist. Based on the different behavior of superconductors in the presence of external magnetic fields one can distinguish between the original, pure Meissner superconductors which were termed type-I superconductors and type-II superconductors which feature the intermediate phase of partial flux penetration (see schematic phase diagrams in Figure 2.4). It was later shown that this partial flux enters the superconductor in the form of vortices, small channels inside which superconductivity is broken.

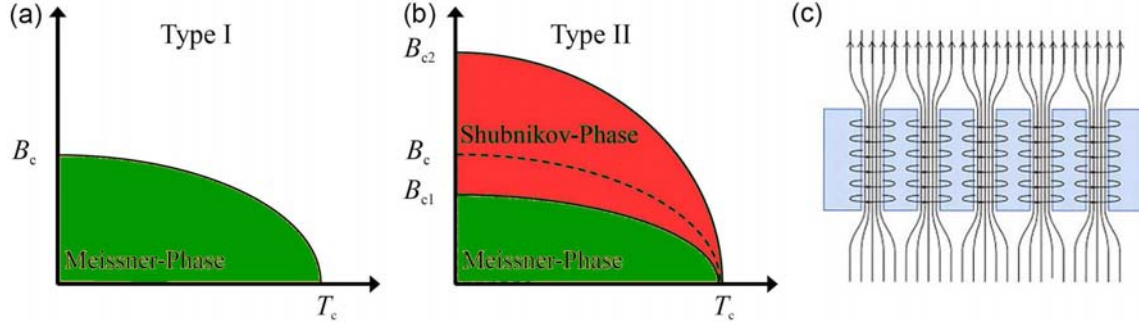


Figure 2.4: (a) Phase diagram of a type-I superconductor and (b) that of a type-II superconductor. In addition to the Meissner phase, there exists another phase above the first critical field B_{c1} which is a mixed state of superconducting bulk interspersed by normal conducting vortices shown in (c).

2.2.2 Abrikosov Vortices

The intermediate phase of type-II superconductors can be explained in the framework of the Ginzburg-Landau (GL) theory [49]. Originally, the GL theory was introduced to describe the physics of standard type-I superconductors (where the phenomenological description by London fails, e.g. why the superconducting phase can be destroyed by currents and magnetic fields). The theory is based on the idea that the normal metal-superconducting transition is a second-order phase transition. The free energy can then be expressed by an order parameter Ψ (which is finite in the superconducting state and zero in the normal-state). A variation of the free energy yields expressions for the order parameter and the supercurrent density $\mathbf{j}(\mathbf{r})$. The so-called GL equations can be used to derive two characteristic length scales – the coherence length ξ_{GL} , describing the typical scale on which variations of the order parameter occur, and the penetration depth λ_{GL} which is the length scale for current and field variations. Based on those length scales the Ginzburg-Landau parameter can be defined as

$$\kappa = \frac{\lambda_{GL}}{\xi_{GL}}.$$

Abrikosov realized that this parameter, which is a fundamental characteristic of a superconducting material, can be used to distinguish between type-I and type-II superconductors [48]. For $\kappa < 1/\sqrt{2}$ the surface energy at the superconductor-normal state interface is positive and the material is of type-I. If $\kappa > 1/\sqrt{2}$, the free energy is negative at the interface and it becomes energetically more favorable to form a mixture of superconducting and normal-conducting regions.

These normal conducting regions have a tubular shape, carry a certain amount of flux (flux quanta), and are surrounded by circular supercurrents, effectively shielding the normal conducting region from the superconducting bulk. These so called Abrikosov vortices carry at least one flux quantum $\Phi_0 = h/2e$ (two electron charges originating from the Cooper pairs acting as charge carriers [50]) and are characterized by its magnetic field profile (extension in the order of $\mathcal{O}(\lambda_{GL})$), the supercurrent density distribution and the normal conducting core region with a diameter in the order of $\mathcal{O}(2\xi_{GL})$ in which the order parameter is suppressed. With increasing magnetic field, the vortex density also increases until at one point (B_{c2}) the normal conducting core regions overlap and the sample becomes normal conducting.

Taking the Lorentz force between individual vortices, arising from the interaction of the supercurrents of one vortex with the magnetic field of another one, into account, it can be shown that vortices tend to repel each other [51, 52]. This leads to the formation of a stable hexagonal vortex lattice, known as Abrikosov lattice. In the presence of a dc or ac transport current density \mathbf{j} the Lorentz force \mathbf{f}_L results in a collective motion of the Abrikosov vortices. The direction of this vortex movement is oriented perpendicular to both the vortex axis (along the magnetic flux Φ_0) and the applied current since

$$\mathbf{f}_L = \mathbf{j} \times \Phi_0.$$

With the vortices in motion with a velocity of \mathbf{v} , an electric field \mathbf{E} parallel to the current density

$$\mathbf{E} = \mathbf{v} \times \mathbf{B} = \rho_{ff} \mathbf{j}$$

is induced in the superconductor [51, 52] (with \mathbf{B} being the magnetic field averaged over several vortices). The so-called flux-flow resistivity ρ_{ff} is a measure for the dissipation caused by the movement of the vortex lattice.

Since for most applications it is desirable and often stringently required to reduce the losses to the highest possible extent, one has to find ways to prevent the vortices from moving. This can be realized by creating local energy minima which act as pinning centers for the vortices. These energy minima can be defects which weaken the superconducting phase so that the total free energy of the superconductor is minimized if the vortex occupies that position. Defects can also be created artificially, e.g. by periodically placing defect atoms in a lattice structure on top of the superconducting surface or by simply perforating the superconducting material (along the external

field direction) in a regular pattern in the case of thin films [31–40].

In doing so, the pinning potential for vortices can be described by a simple harmonic potential with a pinning constant k_p , resulting in a pinning force of [51]

$$\mathbf{F}_p = k_p \mathbf{x}. \quad (2.1)$$

The resulting equation of motion can then be written as

$$\mathbf{f}_L = \eta \dot{\mathbf{x}} + k_p \mathbf{x} = \mathbf{j} \times \Phi_0. \quad (2.2)$$

Depending on the magnitude of the current density, as well as its orientation with respect to the external field (and hence the flux trapped in the vortex), the vortices remain effectively pinned until the Lorentz force exceeds the pinning force and the viscous movement is again dominant, similar to superconductors without any pinning sites.

2.3 Superconducting Microwave Resonators in Magnetic Fields

In the last sections it was shown that the dissipative vortex movement strongly depends on the current density in the superconducting material, the amount of flux present in the superconductor, and their respective orientation (For a parallel alignment of flux and current the vector product vanishes and hence does the Lorentz force driving the vortex motion!). To get a picture of how superconducting coplanar resonators behave in external magnetic fields it is therefore imperative to know the flux and current density distributions for such a structure. Furthermore, it is necessary to apprehend how external flux penetrates the superconducting thin film structure in a zero field cooled procedure and how the vortex lattice responds to high frequency ac currents.

2.3.1 Current and Flux Distribution

Due to the skin effect any high frequency current flowing in a conductor is mainly located within a thin sheet at the conductor surface. For superconducting materials the corresponding length scale is given by the penetration depth λ_L . For a structure following the coplanar geometry the microwave current density j_{rf} is shown for a cross section of the waveguide and the case that the penetration depth is much smaller than the width of the center conductor S in Figure 2.5 (a) according to [53]. It is to note that the absolute value of the current density is maximized at the conductor edges.

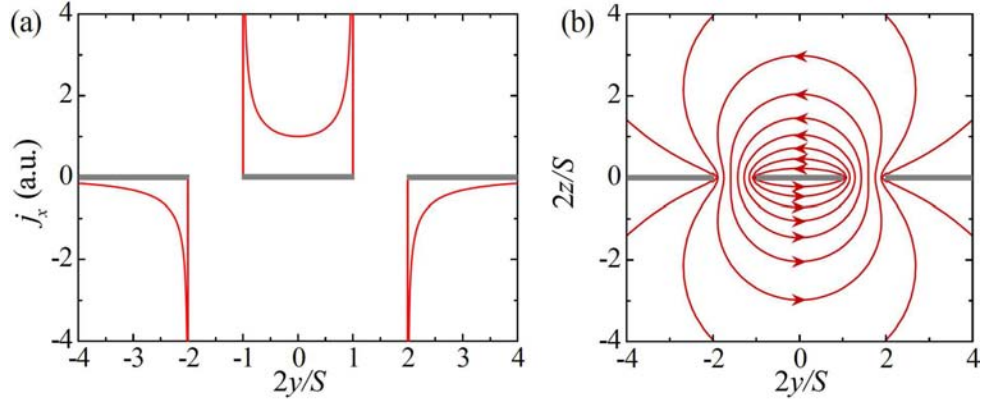


Figure 2.5: (a) Current density amplitude along the cross section of the coplanar resonator structure. (b) Magnetic field lines. Figure modified from [41]

On the other hand, the microwave magnetic field B_{rf} , generated by the alternating microwave current j_{rf} , encircles the center conductor and is maximized in the gap between center conductor and ground planes (see Figure 2.5 (b)). To determine the behavior of resonators in magnetic field it is therefore important to know how external flux enters the high current density regions of the center conductor and ground planes.

2.3.2 Flux Penetration in Thin Film Structures

Previously, it was already mentioned that for pure Meissner superconductors external magnetic fields are always completely expelled from the material independent from the way the field is applied. It was also described that for type-II superconductors the sample material does not remain a pure superconductor for fields above the first critical field. Considering thin film type-II superconductors, however, the way the flux penetrates the film strongly depends on the way the field application is executed. For a field-cooled scenario the film is already permeated by flux above the critical temperature and a regular vortex lattice is formed when the sample is cooled below T_c . The higher the external flux, the denser the vortex lattice. However, if the film is cooled in zero field, the situation evolves quite differently. The field at the edges of the film is enhanced due to shielding currents and once it exceeds the first critical field vortices start to enter the film from the edges. This first generation of vortices gets pinned at natural or artificial pinning sites close to the edge until the field gets strong enough for the next generation of vortices to enter the film against the repulsive force of the first generation. In this way, the vortices move further and further towards the film center, ‘jumping’ from pinning site to pinning site. This

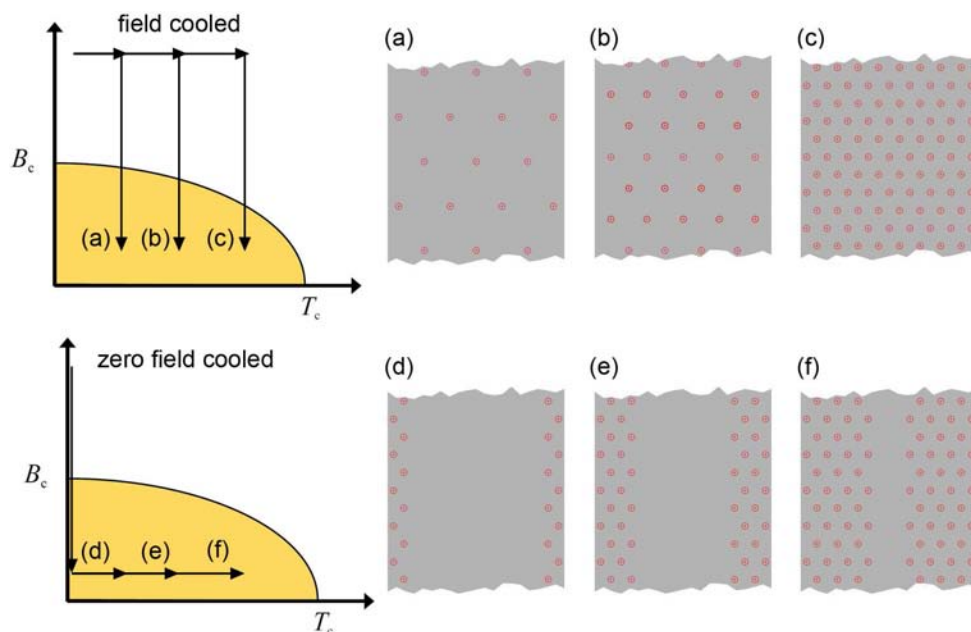


Figure 2.6: Schematic illustration of flux penetration into a superconducting film for different ways of applying magnetic field. (a) to (c): Field-cooled case; the vortex lattice is homogeneously distributed over the film and only the density differs for different field strengths. (d) to (f): Zero-field-cooled scenario; flux enters the film at the edges and with increasing field strength more and more vortices enter and push the lattice further inwards.

kind of flux penetration forms a vortex density gradient at the film edges. This state is also called the critical state since each vortex is nearly subjected to the critical depinning current density provided by all other vortices.

The critical state was first quantitatively modeled by C. P. Bean in 1962 [54, 55] for bulk superconductors as well as slabs and cylinders in longitudinal fields. The model was later on revised by Norris [56] and Brandt and Indenbom [57] for thin films in perpendicular fields. Although these models do not include the individual behavior of vortices or pinning effects but rather assume continuous current and flux densities, they yield results for current and flux penetration which are in good agreement with magneto-optical imaging experiments [58, 59]. In a vortex picture, the continuous flux and current density can be regarded as the combined flux and current density made up by all vortices present in the film. In Figure 2.7 (a) such flux and current density profiles are shown as they enter the film during an external magnetic field up-sweep. The region of maximum current density j_c , in this case the depinning current density, moves further towards the center of the film as the fields strength is increased. The flux density shows a similar behavior with ever growing sharp flux

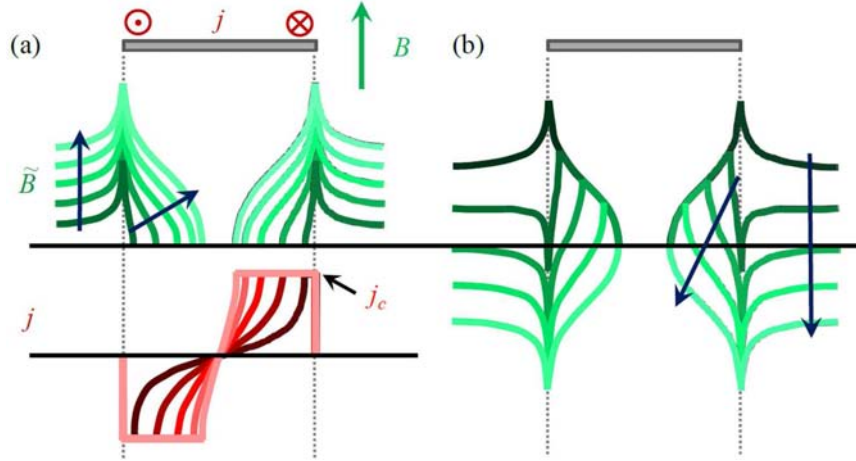


Figure 2.7: Flux and current density profiles across a thin film superconductor while a magnetic field up-sweep (a) and during the down-sweep (b). The arrows indicate increasing (a) and decreasing (b) fields. Figure reprinted from [41].

density maxima at the film's edges.

Most interestingly, however, is what happens once the field sweep direction is reversed at a given field B^* . As can be seen in Figure 2.7 (b) the flux density shows a sharp negative peak at the edge of the film directly after reversing the sweep direction - while the external field is still positive. This effect can be explained by the field lines of the outermost vortices closing around the edge of the film in the reduced field and thus forming a region of negative flux which also partly enters the film as anti-vortices. Vortices and anti-vortices annihilate each other and a vortex free region is formed at the edge of the film.

Recently, D. Bothner *et al.* [60] applied the model by Norris, Brandt and Indenbom to a coplanar waveguide geometry and derived an expression for the spatial distribution of vortices and their driving forces. This quantity is assumed to be proportional to the vortex associated losses and could reproduce the hysteresis loops of the inverse quality factor for perpendicular fields very well. Figure 2.8 shows the losses obtained from experimental data and the calculated losses derived from the spatial current and flux distributions and the vortex movement driving forces. Both plots show a reduction of the losses starting directly after reversing the field sweep direction. This behavior is due to the above mentioned appearance of anti-vortices and depends largely on the current density distribution. For a current density maximized at the film's edges as depicted in Figure 2.5 (a), the effect of a vortex-free region at those edges has a high impact on the vortex induced losses. As the external field decreases ($0 < B < B^*$) the losses also decrease since a small vortex-free region emerges at

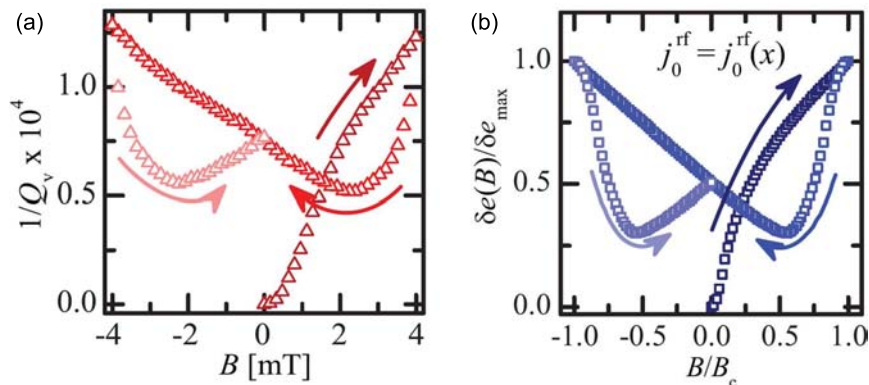


Figure 2.8: (a) Hysteresis loop of the vortex associated losses and the calculated losses (b) derived from the Norris, Brandt, Indenbom model [56, 57]. Figure modified from [60]. ©2012 by the American Physical Society.

the position where the current density is maximized and the Lorentz force would otherwise drive the vortices the strongest. The losses keep on decreasing until the vortex-free area has moved so far into the interior of the film that it has no big effect on the losses anymore and the increasing number of anti-vortices at the current density maxima get more and more dominant.

For this work, the magnetic field dependence of the quality factor for a parallel applied field are of greater interest. D. Bothner *et al.* also investigated this scenario and found that the classical Bean model flux density distributions lead to a better agreement with the experimentally obtained results. A precise analysis, however, gets increasingly difficult since (i) one has to ensure absolute parallel alignment of field and film and (ii) the film thickness is only ≈ 300 nm which is just about three times the penetration depth ($\lambda_{\text{eff}} \approx 100$ nm) and therefore only 1.5 times the diameter of an Abrikosov vortex. In our case, guaranteeing absolute parallel alignment is not possible and a misalignment of ± 1 to $\pm 3^\circ$ is within the error (a misalignment of only 0.5° at 100 mT already yields a perpendicular component of 1 mT which has severe effects on the losses, cf. Figure 2.8 (a)).

note

The above described properties of type-II superconductors and superconducting thin films in the presence of external magnetic fields and applied currents and their consequent implications for superconducting coplanar waveguides should only be regarded as a summary or an

outline. For more details one should consult [41, 60] and references therein. This part was merely meant to provide an overview and to point out that, from an applicational point of view, the performance of superconducting circuitry in magnetic fields can be enhanced by a strategically placement/introduction of pinning sites.

3 Investigated Systems

In this work four different materials were studied for varying purposes.

1. An organic radical of the Nitronyl-Nitroxide family,
2. CrIII centers in corundum (Al_2O_3 ; sapphire),
3. a gadolinium (Gd) based single ion magnet, and
4. the heavy fermion metal YbRh_2Si_2 .

While the organic radical as well as CrIII centers in sapphire were used as model systems to prove the working principle of the presented technique the Gd based single ion magnet and the heavy fermion metal YbRh_2Si_2 lead to results that lack precedent observations (at least in the temperature and field range accessible with this technique). This section will briefly introduce those materials while restraining itself to the magnetic properties of each individual system.

3.1 Nitronyl-Nitroxide Radical NITPhOMe

The radical NITPhOMe, which is a short form of the IUPAC expression 2-(4'-methoxyphenyl)-4,4,5,5-tetra-methylimidazoline-1-oxyl-3-oxide, is a member of the Nitronyl-Nitroxide family. Those or similar radicals represent very clean and isotropic spin $1/2$ systems that are often used as spin labels in biological systems [61] as well as building blocks for molecular magnets (single molecular magnets, single chain magnets) [62–64]. The molecular structure is given in Figure 3.1.

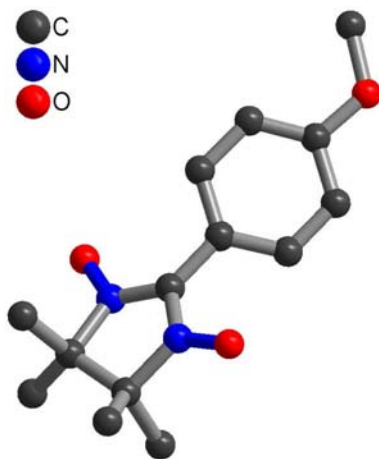


Figure 3.1: Molecular structure of NITPhOMe. The spin density is maximized around the N-O bonds.

In molecular magnet systems those radicals can act as ligands separating neighboring molecules or chains from each other. Even more so, by tuning the ligands of molecular magnets the magnetic behavior can be tailored to a large amount (more in section 3.3).

3.2 Chromium III in Al_2O_3

Chromium-doped corundum (ruby, $\text{Al}_2\text{O}_3:\text{Cr}^{3+}$) is a well studied material with a more complex spin level diagram than the simple spin $1/2$ compound NITPhOMe. This makes it a perfect model system to demonstrate the abilities of the broadband technique.

Ruby was thoroughly investigated in the early days of the maser and the laser [65–72]. The spin Hamiltonian of this $S = 3/2$ system can be given as

$$\mathcal{H} = \mu_B \mathbf{H}_{\text{ext}} \cdot \mathbf{g} \cdot \mathbf{S} + D \left[S_z^2 - \frac{1}{3} S(S+1) \right]. \quad (3.1)$$

The first term expresses the Zeeman splitting with the Bohr magneton μ_B , the g -

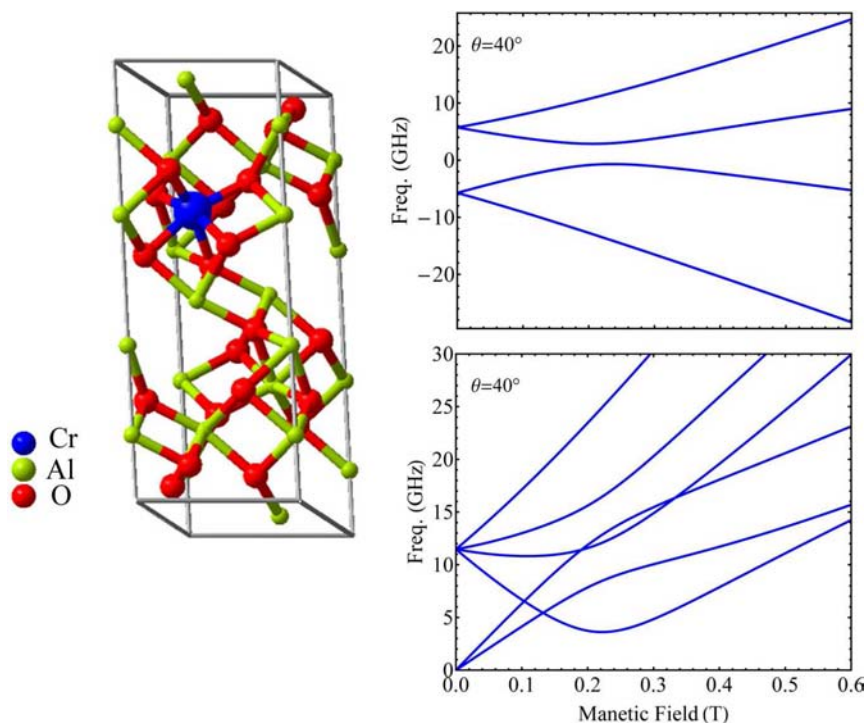


Figure 3.2: Crystal structure of ruby. The left panel shows the unit cell of ruby with one Al atom substituted by Cr. On the right side are the Eigenvalue solutions to the spin Hamiltonian (top) and the resulting possible transition (bottom) for a field orientation of $\theta = 40^\circ$.

tensor \mathbf{g} and the external field \mathbf{H}_{ext} . The second term describes the anisotropy with the zero-field splitting term D . The solutions to this Hamiltonian are discussed in more detail in section 6.2. The crystal structure as well as the energy Eigenvalues and possible transitions as a function of magnetic field are shown in Figure 3.2 for an orientation of the external field with respect to the crystallographic c -axis of $\theta = 40^\circ$. Since the anisotropy term is in the order of a few GHz ($D \approx -5.7$ GHz) the $m_s = \pm 3/2$ and $m_s = \pm 1/2$ doublets are separated in energy by $\Delta\mathcal{E}/h \approx 11.4$ GHz, thus rendering ruby into a perfect candidate to test the performance of the broadband ESR technique for multilevel spin systems.

3.3 Gadolinium III based Single Ion Magnet

In contrast to magnetism as experienced in everyday life, which stems from a collective arrangement of magnetic moments, molecular magnets represent a new and interesting playground concerning observable quantum phenomena and functionalization [73–76]. One individual magnetic molecule can, for example, maintain its magnetization for extremely long times (several months!), provided sufficiently low temperatures (several K) [73]. It can therefore be regarded as a tiny magnet. This behavior is further emphasized by the observation of a magnetic hysteresis otherwise only known from bulk ferromagnetic materials.

Molecular magnets consist of a magnetic core surrounded by a ligand shell. Both building blocks can be artificially synthesized and their physical and chemical properties can be tailored to a great extent according to the desired functionality. By engineering the type and interaction of the magnetic elements in the core, one can generate a giant-spin ground state, a typical characteristic of these magnetic systems. By configuring the ligand shell, on the other hand, one can tailor the magnetic anisotropy, resulting in easy and hard magnetic axes and a zero field splitting of the ground state multiplet.

The origin of the magnetic anisotropy lies in exchange anisotropy, field dependent g value anisotropy and, in most cases of molecular magnetism, in the single ion anisotropy, which depends on the interaction between the spin orbit coupling and the crystal field. This results in a preferential orientation of the magnetization leading to a double well potential for different spin states. Depending on the height of the energy barrier between those wells, the molecule shows slow relaxation of the magnetization leading to the opening of a hysteresis cycle for sufficiently low temperatures. Steps in this hysteresis are due to the macroscopic quantum tunnelling which represents another intriguing property of molecular magnets. This tunnelling occurs

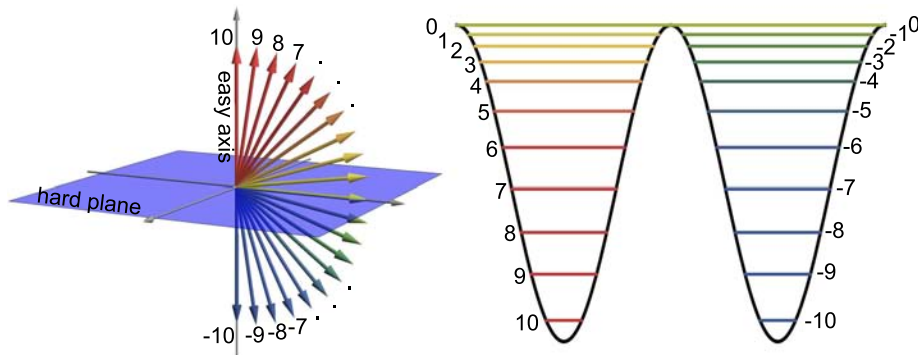


Figure 3.3: (a) Schematic picture of a Spin $S = 10$ magnetic molecule. Shown are different m_s states of the ground state multiplet and their orientation with respect to the easy axis and hard plane. (b) Since the magnetization is preferentially oriented parallel or antiparallel to the easy axis the resulting energies of the spin states form a double-well potential.

since the m_s states which correspond to different orientations of the spin ground state, are quantized in energy. At certain magnetic fields two opposing m_s states can be degenerate in energy, opening up an additional relaxation channel using quantum tunnelling. The energy difference between individual m_s states within the ground state multiplet are typically in the microwave regime, making these compounds favorable candidates for coupling them to controllable solid state microelectronic devices (SQUIDs, quantum dots, graphene, etc.).

The compound studied in this work belongs to the class of single ion magnets (SIMs) which represent a borderline case of the more general class of single molecular magnets (SMMs). While most SMMs are complexes built up by a number of metallic centers, interconnected and shelled by (typically organic) ligands, SIMs contain only a single metallic ion. Within one such SMM complex the different magnetic moments are coupled via an exchange interaction J_{ex} , thus forming a so called giant spin of the whole molecule (Not necessarily the sum of all S_i contributions. The total spin depends on the sign of the exchange interaction between the individual constituents). In the case of SIMs the total magnetic moment is simply given by that of the metallic ion. Both classes, however, typically show a strong magnetic anisotropy which is caused by the metallic center itself as well as the ligand shell and gives rise to an easy axis and a hard plane (or vice versa). Both families can show hysteresis as well as (extremely) long relaxation times of the magnetization which makes them promising candidates for high density magnetic memories, molecular spintronic devices or quantum bits in quantum information processing, just to name

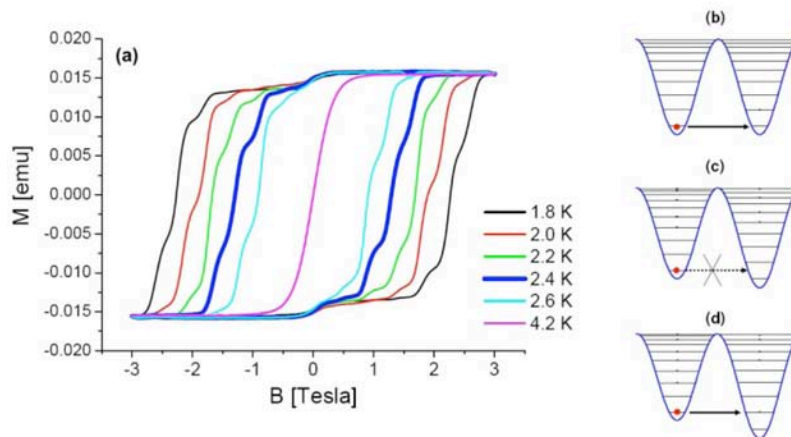


Figure 3.4: (a) Magnetic hysteresis of a Mn_{12} -acetate single crystal at different temperatures with an axially applied magnetic field. The steps indicate changes in magnetization due to spin tunneling at zero field (b) and into excited states (d). Between those steps the energy levels are off resonance and the tunneling probability is highly reduced (c). Figure reprinted from [77].

a few.

The system investigated in this work has a Gd^{3+} ion as metallic center and is surrounded by Hexafluoroacetylacetonate ligands which are well-known for their ability to efficiently block magnetic interactions with the environment. The remaining linking positions of the resulting $[Gd(hfac)_3]$ complex can be used to coordinate the 5,5'-di-*t*-butyl-2,2'-bipyridine ligand (which also provides good magnetic shielding) creating point-like magnetic centers in the form of $[Dy(hfac)_3 5,5'$ -di-*t*-butyl-2,2'-bipyridine] (in the following Gd^t but) complexes even in a tightly packed crystal lattice. The molecular structure as well as a picture of a face indexed single crystal are shown in Figure 3.5. In fact, this particular molecule is just a first specimen in a family of molecular magnets that can be tuned according to the favored behavior [78]. The idea is to set a chemical, molecular toolbox to synthesize molecular magnets tailored towards the desired magnetic properties. In order to do so, three main building blocks have to be provided – a magnetic center with strong anisotropy, a linking block which can be modified to mediate either ferromagnetic or antiferromagnetic exchange interaction and a shielding block, all three of which have to be interconnectable to a high degree. A selection of possible molecular magnet structures synthesized by combining such building blocks is shown in Figure 3.6. The material investigated in this work is labelled with (1). In binuclear compounds the

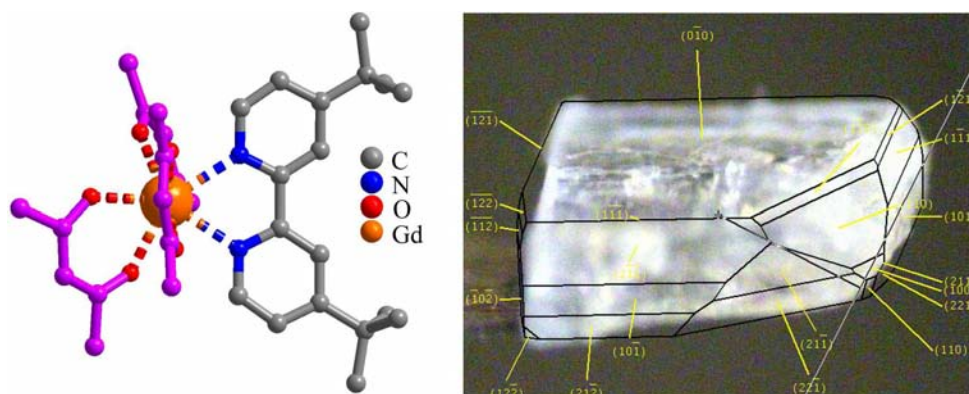


Figure 3.5: Left: Molecular structure of Gd based single ion magnet (for clarity the hydrogen and fluorine atoms are not drawn). Right: Single crystal of Gd^{3+} but with its crystal faces indexed.

interaction strength (exchange interaction) can be tuned by modifying the linking block as shown in (2) and (3). The molecule displayed in (5) contains already three magnetic centers and the number of metallic ions could even be further increased.

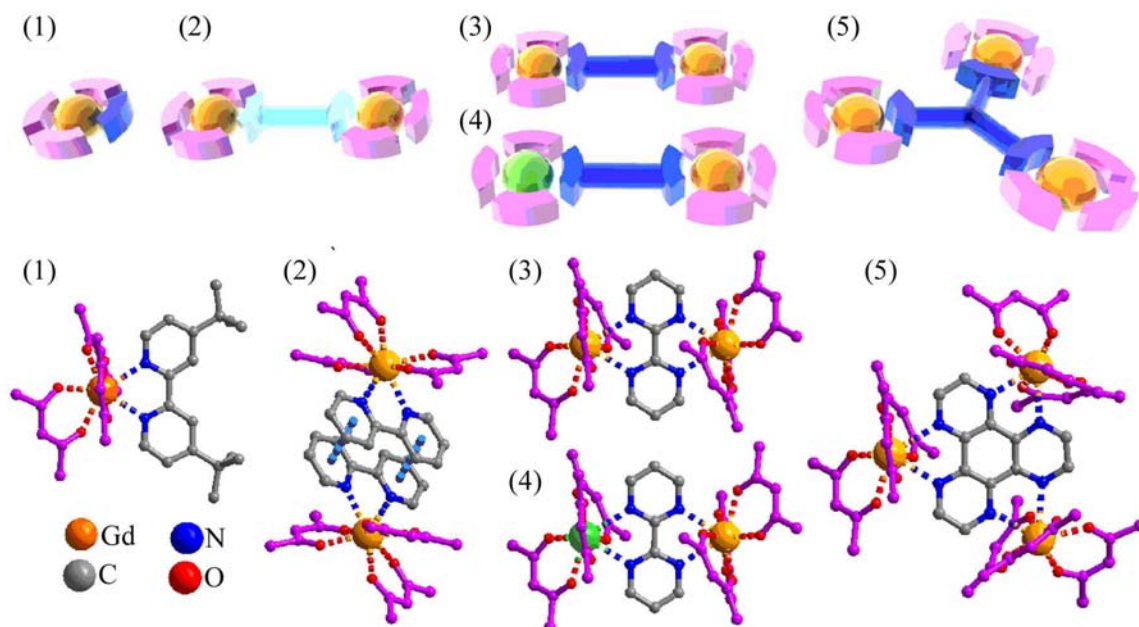


Figure 3.6: Schematic display (top) and molecular structures (bottom) of different molecular magnet systems derived from the same building blocks. The investigated material is shown in (1). (2), (3) and (4) are binuclear molecular magnets with a weaker coupling in (2) and a heteronuclear structure in (4). The compound displayed in (5) couples three magnetic centers with each other. Figure reprinted from [78]

As for the mononuclear Gd^3 but, no prior measurements concerning the magnetic properties were performed. The ESR measurements presented in this thesis were carried out on a single crystal as shown in Figure 3.5 with the (010) face flat on the waveguide and the crystal slightly rotated counter-clockwise so that the magnetic field direction and the (101) face normal enclose an angle of about $\sim 20^\circ$ (in this case the magnetic field points along the crystallographic c -axis). This alignment was chosen since the unit cell contains four molecules with different orientations of the spin moments. If the external magnetic field, however, is aligned along c , the transverse spin components cancel each other out and only the projection along the magnetic field remains.

3.4 Heavy Fermion Metal YbRh_2Si_2

Systems that feature strong electron-electron correlations typically show very interesting physical phenomena once these correlations become the dominant energy scale. Heavy fermion metals present just one striking example of such systems. Reasonable for the ‘heavy’ ground state is the Kondo effect or, more precisely, the formation of a so-called Kondo lattice below a certain threshold temperature, termed the Kondo Temperature T_K . The Kondo effect in general describes the coupling of a local magnetic impurity to the bath of conduction electrons (CE) in terms of scattering processes of CE at those local moments. The situation changes once the scatterers can no longer be considered as dilute impurities randomly distributed within the sample but become a stoichiometric part of the crystal structure. In this case each unit cell contains (at least) one magnetic moment and the Kondo lattice is formed at sufficiently low temperatures. In such a case the local moments (typically d or f orbital electrons) and the conduction electrons hybridize and a small gap is formed at the Fermi energy. The otherwise sharp d or f states broaden significantly and the local spin moments get screened by the CE. As a result, the effective mass of charge carriers close to the Fermi level is highly enhanced (speaking of heavy quasiparticles). A strong coupling of local spins to that of the itinerant CE also favors the Ruderman-Kittel-Kasuya-Yoshida (RKKY) interaction which describes the spin ordering of local moments mediated by the spin bath of conduction electrons. Are both interactions of the same energy scale, the ordering RKKY interaction and the Kondo screening compete with each other and, depending on a tuning parameter (pressure, doping, magnetic fields), the ground state is either a magnetically (ferro or antiferromagnetic) ordered state (RKKY dominant) or a paramagnetic Fermi-liquid (Kondo screening dominant). The heavy fermion metal YbRh_2Si_2 is just such a system. As a function

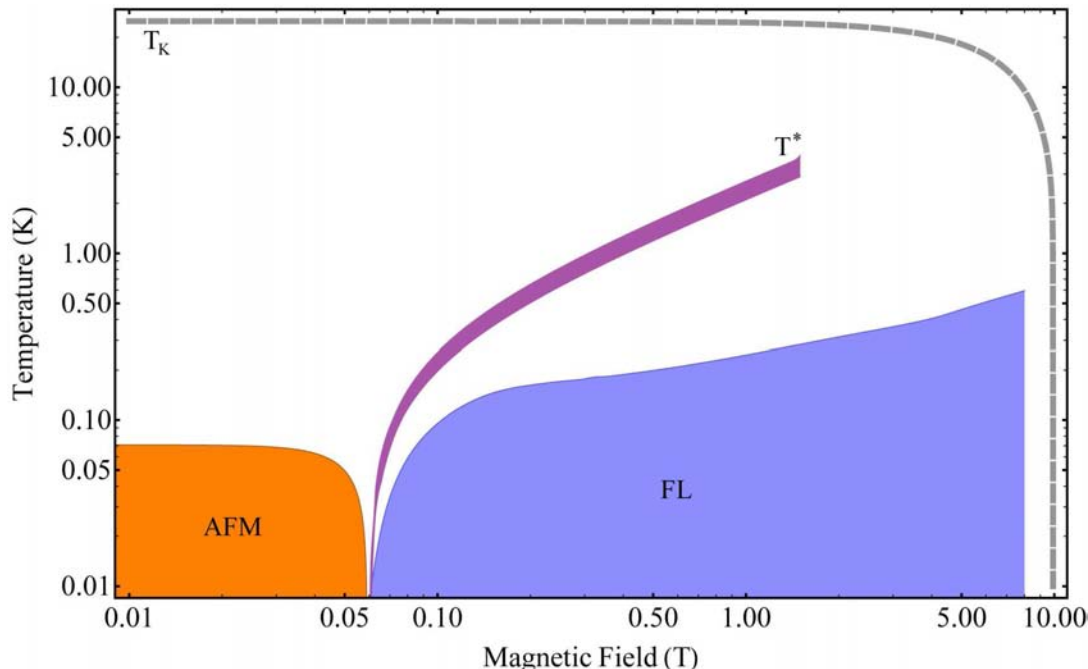


Figure 3.7: Low temperature phase diagram of YbRh_2Si_2 . The dashed gray line represents the Kondo crossover regime at $T_K = 25$ K (for $H = 0$) and the corresponding field which suppresses heavy quasiparticle behavior for $T/T_K < 1$. At low fields and temperatures the system orders antiferromagnetically (AFM). By increasing the field at zero temperature the order is suppressed and the system undergoes a quantum phase transition towards a Landau Fermi-liquid (region where the electrical conductivity exhibits a T^2 behavior; shown in blue). An additional low energy scale is given by the T^* crossover regime which marks the position of crossover in the Hall resistivity and magnetostriction (drawn in dark purple).

of external magnetic field the antiferromagnetic ordering temperature (Néel temperature T_N) can be suppressed down to zero Kelvin creating a quantum critical point (QCP). While ordinary second order phase transitions are driven by thermally activated fluctuations, continuous quantum phase transitions (QPT) happen at absolute zero temperature in the absence of thermal energy and are therefore driven by vacuum quantum fluctuations. Although the QPT can never be observed directly the QCP has severe implications also at finite temperatures. One common signature of a QCP is the formation of a funnel shaped regime (above the QCP in the temperature-field phase diagram; see Figure 3.7) of non-Fermi-liquid behavior. This is revealed, for example, by a linear T dependence of the resistivity compared to a T^2 behavior in the Fermi-liquid regime. In fact, the low temperature phase diagram of YbRh_2Si_2 was obtained by a vast number of experimental techniques such

as electronic (magneto) transport, specific heat, thermal conductivity, magnetostriction, magnetic susceptibility, Hall effect and nuclear magnetic resonance [see 79, and references therein].

Here, obviously, the focus is set on ESR measurements. It has to be pointed out that the observation of ESR at temperatures below the Kondo temperature was a huge surprise on its own. In the Kondo regime the local moments are believed to be sufficiently screened by CE to not allow for any observation of magnetic resonance. This contradiction proves that the origin of ESR in YbRh_2Si_2 cannot be attributed to the local moments alone. After the first measurements of ESR [80, 81] on YbRh_2Si_2 many more followed [82–93] probing the phase diagram at various fields and temperatures to learn more about the magnetic nature of YbRh_2Si_2 and to solve the conundrum regarding the origin of ESR in this Kondo screened system. A comprehensive study was given by Schaufuss *et al.* [88] comparing ESR data, in particular the temperature dependence of the g -factor and the linewidth with that of specific heat and the Knight shift in ^{29}Si nuclear magnetic resonance. Striking similarities can be found between those quantities, strongly suggesting the heavy quasiparticles as the origin of the ESR response.

In addition to the numerous experimental studies theoretical considerations were made [94–99] regarding the nature of ESR in YbRh_2Si_2 and the expected temperature dependence of the line shift and linewidth were discussed in detail and found to be in good agreement to previous measurements. Shortly pointing out the results, it is expected that the line shift vanishes in the FL regime and follows a logarithmic ($\propto \ln T$) temperature dependence in the non-Fermi-liquid region while the linewidth goes with T^2 within the FL regime and is linear in T for $T_{\text{FL}} < T < T_K$. However, due to technical limitations of typical ESR spectrometers the truly interesting region close to the QCP remained unexplored. The lowest temperature for which ESR experiments are reported so far is 500 mK [92] at magnetic fields of about 0.7 T. This measurement therefore was able to cross the T^* line but could not enter the FL regime. At the crossing of T^* a change of slope in the temperature dependence of the g factor as well as a kink in the absorption linewidth could be observed.

In this work, an novel way of recording ESR spectra is presented that allows for the detection of magnetic resonance for many frequencies (of free choice) as well as ultra-low temperatures down to 40 mK. With this technique, which is based on superconducting coplanar resonators, it is for the first time possible to deeply enter the Fermi-liquid state close to the quantum critical point and probe the temperature dependence of the ESR parameters.

4 Design and Fabrication

To achieve optimal performance of the devices in the given experiments the design of the coplanar waveguides and resonators had to follow a few guidelines. It had to be made sure, that

- the characteristic impedance matches the one of the connected microwave equipment (namely $Z_0 \stackrel{!}{=} Z_{\text{ext}} = 50 \Omega$),
- the distance to grounded lateral walls and to the conductive backing has to be long enough to remain in the coplanar limit,
- the distance between neighboring lines has to be long enough to avoid crosstalk,
- the gaps in the center conductor of the resonant structures have to be large enough to work in the under coupled regime and at the same time small enough to get enough signal transmitted.

By fulfilling all above requirements a whole family of coplanar waveguides and coplanar waveguide resonators was designed and later on fabricated.

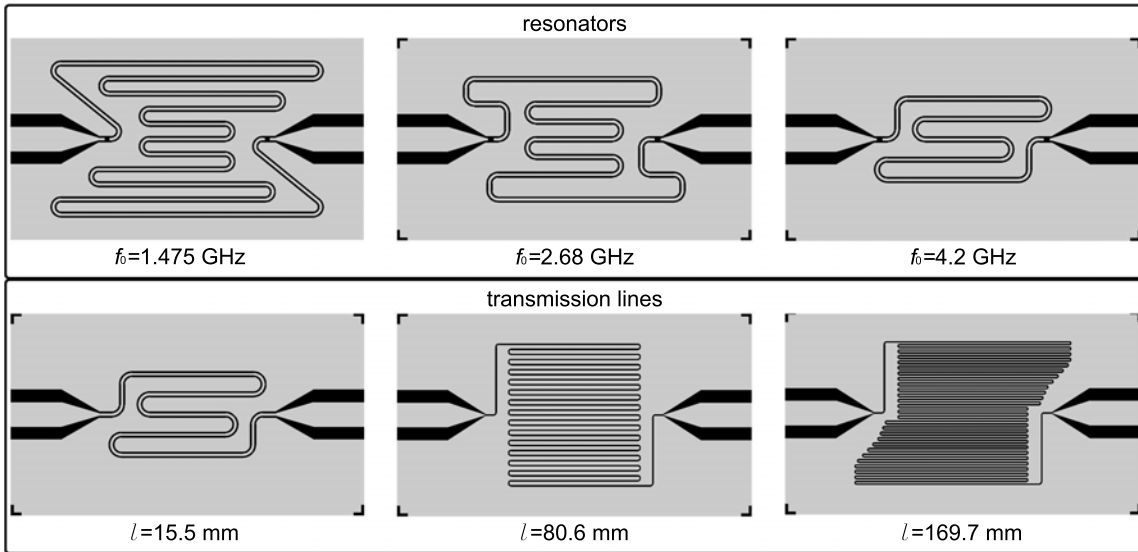


Figure 4.1: Top panel: Selection of different designs of coplanar waveguide resonators for different resonator lengths and hence different resonance frequencies. Bottom panel: Selection of a few coplanar waveguide transmission lines with different center conductor widths and lengths to probe different sample areas.

4.1 Characteristic Impedance

As mentioned already above in section 2.1, the characteristic impedance of a coplanar device is determined by its geometrical parameters. The impedance of the device should be matched to that of the environment to avoid reflections at points of mismatch (the reflection coefficient Γ_{12} is given as $\Gamma_{12} = (Z_2 - Z_1)/(Z_2 + Z_1)$ for different characteristic impedances $Z_{1,2}$ in different transmission line segments 1, 2). A schematic view of all relevant parameters is shown in Figure 4.2. A center conductor with a width S is separated from the ground planes by a gap of width W on top of a substrate with known relative permittivity ϵ_r . The whole structure is surrounded by vacuum and two metallic sheets on top and at the bottom, respectively. Using conformal mapping techniques [101] the unknown conductor separation W can be calculated for any given S so that the characteristic impedance of the coplanar waveguide is approximately 50Ω .

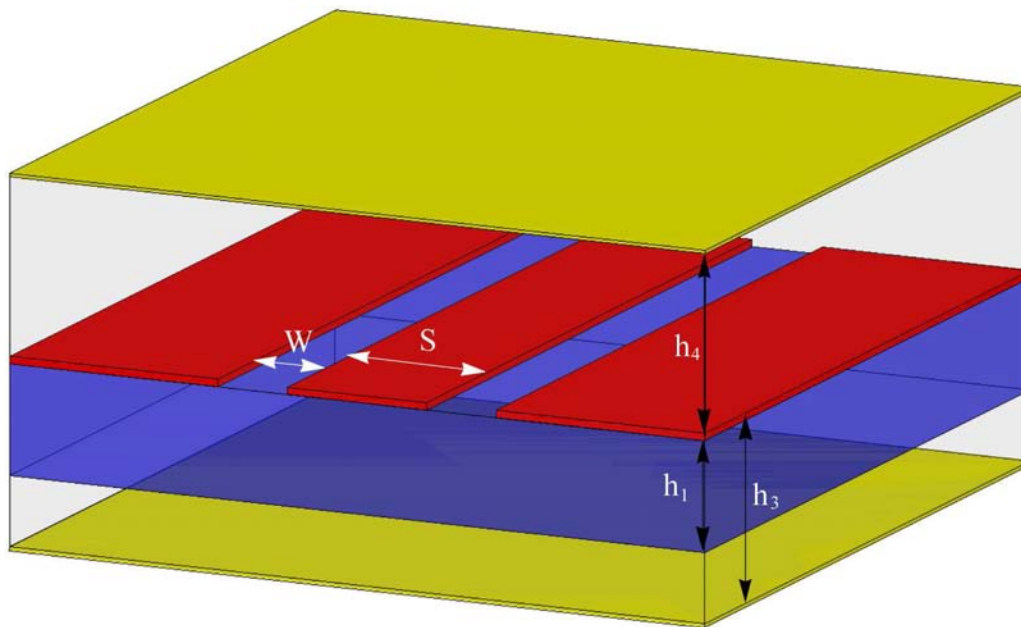


Figure 4.2: Schematic view of the model used for calculating the characteristic impedance of the coplanar waveguide. The structure is modeled as an infinitely thin metallic sheet (red) on top of a substrate (blue) surrounded by vacuum between two grounded planes (yellow).

To obtain the waveguide properties of such a device, one can introduce an effective dielectric constant ϵ_{eff} which combines the substrate and the air/vacuum part of the waveguide surroundings. As a rough approximation, ϵ_{eff} can be given as the average of the two material permittivities above and below the waveguide. To gain more

accurate results, which also take the relative structural dimensions into account, the conformal mapping techniques mentioned above have to be employed. In that case, the effective dielectric constant of the whole assembly can be expressed as

$$\varepsilon_{\text{eff}} = 1 + q(\varepsilon_r - 1)$$

with

$$q = \frac{K(k_1)}{K(k'_1)} \left[\frac{K(k_3)}{K(k'_3)} + \frac{K(k_4)}{K(k'_4)} \right]^{-1}$$

with $K(k_n)$ being the complete elliptic integral of the first kind and

$$\begin{aligned} k_1 &= \frac{\sinh(\pi S/4h_1)}{\sinh([\pi S + 2W]/4h_1)} & k'_1 &= \sqrt{1 - k_1^2} \\ k_3 &= \frac{\tanh(\pi S/4h_3)}{\tanh([\pi S + 2W]/4h_3)} & k'_3 &= \sqrt{1 - k_3^2} \\ k_4 &= \frac{\tanh(\pi S/4h_4)}{\tanh([\pi S + 2W]/4h_4)} & k'_4 &= \sqrt{1 - k_4^2}. \end{aligned}$$

The resulting characteristic impedance is given as

$$Z_0 = \frac{60\pi}{\sqrt{\varepsilon_{\text{eff}}}} \left[\frac{K(k_3)}{K(k'_3)} + \frac{K(k_4)}{K(k'_4)} \right]^{-1}.$$

4.2 Minimal Distance of neighboring Lines

As can be seen from the exemplary designs shown in Figure 4.1 the actual coplanar line is not a straight one, but a meandering structure on top of the substrate. This is done for several reasons. For a coplanar waveguide resonator, the length of the capacitively coupled section of the center conductor determines the resonance frequency. Resonators designed and fabricated in this work have their fundamental mode frequency in the range from 1.475 GHz to 11 GHz which translates into a range of strip lengths varying from $\ell \approx 5.8$ mm (for $f = 11$ GHz) to $\ell \approx 43.3$ mm (for $f = 1.475$ GHz) via the relation

$$\ell = \frac{c}{2\sqrt{\varepsilon_{\text{eff}}}f}.$$

For reasons of practicability, the individual chip size is to be kept the same regardless of the actual resonance frequency. It is therefore reasonable to loop the resonator

line on a much smaller chip until the desired length is reached.

A much more important reason for this, however, is the avoidance of parasitic box modes in the aimed-for frequency range. In the course of the experiment the chip is placed inside a grounded metallic box. Are the dimensions of the enclosed space in the order of half the wavelength in free space ($\lambda_{\text{vac}}/2 = c/2f$, c : vacuum speed of light) for a driving frequency f , standing waves can form in the box and lead to a much more complex transmission spectrum. Keeping the length scales of this enclosed volume small, hence using small chip sizes pushes these modes towards higher frequencies and out of the range to be investigated with the actual device.

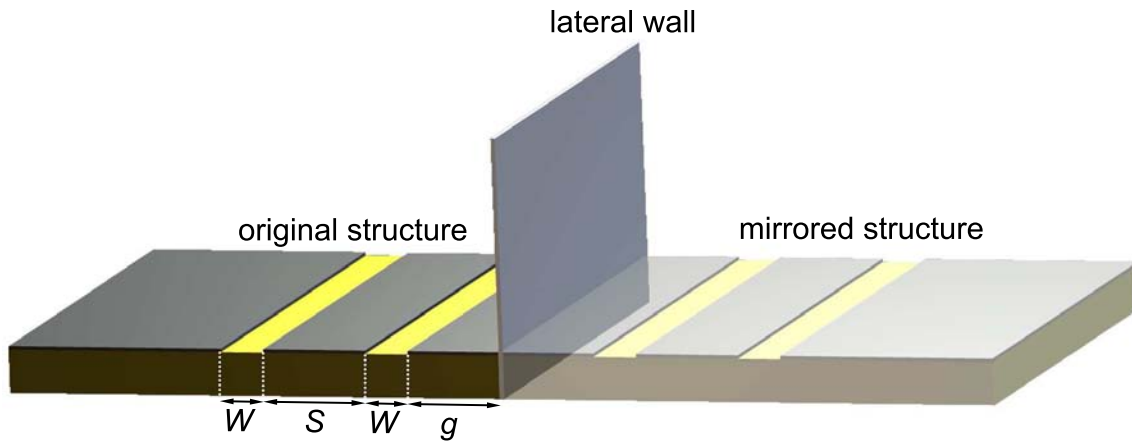


Figure 4.3: Schematic view of a coplanar waveguide structure with a grounded lateral wall. The distance g has to be long enough to avoid a distortion of the mode profile due to the lateral wall. The principle of image charges then ensures, that a parallel line separated by at least $2g$ will be far enough apart so that both lines can be regarded independently.

Having the coplanar line running in meanders on top of the substrate unavoidably leads to parallel lines close to each other. To keep the coplanar character of the waveguide and not to deform the mode profile one has to make sure that the individual lines are far enough apart (avoid crosstalk between the lines).

To estimate the minimal distance of those neighboring lines one can consider a coplanar waveguide structure with a grounded lateral wall. Is the wall very close to the coplanar line (small g in Figure 4.3), the electric field will be distorted with some of the electric field lines ending on the wall. For very large g the effect of the wall is negligible and the waveguide behaves as with infinitely extended ground planes. Instead of a metallic wall one can construct a new structure being the mirrored image of the original one and the problem remains unchanged (method of image charges with the negligence of retardation effects in this quasi static model).

Calculations have shown that, with $g = S/2 + W$ the characteristic impedance, and therefore the propagation properties of the electromagnetic wave are within 1% compared to those for very large g [101]. One can therefore avoid crosstalk between the lines by separating them by at least $S + 2W$.

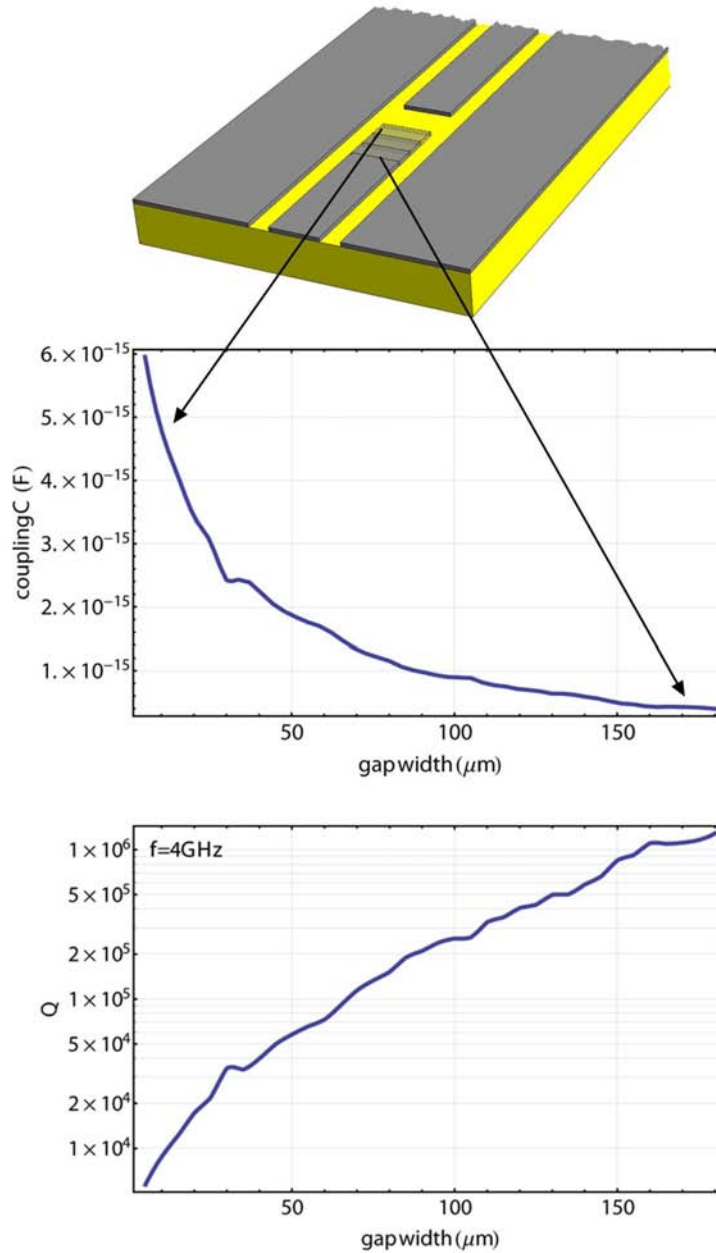


Figure 4.4: Scheme to determine the coupling capacitance gaps. (a) Different gap sizes and their respective mutual capacitances (b) between input feed and resonator were simulated. Using these values, the resulting coupling quality factor Q_c was calculated for a given frequency and a suitable value was picked for the design of the gaps.

4.3 Modelling the Coupling Gaps

Designing the coupling gap of the resonator is of essential importance for the performance of the device. As already mentioned earlier in section 2, the measured, so called ‘loaded’ quality factor Q_l depends on all different quality factors of the complete system

$$\frac{1}{Q_L} = \frac{1}{Q_i} + \frac{1}{Q_e}.$$

It is to point out, that the lowest quality factor determines the loaded quality factor, as it will always be lower than its lowest constituent. For superconducting CPW resonators the internal quality factor Q_i is typically very high (10^5 to 10^6 for low loss substrates and large photon numbers) so that one only has to make sure that the external quality factors Q_e are in the same order of magnitude. The most important part of the external quality factor is the coupling quality factor Q_C . It is given as a function of frequency ω , coupling capacitance C_C and line impedance Z_0 to

$$Q_C = \frac{1}{8\pi^2\omega^2 C_C^2 Z_0^2}.$$

For the resonator designs C_C was simulated as a function of gap length ℓ_C (see Figure 4.4 (a), (b)) using finite element software and the resulting capacitance was then used to evaluate the coupling quality factors at the desired resonance frequency as a function of ℓ_C (Figure 4.4 (c)). Typically, resonators of the same resonance frequency were designed with different coupling capacitances with Q_C ranging always between 10^5 and $2 \cdot 10^7$.

4.4 Field Simulation of Resonator Structures

In order to better understand the field distribution for the designed layout in the experimental environment (for different boundary conditions as will be shown below in section 5) simulations of the actual structures had been performed using CST Microwave Studio software. With this software it is possible to model any device using CAD tools, simulate an electromagnetic excitation and study the response of the system. As a simple model a straight resonator was considered as shown in Figure 4.5 which also shows the mesh cells CST Microwave Studio generates to solve the problem. The finer the mesh structure, the more accurate the solution (the mesh cells have to be small in those areas that show large electric and magnetic field gradients).

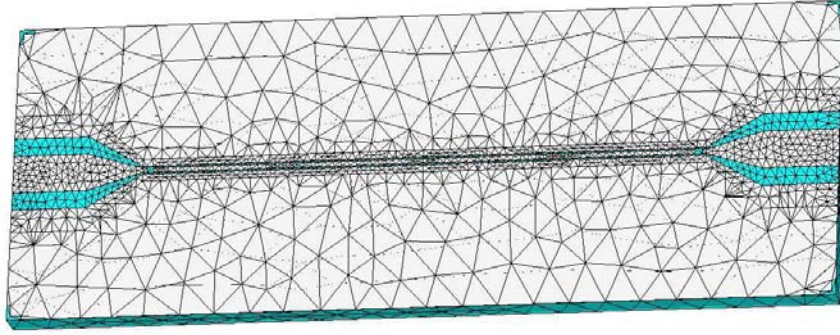


Figure 4.5: Modeled straight resonator. The mesh structure which is used to solve the problem is clearly seen. Close to the resonator line the area is meshed more densely to achieve more accurate solutions.

In this model the resonator length is $\ell = 7.2$ mm which results in a resonance frequency of $f \approx 8.88$ GHz. The resonance frequency gained from the simulation results is approximately 8.9 GHz which is in good agreement with the designed value. The simulated spectrum as well as the field distribution is shown in Figure 4.6. The S -parameter S_{21} (transmission coefficient) was fitted to a Lorentzian model (shown as the dashed curve) which yielded a quality factor of

$$Q = \frac{f_0}{\Delta f_0} \approx 37400.$$

The electric and magnetic field amplitude patterns which are shown in Figure 4.6

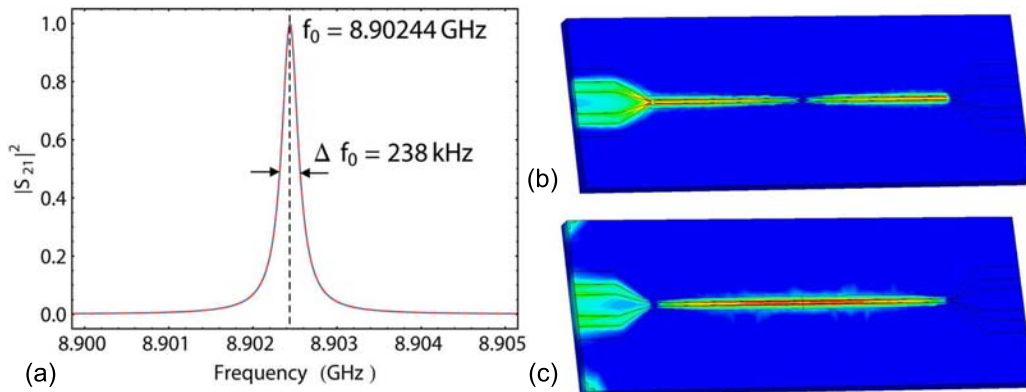


Figure 4.6: Simulation results for the straight resonator. (a) The simulated S_{21} parameter shows a clear Lorentzian shape maximized close to the designed resonance frequency (dashed curve is a Lorentzian fit). (b) and (c): Color coded amplitude patterns for the electric and magnetic field, respectively. The electric field features a node at the center point of the resonator line while the magnetic field exhibits an antinode at that position.

also show the desired form. The electric field has a node in the center position of the resonator ($x = 0$) and antinodes at its ends ($x = \pm 3600 \mu\text{m}$) and the magnetic field shows an antinode in the middle and nodes at ends.

Having demonstrated that the simulation of resonator structures works well for a test layout, the simulation of a real design was performed to get an idea of the spatial distribution of electric and magnetic fields in the region directly above the structure, at the position of the sample in the experiment.

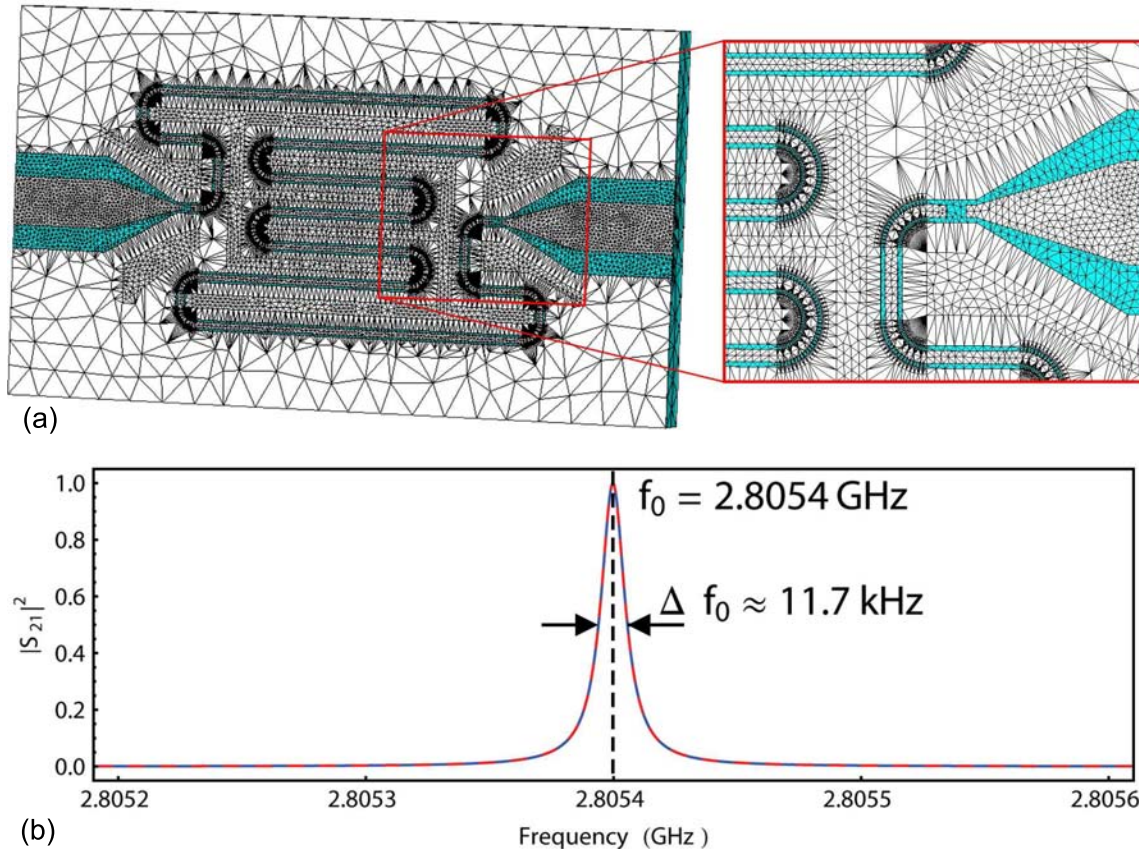


Figure 4.7: (a) Mesh view of a resonator designed for $f_0 = 2.68 \text{ GHz}$. The area around individual lines and between adjacent lines is meshed much finer than that of the rest of the structure. (b) S -parameter results for the simulated transmission properties of the structure. The quality factor evaluates to $Q \approx 2.4 \cdot 10^5$.

The resonator structure is shown in Figure 4.7 (a). The mesh structure for this design is much more complex than for the straight resonator. This is due to the fact, that automatically generated mesh structures tend to be too coarse for this problem, especially in the regions between the lines. Are the mesh cells in these areas too big, those cells lead to interference of neighboring lines and the results will be corrupted

since there are artificially more ways for the signal to propagate than it is the case in reality.

Although great care was taken to mesh the structure, the resulting transmission spectrum shows a resonance at $f_0 \approx 2.8054$ GHz instead of the designed value of 2.68 GHz. This is most likely due to an insufficient dense meshing structure at the curved line segments resulting in a shorter effective length of the resonator line. Further increasing the mesh density was not possible since the computational resources of the computer platform were depleted. However, this offset of the resonance fre-

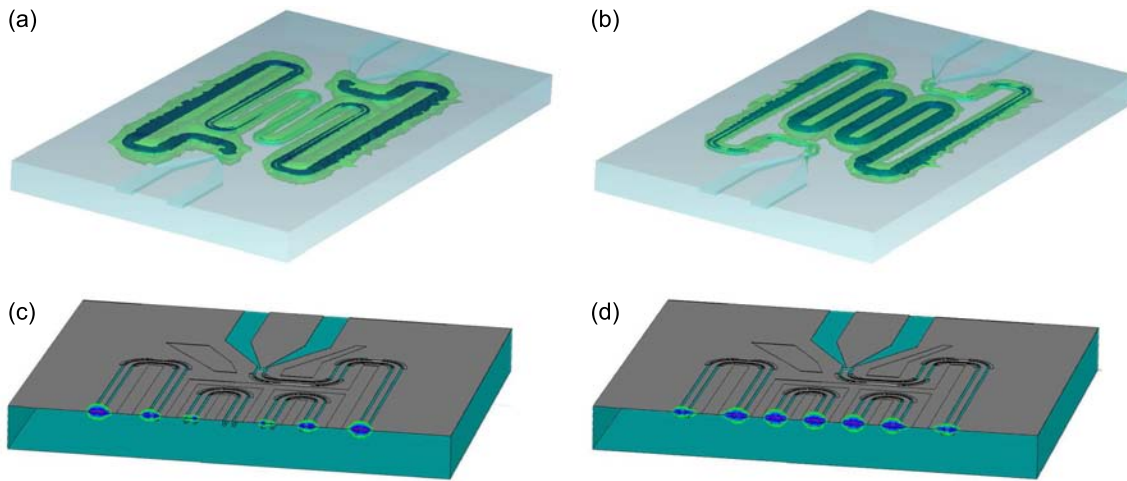


Figure 4.8: (a)+(b) Isosurface representation of electric and magnetic fields, respectively, for two isovalues which differ by the factor of 8. (c)+(d) Cut of the structure at $x = 0$ and isoline representation of electric and magnetic fields ranging from -40 to 0 dB of the maximal value. Both visualizations demonstrate a strong localization of the microwave fields around the coplanar line segments.

quency by about 4.5 % is irrelevant for the studies of the spatial field distribution at the resonance frequency. Figure 4.8 shows the electric and magnetic field arrangement at 2.8054 GHz in two different representations. The top left panel (a) shows isosurfaces of the electric field amplitude at ≈ 4.5 % (inner) and ≈ 0.6 % (outer) of the maximum field amplitude while the top right panel (b) shows the same for the magnetic field at ≈ 2.5 % and ≈ 0.3 % of the maximum value. The lower panel shows field amplitude contours in the cut plane $x = 0$ (middle of the chip structure with respect to the long edge) in a range of 0 to -40 dBm of the field maxima. It is clearly visible, that the microwave fields are highly localized around the coplanar lines and the field amplitude has decreased more than a factor of 10^4 for distances in the range of the center conductor width from the coplanar line center. This fact

is important for the placement of the sample since it is desirable to have as many spins as possible interacting with the microwave field.

4.5 Fabrication

The structures were designed to be placed on 430 μm thick sapphire (Al_2O_3) substrates, cut along the r-plane ($1\bar{1}02$) and polished on top. These substrates are well known for their low dielectric losses and show a relative permittivity of $\varepsilon_r \approx 10$.

The structures were patterned onto a magnetron sputtered 150 nm thick niobium (Nb) film by conventional UV-photolithography followed by reactive ion etching using SF_6 . The wafer was finally diced into individual chips the size of 7 mm \times 4 mm. The whole fabrication process was done in collaboration with the Physikalisches Institut in Tübingen, in particular with the great support by D. Bothner, D. Koelle and R. Kleiner. An overview of the fabricated structures and their geometrical parameters can be seen at Table 4.1. After fabrication most resonators performed within the tolerated error margins (resonance frequencies were in the range of ± 20 MHz from the designed value) exhibiting quality factors in the range from 10^4 to $4 \cdot 10^5$ at 1.6 K. One batch of resonators showed reduced resonance frequencies up to 5 % lower than what they were initially designed for. The reason for this is supposed to be a bad quality Nb film since the film used for these resonators was sputtered using a new Nb target from a new supplier. This assumption was further supported by the fact that the film showed a critical temperature of only slightly above 7 K compared to the standard value slightly above 9 K.

To achieve a better performance in magnetic field some resonators were subjected to yet another fabrication step to create an array of tiny ($\varnothing \approx 300$ nm) holes, so called antidots, to effectively pin the vortex lattice and reduce undesired additional losses due to vortex movement (as described in section 2.2.2). This work was done in collaboration with E. Koroknay, M. Jetter and P. Michler of the IHFG (Institut für Halbleiteroptik und Funktionelle Grenzflächen) in Stuttgart and D. Bothner, D. Koelle and R. Kleiner of the Physikalisches Institut in Tübingen.

To create such an array of antidots, a self assembled monolayer of microspheres with an individual size of 700 nm was transferred to a layer of photoresist on top of the Nb film by a Langmuir-Blodgett deposition process [102] (Figure 4.9 (a)+(b)). This whole assembly was then exposed to UV-light for a very short amount of time. The exposure time is much shorter than it would be necessary for a standard photolithographic mask since each microsphere acts as a microlens and focusses the

S (μm)	W (μm)	G (μm)	f_0 (GHz)	S (μm)	W (μm)	G (μm)	f_0 (GHz)
10	4	5	4.200	10	4	10	4.200
10	4	15	4.200	10	4	20	4.200
10	4	7.5	5.000	10	4	15	5.000
10	4	2.5	6.200	10	4	5	6.200
10	4	10	6.200	10	4	15	6.200
15	6	3.75	6.200	15	6	7.5	6.200
15	6	15	6.200	15	6	22.5	6.200
20	8	20	4.200	20	8	30	4.200
20	8	40	4.200	20	8	25	5.000
20	8	40	5.000	20	8	5	6.200
20	8	10	6.200	20	8	20	6.200
20	8	30	6.200				
30	12	30	4.200	30	12	40	4.200
30	12	50	4.200	30	12	40	5.000
30	12	60	5.000	30	12	7.5	6.200
30	12	15	6.200	30	12	30	6.200
30	12	45	6.200				
40	17	10	5.000	40	17	20	6.200
40	17	40	5.000	40	17	60	6.200
50	21	12.5	6.200	50	21	25	6.200
50	21	50	6.200	50	21	75	6.200
60	25	60	1.475	60	25	80	1.475
60	25	60	2.000	60	25	90	2.000
60	25	90	2.300	60	25	90	2.400
60	25	90	2.500	60	25	60	2.600
60	25	100	2.600	60	25	60	2.680
60	25	100	2.680	60	25	60	2.760
60	25	100	2.760	60	25	60	3.000
60	25	100	3.000	60	25	60	4.000
60	25	100	4.000	60	25	60	4.200
60	25	90	4.200	60	25	120	4.200
60	25	75	5.000	60	25	120	5.000
60	25	15	6.200	60	25	30	6.200
60	25	60	6.200	60	25	90	6.200
10	4	-	-	20	8	-	-
30	12	-	-	60	25	-	-
100	41	-	-				

Table 4.1: Overview of fabricated structures and their geometrical parameters. Shown are center conductor width S , center conductor - ground plane separation W , coupling gap G and resonance frequency f_0 . The last three rows show the geometrical parameters of designed transmission lines.

light towards its vertical center axis into an area about a few 100 nm in diameter (Figure 4.9 (c)). After ensuing development of the photoresist the antidot lattice

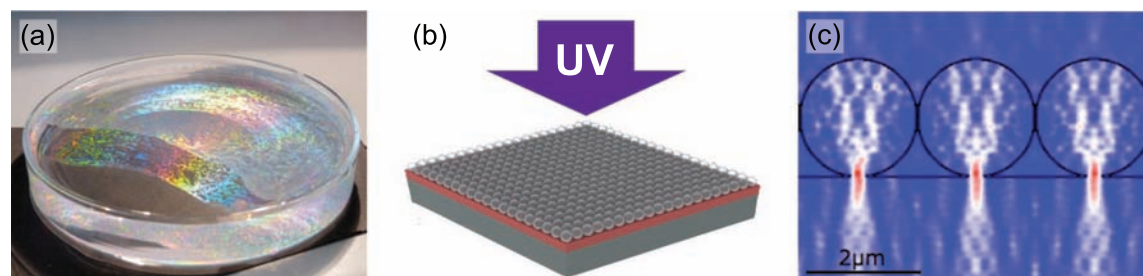


Figure 4.9: Depictions of the monolayer of microspheres acting as self assembled photolithography mask. (a) Monolayer of polystyrene microspheres on water surface to prepare for the Langmuir-Blodgett deposition process. (b) Microsphere monolayer transferred to the sample on top of a layer of photoresist. (c) Simulation of the spatial distribution of photon density in the presence of microspheres during UV exposure - due to the microlense effect the light gets strongly focussed at the bottom of the spheres [see also 103].

(see Figure 4.10) was transferred to the Nb film via reactive ion etching. Due to inhomogeneously distributed sizes of microspheres and process related defects in the lattice structure forming on the water surface, the microspheres do not order over long length scales and hence only domains with a regular lattice structure and defects at their connecting domain walls. The typical size of these domains varies in the range of a few 10 μm to a few 100 μm . The influence of these defects on the effectiveness of pinning vortices is unclear, but assumed to be negligible since they only cover a small fraction of the overall area. The performance of antidot perforated resonators and similar devices was then tested in magnetic fields oriented perpendicular to the film [37, 40]. The results showed a clear reduction of resonator losses in magnetic fields. Since for this work, the magnetic field is always oriented parallel to the film, the structures were also tested in this orientation which is shown in Figure 4.11. In panel (b) the quality factor as a function of external magnetic field is plotted for two identical resonator structures once with an antidot perforated Nb film and once with a plain one for a temperature of 1.6 K. The zero field quality factor of the plain resonator is with ≈ 170000 much higher than the one of the antidot resonator with ≈ 70000 but decreases on its virgin curve very quickly to values below 10^4 which are almost not recovered throughout the whole magnetic field cycle. It also shows a very strong hysteretic behavior which is expected for these structures due to vortex antivortex interaction at the film edges. The resonator fabricated on the perforated film, however, shows a very different behavior. Starting at a lower

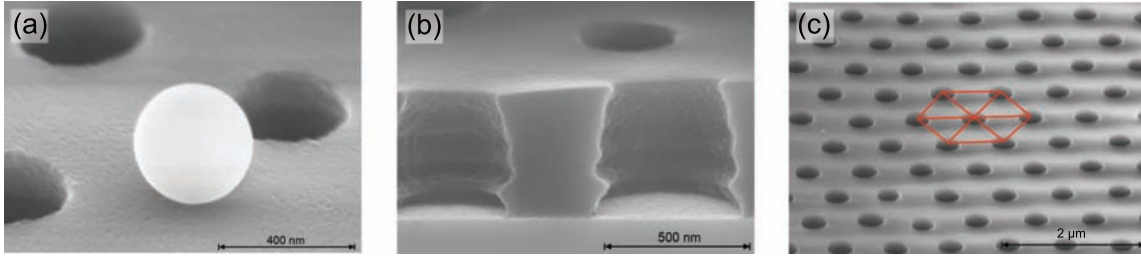


Figure 4.10: Scanning electron micrograph images after development of the photoresist. (a) Picture of three hole structures and a remaining microsphere on top of the photoresist. The sphere is significantly smaller than the typical size of 700 nm due to a non-homogeneous distribution of sizes. (b) View into holes in the photoresist. The average diameter at the top is about 350 to 400 nm. The shape of the walls is due to interference of the incident light with light reflected at the sample surface. (c) Area of a few μm^2 with a highly regular hexagonal lattice structure.

value of Q the quality factor decreases much slower and much higher fields can be realized (the point where the sweeping direction is reversed is determined automatically in the measurement procedure by a critical value of signal to noise ratio - if the peak amplitude of the resonance is below a certain factor of the noise the magnetic field sweeps back again. This precaution was implemented in order not to ‘lose’ the resonance peak.). Most interestingly, though, is the fact, that this resonator shows almost no hysteresis and the zero field quality factor is almost recovered.

However, since both measurements were performed on different devices and the zero field quality factors can change significantly between different resonators of the same layout it is more instructive to compare the vortex induced losses of both resonators than their absolute Q values. As can be seen in Figure 4.11 (c), for fields up to 50 mT the losses in the plain resonator are actually slightly lower than those of the perforated one. Above that value, however, both devices show completely different slopes. While the losses in the plain resonator increase sharply until the maximum field of 132 mT, those of the antidot one remain low and the losses at that field value are more than 20 times less. Eventually, the losses start also to increase at a higher rate until the resonance was lost at fields as high as 273 mT. It is be pointed out, though, that resonances were simply no longer visible only due to a poor signal to noise ratio. More recent measurements utilizing a network analyzer (instead of microwave source and power meter) for detection together with a 35 dB amplifier at the resonator output, it was possible to follow resonances up to fields as high as 1 T [104].

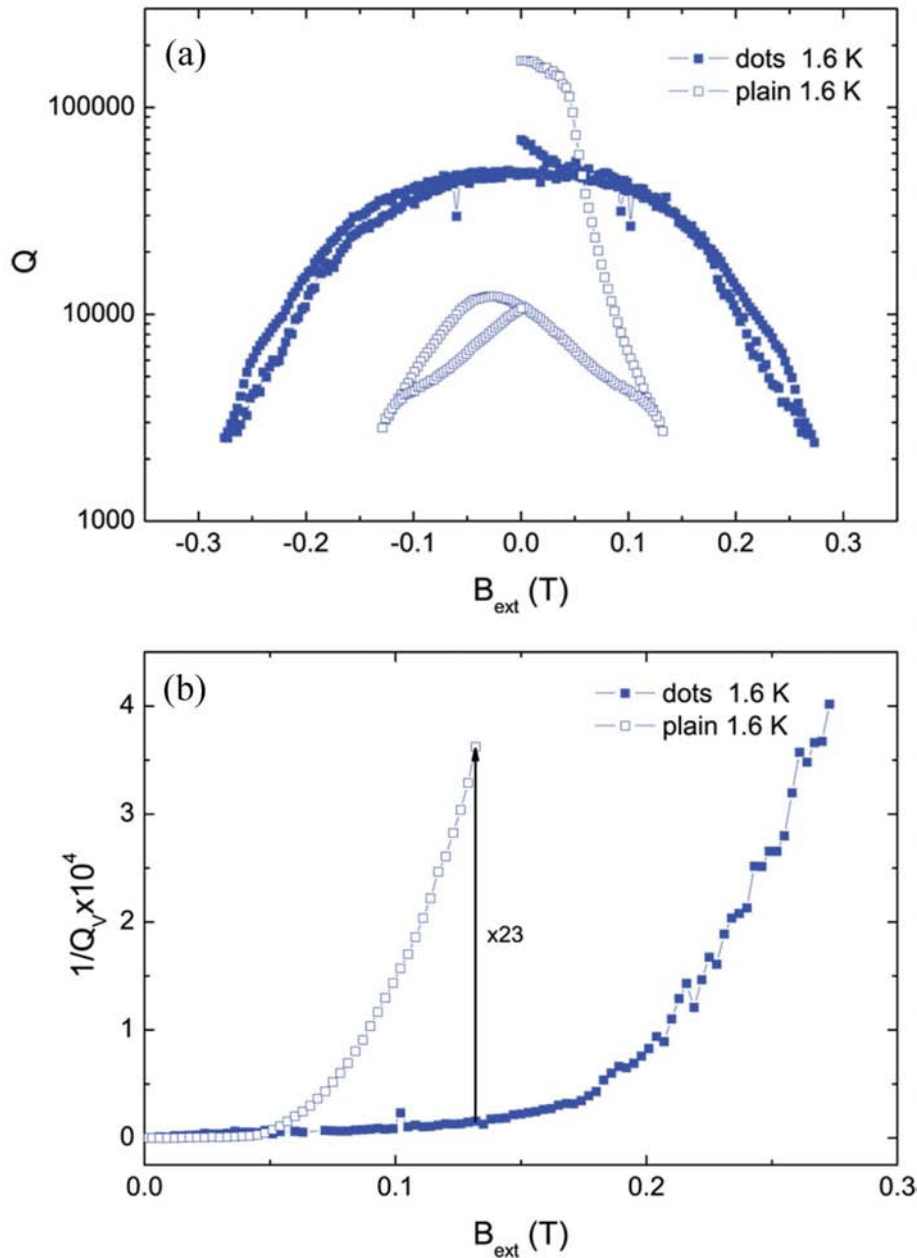


Figure 4.11: Results of field dependent measurements. (a) Field dependent quality factor for a resonator perforated with microsphere fabricated antidots in comparison to a plain resonator without any antidots (discussion see text). (c) Vortex associated losses for both resonators. The perforated resonator displays a highly improved performance in magnetic field.

5 Experimental Setup

The general working principle for resonant or broadband electron spin resonance (ESR) experiments using superconducting coplanar structures is quite straight forward. To induce spin-state transitions the sample under investigation is positioned in the vicinity of the transverse microwave magnetic fields. The chip together with the sample is placed in a metallic box, acting as chip carrier, which allows $50\ \Omega$ impedance matched signal input and output. This whole assembly then needs to be cooled to low-enough temperatures to ensure sufficiently high differences of the thermal population of the various spin states (otherwise the rates for stimulated emission and absorption are equal and no net absorption is visible). The actual measurement is then a simple recording of the transmitted microwave signal as a function of frequency and external magnetic field.

The first requirement, however, of positioning the sample in a way that the microwave field amplitudes are high enough to drive the spin transitions at a high probability, is not as trivial as it may seem. Figure 5.1 and Figure 5.2 show the electric and respective magnetic rf fields of a coplanar structure. The electric field points from

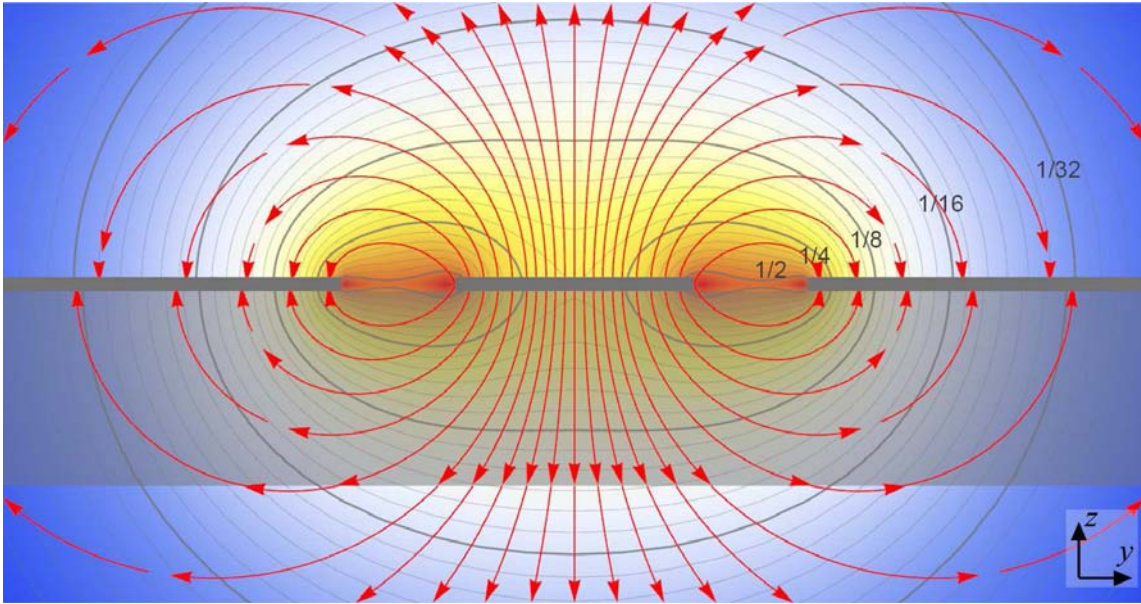


Figure 5.1: Cross sectional view of the electric field distribution for a coplanar structure. Contours denote regions with identical total field amplitudes. Thin film structure and substrate are shown as gray stripes and transparent gray rectangle, respectively.

the center conductor towards the ground planes (for one half cycle; the direction is reversed for the second half cycle) while the magnetic field encircles the center

conductor clockwise (counterclockwise for the other half cycle). The field strength (indicated by the color coding and the contour lines) decreases exponentially with increasing distance from the film edges at the separation between center conductor and ground planes. The thick gray contour lines mark the points at which the field strength has dropped below $\frac{1}{2}$, $\frac{1}{4}$, $\frac{1}{8}, \dots$ of the maximum field strength. One can clearly see that for distances of only the order of the center conductor width S the electric as well as the magnetic field strength has dropped already about one order of magnitude and by double that distance it has dropped about two orders of magnitude. Since these structures are supposed to generate rf magnetic fields which

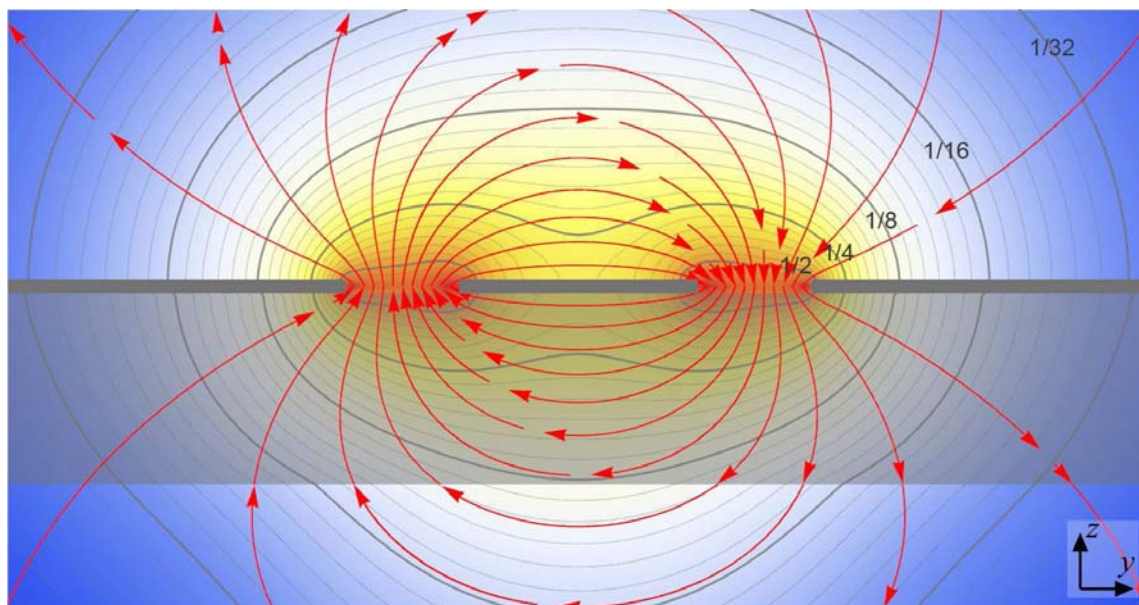


Figure 5.2: Cross sectional view of the magnetic field distribution for a coplanar structure. The field strength decreases quickly with increasing distance from the center conductor ground plane separations.

drive spin transitions in a magnetic sample, the relevant magnetic field components which can stimulate such transitions are shown in Figure 5.3. Displayed are the y and z components (panel (a) and (b), respectively) directly at the film-air (or film-vacuum) interface for $z = 0$ scaled to their maximum value. The y component bears a strong resemblance to the current density profile already shown in Figure 2.5 (a), which is not surprising, since the fields and their components shown in Figure 5.1 to Figure 5.3 were derived from a summation of all the TE and TM modes propagating in such a structure. The total sum of all magnetic modes is, according to Ampère's circuital law, proportional to the total current or to the surface integral of the current density. Since the z component only adds a constant in the gap regions (and

a change of sign which is needed because the line element $d\mathbf{s}$ also changes sign at different sides of the center strip) the spatial profile of the current density is given only by the y component. The fields were calculated according to [105, 106] and all parameters and used terms are given in the Appendix A. Panels (c) and (d) again show the scaled y and z components across the whole half-space region above the coplanar structure. The z component maxima are mostly restricted to the space between center conductor and ground planes and extend further into the half-space above the structure than the y component. It is to note that the z axis in Figure 5.3

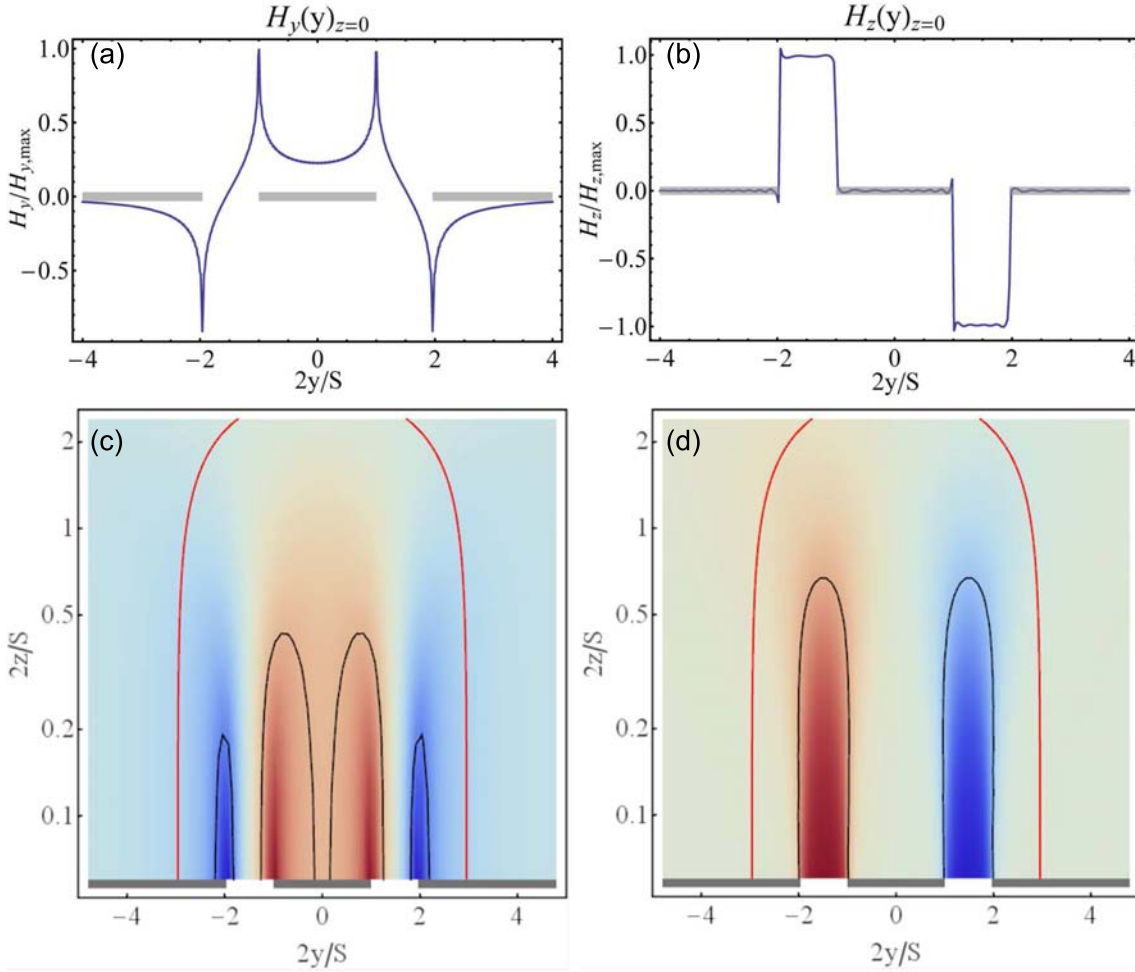


Figure 5.3: Plot of the y (a) and z (b) component of the magnetic field directly at the substrate surface and for the whole half-space region above ((c) and (d), respectively). The black line indicates the positions where the field amplitude has dropped below $1/e$ of its maximum value. The red lines enclose a half circle area with radius $S + W$.

(c) and (d) is scaled logarithmically and the open half-space region is cut already at about $z = S/2 + W$. The thick black lines show the area for which the field amplitude

has decreased to $1/e$ of its maximum value. These areas, integrated over the length of the structure define the effective mode volume V_m (volume area to which the field is effectively confined). The red line is actually a circle with radius $S + W$ around the midpoint of the center conductor. Here, it is assumed that the fields beyond this circle are too low to significantly contribute to any detectable ESR signal. As can be seen from Table 4.1, typical values for S are always $\leq 100 \mu\text{m}$ and therefore the accessible sample space is limited in the z direction to approximately $140 \mu\text{m}$ for the largest structure. On the other hand, however, this also means that by decreasing the center conductor width, one can get more sensitive to the surface of the sample instead of the bulk. The two transmission line structures shown in the right of the lower panel of Figure 4.1 were designed to probe just an epitaxial grown thin layer (5 to $10 \mu\text{m}$ thick) on top of a semiconducting substrate.

5.1 Broadband ESR Sample Preparation

For broadband ESR measurements it is most important to cover an area as large as possible of the waveguide structure with the sample material. Since the electromagnetic wave propagates through the structure (see Figure 5.4) all points which have the same lateral distance ($\Delta y, \Delta z$) from the middle of the center conductor show the same time-averaged microwave magnetic field amplitude. This considera-

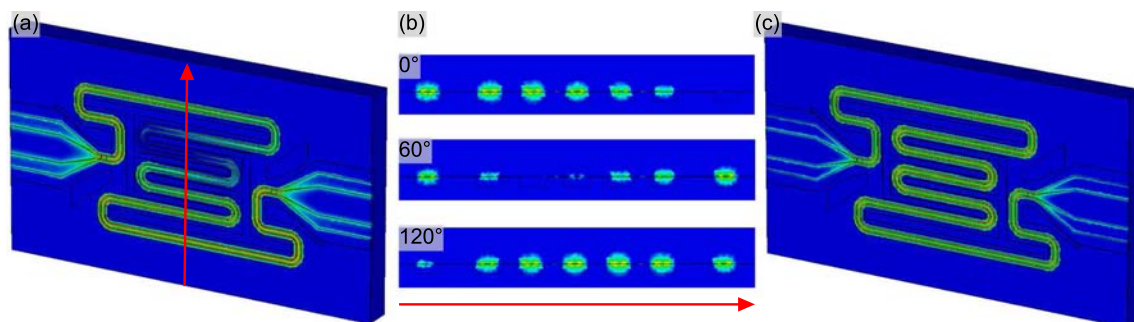


Figure 5.4: Simulation results for a waveguide structure. (a) Amplitude profile of an electromagnetic wave propagating through the structure at an arbitrary phase angle. (b) Sectional view along the red line in (a) for three different phase angles of one half-cycle. (c) Time-averaged amplitudes are the same over the whole length of the waveguide.

tion, however, becomes irrelevant once the absolute distance $\sqrt{\Delta y^2 + \Delta z^2}$ exceeds the characteristic distance of $S + W$ for which the field amplitudes are considered too low to effectively contribute to the ESR signal. To validate the calculated fields, their values were compared with those gained from electromagnetic field simulations.

For an input power of 1 W *, a center conductor width of $S = 60 \mu\text{m}$ and a center strip ground plane separation of $W = 25 \mu\text{m}$ the calculated field maximum at $\pm S/2$ is $\approx 3280 \text{ Am}^{-1}$ which agrees reasonably well with the simulated result of $\approx 3380 \text{ Am}^{-1}$. With decreasing distance between center conductor and ground planes (while maintaining the same input power) the fields are confined to smaller and smaller areas and hence the maximum field amplitude increases due to decreasing modal volume V_m ($E_{\text{max}} \propto 1/\sqrt{V_m}$).

The samples were attached using different techniques, depending on the type of sample. The first measurements were performed on the organic radical NITPhOMe of the Nitronyl-Nitroxide family. This compound was transferred to the waveguide while dissolved in isopropyl and it stuck to the structure by forming micro-crystallites when the solvent evaporated. To protect the contact areas of the coplanar waveguide the

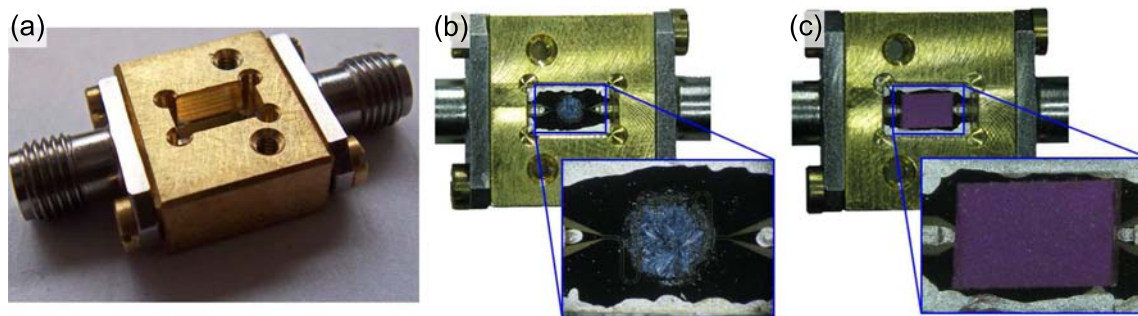


Figure 5.5: (a) Photograph of a sample holder box with attached SMA connectors. (b) and (c) Top view of a mounted waveguide with NITPhOMe crystallites and a ruby single crystal on top, respectively. The silverish areas at the top and bottom as well as on the sides are silver paint contacts from the ground planes to the box walls and from the center conductor to the stripline connectors.

chip was covered with an adhesive tape with a round notch about 3 mm in diameter in the middle. Tiny droplets of the highly concentrated NITPhOMe solution were then applied to the surface of the chip while the solvent was given time to evaporate. In that way, the NITPhOMe radicals recrystallized on the chip and mechanically stuck on its surface. By stripping off the adhesive tape only crystallites in the cut-out section remain on the waveguide structure (see zoom view in Figure 5.5(b)) while the excess is removed with the tape. To ensure good microwave signal injection, the contact pads were subsequently cleaned with isopropyl to remove any potential adhesive residue.

*standard for the waveguide port of the simulation program; typical realistic input powers are lower by 6 to 9 orders of magnitude

The waveguide structure is then placed in a gold plated brass box and the center conductor is connected to sub-miniature A (SMA) stripline connectors with silver paint (ground planes are connected to the grounded box walls).

Other samples investigated were single crystals of ruby ($\text{Al}_2\text{O}_3:\text{Cr}$) and the single ion magnet Gd^{t} -bubpy. In those cases, the waveguide was first mounted into the box and the crystals were then fixed to the film surface by a tiny amount of N-Apiezon vacuum grease.

5.2 Resonant ESR Sample Preparation

Besides broadband ESR measurements using superconducting coplanar waveguides, also resonant ESR experiments were performed, in this case utilizing coplanar waveguide resonators with fundamental frequencies ranging from 1.475 to 2.60 GHz. These experiments were done to study the magnetic response of the heavy-fermion material YbRh_2Si_2 . As explained earlier, this compound exhibits a quantum phase transition from an antiferromagnetic to a paramagnetic Fermi-liquid ground state at around 60 mT (for \mathbf{H} applied perpendicular to the crystallographic c -axis) at very low temperatures ($T \lesssim 70$ mK).

In contrast to the sample materials used in the broadband ESR, however, this heavy-fermion material is a very good conductor at low temperatures. This has severe consequences for the way the sample has to be mounted. While for the broadband

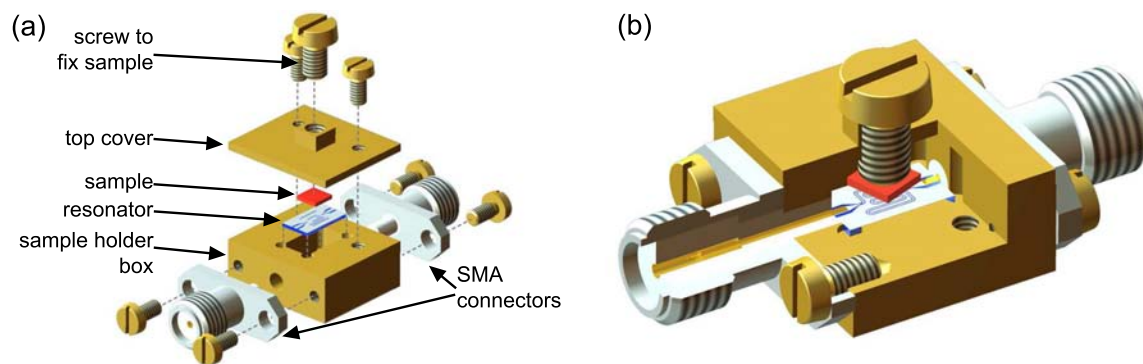


Figure 5.6: Schematic view on how the sample was mounted for the resonant ESR measurements of YbRh_2Si_2 . Panel (a) shows an exploded diagram and panel (b) a sectional view of the mounted sample.

ESR the peak signals are maximized when the sample is closest to the structure, in the case of dissipative metallic samples one has to make a compromise between exposing the sample to strong enough fields while keeping it far enough from the

structure to not dissipate too much energy in ohmic transport. In this work, this goal was achieved by gluing the sample to the tip of a bolt which itself is screwed into the lid of the sample holder box. Mounting the sample like this, the distance between sample and waveguide can be adjusted rather easily without the need to reassemble the whole device. To investigate the influence of the lossy sample on the field distributions above the resonator structure the system was modeled and simulated using CST simulation software. The model, as well as the field profiles

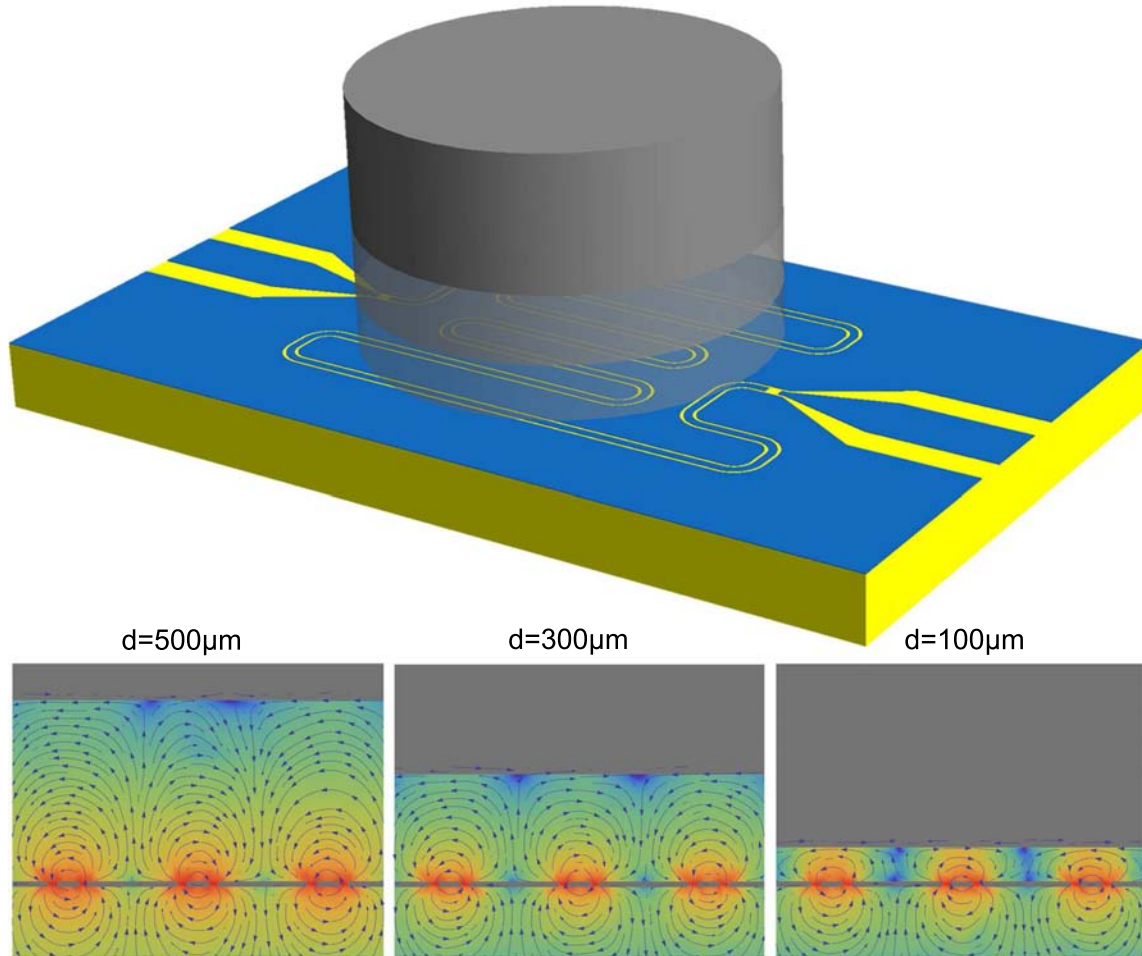


Figure 5.7: Schematic view of the model used for simulating the transmission spectra with the lossy sample at different distances above the resonator structure (top). Depending on the sample distance different magnetic field profiles arise (cross sectional views; bottom).

are depicted in Figure 5.7 for three different sample distances. As can be seen in the bottom three panels of Figure 5.7, the magnetic field gets squeezed into the volume between the resonator and the sample and only the y -components of the magnetic fields are present at the sample surface. The sample distance d was varied from 500

to 300 μm in 50 μm steps and from 300 to 80 μm in 20 μm steps. The resulting transmission coefficients S_{21} are plotted in Figure 5.8 as a function of frequency.

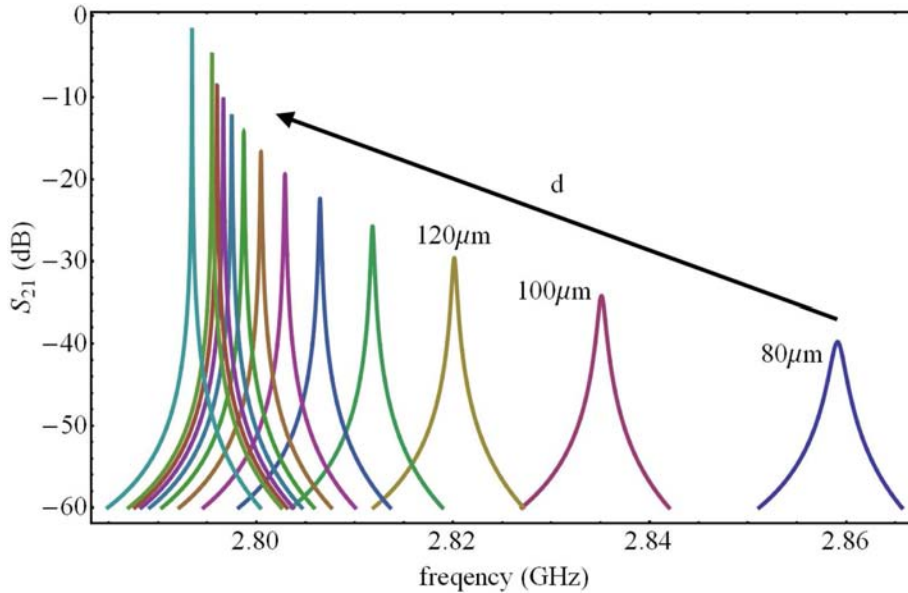


Figure 5.8: Simulated transmission spectra for different distances between sample surface and resonator structure. With decreasing distance the insertion loss and resonance frequency increases while the quality factor decreases (see text).

These transmission spectra directly show a few effects of the sample, namely

- (i) the resonance frequency shifts towards higher frequencies with decreasing sample distances d .
- (ii) The insertion loss increases with decreasing d from about 1 dB at $d = 500 \mu\text{m}$ to about 40 dB at $d = 80 \mu\text{m}$.
- (iii) The quality factor decreases significantly with decreasing d from $Q \approx 150000$ at $d = 500 \mu\text{m}$ to only $Q \approx 2000$ at $d = 80 \mu\text{m}$.

The frequency shift, which is shown in Figure 5.9, is actually composed of two different effects. The first effect, which leads to a shift of the resonance frequency to higher values is just the result of lowering an electric wall towards the coplanar waveguide surface and can be expressed by decreasing h_4 in the formulas quoted in section 4.1 and is therefore of purely geometrical origin. The actual frequency shift due to ohmic losses in the sample is the difference between the non-dissipative geometrical shift and the total shift, which is actually a downshift and increases with decreasing d as expected due to higher damping (shown in the inset of Figure 5.9).

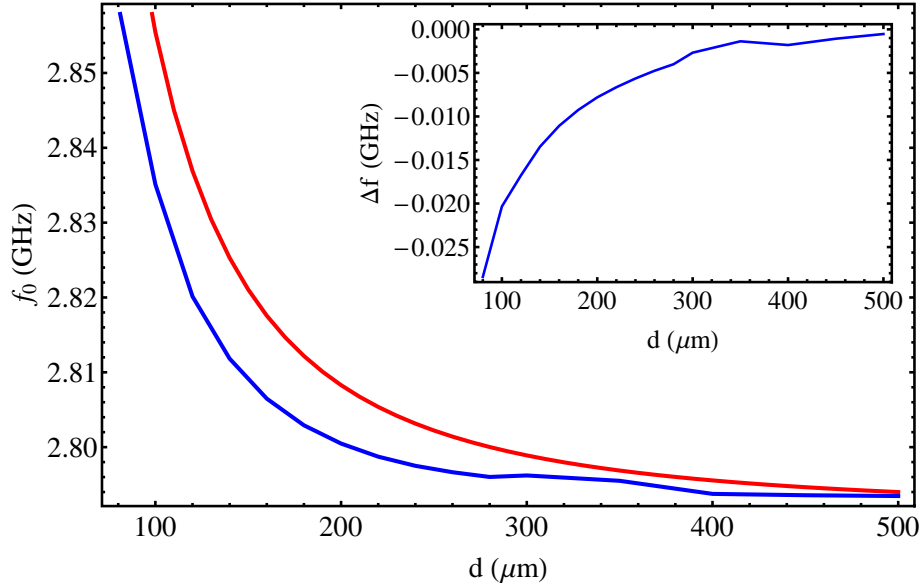


Figure 5.9: Resonance frequency as a function of sample distance. The frequency increases due to lowering a perfect electric wall (red line). The actual shift to lower frequencies due to ohmic losses is shown in the inset as the difference between the simulated (blue) and calculated (red) resonance frequencies.

The change of the quality factor and the insertion loss, however, are of greater significance for the measurement performance. Both quantities are plotted as a function of sample distance d in Figure 5.10. As the sample is lowered towards the resonator structure, ever stronger surface currents are induced within the sample and the total power loss increases, resulting in a reduction of the overall quality factor as well as a rise in the insertion loss. The increasing surface current has direct implications for the measurement as the increasing dissipated power is heating the sample stronger the closer it gets to the resonator. At mK temperatures this effect no longer can be neglected and the input power needs to be adjusted accordingly.

A higher insertion loss, however, represents no substantial drawback since the transmitted signal can be amplified and detected as long as the peak amplitude is larger than the background noise. Depending on the actual signal to noise level, resulting from the ohmic damping at a given sample distance as well as from the input power adjustments needed to avoid heating, many averaging cycles might be needed to resolve the transmission peak satisfactorily which might effect the data acquisition time considerably.

The quality factor, on the other hand, is directly related to the ESR signal strength. The maximum field amplitudes at the gaps between center strip and ground planes

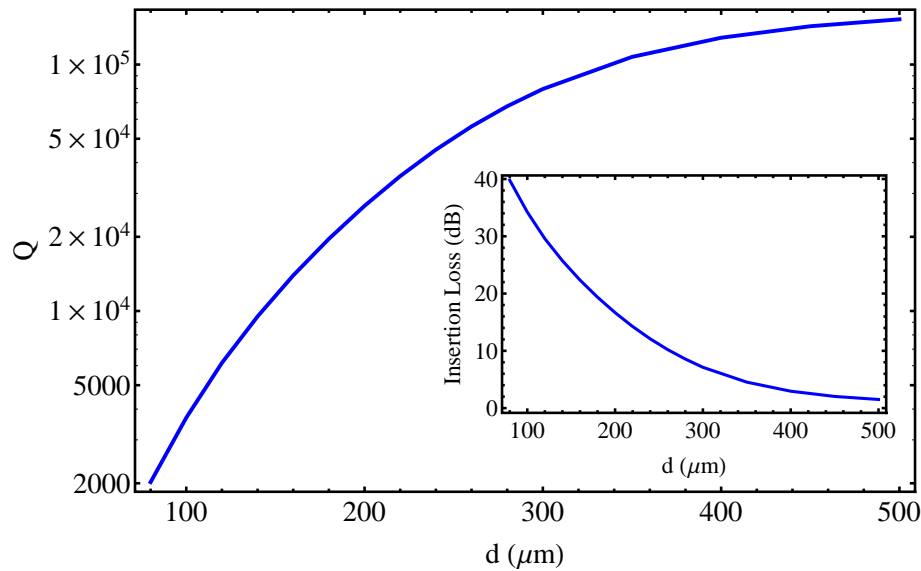


Figure 5.10: Quality factor (main panel) and insertion loss (inset) as a function of sample distance. With the sample close to the resonator structure more and more energy dissipates via ohmic loss channels and the quality factor is reduced significantly while the insertion loss increases.

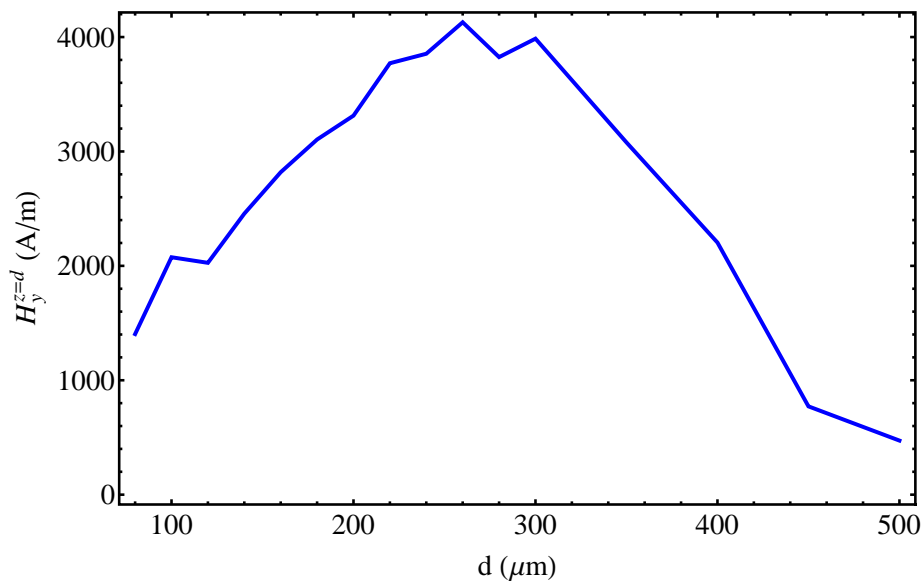


Figure 5.11: Magnetic field y -component directly at the sample surface as a function of sample distance.

scale with \sqrt{Q} (the quality factor is a quantity connected to the energy of the electromagnetic field which scales with the square of the amplitudes), and one would therefore assume a maximum effect for the highest quality factor. In general, this conclusion is well justified if a non-dissipative sample is placed close to the maximum field positions. A lossy metallic sample, though, cannot be placed arbitrarily close to the resonator structure due to the consequences mentioned above. As can be seen in Figure 5.10, the highest quality factors are achieved for the largest sample distance. Unfortunately, the microwave magnetic field amplitude decreases exponentially with increasing distance from the coplanar structure. To obtain an optimum conversion efficiency the field amplitudes at the sample surface for the different sample distances have to be regarded. Figure 5.11 shows the y -component of the magnetic field amplitude directly at the sample surface ($H_y^{z=d}$) as a function of sample distance. Two regimes can easily be distinguished. For $d \lesssim 280 \mu\text{m}$ the field amplitudes increase with increasing distance due to the increase of Q and a better power to field conversion owing to the reduction of the insertion loss. For distances $d \gtrsim 280 \mu\text{m}$ the field amplitudes decrease again although the quality factor still increases and also the insertion loss further decreases. The reduction of $H_y^{z=d}$, in this case, is due to the exponential decrease with increasing distance. In fact, one can reproduce the behavior of the magnetic field amplitudes at the sample fairly well by multiplying the maximum field directly above the center strip with a generic exponential decay in the form

$$H_y^{z=d} \approx H_y^{z=0} \cdot a e^{-\gamma d}.$$

Figure 5.12 shows the magnetic field y -component directly at the Nb film surface above the middle of the center strip (blue curve) and an ordinary exponential decay curve (red). For the parameter set of $a = 0.529$ and $\gamma = 0.0095$ the curve resulting from the simulations could be reproduced to an acceptable extend (see Figure 5.13). It is to note, that for the optimum distance of about $280 \mu\text{m}$ the field amplitude at the sample is in the order of the maximum field amplitude of the transmission line structure, although the unperturbed system shows maximum field amplitudes almost 500 times higher than that (cf. Figure 4.7(b); $\sqrt{Q} \approx 490$).

Further to note is the fact, that all previous field considerations were done at the midpoint of the resonator length ($x = \ell/2$) at which position the magnetic field has an antinode (for the fundamental mode). In contrast to the transmission line the time averaged amplitudes are not the same over the whole length of the structure but show a sinusoidal profile along the resonator length with

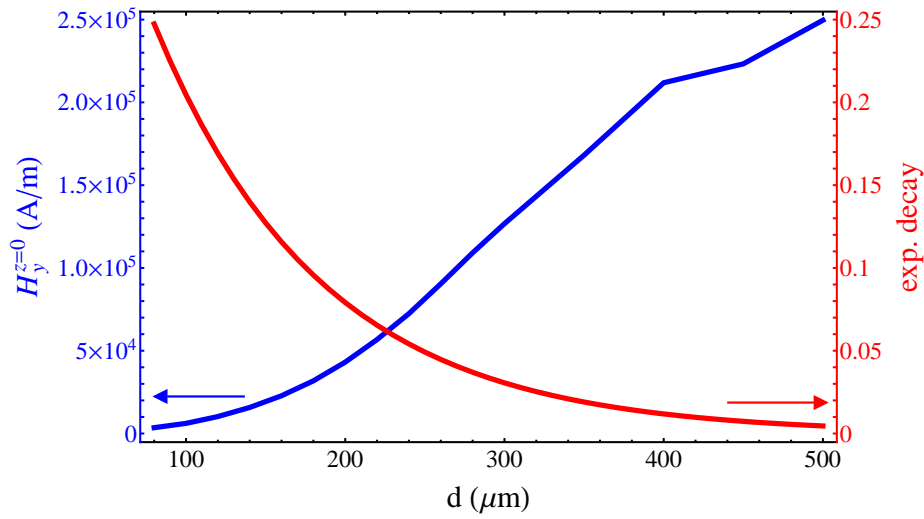


Figure 5.12: Magnetic field y -component directly above the Nb film (at $y = 0$) and generic exponential decay curve.

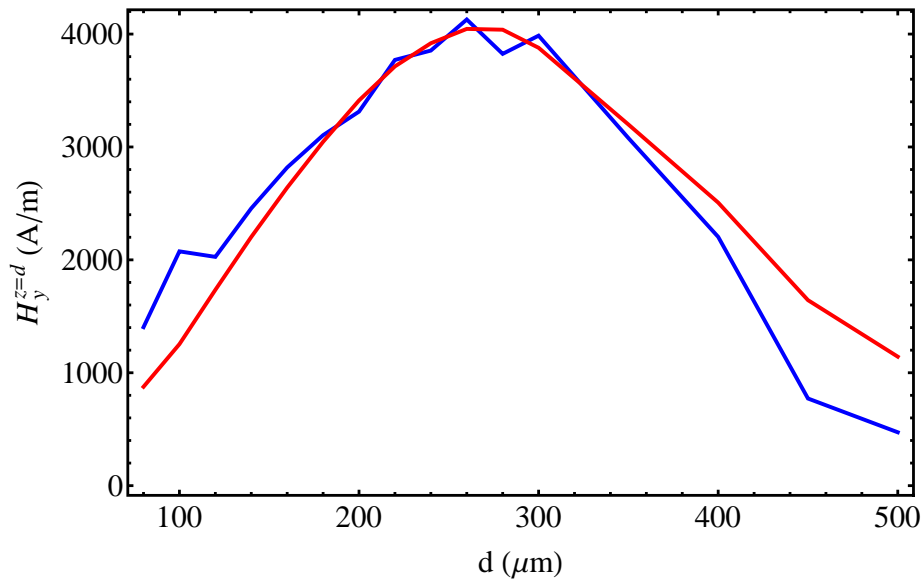


Figure 5.13: Magnetic field y -component directly at the sample surface as simulated (blue) and as approximated from the maximum field at the resonator surface multiplied with an exponential decay (red).

$$H_y^{z=z_0}(x) = H_{y,\max}^{z=z_0} \cdot \sin\left(n\frac{\pi x}{\ell}\right) \quad \text{with} \quad n = 1, 2, 3, \dots$$

Here, n denotes the n th mode which is supported by the resonant structure. A more detailed analysis of this mode profile along the resonator length is given in the results section when discussing the sensitivity of broadband transmission line and resonant ESR.

Depending on the desired base temperature the devices are cooled to temperatures as low as 1.6 K using a variable temperature insert (VTI) or even down to about 40 mK utilizing a dilution refrigerator. The typical machinery involved in the measurement procedure is depicted in Figure 5.15 for the VTI insert. For ultra-low temperature measurements the whole insert is replaced by a dilution refrigerator insert which fits into the same magnet cryostat. In contrast to the experiments performed with the VTI, the sample is in vacuum in the dilution refrigerator and thermally coupled to the mixing chamber by a copper cold finger. Due to the small inner bore of the superconducting magnet coil, the cold finger has a length of about 35 cm and the mixing chamber temperature ($T_{\text{base}} \approx 20$ mK) is not necessarily the actual sample temperature. For that reason, an additional RuO temperature sensor is attached to the head of the bolt to which the sample is glued (see Figure 5.14) and its resistance is read out via an AVS 47 resistance bridge. To further improve the thermal coupling to the sample, a 1 mm diameter silver wire is attached to the sample holder box on one end and to the cold plate on the other.

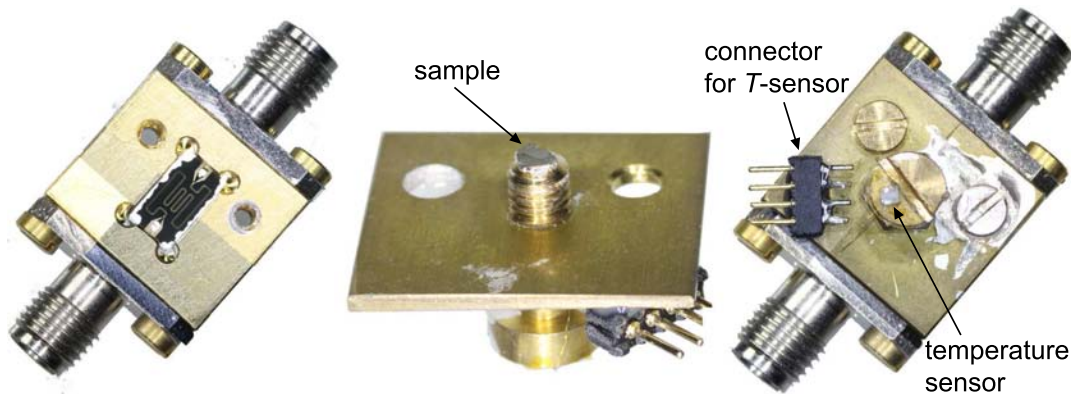


Figure 5.14: (left) Photographs of the open sample holder box with a resonator mounted and contacted. (middle) Sample holder box cover with the bolt screwed into and the YbRh_2Si_2 sample fixed to it. (right) Closed sample holder box with the RuO sensor and its connector visible. The silver blotch at the right is where a 1 mm diameter silver wire is attached for additional thermal anchoring.

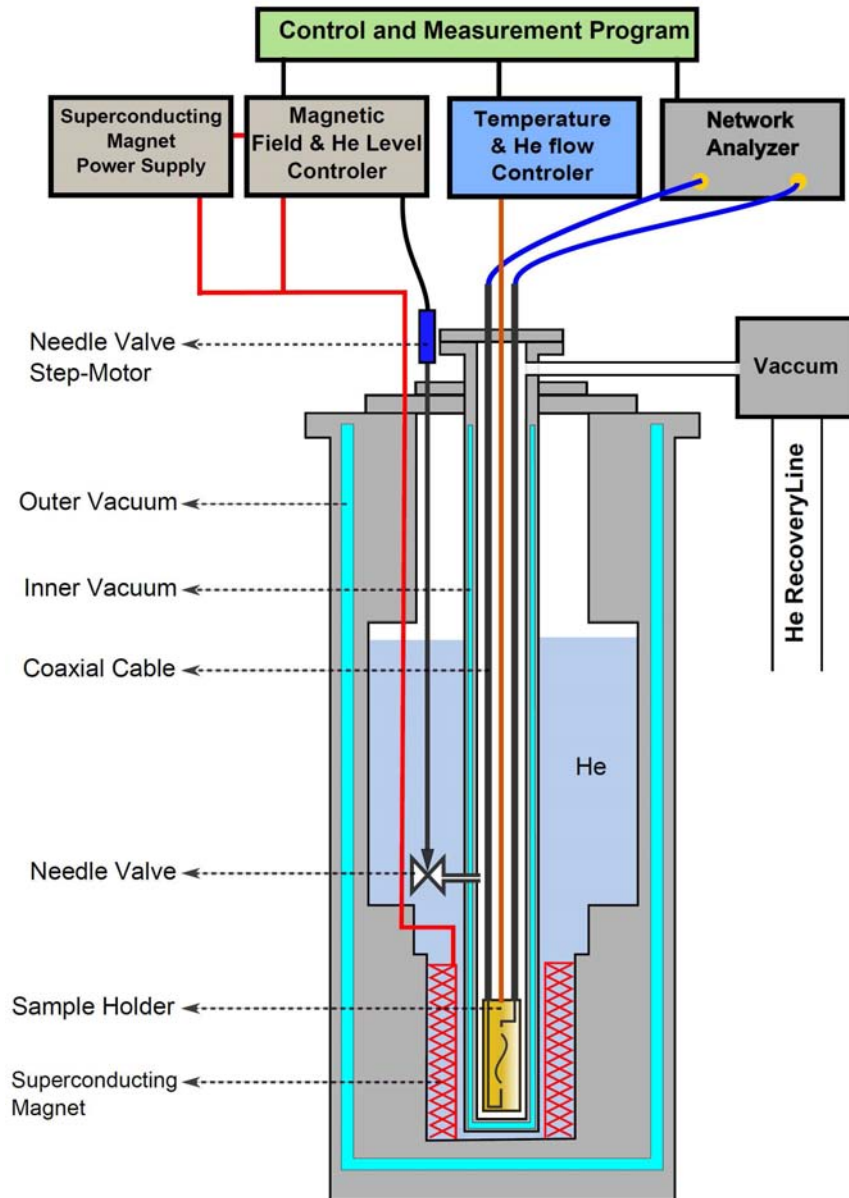


Figure 5.15: Schematic depiction of the experimental setup for measurements performed at temperatures ≥ 1.6 K. Figure reprinted from [104]

6 Broadband Electron Spin Resonance

This chapter will discuss the results obtained from broadband ESR measurements performed on the organic radical NITPhOMe, a ruby single crystal, a Gd-based single ion magnet and on the heavy fermion material YbRh_2Si_2 . The former two materials were investigated at temperatures of $T \geq 1.6$ K while the latter two were measured at temperatures down to about 50 mK. While the NITPhOMe compound was measured mainly as a proof of principle of the experimental setup, the studies performed on the other materials show the full potential of this technique. Additionally, the results on NITPhOMe can be used for quantitative considerations of the sensitivity of this broadband measurement scheme which can also be directly applied to the resonant ESR.

6.1 Broadband ESR on NITPhOMe

The studies on NITPhOMe were done with the first generation of coplanar waveguides. The layout is shown in Figure 6.1. Subsequent layouts were better customized to the experiment (longer lines by increased number of meanders; meanders along the long edge to increase the area which is in Voigt geometry ($\mathbf{H}_{\text{rf}} \perp \mathbf{H}_{\text{ext}}$)).

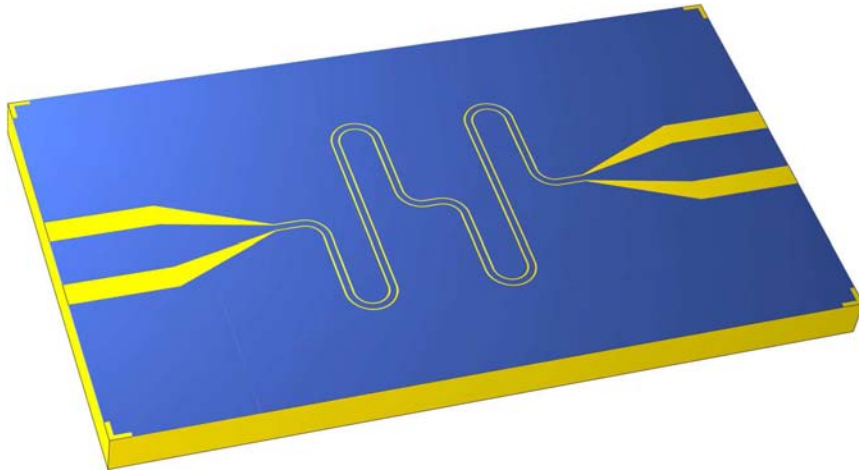


Figure 6.1: Design of the coplanar waveguide used for the NITPhOMe broadband studies.

6.1.1 Frequency Sweep Spectroscopy

Most of the broadband measurements presented in this work follow the same procedure. At a certain fixed temperature and magnetic field a frequency-swept transmission spectrum is recorded. Afterwards the external magnetic field is changed to

a slightly elevated value and the procedure is repeated. In this way, a map of transmitted microwave power as a function of frequency and magnetic field is obtained. Figure 6.2 shows such a typical frequency-swept transmission spectrum of the waveguide structure with the NITPhOMe sample in zero field. The transmitted power is governed by the frequency dependent damping of the coaxial lines which leads to the exponential decrease of transmission with increasing frequency over several orders of magnitude. The attenuation of the waveguide structure itself (in the superconducting state) is much smaller and does not show up on this scale. Indirect effects of the waveguide structure, however, can be clearly seen as they produce characteristic features in the spectrum. So can, for one, the sample holder box act as a cavity within which standing waves can form at certain frequencies. Apart from that, there remains always the possibility that the connections from the stripline connectors to the center conductor of the waveguide are not perfectly matched to the 50Ω line impedance and partial reflections occur at both ends, also leading to standing waves on the center strip (the features seen around 5 GHz are believed to originate from that effect). Finally, if the ground planes of the waveguide are only poorly connected to the sample holder box, standing waves can also form there, leading to unpredictable features in the frequency spectra. Whatever the cause for these parasitic modes, the thus formed features in the frequency-swept spectra are typically much

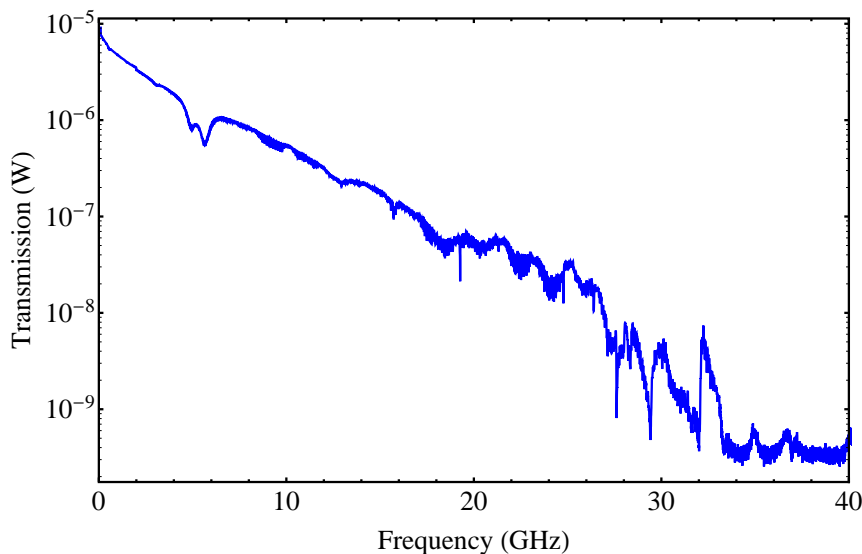


Figure 6.2: Typical frequency-swept power spectrum for an input power of -20 dBm. The transmitted power decreases exponentially up to frequencies of about 33 GHz. For higher frequencies the transmitted signal is close to the detector noise and the detection becomes more difficult.

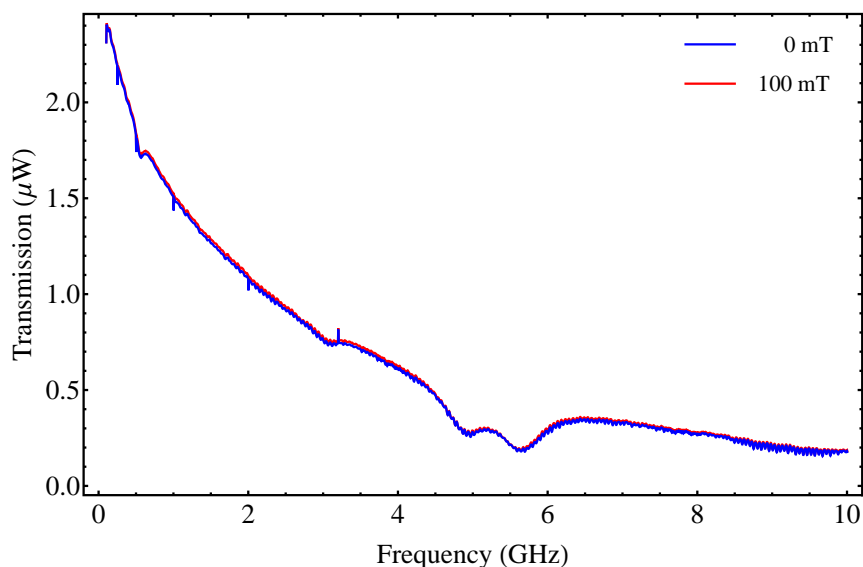


Figure 6.3: Transmission spectra up to 10 GHz at zero field and at 100 mT for which an ESR absorption is expected at ≈ 2.83 GHz. On this scale, however, the ESR feature is too small to be observed directly.

larger than the ESR absorption one is actually interested in, and can therefore obscure the desired signal. For an ordinary spin 1/2 system, like NITPhOMe, one does not expect any ESR signature in zero field. To get the desired information, spectra recorded at different magnetic fields have to be compared. Figure 6.3 shows the zero field spectrum as well as one taken at an external field of 100 mT. For a g -factor around 2, the ESR absorption should be located around 2.8 GHz. However, for this ‘low’ field value, the absorption peak is too small to be seen on this scale and the curves appear to lie on top of each other. To clearly make out the absorption feature the spectrum taken at a finite external magnetic field has to be normalized to a standard spectrum. Naturally, the spectrum taken at zero field would be the first choice candidate for this normalization procedure. The result of such a normalization is illustrated in Figure 6.4. If the spectrum taken at 100 mT is normalized to the zero field spectrum, the ESR peak is clearly visible, but equally so are a few undesired artifacts. Two effects in particular are very prominent in the normalized spectrum; (i) the shape of the background curve deviates significantly from unity, which would not be expected if only the absorption of the sample material changed with magnetic field, and, (ii) a strong feature between 5 and 6 GHz dominates the spectrum and is larger than the actual ESR absorption. The former effect can be explained by means of magnetic field history. Before the measurement started, the external field was ramped to values greater than 100 mT in order to check if the absorptions are

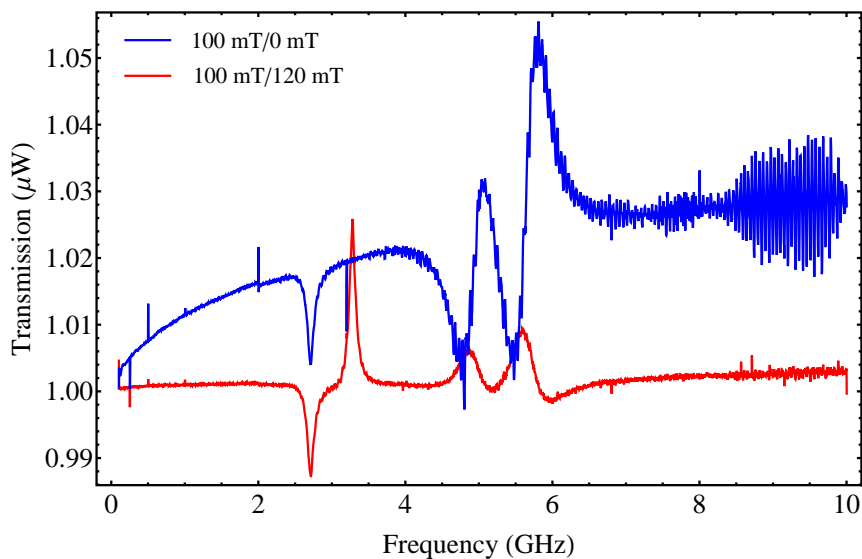


Figure 6.4: Normalized transmission spectra to remove the frequency dependent damping of the coaxial lines. The spectrum taken at $H_{\text{ext}} = 100$ mT is once normalized to the zero field spectrum and once to a spectrum taken at 120 mT.

present. By doing so, flux vortices entered the film which resulted in a hysteresis of high frequency transport properties similar to the one described in section 2.3.2. Since the high frequency response of such a superconducting waveguide is always susceptible to external magnetic fields, a baseline deviation from unity (positive or negative, depending on external field strength and field history) is always present when the finite field spectra are normalized to the zero field one.

The second effect can also be explained by the penetration of vortices or, more general, by changes of transport properties with increasing magnetic fields. The observed feature is believed to result from partial reflections at both ends of the center conductor of the waveguide structure. Since the transport properties change with magnetic field, the strength of this feature inevitably also changes, manifesting itself by artifacts in the normalized spectra.

Both effects can, however, be suppressed or at least reduced if the individual finite field spectra are normalized not to the zero field spectrum but to one taken at a slightly different field strength. For small field differences the transport properties of the superconducting waveguide do not change significantly but the ESR absorption feature will be at a different frequency. Figure 6.4 also shows an example of such a moving normalization. The shift of the baseline from unity is no longer present and also the feature around 5 GHz is highly suppressed. Figure 6.5 illustrates this normalization scheme for different magnetic fields and shows the resulting spectra

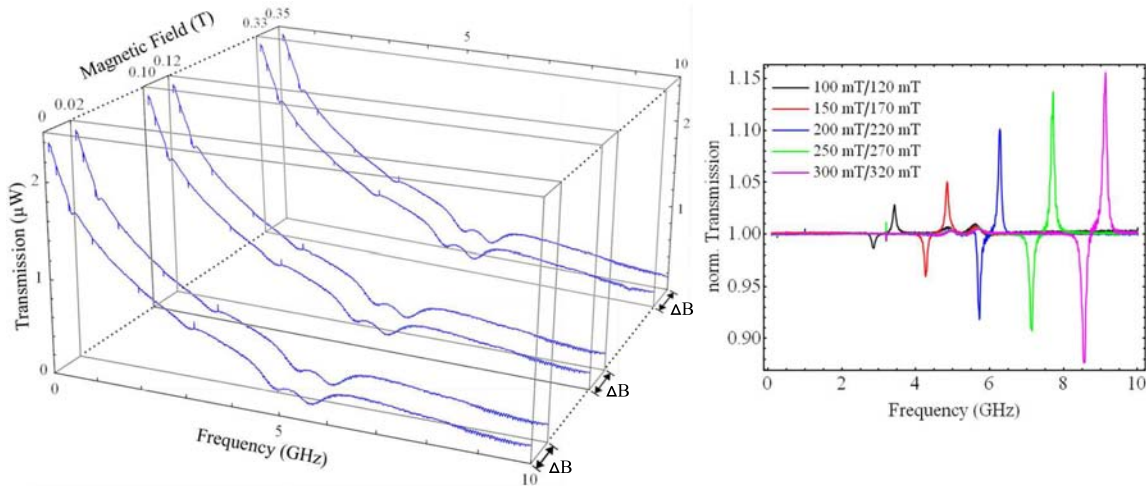


Figure 6.5: Schematic illustration of the normalization method. Individual spectra are normalized to those at magnetic fields elevated just as much for the lines not to overlap (to conserve the actual ESR minimum as the minimum of the curve).

and Figure 6.6 shows a color map of all normalized spectra for this frequency range. Spectra were taken for every 5 mT and each spectrum was normalized with that taken at 20 mT higher field values. Normalizing spectra in that way works very well for materials with narrow ESR lines. Are the lines very broad, the spectrum to use for normalization has to be recorded at much higher or much lower fields which then again results in strong artificial features.

Another way to obtain the ESR absorption from the raw data is to divide each point in frequency and magnetic field by the average transmission value of all points (in field) for that given frequency resulting in

$$Tr_{\text{avg}}(f_i, H_j) = \frac{Tr(f_i, H_j)}{\left(\sum_{j=1}^k Tr(f_i, H_j)\right)/k}.$$

This data treatment has the advantage, that the ESR signature becomes visible regardless of the width of the line. On the other hand, the parasitic features get only reduced and do not vanish completely. Figure 6.7 and Figure 6.8 show the averaging scheme and a color map of the data treated in this manner. Comparing Figure 6.6 and Figure 6.8 it is noticeable that the resonance can be followed down to lower fields/frequencies in the spectra created by moving normalization. This comes as no surprise, since for low field strengths the averaged spectra are slightly shifted above unity (magnetic history effect) and the very small absorption feature no longer ap-

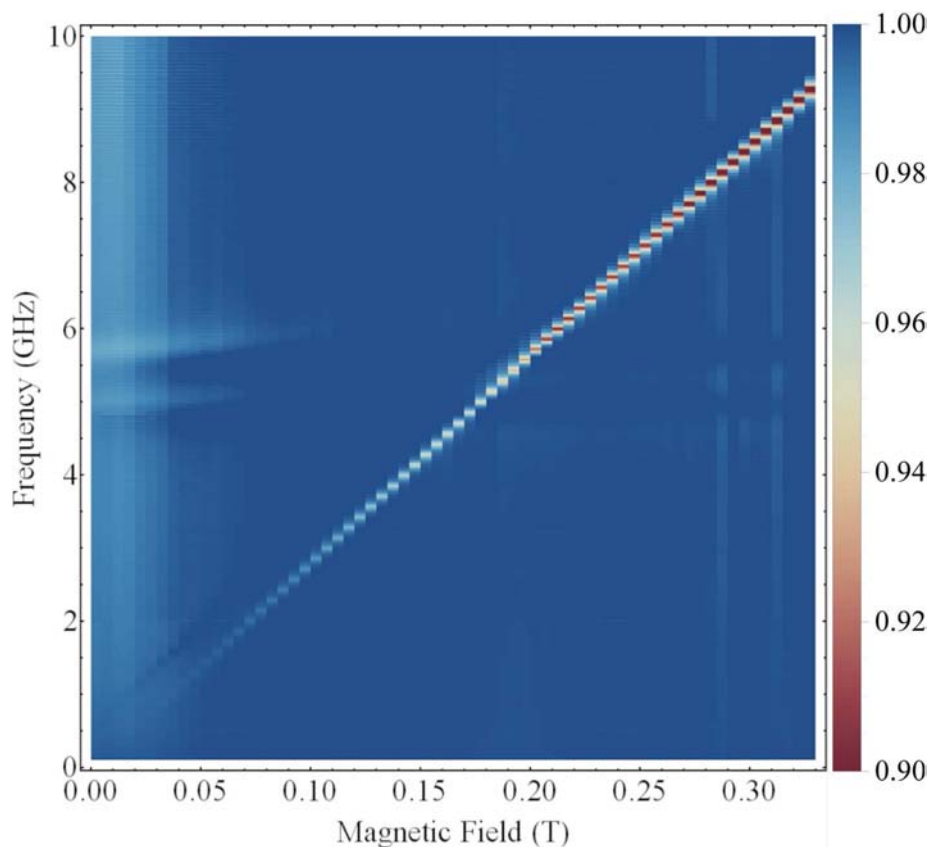


Figure 6.6: Color map of normalized spectra as a function of magnetic field and frequency.

pears in the displayed range. Another distinctive feature is that for the averaged data, the artifacts remain more prominent, as it is expected.

For materials which only show a single straight ESR line, the moving normalization method is the best way to treat the data. Does the transition frequency level off towards a finite frequency for low fields, as the case for all materials which exhibit a zero field splitting of energy levels, the moving normalization fails in these areas and information is lost. Are there more than one transition and the ESR lines get very close to each other, the moving normalization might also produce incorrect results (for the case, that another transition of the normalization spectrum is at the position of the original one of the initial spectrum). Therefore, it is more advantageous to treat complex transition field-frequency diagrams with the averaging method.

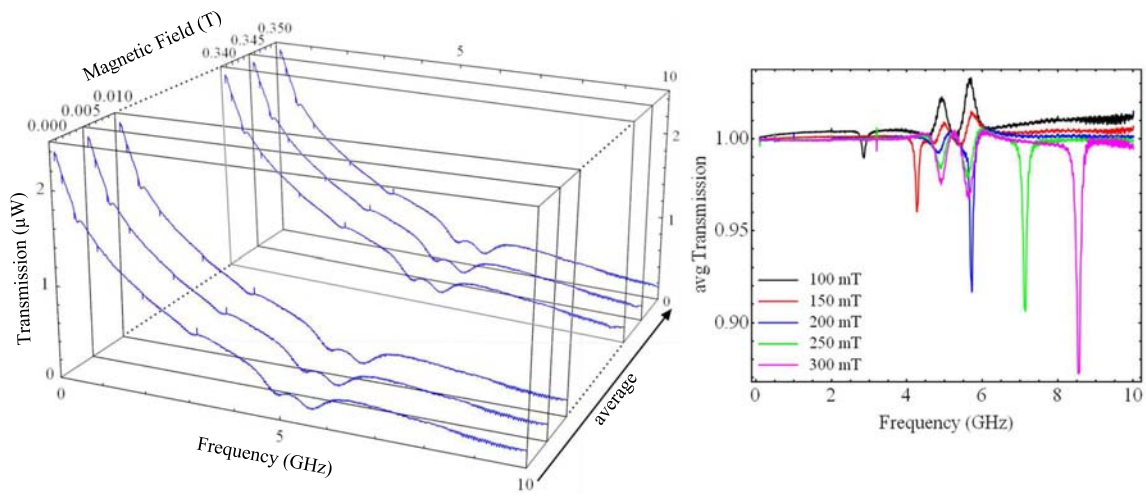


Figure 6.7: Schematic illustration of the averaging method. Each point in frequency and magnetic field is divided by the average value of all points at that frequency.

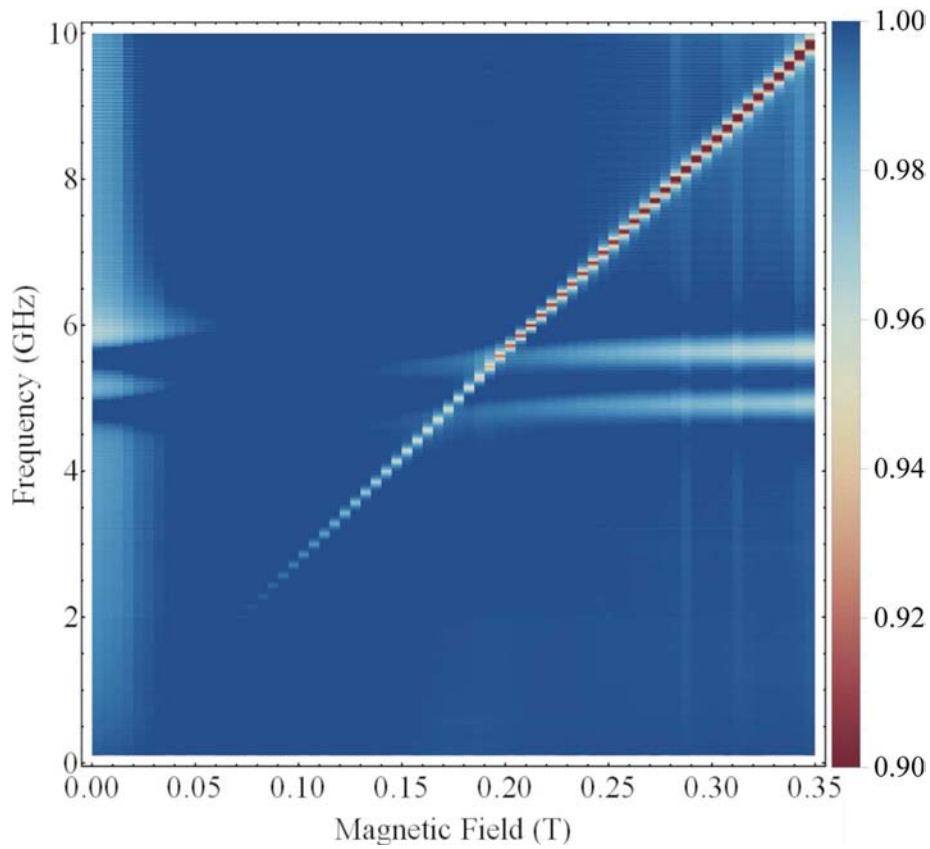


Figure 6.8: Color map of averaged spectra as a function of magnetic field and frequency.

6.1.2 Field Sweep Spectroscopy

Yet another way to perform ESR measurements with superconducting coplanar waveguides is to sweep the magnetic field while recording the transmitted power at single frequencies. This is closer related to ESR experiments in the traditional way in which the frequency is given by the fundamental mode frequency ν_{cav} of a three dimensional cavity and the external magnetic field is driven through the resonance criterion

$$H_{\text{res}} = \frac{h\nu_{\text{cav}}}{g\mu_B}.$$

For a selection of frequencies the field dependent transmission is shown in Figure 6.9. The ESR absorption peaks are clearly visible as is the increase of peak amplitude due to an increase of thermal occupation difference of the Zeeman-split energy levels. The

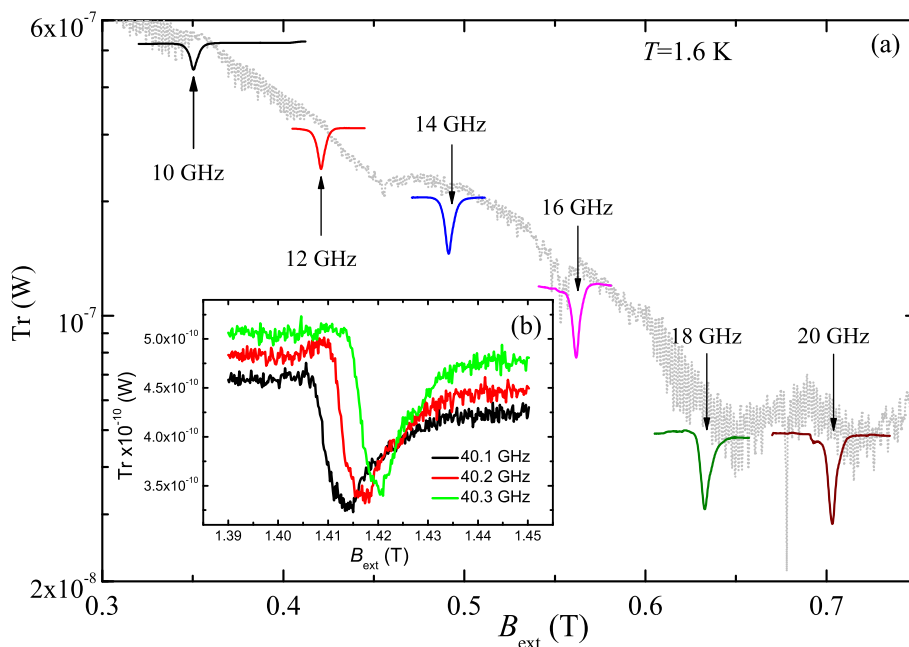


Figure 6.9: Field-swept spectra at different selected frequencies. The baseline for each frequency is located at the transmitted power governed by the frequency dependent damping of the coaxial lines (gray line in the background). Inset (b) shows field-swept spectra at the high frequency limit of the setup.

baseline transmission for each frequency is determined by the frequency dependent damping of the coaxial lines as it follows the gray line seen in the background which is derived from the zero field transmission shown in Figure 6.2 by

$$Tr(H) = Tr(h\nu/(g\mu_B))$$

with a g -factor of $g = 2$. To obtain the spectra shown in Figure 6.9 the transmitted power was recorded for every 0.2 mT. In principle, the same information could be extracted from the data plotted in Figure 6.8 had the magnetic field step width been accordingly small. A complete scan of frequency and fields, in general, holds all the information of the investigated system. For that reason, the data presented in the following sections was always obtained by performing frequency sweeps for a large number of magnetic fields within the interested and accessible frequency-field range.

6.1.3 Temperature Dependence

The last sections have demonstrated, that superconducting coplanar waveguides are well suited to perform broadband ESR measurements over a wide range of frequencies and fields at low temperatures. Low temperatures have the advantage of a greater difference in thermal occupation of the different spin levels even for small splittings, leading to a stronger ESR absorption feature. Additionally, the waveguide is in the superconducting phase and the microwave losses are minimized.

To study how the technique performs with respect to temperature, frequency-swept spectra were recorded at an external magnetic field of 1 T for different temperatures up to 30 K. The resulting spectra (normalized with 1.05 T) of these measurements are shown in Figure 6.10 as a color map and for a selection of temperatures in the inset. Surprisingly, the ESR absorption is still visible at the highest temperature of 30 K. Above the critical temperature of niobium around 9 K (in zero field) the transport properties of Nb are rather poor (over the length of the center conductor the total resistance is about 200 Ω) and ohmic losses play an increasingly important role. Nevertheless, a distinct ESR feature can be made out at 30 K which increases in strength with decreasing temperature (due to increasing population difference). Upon entering the superconducting phase around 5 K (at $H = 1$ T) additional effects occur; (i) the baseline is shifted above unity due to the fact that around the transition temperature the spectrum taken at 1 T has entered the superconducting phase further than the one taken at 1.05 T for normalization. Thus, the overall transmission is higher for the 1 T spectrum. (ii) The ESR absorption shifts towards higher frequencies with decreasing temperature below T_c . This effect can be explained by a local modification of the static external magnetic field due to shielding currents in the superconductor. Directly at the surface of the superconductor as well as in the gaps between center conductor and ground planes the magnetic field is enhanced

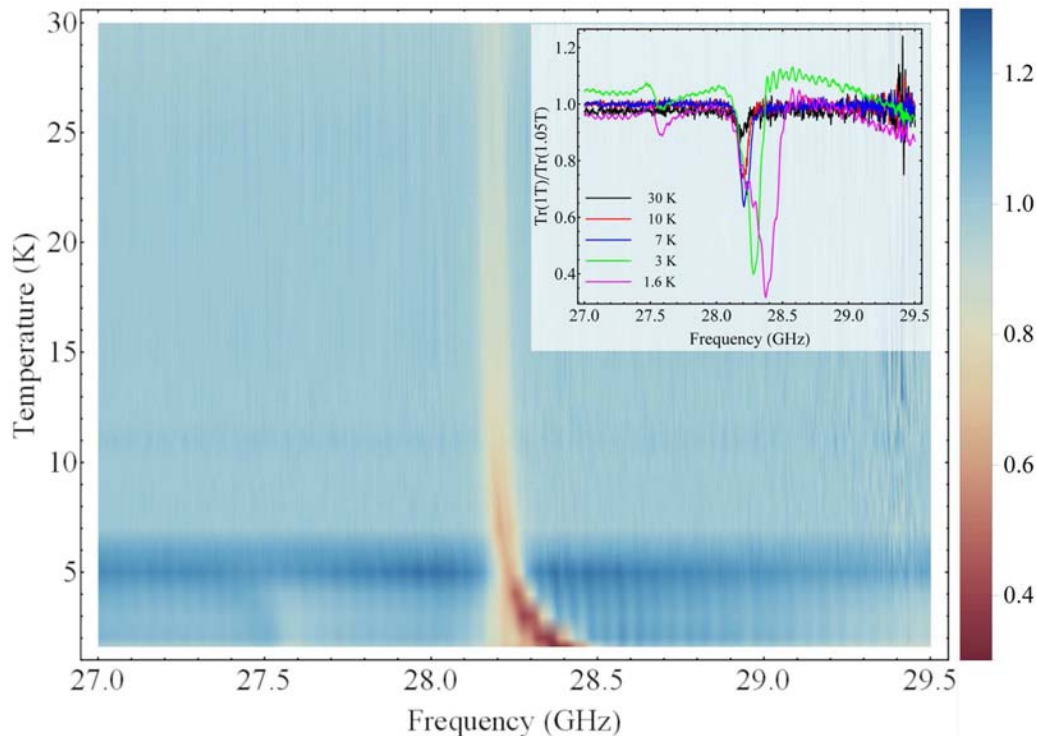


Figure 6.10: Color map of ESR absorptions at different temperatures. The signal is still observable for temperatures far exceeding the critical temperature of Nb. For temperatures below T_c the absorptions are shifted towards higher frequencies due to evolving shielding currents (see text). The inset shows frequency-swept spectra for a selection of temperatures.

compared to the normal conducting state. This consequently results in a shift of the Zeeman splitting towards higher values for spins located in this area. Additionally, with increasing distance from the Nb surface the magnetic field approaches H_{ext} and the measured ESR line is not only shifted but also slightly broadened due to this field inhomogeneity. The effect is rather small (about 1%), but nevertheless has to be considered for precise determination of ESR frequencies with superconducting waveguides. This consideration, however, becomes obsolete when the measurements are performed using non-superconducting metallic waveguides which show no field enhancement and allow the observation of magnetic transitions in NITPhOMe for temperatures even up to room temperature (not shown).

6.2 Broadband ESR on Ruby Single Crystals

The last section dealt with a clean spin 1/2 system which shows a single sharp transition that can be nicely traced in the field-frequency diagram but is otherwise rather uninteresting. Materials with a higher spin which leads to zero field splitting and magnetic anisotropy show a richer field-frequency diagram and are therefore predestined for broadband electron spin resonance. Chromium substituted Al_2O_3 , or ruby, is such an exemplary system. It is an $S = 3/2$ system consisting of two zero field split doublets and can be described by the Hamiltonian [69, 70]

$$\mathcal{H} = \underbrace{\mu_B \mathbf{H} \cdot \mathbf{g} \cdot \mathbf{S}}_{\text{Zeeman term}} + \underbrace{D \left[S_z^2 - \frac{1}{3} S(S+1) \right]}_{\text{anisotropy term}}. \quad (6.1)$$

Here, D is the zero field splitting parameter and given by $D = -5.735$ GHz. For an isotropic $\mathbf{g} = g \cdot \mathbf{I}$ the Eigenvalue equation is given by

$$\left(\left(\frac{\mathcal{E}}{|D|} \right)^2 - 1 \right)^2 - \frac{5}{2} \frac{1}{|D|^2} x^2 \mathcal{E}^2 + \frac{9}{16} x^4 - \frac{x^2 (5g^2 \cos^2 \theta - g^2 \sin^2 \theta)}{2g^2} + \frac{2\mathcal{E} D x^2 (g^2 \sin^2 \theta - 2g^2 \cos^2 \theta)}{|D|^2 g^2} = 0 \quad (6.2)$$

with θ being the angular orientation of crystallographic c -axis with respect to the magnetic field and

$$x = \frac{g\mu_B H}{|D|}.$$

The four solutions to the Eigenvalue equation Equation (6.2) are shown as a function of magnetic field and for different orientations in Figure 6.11. All resulting possible transitions are depicted in Figure 6.12 for the same orientation angles.

The actual experimental data which was recorded for frequencies ranging from 1 to 30 GHz in steps of 6 MHz and magnetic fields from 0 to 0.6 T in 7.5 mT steps is shown in Figure 6.13 (the data was treated with the averaging method). The visible absorptions agree very well with a simulated transition spectrum for a crystallographic orientation of the c -axis of 78° with respect to magnetic field.

The results of the broadband measurement on the ruby single crystal demonstrate in an impressive way the full potential of the technique. The system covers not only the typical microwave bands L (≈ 1 GHz), S (≈ 3 GHz), C (≈ 4 GHz), X (≈ 10 GHz), P (≈ 15 GHz) and K (≈ 24 GHz) but also all desired frequencies in between. With a

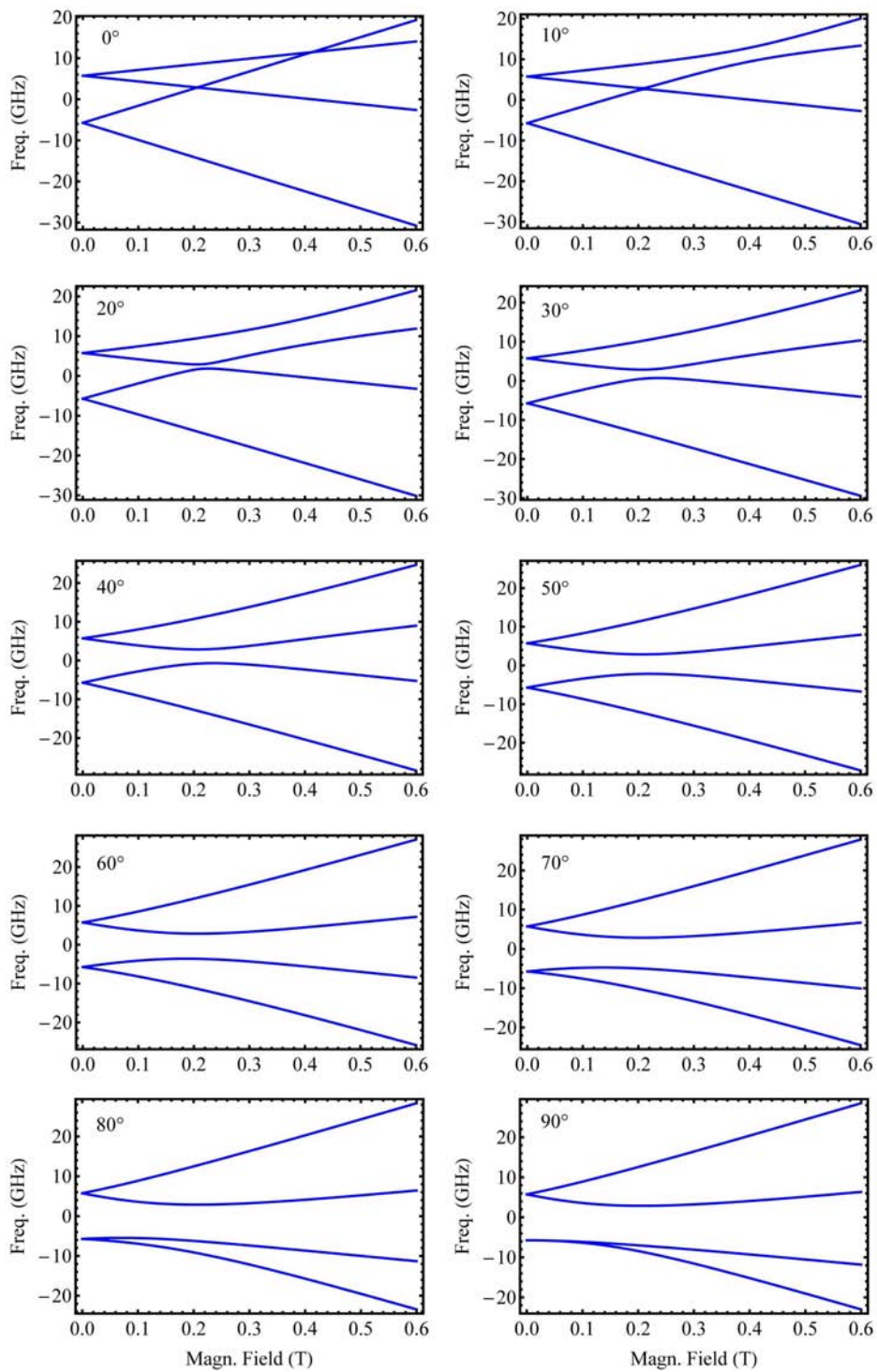


Figure 6.11: Eigenstates of the spin levels in Cr^{3+} as a function of magnetic fields for different orientations of the crystallographic c -axis with respect to the external magnetic field.

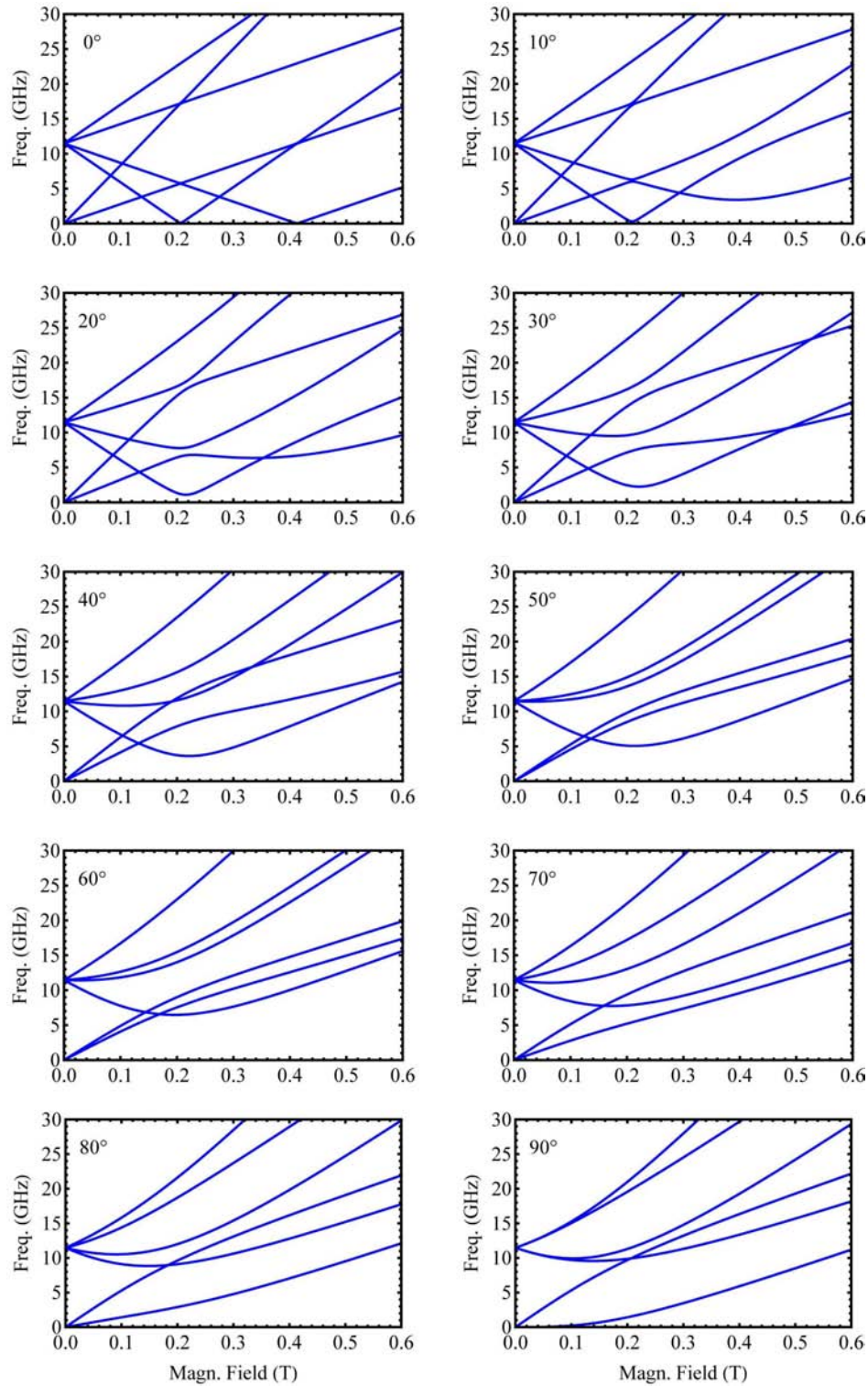


Figure 6.12: Possible transitions between the spin levels in Cr^{3+} as a function of magnetic fields for different orientations of the crystallographic c -axis with respect to the external magnetic field.

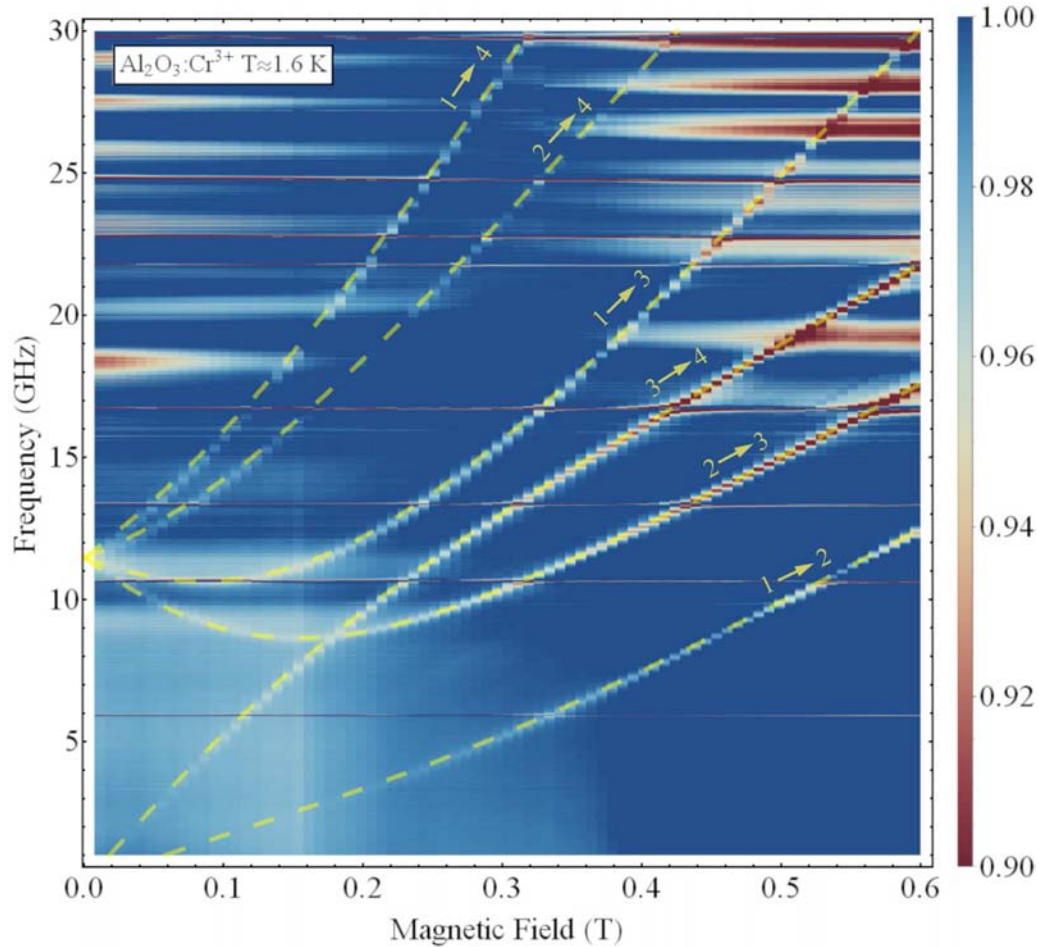


Figure 6.13: Color map of the averaged transmission spectra for the measurement on ruby. The transitions are clearly visible and their progress could be modeled to the Eigenfunctions for a magnetic field orientation of 78° to the c -axis. The numbers represent the different m_s states as: $1 \rightarrow -\frac{3}{2}$, $2 \rightarrow -\frac{1}{2}$, $3 \rightarrow +\frac{1}{2}$, $4 \rightarrow +\frac{3}{2}$.

slightly modified system it was recently also possible to extend the frequency range even up to 67 GHz including the Q (≈ 35 GHz), U (≈ 50 GHz) and V (≈ 65 GHz) band.

6.3 Broadband ESR on Gd-based Single Ion Magnets

Another great advantage of the broadband ESR technique with superconducting waveguides is the easy implementation into ultra-low temperature systems such as dilution refrigerators. So far, there exist only a few highly sophisticated examples of combining ultra-low temperature systems with ESR spectrometers [107–111] due to immense technical challenges.

Working with materials that show a zero-field splitting of just a few GHz, however, suggests their investigation in the mK-regime ($1 \text{ GHz} \approx 50 \text{ mK}$). This section demonstrates the successful realization of ESR measurements at mK temperatures on a newly synthesized Gadolinium (Gd) based single ion magnet, introduced before in section 3.3. The measurements were performed as frequency sweeps up to 30 GHz in 10 MHz steps at magnetic fields increasing by 2.5 mT from 0 to 1 T. The temperature covered a range from $\approx 60 \text{ mK}$ up to 700 mK in varying steps. To maintain a rather constant input power at the waveguide the power was swept from -33 dBm at 0.1 GHz with 0.4 dB/GHz (to make up for the damping in the coaxial input line). The outputted signal was amplified at room temperature by 35 dB and each frequency point was averaged 2048 times.

The crystal was placed on the chip with the crystallographic c -axis parallel to the magnetic field. Due to the low symmetry of the system (C_2) the spin Hamiltonian contains a variety of anisotropy terms and is given as

$$\mathcal{H} = \mu_B \mathbf{H} \cdot \mathbf{g} \cdot \mathbf{S} + \frac{1}{3} \sum_{q=0,2} B_2^q O_2^q + \frac{1}{60} \sum_{q=0,2,4} B_4^q O_4^q + \frac{1}{1260} \sum_{q=0,2,4,6} B_6^q O_6^q \quad (6.3)$$

with the Stevens spin operators O_k^q and their coefficients B_k^q . Together with an unknown orientation of the easy axis there are in total 10 unknown constants to describe the system. Since Gd III is a spin $S = 7/2$ system there exist eight different spin levels which are pairwise degenerate at zero field and, depending on the higher order spin Hamiltonian terms, mix with each other. For such a complex system it is very hard to tell which transitions are allowed and which are forbidden because the states are no longer pure $m_s = -7/2, -5/2, \dots, +7/2$ states. One can, however, for any given set of parameters (B_k^q, θ, B) get the Eigenvalues and Eigenvectors of the Hamiltonian and determine all possible transitions and their probabilities. The Eigenvalues give the energy levels and the Eigenvectors can be used to get the transition matrix elements. The transition probability $P_{i,f}$ is proportional to the population difference of the levels, the transition frequency and to the square of the transition matrix elements. For an initial state $|M_i\rangle$ with energy \mathcal{E}_i and a final state

$|M_f\rangle$ with \mathcal{E}_f it can be written as

$$P_{if} \propto |\langle M_i | S_x | M_f \rangle|^2 \cdot \underbrace{\left(e^{-\frac{\mathcal{E}_i}{k_B T}} - e^{-\frac{\mathcal{E}_f}{k_B T}} \right)}_{n_i - n_f} \cdot (\mathcal{E}_f - \mathcal{E}_i). \quad (6.4)$$

Figure 6.14 shows all possible transitions of the Gd spin system for two different sets

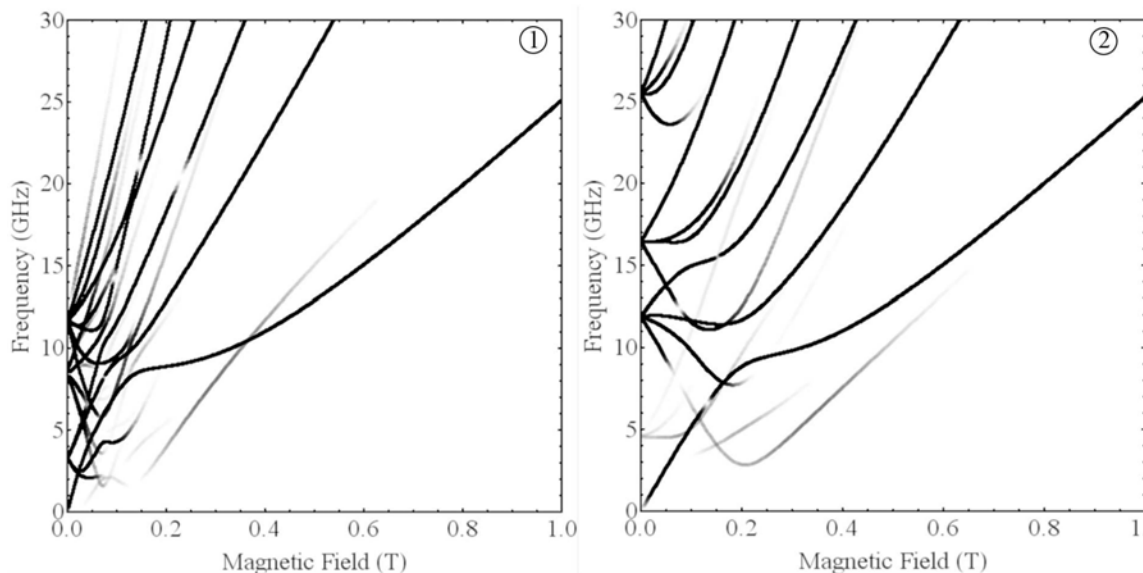


Figure 6.14: Possible transitions between various spin states of Gd III for two arbitrarily chosen parameter sets B_k^q , θ , given in Table 6.1, which both reproduce some of the key features observable in the experimental data (Figure 6.15). The opacity of the lines is scaled to the transition probability as expressed in Equation (6.4).

of parameters (given in Table 6.1). The strength of individual lines is proportional to the transition probability. Both sets reflect some of the key features in the measured data (displayed in Figure 6.15) but far from all of them. It is to note, that there exists an abundance of such sets for which always a few lines are matched quite well, while others do not fit at all. This is somewhat not surprising since only one set of parameters describes the system correctly. Another problem might arise from

	B_2^0	B_2^2	B_4^0	B_4^2	B_4^4	B_6^0	B_6^2	B_6^4	B_6^6	θ
①	0.92	-0.21	-0.14	0.26	-0.43	-0.31	-0.12	0.42	0	45°
②	-1.88	0.19	0.06	0.18	-0.31	-0.28	-0.8	-0.71	0.57	74°

Table 6.1: Anisotropy parameters which lead to the respective transition lines shown above.

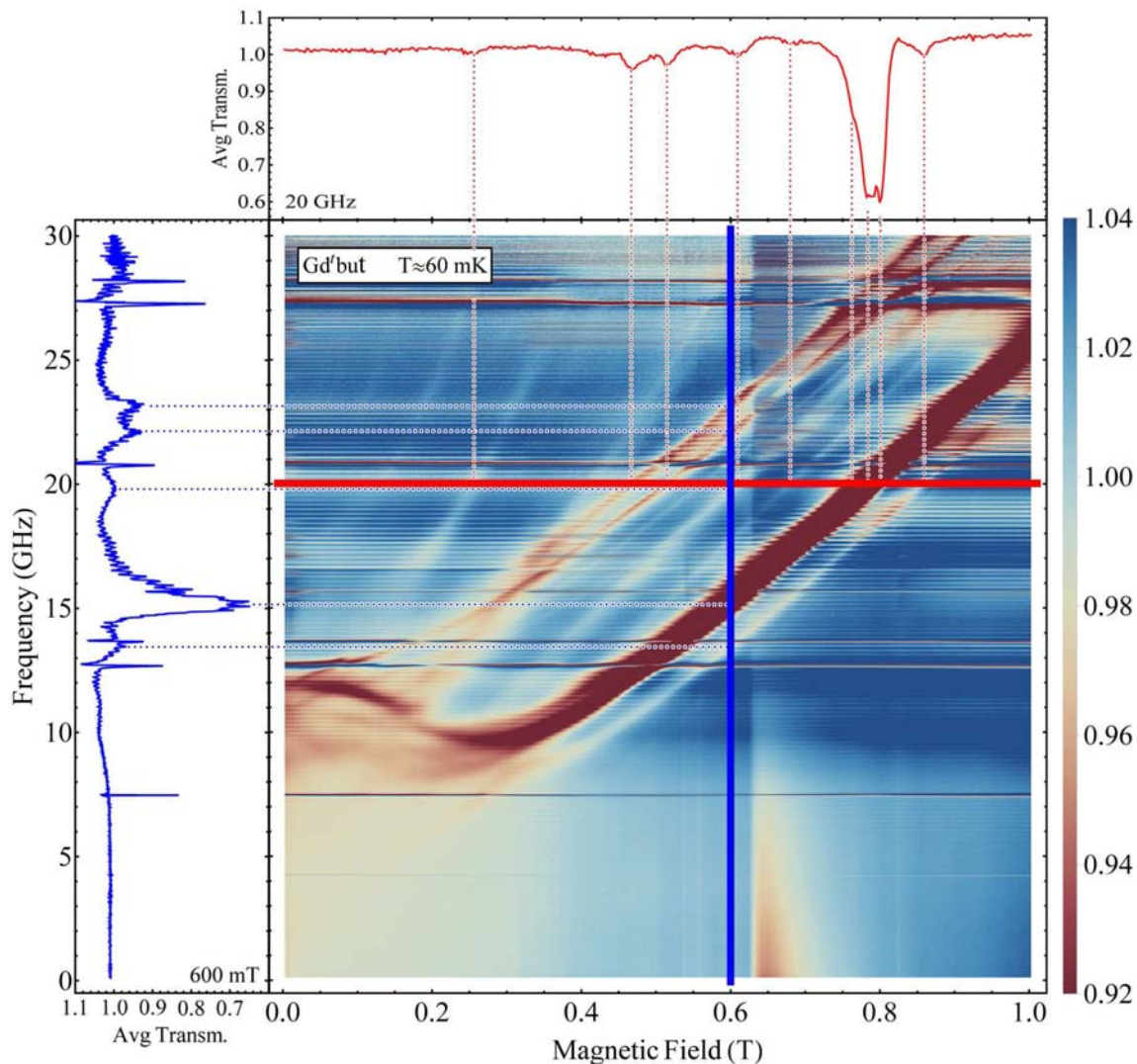


Figure 6.15: Experimental data of the broadband measurement on the Gd based single ion magnet at the lowest achievable sample temperature of around 60 mK. A variety of transitions which differ in strength is visible. The red and blue line marks positions in frequency and magnetic field, respectively, for which the averaged transmission is displayed in the graphs at the top and on the left.

imperfect crystal orientation. As mentioned earlier in section 3.3, the individual spins in one unit cell are situated around a screw axis along the crystallographic b -axis. Only for a parallel alignment of the orientation of the external field with either the b or the c -axis do the transverse spin components cancel each other out. The crystal was placed on the waveguide in a way that the c -axis should align with the field. However, if the alignment is slightly off, additional lines appear, making it even more difficult to simulate the absorption spectra. In this case a set of three

Euler angles would be needed to correctly describe the measured data.

Figure 6.15 also shows frequency and magnetic field sweeps extracted from the averaged data at a certain arbitrarily chosen field and frequency, respectively. From those sweeps many absorptions can be distinguished as individual lines. The strongest feature, however, combines at least three separate lines which are hard to differentiate. If one had knowledge about which measured line originates from a transition between which states i.e. one could label the lines observed in the data, one could get the correct set of parameters from this information, or at least give some upper and lower limits for said parameters. This, however, is not easily possible due to the strong mixing of the levels and due to the fact that the lines can not be individually traced over the whole field-frequency diagram.

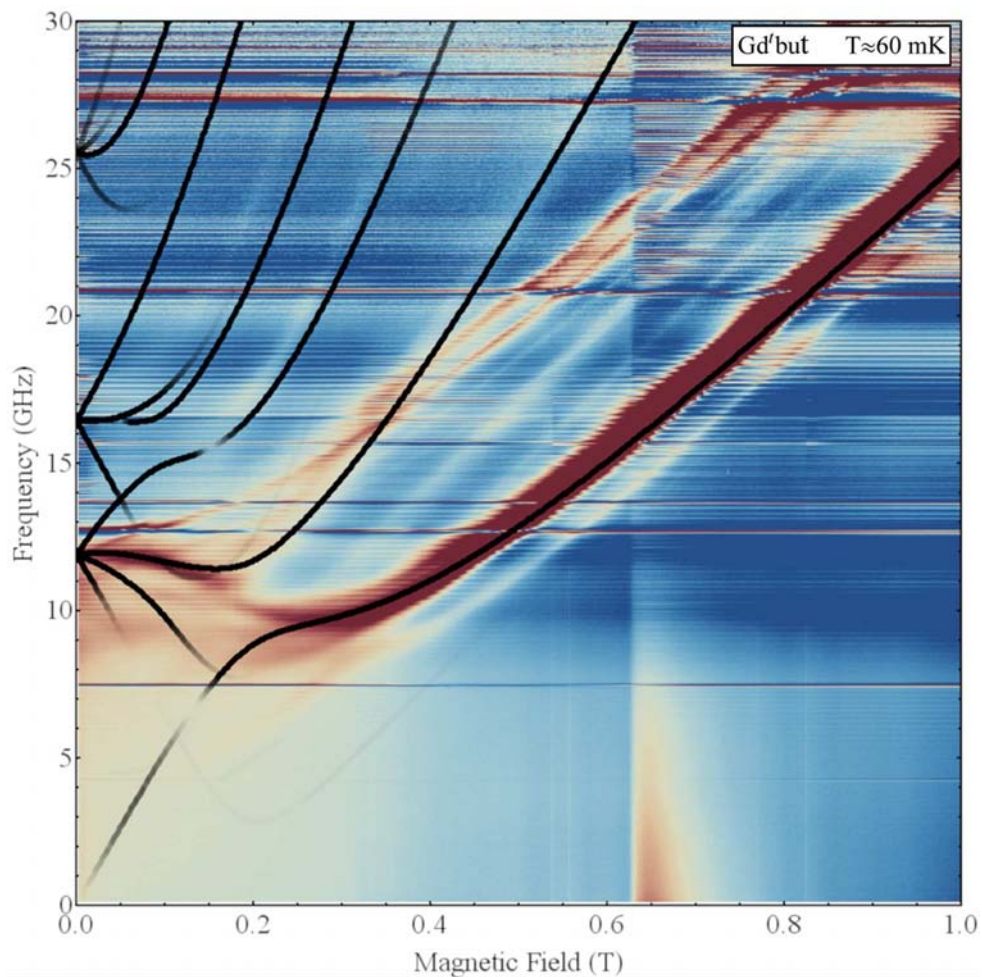


Figure 6.16: Experimental data with an overlaid plot of possible spin transitions for parameter set 2.

To get at least a hint about the origin of some features one can study the development of the different absorption lines with increasing temperature. Figure 6.17 shows the field-frequency diagram for a temperature of about 700 mK. The very strong signa-

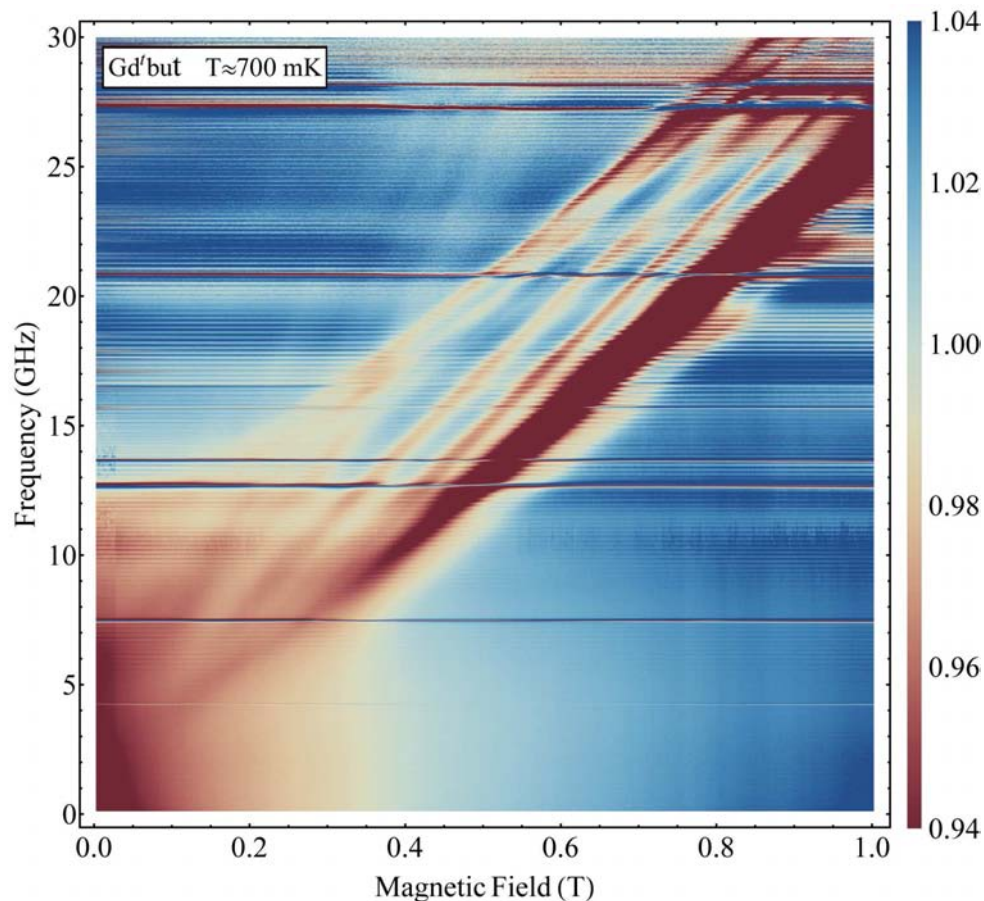


Figure 6.17: Color map of the ESR transitions at a temperature of approximately 700 mK. At low fields the results differ significantly from those taken at around 60 mK.

ture of transitions between zero-field-split levels around 12 GHz in the data recorded at 60 mK is significantly weakened and a stronger trend of the lines towards zero frequency for decreasing magnetic field is evident. This leads to the conclusion that these lines stem from transitions between higher zero field split Kramers doublets which are not occupied at much lower temperatures. Unfortunately, also this additional knowledge is not enough to obtain a unique set of anisotropy parameters. Without any a priori information about the parameters or any possible labeling of the absorption features it remains strikingly challenging to get the correct parameters even with this large amount of data.

6.4 Broadband ESR on the Heavy Fermion Metal YbRh_2Si_2

As mentioned before in section 3.4, YbRh_2Si_2 shows many interesting phenomena at very low temperatures and moderate magnetic fields. Many of those intriguing aspects are directly or indirectly connected with the interaction of magnetic moments with either each other or with itinerant electrons. Therefore, electron spin resonance represents a powerful tool to study the magnetic behavior of YbRh_2Si_2 . The most interesting regions, in particular close to the quantum critical point (QCP), are located at low fields (below several hundred mT) and very low temperatures ($T \ll 1$ K). Without any zero field splitting the absorptions at such low fields are also located at low frequencies of the order of a few GHz (around 2.4 GHz at the QCP), leaving only a tiny fraction of typical microwave bands to theoretically being able to investigate that regime. The broadband technique, however, provides the means to investigate the whole phase diagram (at least around the QCP) at any chosen frequency and field and could offer new insights into the magnetic properties of YbRh_2Si_2 close to quantum criticality.

In the framework of this thesis such experiments were performed for magnetic fields up to 350 mT, frequencies up to 20 GHz and temperatures down to 60 mK. The result at the lowest temperature is shown in Figure 6.18. The data displayed there was treated with a slightly modified version of the averaging scheme explained earlier in section 6.1.1. Since in this case the signal is very small and the averaging scheme leaves the resulting transmission spectra slightly elevated at low fields and slightly lowered at higher fields* this could already be enough to obscure the signal. In addition, very small changes in the overall transmission due to thermalization effects of the coaxial lines can shift the averaged spectra by a small amount (e.g. when liquid helium is transferred to the cryostat during the measurement). Both effects result in a baseline deviation from unity which varies with magnetic field.

To cancel out this systematic shift another averaging step was performed, this time dividing each point at a certain magnetic field by the average of all points at that field, thus performing a ‘vertical’ averaging after the ‘horizontal’ averaging with

$$\text{horizontal } Tr_{\text{avg}}^{\text{hor}}(f_i, H_j) = \frac{Tr(f_i, H_j)}{\left(\sum_{j=1}^k Tr(f_i, H_j)\right)/k} \quad (6.5)$$

*due to hysteresis effects described earlier; the field was swept up and down prior to the initial measurement to load the waveguide with vortices. Were this not done, the spectra of the first measurement would differ from all subsequent ones.

$$\text{vertical } Tr_{\text{avg}}^{\text{vert}}(f_i, H_j) = \frac{Tr_{\text{avg}}^{\text{hor}}(f_i, H_j)}{\left(\sum_{i=1}^m Tr_{\text{avg}}^{\text{hor}}(f_i, H_j)\right)/m}. \quad (6.6)$$

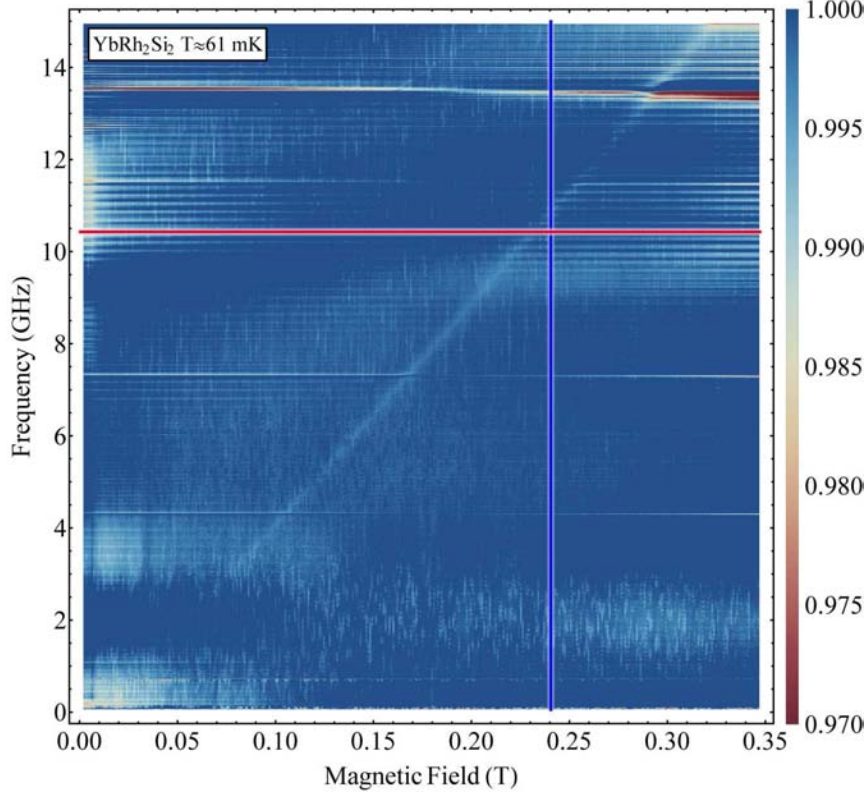


Figure 6.18: Color map of the broadband ESR data on YbRh_2Si_2 for the lowest achievable sample temperature of ≈ 61 mK. The ESR line is faintly visible but the signal to noise ratio is rather poor. The red and blue lines mark the respective positions of field and frequency sweeps on which the data treatment will be explained in the following.

The resulting color map shows a very weak signal of the ESR absorption as a seemingly straight line more or less diagonally traversing the field-frequency diagram. The peak amplitude, however, is only about 0.5 % deep and therefore drowns in the noise which is in the same order of magnitude. From a single frequency or field sweep spectrum the absorption is not observable; it is only in the color map that the line appears as ‘systematic’ noise. To yet be able to obtain the desired information about the position of the ESR absorption another data treatment scheme was devised. As a first step a low pass filter is applied to the frequency sweep raw data to filter out the high frequency noise. The appropriate cutoff frequency depends largely on the number of points in the spectrum and has no physical relevance. All frequencies

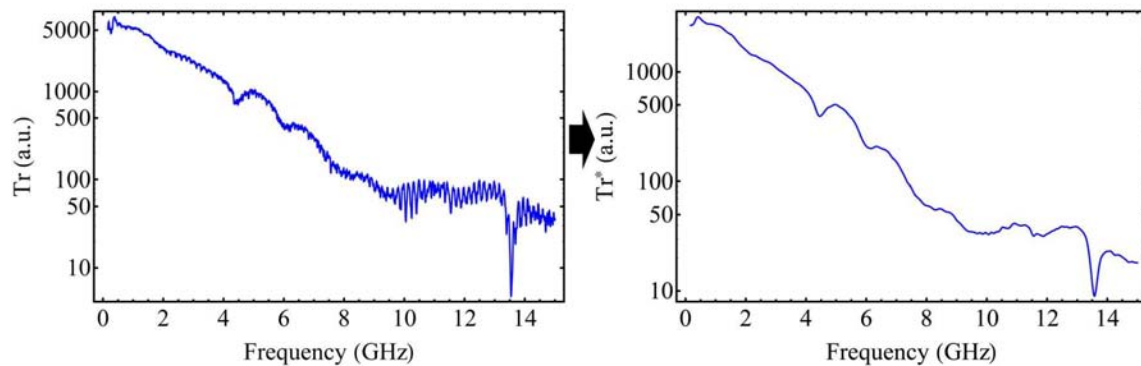


Figure 6.19: Left panel: Frequency sweep raw data for $H_{\text{ext}} = 241$ mT. Right panel: Treated data with a low pass filter to cancel out high frequency noise.

are mapped to a range from 0 to π and the cutoff frequency is defined as a fraction of that range (in this case $\pi/52 \approx 0.06$). This step is sensible since changes of the high frequency noise with magnetic field only add noise in the averaged spectra with frequencies (Fourier frequency components) much higher than the desired absorption feature.

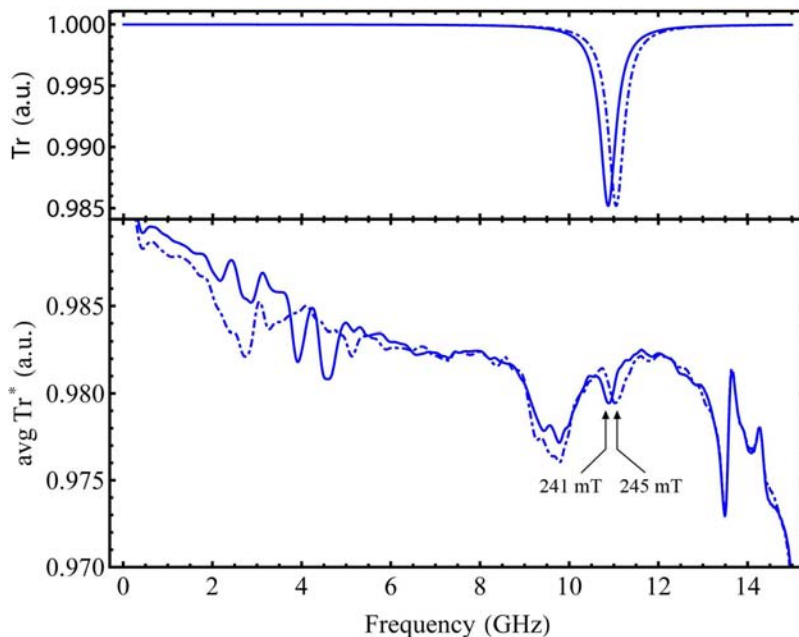


Figure 6.20: Simulated and real (averaged) frequency sweep data at 241 mT and 245 mT. The ESR frequency shift is observable although other features change as well.

As a next step each frequency point is averaged over all magnetic fields following the horizontal averaging scheme as described earlier (see Equation (6.5)).

With the spectra leveled to some degree a ‘pseudo’ derivative is formed with respect to the magnetic field according to

$$\partial_H \text{Tr}^*(f, H) = \text{Tr}^*(f, H) - \text{Tr}^*(f, H + \Delta H). \quad (6.7)$$

The asterisk expresses that the data is not the ‘real’ transmission but a quantity which is merely related to the transmission since it was filtered and averaged before this analysis step. Figure 6.20 shows two such averaged spectra at fields separated by $\Delta H = 4 \text{ mT}$ and the results of this discrete derivative is displayed in Figure 6.21.

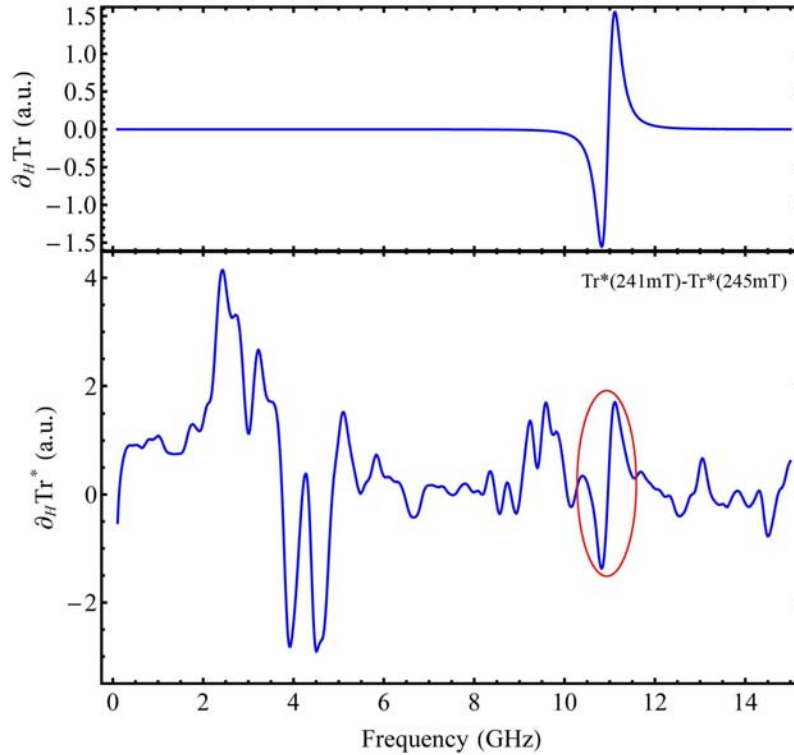


Figure 6.21: Simulated and real results of the quasi-derivation of the frequency sweeps.

The top panels in Figs 6.20 and 6.21 show idealized absorption spectra to demonstrate the various analysis steps in the absence of any artifacts or noise, simulated with Lorentzian absorption peaks.

In general, this (negative) derivative is similar to the moving normalization only that the baseline of the resulting spectra is located at zero instead of unity. Another difference is that for the moving normalization the separation in magnetic field ΔH had to be large enough for the lines not to overlap. Here, the width of the line is not easily determined and the minima and maxima around the ESR peak position (see Figure 6.21) are no longer necessarily the exact positions of the absorptions. Instead,

the position of ‘zero’-crossing between both spectra is the only distinguished point. Let the original absorption be at (H_0, f_0) and the initial spectrum at H_0 is replaced

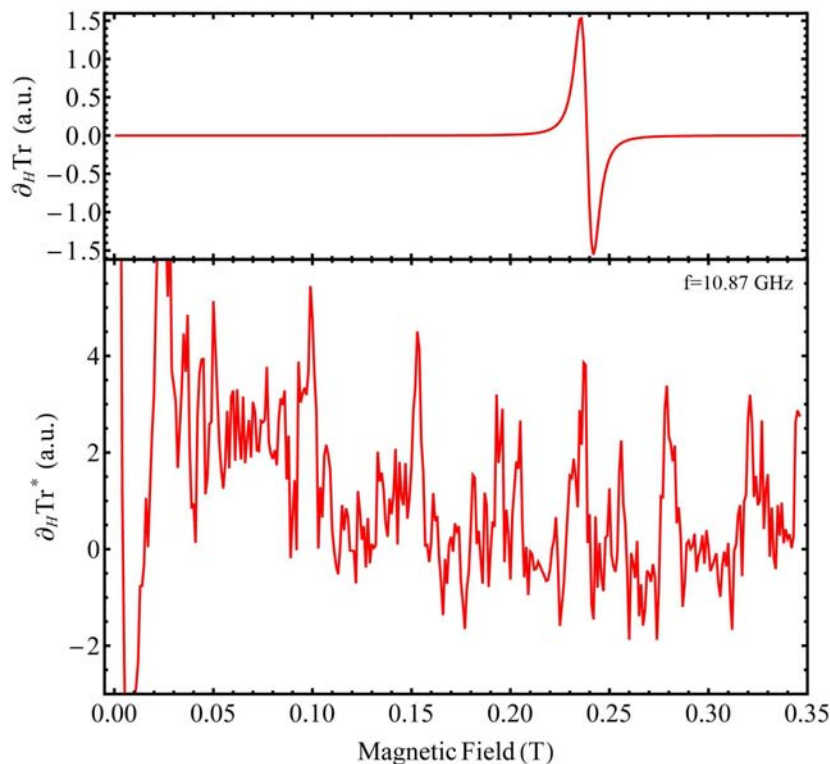


Figure 6.22: Simulated and real field sweep data at $f = 10.87$ GHz. The expected signature is not visible in the H sweep data.

with the discrete derivative, then the position of zero-crossing is frequency shifted by Δf^* with

$$f_1 = f_0 + \Delta f^* = f_0 + g \frac{\Delta H}{2} \quad (6.8)$$

with a g -factor of $g = 3$ (which can be estimated from any point on the ESR line barely seen in Figure 6.18). Regarding the field-swept spectra of the treated data (see Figure 6.22), the expected signature is not discernible from the high noise level. However, the noise in those spectra shows only minute changes for adjacent frequencies (not shown) which suggests another discrete derivative along the frequency with

$$\partial_f(\partial_H Tr^*(f, H)) = \partial_H Tr^*(f, H) - \partial_H Tr^*(f + \Delta f, H).$$

The result of this analysis step is shown in Figure 6.23 and Figure 6.24 as field and frequency-swept spectra, respectively. Although the noise is still quite high, the

absorption peak is now visible as a distinct feature and after another low pass filter of the field-swept spectra (with a cutoff at $\pi/5$) the signal to noise ratio is improved to an extent that allows for the extraction of the exact ESR peak position.

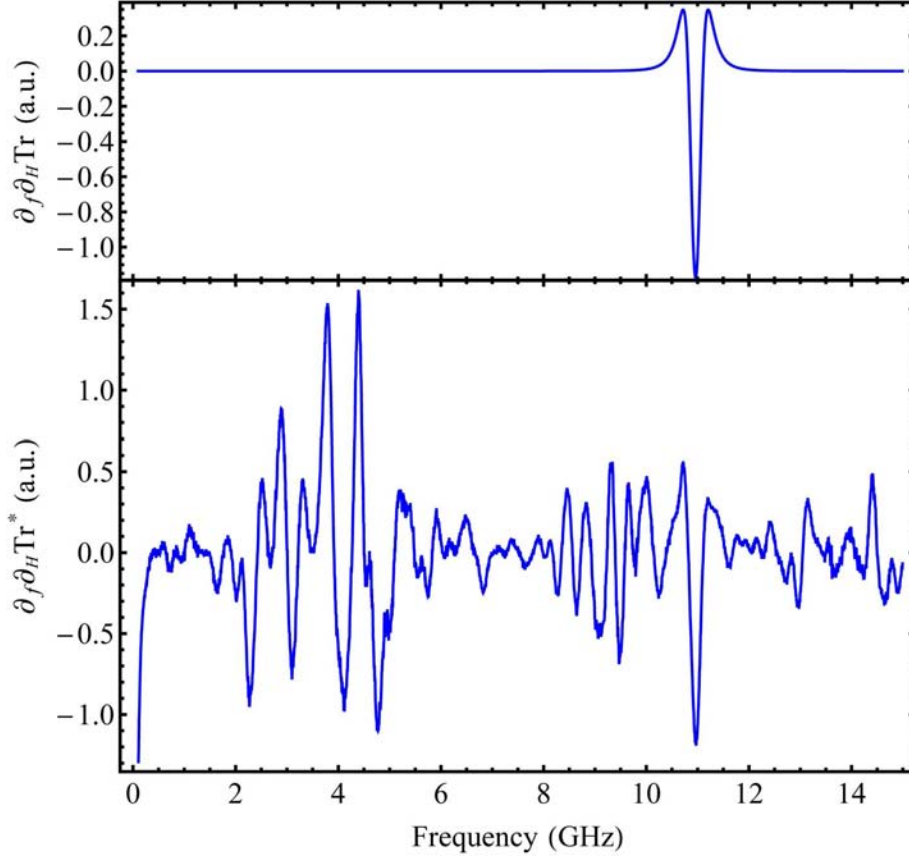


Figure 6.23: Simulated and real frequency-swept spectra after the discrete derivative with respect to frequency.

One has to consider that also the last discrete derivative introduces yet another shift - this time in magnetic field. For any fixed frequency the local minimum in the treated data is located at

$$H_1 = H_0 + \Delta H^* = H_0 + \frac{1}{g} \frac{\Delta f}{2}. \quad (6.9)$$

With Equation (6.8) and Equation (6.9) the original peak position was transformed to

$$(H_0, f_0) \longrightarrow \left(H_0 + \frac{1}{g} \frac{\Delta f}{2}, f_0 + g \frac{\Delta H}{2} \right).$$

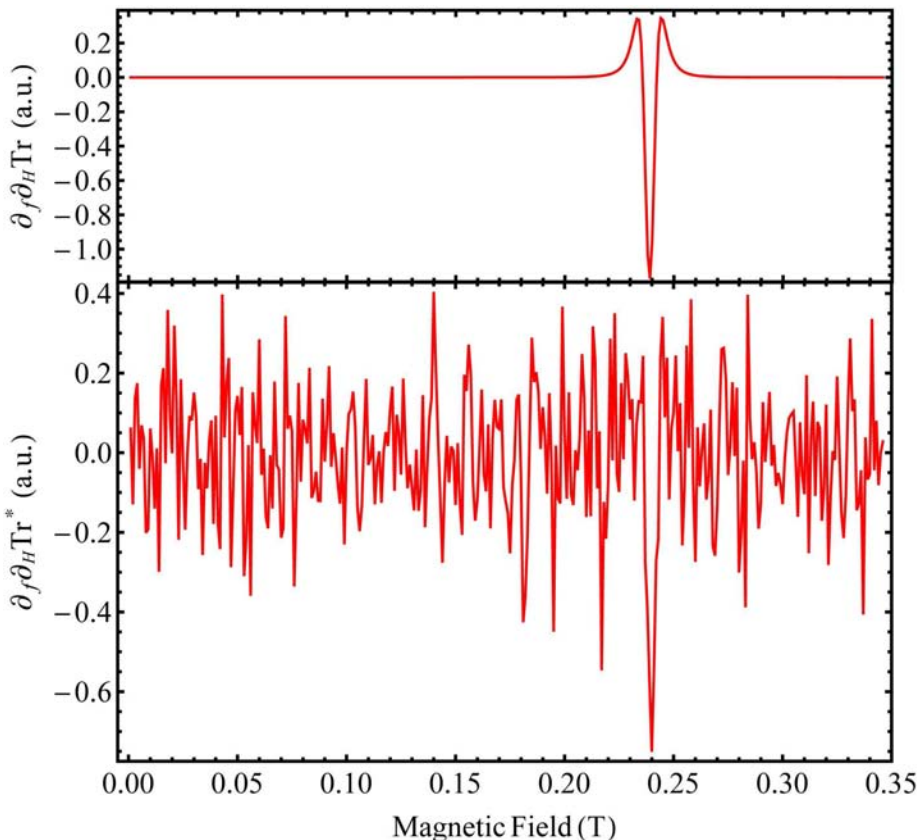


Figure 6.24: Simulated and real field-swept spectra after the discrete derivative with respect to frequency. The ESR feature is clearly visible above the noise.

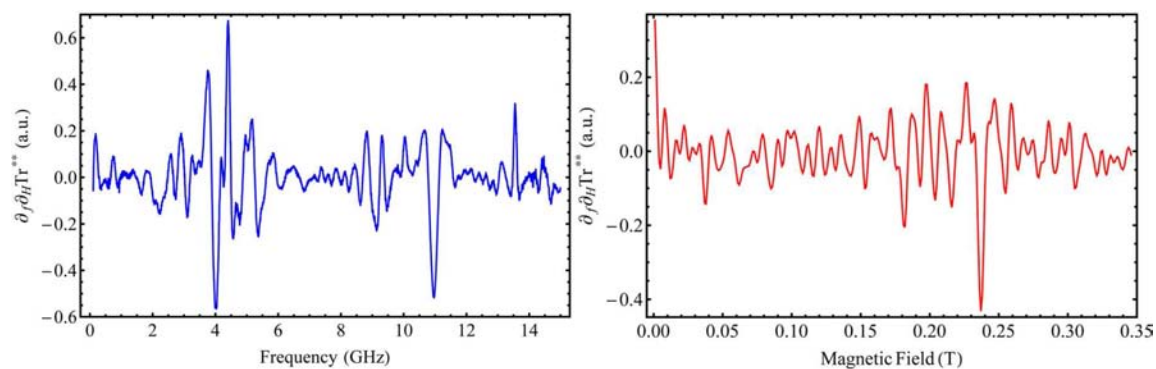


Figure 6.25: Frequency and field-swept spectra after another low pass filter over all field sweeps. The noise is reduced significantly and centered around a straight baseline.

In this way, the whole data set can be shifted in reverse to move the characteristic minima to the initial ESR position (here $\Delta H = 4$ mT and $\Delta f = 6.475$ MHz, hence $\Delta H^* \approx 0.0717$ mT and $\Delta f^* \approx 90$ MHz). Figure 6.26 shows the result of the

data treatment described above. The ESR absorption line sticks out much clearer and allows for the extraction of the peak positions. To do so, the local minima are determined in a region confined by two straight lines above and below the absorption ($f(H) = 48 \frac{\text{GHz}}{\text{T}} \cdot H$ and $f(H) = 48 \frac{\text{GHz}}{\text{T}} \cdot H - 1.2 \text{ GHz}$) for sweeps along H for each frequency f_i as well as for frequency sweeps for each H_i . To further reduce the

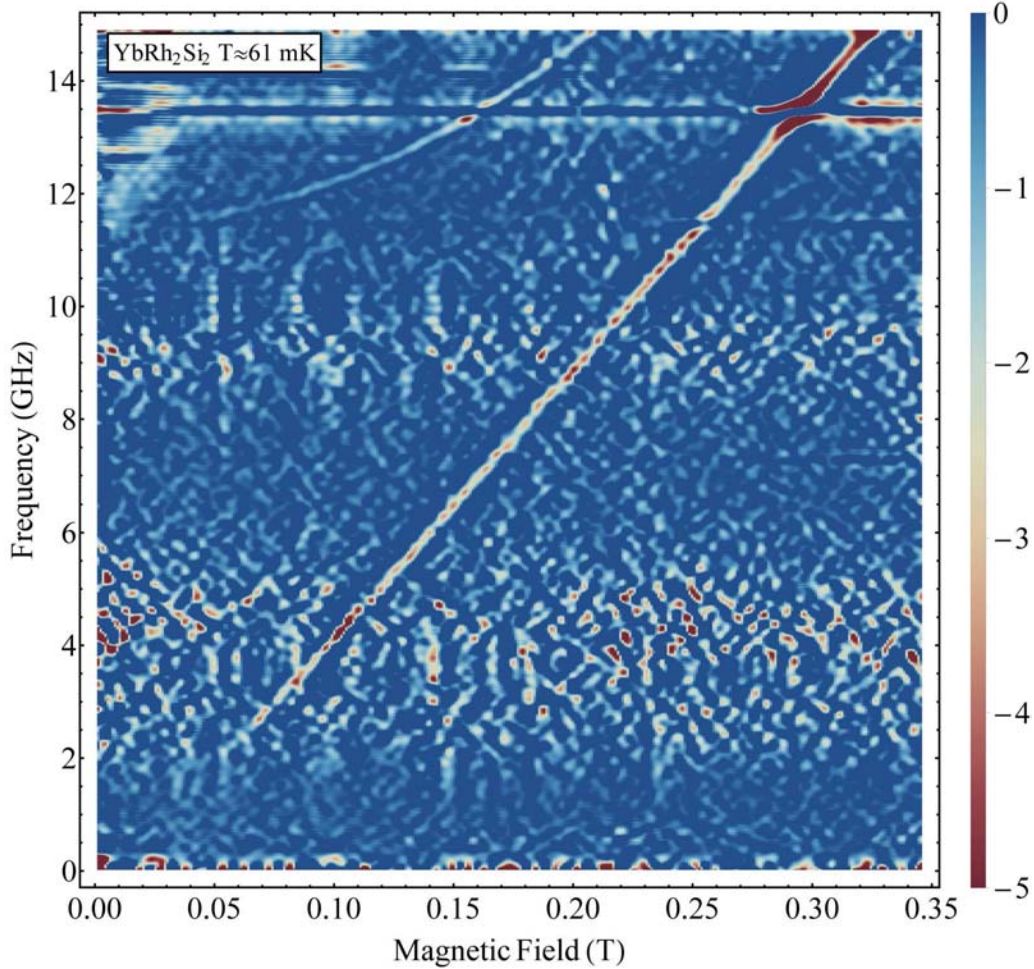


Figure 6.26: Color map of the broadband ESR data treated with the above mentioned scheme. The line is much clearer than before and the peak positions can be extracted.

possibility to get false results, only minima which coincide along both sweeping directions are considered to be the actual absorption positions. A selection of ESR positions obtained in that way is shown in Figure 6.27 together with the original and treated data. These points can then be used to determine the g -factor from the absolute position of the absorption peak (with respect to frequency and field) using the Zeeman relation $hf = g\mu_B H$. The g -factors gathered in that way are plotted in Figure 6.28 for all measured temperatures. In general, all curves follow

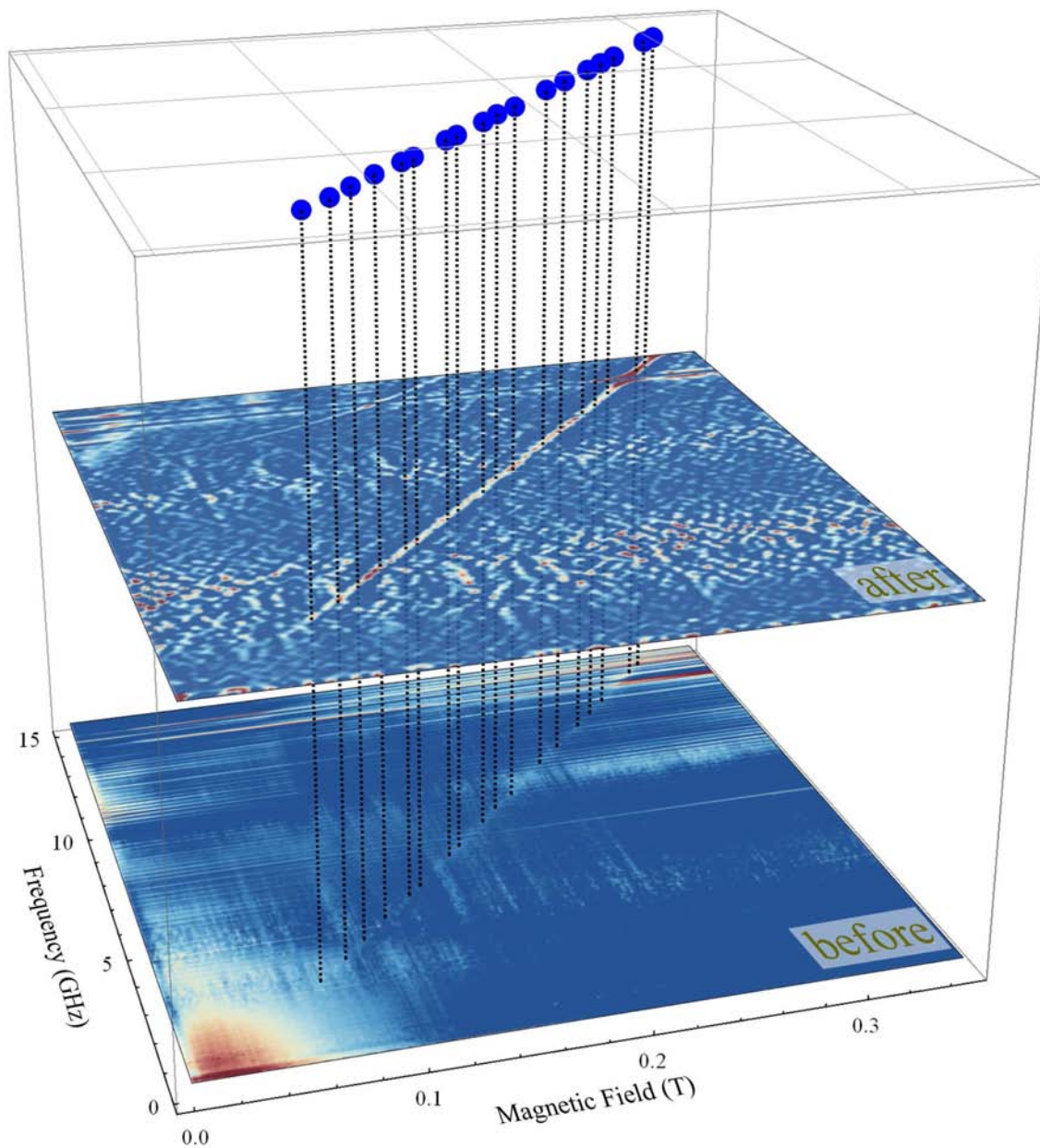


Figure 6.27: Plots of untreated and refined data and a selection of extracted ESR position points.

a common trend, namely the g -factors increase with increasing field and seem to level off around $g \approx 3.3$ for high fields. With increasing temperature the population difference between the spin states decreases and the absorption peak gets weaker. As a result, the peak positions can only be traced reliably above a certain threshold level splitting which increases with temperature. Therefore, the lowest field, for which the g -factor could be determined increases with temperature. For the highest

temperature of $T \approx 302$ mK the field dependence of the g -factor deviates at low fields slightly from those at lower temperatures indicating a change of properties. Regarding the phase diagram of YbRh_2Si_2 (see Figure 3.7) it becomes evident that the 300 mK curve always stays well above the Landau Fermi-liquid (LFL) phase within which the g -factor is expected to be constant [95]. Also the 200 mK curve never enters the LFL phase for the investigated fields, but is still in close vicinity and a change in g might only be large enough to register in this plot for fields below the threshold field.

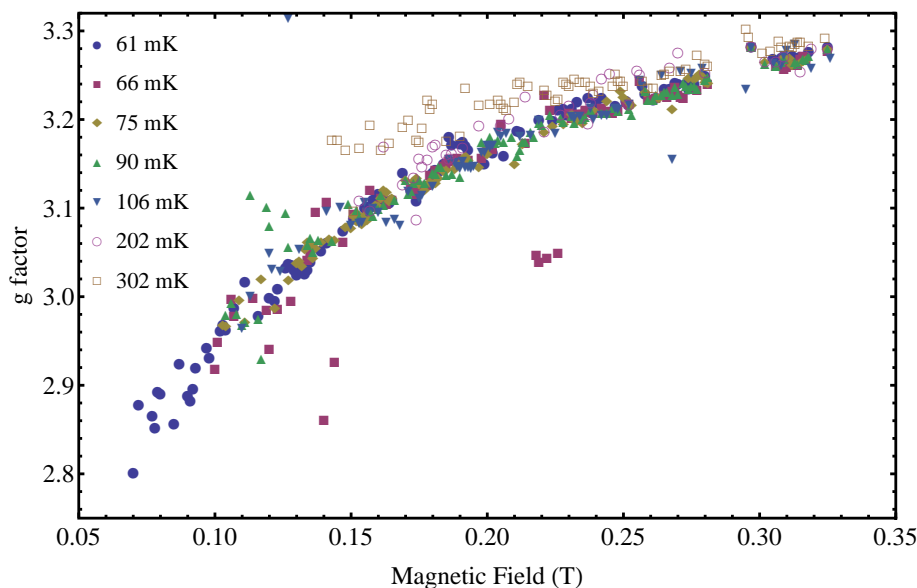


Figure 6.28: ‘Local’ g -factors for all measured temperatures. With increasing temperatures the absorption gets weaker at low fields/frequencies and the positions can only be traced starting from an ever increasing threshold frequency.

Regarding the field dependence of g one has to be very careful not to jump to unjustified conclusions. If the line shown in Figure 6.26 is extrapolated to zero frequency it seems to intersect the H -axis at finite fields which is impossible from a physics point of view. The left panel in Figure 6.29 mimics such a frequency-field relation and the right panel shows the resulting g -factor as a function of external magnetic field for the case that g is extracted from the absolute resonance positions ($H_{\text{res}}, f_{\text{res}}$) using the Zeeman resonance condition. The resulting behavior of $g(H)$ resembles the one extracted from the measured data.

The broadband technique, however, offers another way to determine the g -factor. If the points $(H_{\text{res},i}, f_{\text{res},i})$ are sufficiently close g can be obtained from the slope of the curve given by $(H_{\text{res},i}, f_{\text{res},i})$. It is found that the resonance frequency in-

creases linearly with increasing field and $g_{\text{slope}} (= h\Delta f_{\text{res},ij}/\mu_B\Delta H_{\text{res},ij})$ can be given as $g_{\text{slope}} = 3.412 \pm 0.006$.

The decrease of g towards lower fields, as shown in Figure 6.28, might therefore merely be an artifact reflecting the fact that the Zeeman resonance condition $f_{\text{res}} = g\mu_B H/h$ by default extrapolates to zero frequency for zero field.

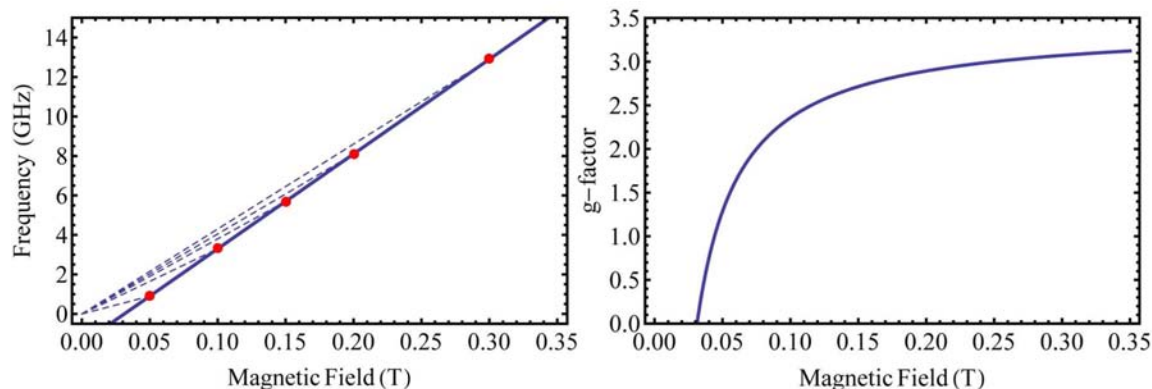


Figure 6.29: Simulated resonance positions (left panel thick line) for the case, that the positions intersect the H -axis at finite fields and resulting g -factor obtained from the Zeeman resonance condition. The curve shows the same trend as observed in the g -factors extracted from the measured data. The ‘real’ g -factor is approached for high fields.

The question of what happens at low fields/rfrequencies, however, still remains (since the curve has to intersect the frequency axis either at zero or at positive finite values for $H = 0$).

Taking a close look at the low field/frequency region in Figure 6.26 one could speculate a change towards a shallower slope for fields below ≈ 65 mT. From resonant measurements of YbRh_2Si_2 (using a coplanar resonator; discussed in the following section) one can extract a g -value using the Zeeman resonance condition of $g \approx 2.83$ at 61 mK at a frequency of 1.5 GHz. A change of g does not come as a surprise at this point, since the system enters the antiferromagnetic (AFM) phase around those fields and temperatures and the magnetic response differs from that in the paramagnetic non-Fermi-liquid regime. Unfortunately, the ESR absorptions cannot be traced in the AFM phase since the signal is too weak to be detected due to the very small magnetic moment in the ordered phase (only around $2 \times 10^{-3}\mu_B$ per Yb atom [112]). Interestingly, the effect of the (extrapolated) line of ESR positions intersecting the field axis at finite fields remains also for temperatures above the Néel temperature. This leads to the conclusion, that it is an intrinsic property of the Yb spin response. Since the Kramers doublet has to be degenerate at zero field, the

transition frequency has to show a quadratic behavior for low fields while it becomes highly linear for stronger fields.

Although the low frequency/field regions remain inaccessible, so far, the results again impressively demonstrate the potential of the broadband technique. By performing an ESR measurement at a single frequency, one has no other chance but to ‘put’ all interactions that might lead to unexpected phenomena into the g -factor which could, in turn, provoke deceitful conclusions about the studied system. The broadband technique, on the other hand, provides much more information over a wide range of frequencies and fields and has the capability to unveil a more accurate description of the system under study. Obviously, a future goal for this compound is the investigation of the low field/frequency region which remained obscured in the measurement described here. To do so, one could either repeat the measurement with a larger sample (the sample used in this study was of undefined shape around 2 mm in diameter) and a longer waveguide to extend the interaction area and thus effectively address more spins or improve the detection scheme, e.g. by modulating the field and using lock-in amplifiers. Reducing the distance between sample and waveguide might additionally help since the presence of a highly conducting surface slightly above the waveguide structure further ‘squeezes’ the microwave magnetic fields leading to higher rf field amplitudes and hence a stronger ESR signal. This has to be done with extreme caution since rf currents which are subjected to ohmic losses are induced in the sample, effectively heating the small fraction which is studied. In that way, the gathered data might reflect sample properties at a higher sample temperature than intended, leading to erroneous results.

Before finalizing this section another feature visible at the upper limit of the investigated frequency range, as seen in the top left in Figure 6.26 will be discussed for the sake of completeness. This line, which is tightly bent and intersects the frequency-axis at around 11.5 GHz strongly resembles those observed already in the ruby sample. In fact, this line could easily originate from Cr^{3+} impurities in the sapphire substrate since it can be simulated by the Eigenfunctions of the CrIII Hamiltonian expressed in Equation (6.2) in section 6.2 on page 73. For an angular orientation of the magnetic field with respect to the crystallographic c -axis of $\theta = 51^\circ$ two transitions lie on top of each other at the very position of the observed absorption giving rise to the enhanced visibility of this line with respect to the other transitions in ruby.

7 EPR on Heavy Fermions at mK Temperatures

As already outlined before in section 2 it is rather straight forward to design and fabricate resonators based on superconducting coplanar waveguides which feature quality factors ranging around several 10^5 . It therefore stands to reason to also perform resonant magnetic resonance experiments utilizing superconducting coplanar waveguide resonators (thereby profiting from the Q -enhanced line intensity). The investigated material was again the heavy fermion metal YbRh_2Si_2 . This material is predestined for this measurement technique since the most interesting physical phenomena happen to be located at very low temperatures while still at moderate magnetic fields (for an alignment of the external magnetic field perpendicular to the crystallographic c -axis), a combination perfectly suitable for coplanar waveguide resonators. Since the low frequency/field region is of the highest concern three different resonator structures were chosen to investigate the compound. Their designs are depicted in Figure 7.1. The only difference amongst them is the length of the resonator line and hence the resonance frequency. Other geometric parameters like the center conductor width remained unchanged. They were also designed to feature approximately the same quality factor. The ‘longest’ resonator has a fundamental resonance frequency of $f_{\text{res}} \approx 1.5$ GHz, the next shorter one around 2.0 GHz and the shortest one around 2.6 GHz. In the following they will be referred to as R1, R2 and R3, respectively.

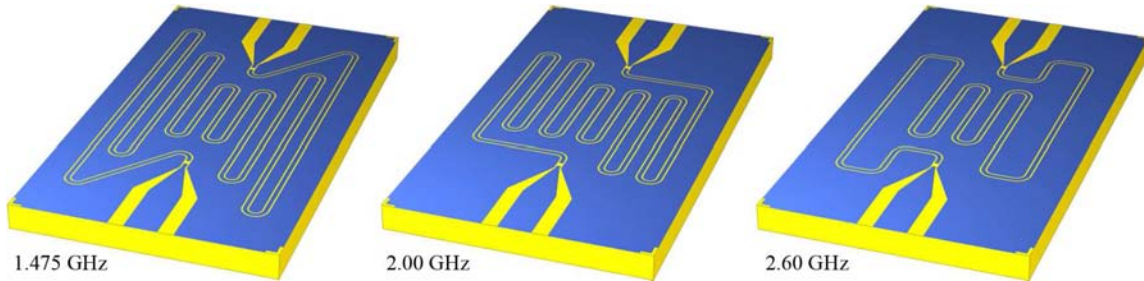


Figure 7.1: Resonator structures of the three different resonators used for resonant ESR on YbRh_2Si_2 and their fundamental frequencies.

The first mode of R1 was measured with a quality factor of $Q_{\text{init}} \approx 1.5 \times 10^5$ without any sample and at temperatures of 1.6 K. With the sample ‘hovering’ approximately 120 to 150 μm above the resonator structure this quality factor was immensely reduced by a factor of 50 to only about 3000. This effect was discussed earlier in section 5.2 and is therefore only mentioned briefly at this point.

Is the resonance recorded for different magnetic fields (see Figure 7.2) a few effects

become immediately evident, namely

- (i) the resonance frequency changes slightly, first towards higher then to lower values (see red curve in the frequency-field plane in Figure 7.2),
- (ii) the peak amplitude of the resonance decreases for magnetic fields greater than some threshold field,
- (iii) at a certain magnetic field a clear, strongly pronounced dip can be seen in the peak amplitude (see blue curve in the transmission-field plane in Figure 7.2).

The first effect was also already mentioned earlier as a result from the magnetic field sweep history and can be explained by vortex-antivortex dynamics at the supercon-

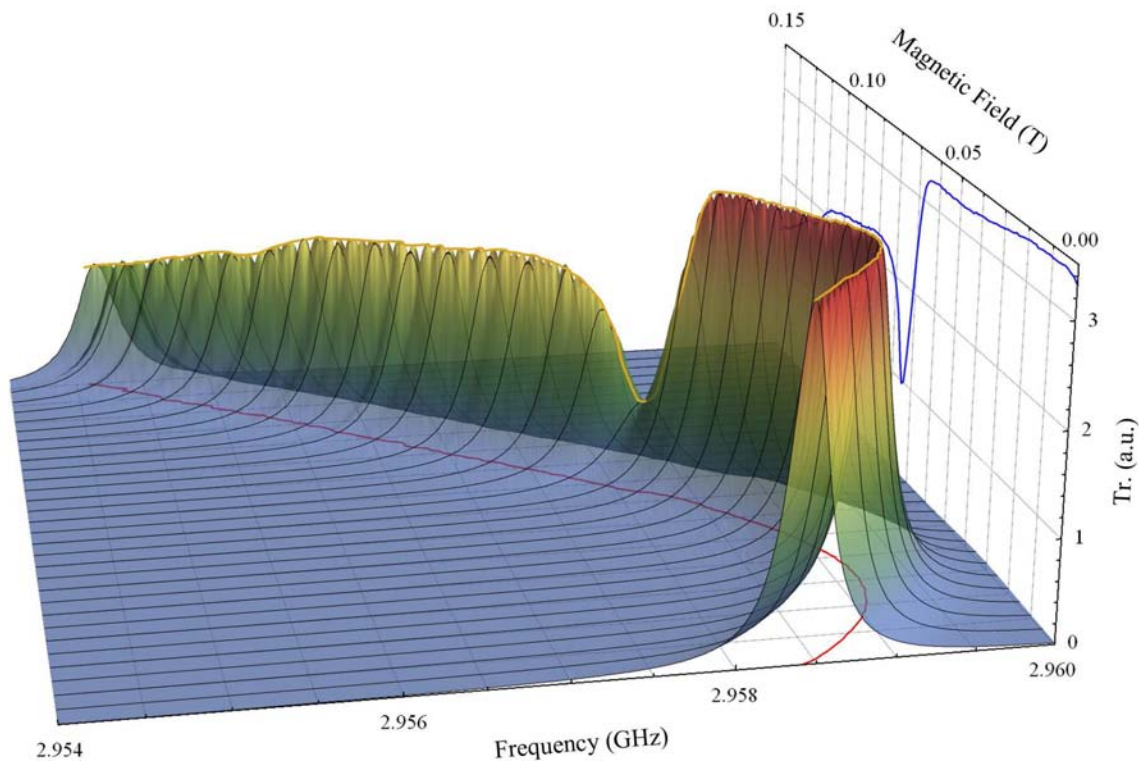


Figure 7.2: Typical resonance spectra as a function of magnetic field (in this case those of the second mode of R1). The red curve in the frequency-field plane follows the resonance frequency which changes by less than 1 % of its absolute value and the blue curve in the transmission-field plane reflects the peak amplitude as a function of magnetic field. The ESR absorption around 73 mT is clearly visible.

ducting film edges. However, since the change in frequency is very small for the whole magnetic field range this effect can be promptly neglected. The second effect,

that of a reduction of the peak amplitude is also related to the resonators response to external magnetic fields. For field strengths greater than the first critical field (at the film's edges; strongly orientation dependent) vortices start to enter the film and the microwave losses increase. The peak amplitude (or the insertion loss), however, is not a very good measure for this effect. To quantify losses the quality factor is the much better suited quantity since its inverse directly reflects all losses present in the system.

The third point, eventually, is the wanted magnetic resonance signal. Equals the Zeeman energy splitting $\Delta\mathcal{E} = g\mu_B H_{\text{ext}}$ the energy of the microwave signal $\mathcal{E}_{\text{rf}} = hf$ the resonance condition is fulfilled and the transmitted signal strength is reduced significantly. This manifests itself in a drop of the resonance peak as well as a dip in the quality factor as a function of external magnetic field.

The complete measurement and data treatment procedure is schematically displayed in Figure 7.3, again using the second mode of R1 as an example. The whole routine can be divided into several parts:

- (1) Frequency swept spectra of the resonators resonance are recorded for different magnetic fields. Data presented in this work was typically taken in field intervals ranging from 0.6 to 3 mT (smaller steps close to the resonance field). Each spectrum is then fitted to a Lorentzian model to extract the exact resonance frequency f_{res} and the full width at half maximum Δf in order to obtain the quality factor with the generic expression

$$Q = \frac{f_{\text{res}}}{\Delta f}.$$

- (2) The quality factor as a function of external magnetic field already shows a very strong signature of the magnetic resonance. However, it proves to be very difficult to extract the correct absorption line parameters from this $Q(H)$ dependence since the quality factor of the coplanar waveguide resonator itself strongly depends on the external field. The behavior of $Q(H)$ is analytically extremely hard to grasp as many external factors play an important role (orientation, waveguide design, spatial flux and current density as well as the close environment). For this reason, the field dependence of the quality factor (with the magnetic resonance part cut-out) was modeled by a non-physical expression to reproduce the background in absence of the absorption peak for each harmonic and each temperature. This arduous task was completed by Mojtaba Javaheri to whom I hereby express my gratitude.

- (3) After successful subtraction of the background the magnetic resonance line can be fitted to a Dysonian line shape model in the form [113–115]

$$P(H) = a \frac{\Delta H + \alpha(H - H_0)}{4(H - H_0)^2 + \Delta H^2} + \frac{\Delta H + \alpha(H + H_0)}{4(H + H_0)^2 + \Delta H^2} \quad (7.1)$$

with the resonance field H_0 , the linewidth ΔH , α as the dispersion-to-absorption ratio and a simple prefactor a . $P(H)$ is the absorbed power as the external field $H = H_{\text{ext}}$ is swept through the magnetic resonance.

- (4) + (5) By doing so for all temperatures and all accessible modes, the relevant parameters like the resonance field and the linewidth can be plotted as a function of temperature.

In this way, the resonance fields and linewidths could be determined for many different frequencies and temperatures. In total, the first nine modes of R1, the first six of R2 and the first four of R3 could be measured over a temperature range from ≈ 40 mK up to 4 K, spanning two orders of magnitude. Frequency-wise a range from around 1.5 up to ≈ 13.4 GHz was covered. All frequencies and respective (approximate) resonance fields of the various modes of the individual resonators are given in Table 7.1.

A complete overview of all measured spectra, however, is given in Figure 7.4. The figure shows a section of the phase diagram introduced already in Figure 3.7 in section 3.4 (displayed section is indicated by the gray shaded area in the inset). The different modes that could be used to measure the magnetic resonance are drawn as connected points in blue (for R1), red (R2) and green (R3) for the whole accessible temperature range. The dots mark the position of the magnetic resonance for the given frequency as a function of temperature.

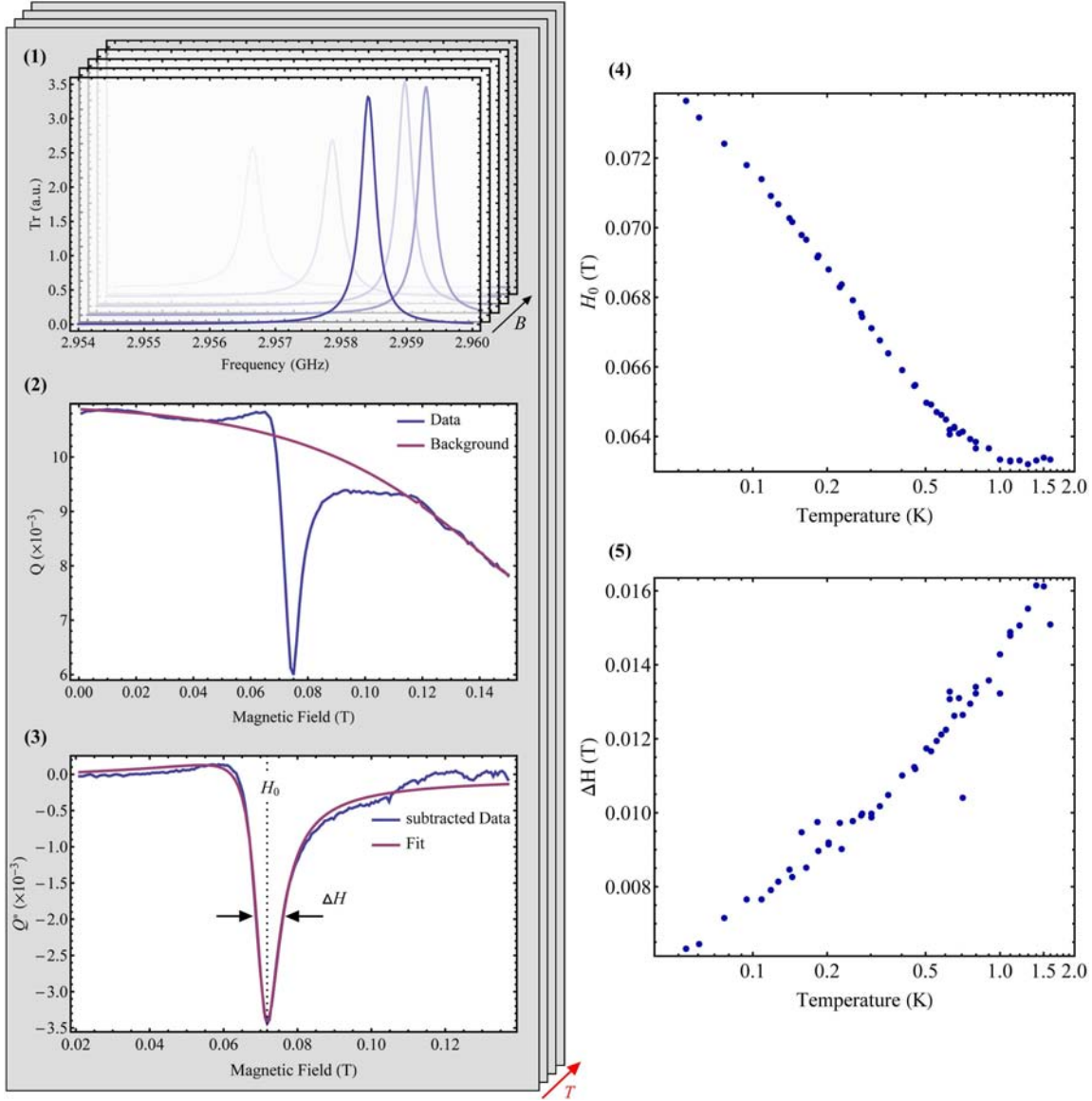


Figure 7.3: Data acquisition and analysis steps. (1) As a first step, frequency-swept spectra are recorded around the resonators resonance frequency for consecutive external magnetic fields (top panel, also compare Figure 7.2). These spectra are fitted with a Lorentzian model and the quality factor Q is extracted as a fitting parameter. (2) As a function of magnetic field Q clearly shows the magnetic resonance on top of a bothering background which is basically given by the high frequency response of the resonator to an external magnetic field (middle panel). (3) After subtraction of the background the magnetic resonance can be fitted using a Dysonian model fit and parameters like the resonance field H_0 and the linewidth ΔH can be obtained (bottom panel). The whole process is repeated for different temperatures and frequencies to acquire a whole set of parameters as a function of H and T [(4) and (5)].

Mn	1	2	3	4	5	6	7	8	9
Freq. (GHz)	1.5	2.96	4.45	5.88	7.34	8.8	10.21	11.86	13.41
$H_0(0.2 \text{ K})$ (mT)	34	68	102	134	165	197	227	262	293
Freq. (GHz)	2.07	4.09	6.14	8.12	10.12	12.13	-	-	-
$H_0(0.2 \text{ K})$ (mT)	47	94	138	182	225	266	-	-	-
Freq. (GHz)	2.66	5.26	7.90	10.52	-	-	-	-	-
$H_0(0.2 \text{ K})$ (mT)	60	119	177	232	-	-	-	-	-

Table 7.1: Resonator resonance frequencies and corresponding magnetic resonance fields at 200 mK for all modes (Mn , $n = 1, 2, 3, \dots$) of R1 (top), R2 (middle) and R3 (bottom).

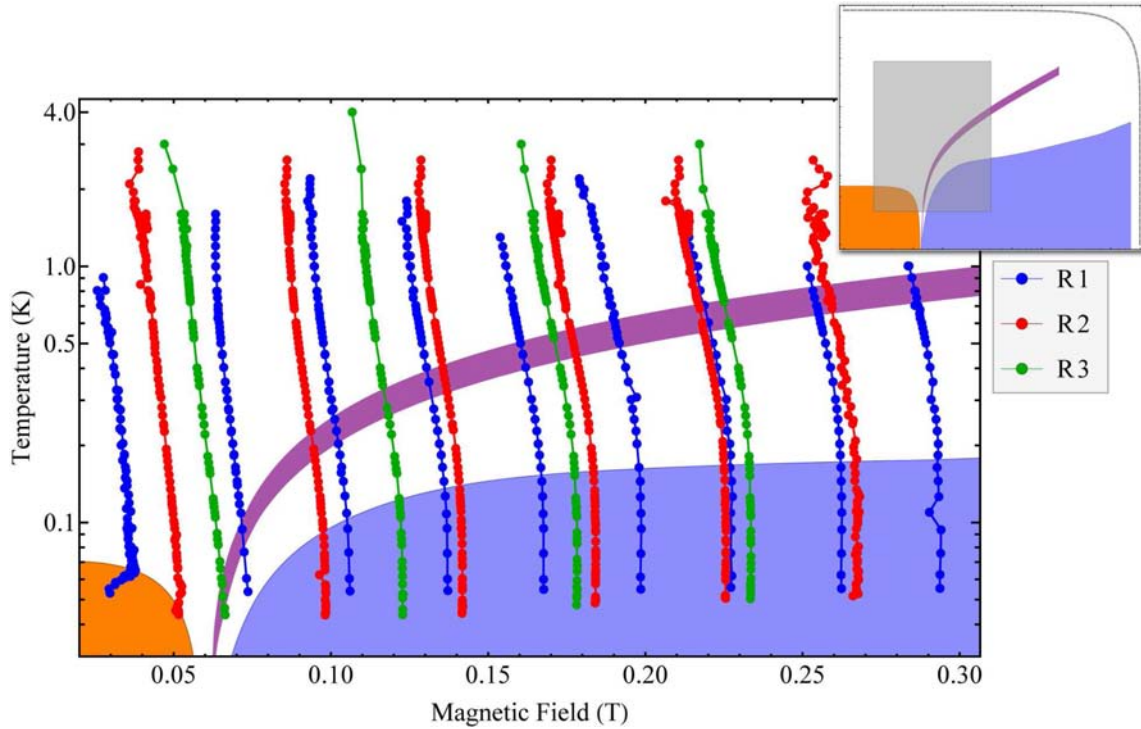


Figure 7.4: Resonance positions as a function of magnetic field and temperature for all measured frequencies with the underlying phase diagram of YbRh_2Si_2 . Modes of different resonators are colored blue, red and green for R1, R2 and R3, respectively. The inset maps the displayed section with respect to the full phase diagram as displayed in Figure 3.7 on page 32.

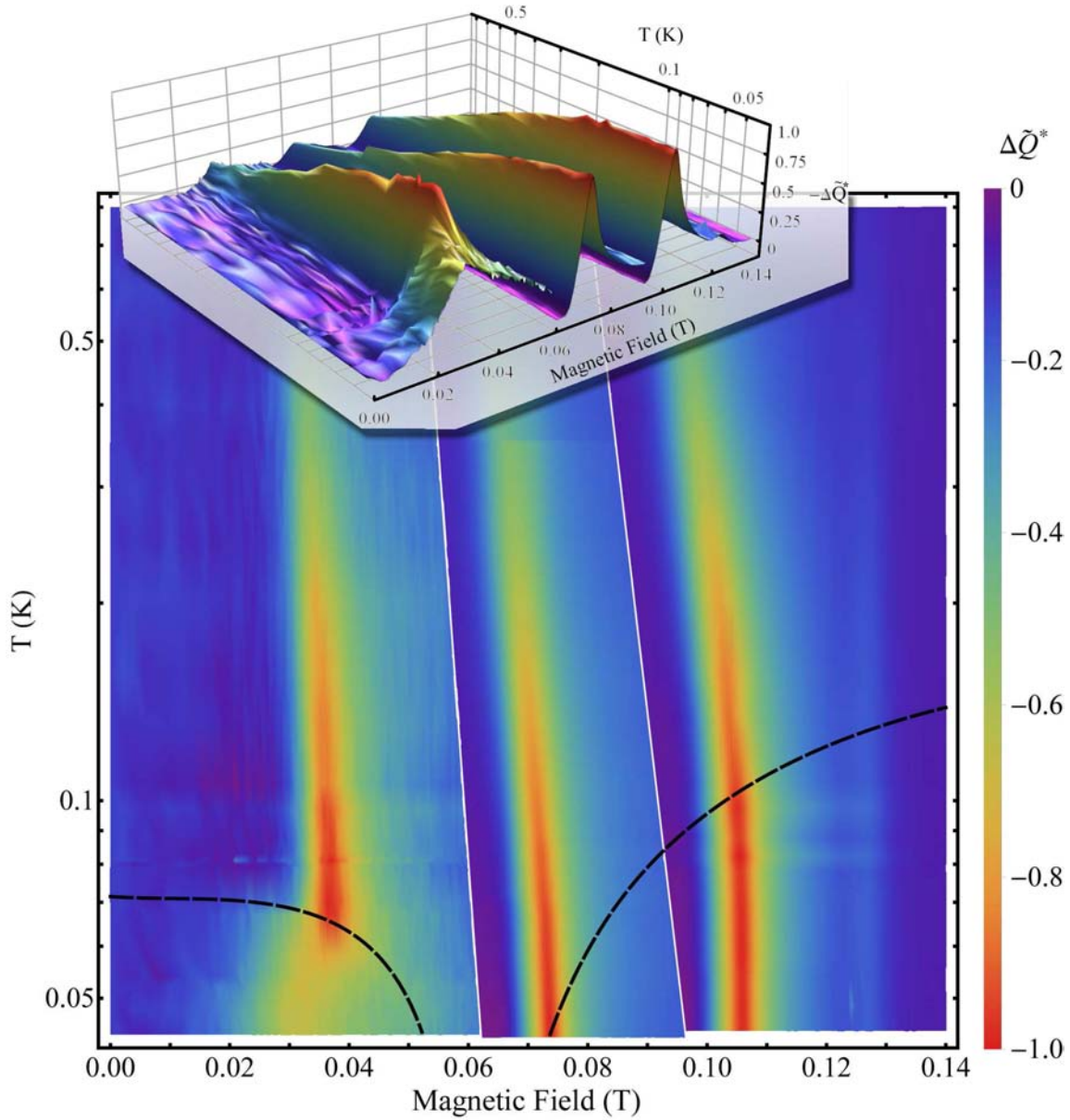


Figure 7.5: Color map of the quality factor as a function of external field and temperature for the first three modes of R1. For better comparison of the different datasets the quality factor for each mode was normalized in a way that the minimum Q of the background subtracted data was set to -1 . The dashed lines indicate the AF phase boundary (at $H \rightarrow 0$) and the Fermi-liquid crossover temperature. The small inset shows the same data in a three dimensional view. Further description see text.

note

Not all modes cover the whole temperature range from 40 mK to 4 K. The thermal coupling of the sample was better in the runs with R2 and R3, consequently leading to lower achievable temperatures. Concerning ‘high’ temperatures it gets increasingly difficult to maintain stable temperatures in a dilution refrigerator for $T \geq 1$ K (causes the ‘noisy’ tails at high T). It also strongly depends on the mode of each individual resonator until what temperature a magnetic resonance signal is still discernible (different design leads to distinct spatial microwave field distributions for different harmonics, some of which might be more favorable by the irregular sample shape).

Figure 7.4 already shows a few key features obtained from magnetic resonance measurements at ultra low temperatures. For one, regarding the fundamental mode of R1 and R2 (the only two resonator frequencies low enough to study the AF phase) one can observe a significant change of the temperature dependence of the resonance field upon entering the antiferromagnetic phase. For temperatures above the Néel temperature T_N the resonance field increases with decreasing temperature. This direction is completely reversed once the phase boundary is crossed.

Another common feature is the ‘s’-shaped course of the resonance field as a function of temperature for all magnetic resonances that enter the Fermi-liquid regime. Within the FL phase H_0 stays rather constant and starts to decrease with increasing temperature above the crossover region. At higher temperatures ($T \geq 2$ K) this trend levels off and the resonance field becomes constant once again (best seen for modes 2 through 5 of R2).

For a qualitative description, however, one does not necessarily go through the whole analysis procedure. Figure 7.5 shows the temperature and field dependence of the (background subtracted) quality factor for the first three modes of R1 in a color map and in a three dimensional view. To match the color scales and the absolute values of the different modes, $Q(H_{\text{ext}}, T)$ of each mode was normalized so that $\min[Q(H_{\text{ext}}, T)] \stackrel{!}{=} -1$. With this set of frequencies all three magnetic resonance lines show a unique behavior at the low temperature limit.

- Mode one enters the AF phase at around 67 mK upon which point the absorption peak amplitude drops significantly to only about 60% of the value just above the transition. Further decreasing the temperature leads to a shift of the resonance frequency towards lower fields. Another effect, which is better

visible in the small 3D inset is an abrupt change of the linewidth and lineshape. The lineshape gets more of a Lorentzian character as the α parameter in Equation (7.1) approaches zero for temperatures below T_N . This effect goes hand in hand with a drastic increase of the linewidth by more than a factor of two indicating additional relaxation channels within the AF phase.

- The second mode stays in the non Fermi-liquid regime for the whole displayed temperature range and shows a constant increase of the resonance field with decreasing temperature.
- The third mode, finally, shows the same temperature dependence as the other two modes for the high temperature limit (namely an increase of the resonance field with decreasing temperature) but the steady shift levels off upon entering the FL regime within which the resonance field stays constant. In addition, the absorption peak amplitude also remains constant within the Fermi-liquid phase.

The first mode of resonator R1 as well as that of R2 is low enough in frequency for the magnetic resonance to enter the antiferromagnetic phase at which point the absorption line parameters change drastically. For a better understanding of the behavior of the magnetic resonance close to the phase transition it is helpful to scrutinize this field and temperature range more closely. Figure 7.6 shows a selection of spectra for temperatures very close to the Néel temperature.

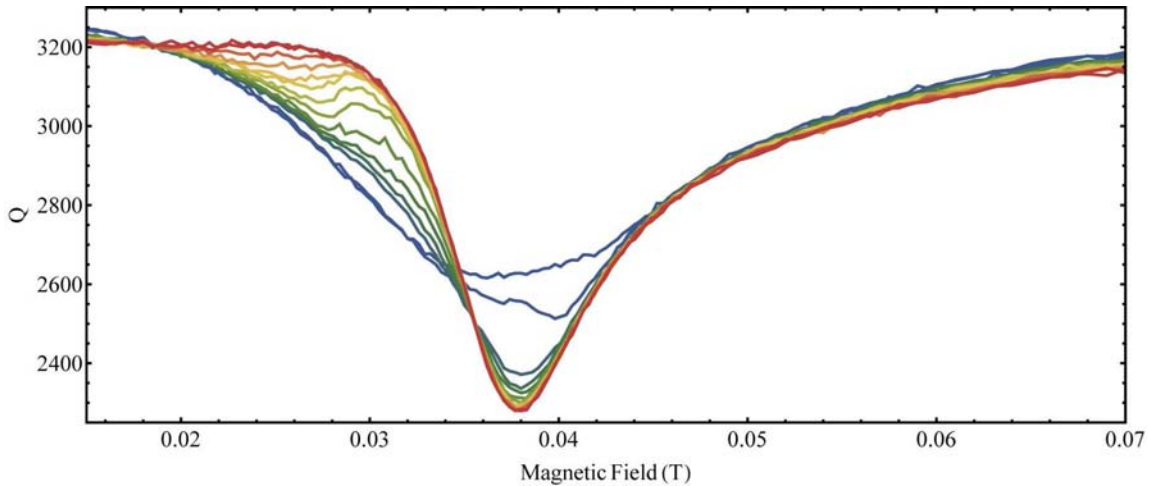


Figure 7.6: Quality factor as a function of magnetic field for temperatures close to the AF phase transition. Colors indicate different sample temperatures from $T < T_N$ (blue) to $T > T_N$ (red).

In the vicinity of the phase boundary the spectra show contributions of both the antiferromagnetic and the non-Fermi-liquid lineshape; in fact, it seems as if the resonance signal gradually develops from the AFM lineshape to that of the NFL regime while passing the phase transition. To put this finding in relation with the phase diagram (which was derived from results obtained with different experimental techniques, e.g. dc transport, specific heat and Hall effect) spectra for four different temperatures are plotted as a function of external magnetic field in Figure 7.7. The sample temperature was determined as the mean temperature of all temperatures measured within the gray shaded magnetic field regime (25 to 45 mT). This range was chosen since the interesting effects appear just within this region and since for higher fields all considered spectra share the same NFL tail. The spectrum at

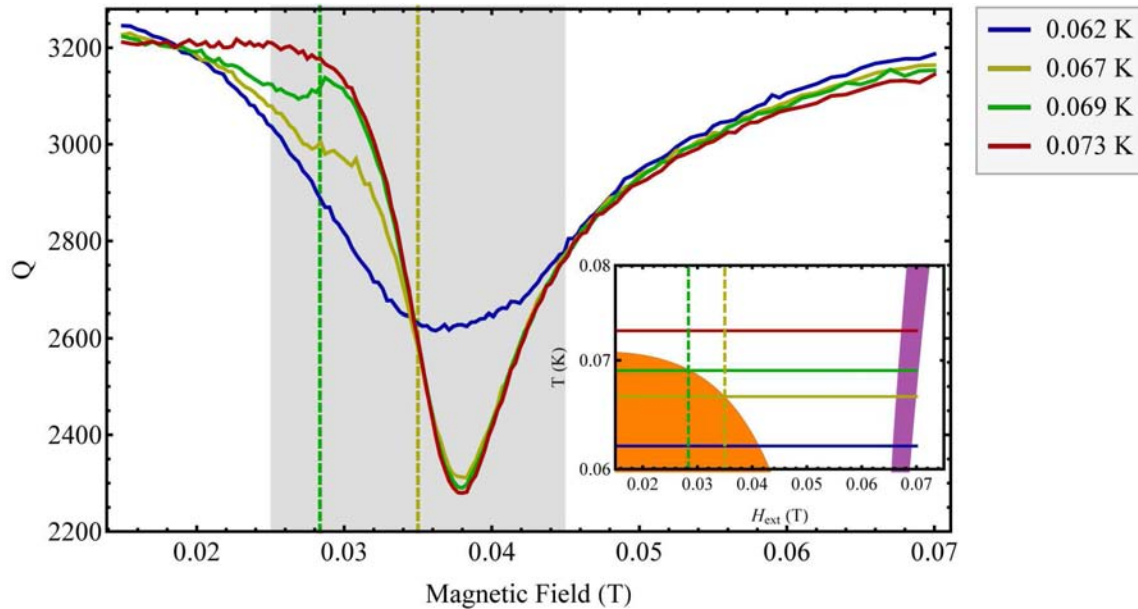


Figure 7.7: Magnetic resonance spectra for a selection of temperatures. The temperature is determined by the mean value of all temperatures measured within the gray shaded field range. The inset shows the position of the individual spectra within the B - T diagram and the dashed lines indicate the transition fields. The 67 and 69 mK spectra show a distinct change of lineshape within the absorption resonance.

62 mK displays a lineshape as it is typically observed within the AFM phase (at least up until ≈ 42 mT) while that at 73 mK resembles those also obtained at higher temperatures in the NFL regime. The 67 mK (dark yellow) and 69 mK (green) spectra, however, show characteristics of both regimes. The transition fields extracted from the phase diagram for the two intermediate temperatures shown in Figure 7.7 are drawn as vertical dashed lines in the plot as well as the small inset

displaying the relevant part of the phase diagram. In the case of the 67 mK spectrum the line follows the NFL shape from the point of intersection but a characteristic feature appears already at lower fields. Also the 69 mK spectrum follows the NFL behavior for fields higher than the transition field while exhibiting a lineshape as if composed of both AFM and NFL contributions even at lower magnetic fields. Figure 7.8 shows all the spectra already displayed in Figure 7.6 as a function of both

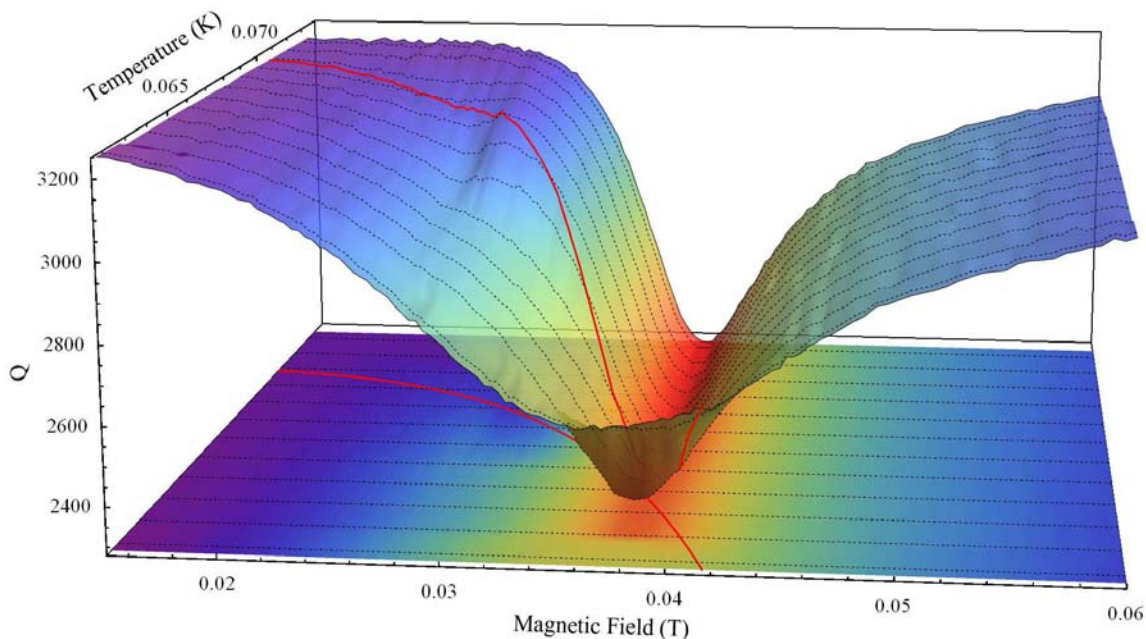


Figure 7.8: Quality factor as a function of magnetic field and temperature close to the antiferromagnetic phase transition. The red lines marks the transition in field and temperature. Even for temperatures below the Néel temperature the spectra show signatures of the paramagnetic lineshape.

magnetic field and temperature. To relate those spectra to the phase diagram the AFM phase boundary is also projected onto the $Q(H, T)$ surface. The transient feature is clearly visible at temperatures and fields lower than those of the actual phase transition. In fact, it seems as if the continuous phase transition can directly be observed with these magnetic resonance spectra.

note

The highest uncertainty for these spectra is the actual sample temperature. The readout of the sensor (attached to the head of the

bolt to which the sample is glued at the tip) is quite noisy due to low excitation signals and pick-up noise by the wiring. In addition, the temperature is not read out continuously but only every fourth magnetic field. Another analysis of these spectra by taking the temperature as a function of magnetic field into account is given in the appendix. The result, however, is the same, thereby justifying taking the average of the measured temperatures within the appropriate field range as effective sample temperature.

Studying the intermediate spectra in Figures 7.6 and 7.7 suggests to formulate an expression $p(H)$ with $0 \leq p(H) \leq 1$ which reflects the ‘degree’ of the antiferromagnetic order ($p(H) = 1$: fully developed AFM order, $p(H) = 0$: no order). Here, $p(H)$ is given as

$$p(H) = p_{\text{AFM}} \frac{1}{\exp\left[\frac{1}{\Delta_{\text{tr}}}(H - H^*)\right] + 1} \quad (7.2)$$

with the zero-field antiferromagnetic ordering p_{AFM} , the transition width Δ_{tr} and the transition field H^* . Using Equation (7.2) one can compose the intermediate spectra

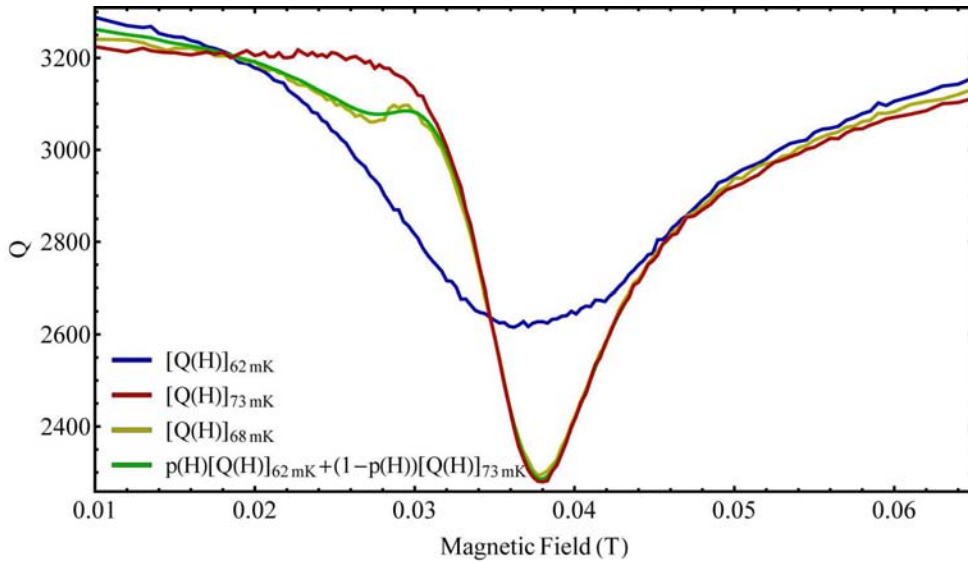


Figure 7.9: Spectra which cross the phase boundary within the resonance feature can be simulated as a combination of both low and high temperature spectra. The quantity $p(H)$ gives the field dependent ratio between low (AF lineshape) and high (NFL lineshape) temperature spectra contribution.

by a mixture of a spectrum still in the AFM phase and one slightly above the phase boundary (here the 62 mK and 73 mK spectra from Figure 7.7) in the way

$$\left[Q(H)\right]_{62\text{mK} < T < 73\text{mK}} = p(H)\left[Q(H)\right]_{62\text{mK}} + (1 - p(H))\left[Q(H)\right]_{73\text{mK}} \quad (7.3)$$

The original and recomposed spectrum for an arbitrarily chosen sample temperature in the intermediate range is shown in Figure 7.9. The simulated spectrum reproduces the actual measured data over the whole field range to a fair extent and also the typical protruding feature is reproduced nicely. By plotting $p(H)$ for a selection of temperatures in the intermediate region (as shown in Figure 7.10) the ‘strength’ of antiferromagnetic order can be determined. With increasing temperature (from

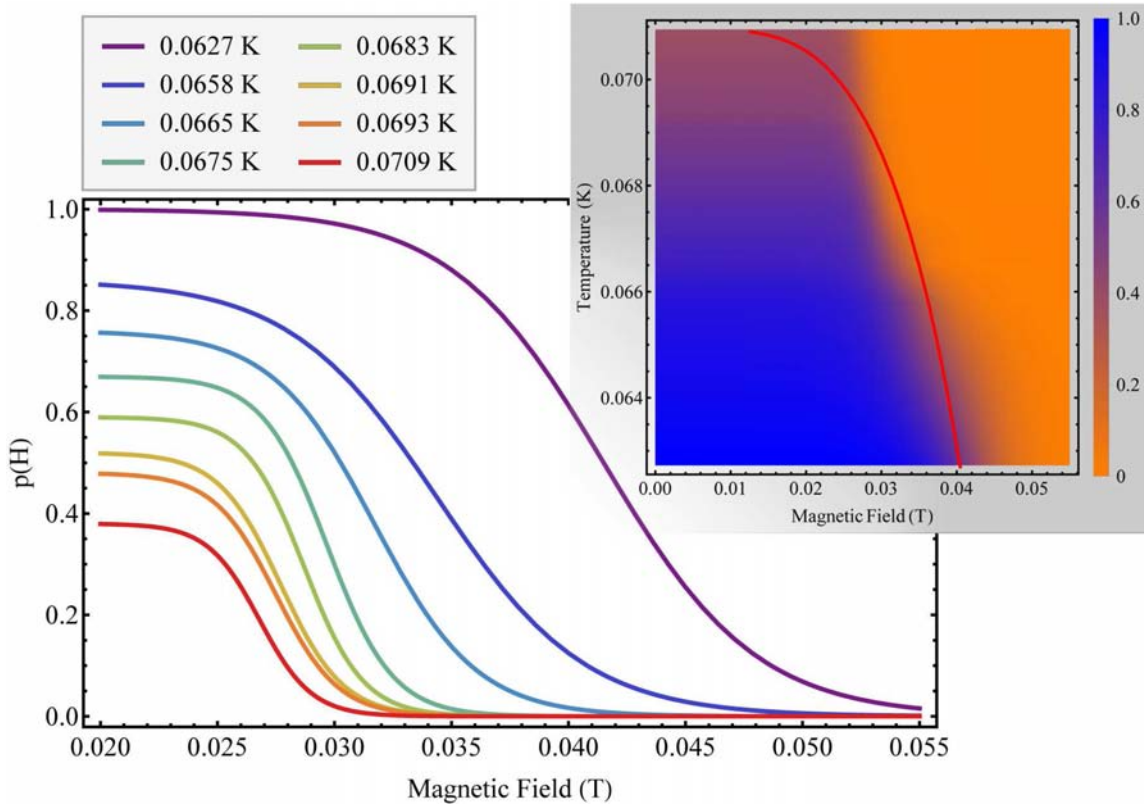


Figure 7.10: Antiferromagnetic and non-Fermi-liquid contributions to the magnetic resonance spectra for different temperatures close to the AF phase transition. The color map displays the same data and the position of the AFM transition boundary.

62 mK on upwards) the sample loses more and more of its AFM character as p_{AFM} decreases. In addition, it can be observed that the transition from the AFM phase to the NFL regime gradually gets sharper with increasing temperature. This is somehow counterintuitive if the slope of the phase boundary is taken into account. Assuming

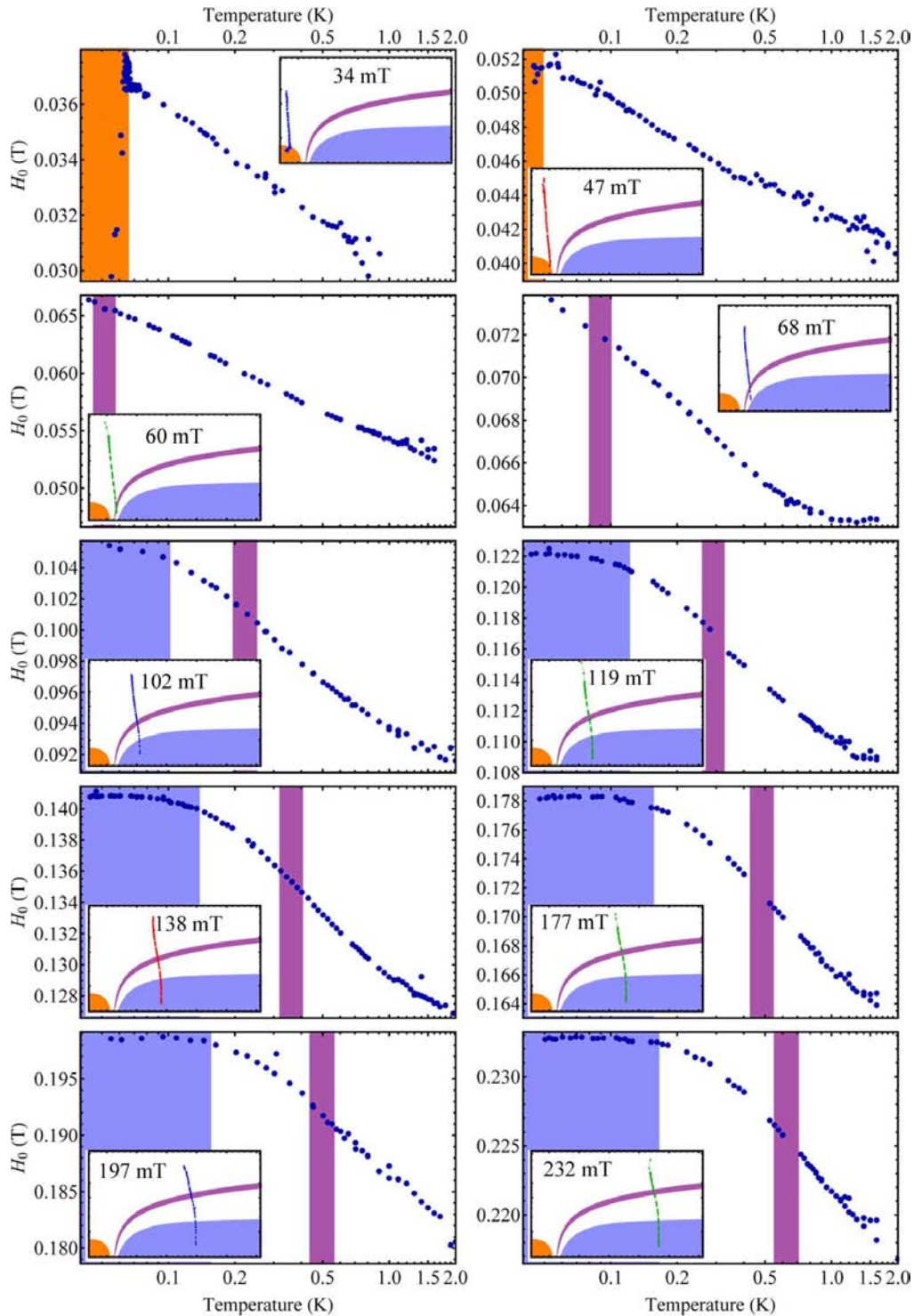


Figure 7.11: Resonance fields as a function of temperature for a selection of resonator modes of R1, R2 and R3. Colored regions within the plots indicate the temperature regimes (AF, FL, T^*) for that particular mode. The insets show the positions of the individual resonance fields as shown in Figure 7.4.

a fluctuation regime around the phase transition running somewhat parallel to the AFM phase boundary this fluctuation region gets smaller for magnetic field sweeps performed at lower temperatures as the slope of the phase transition line gets steeper. It is therefore surprising to observe the reversed effect of Δ_{tr} decreasing with increasing temperature (by a factor of about three). On the other hand, any deviation of p_{AFM} from unity inevitably signifies that the system is already within the fluctuation regime. The sharp transition, then, merely marks the eventual transit into the NFL region.

Concluding this part of the analysis of magnetic resonance spectra of YbRh_2Si_2 it is shown that very close to the AFM transition signatures arise which could be interpreted in terms of increasing antiferromagnetic fluctuations (related to fluctuations of the order parameter?). Since these are the very first measurements of that type a definitive conclusion is still pending.

The resonance fields H_0 extracted from the Dysonian model fit to the background subtracted data is shown in Figure 7.11 for a selection of resonator frequencies as a function of temperature. The color shaded areas denote the temperature ranges of the antiferromagnetic ordered state, the Fermi-liquid regime and the T^* crossover region for each individual resonator mode in the same color scheme as already shown in Figure 7.4. The small insets show the particular magnetic resonance positions in the temperature-field phase diagram and give the resonance field at $T = 200$ mK as stated in Table 7.1. For the lowest resonator frequency (that of the fundamental mode of R1; $f_{\text{res}} \approx 1.5$ GHz) the resonance field increases sharply with increasing temperature within the AFM phase. Close to the phase transition the resonance fields ‘pile up’ at around 35 mT and start to decrease in the non-Fermi-liquid regime with further increasing temperature. The effect of piling up of resonance fields very close to the transition temperature can be attributed to the fact that at this temperature range the line is composed of two different contributions, as mentioned just above. At low fields, the line is more of the character typically seen in the AFM phase while at higher fields it shows the typical paramagnetic shape. Therefore, the fits do not reliably reflect the resonance position. Only for temperatures low enough, meaning temperatures for which the transition field ($H_{\text{AFM}}(T)$) is significantly higher than the observed minimum of the field dependent quality factor, the fits yield a trustworthy resonance field and actually show the shift towards much lower fields.

The magnetic resonance observed with the fundamental mode of R2 scarcely enters the AFM phase and, therefore, only shows the onset of the shift towards lower fields.

Leaving the behavior of the magnetic resonance in the AFM phase aside, one can discern a uniform trend of the resonance fields for all resonator frequencies. Within the Fermi-liquid regime H_0 stays rather constant (at high values) and starts to decrease with increasing temperature upon entering the non-Fermi-liquid region. In contrast to former findings at much higher fields [88] no noticeable changes can be observed at the T^* crossover temperature. The slope of the temperature dependent resonance field in the non-Fermi-liquid regime is linear in $\ln T$ which is in agreement with theory [95]. A comparison with the temperature dependence of the electronic specific heat [100] yields strong similarities. This can be an indication that the ESR is in fact the response of the heavy quasiparticles.

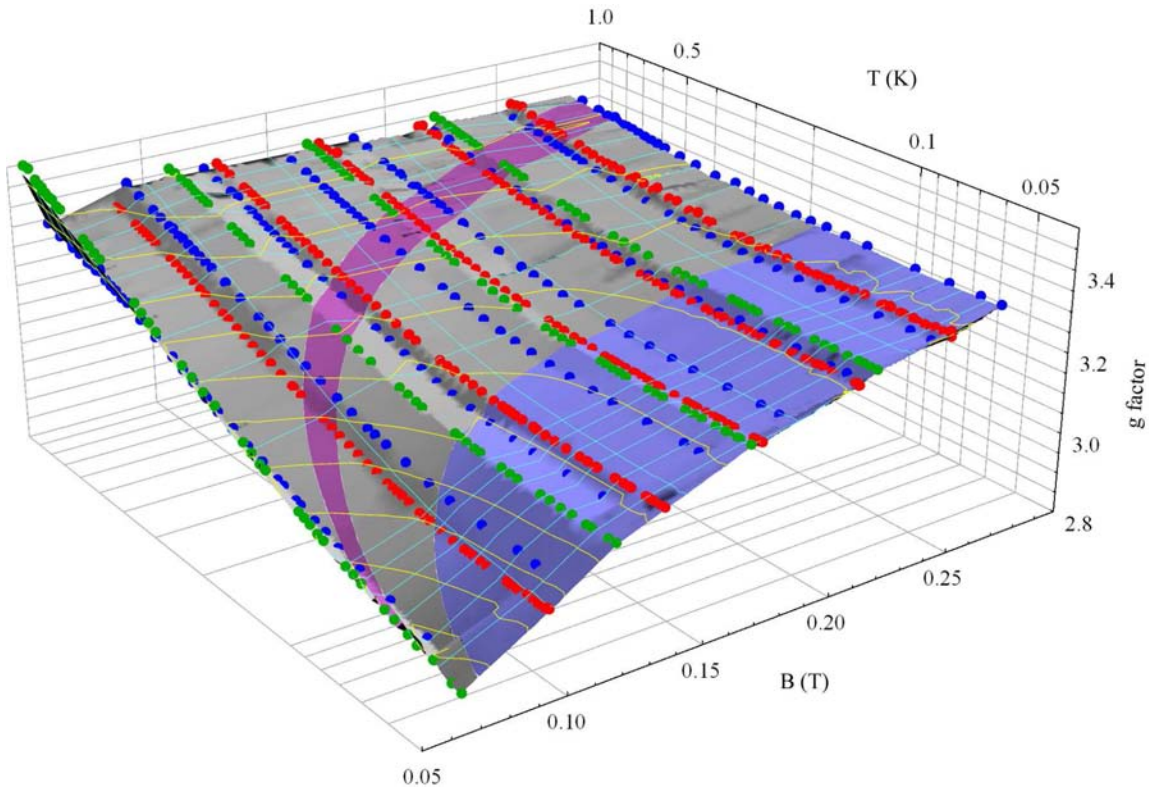


Figure 7.12: Magnetic field and temperature dependence of the g -factor extracted from the Zeeman resonance condition for all modes with $f_{\text{res}} > 2.5$ GHz (to exclude the AF phase). Blue, red and green points represent actual data in the same color scheme as above. The surface is an interpolation of those points. For better visualization of the effects the relevant crossover regimes are projected onto that surface. Further description see text.

To relate the various resonance fields to each other, the g factor can be expressed using the Zeeman resonance condition $g_i(H, T) = hf_{\text{res},i}/\mu_B H_{0,i}(T)$ with the resonance frequency $f_{\text{res},i}$ of the resonator mode in question. The result is shown in Figure 7.12

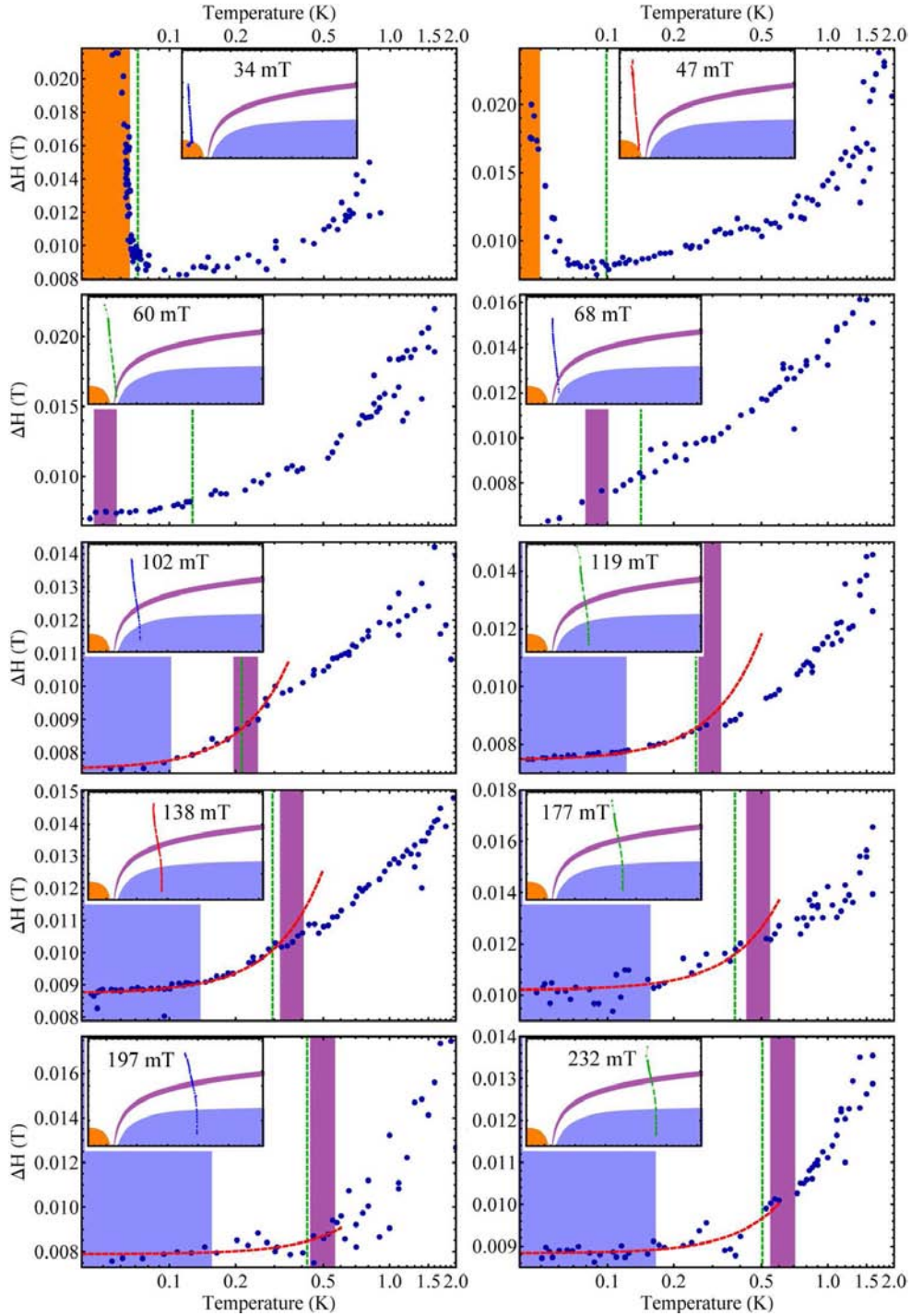


Figure 7.13: Linewidth of the absorption line for the same selection as in Figure 7.11. Upon entering the AFM phase the linewidth increases sharply. For all other resonator modes ΔH increases with temperature for temperatures above the Fermi-liquid crossover temperature. The red lines are fits to a quadratic temperature dependence and the green line marks the temperature for which $k_B T = \hbar f_{\text{res}}$ above which phonon-assisted relaxation can lead to an increase on the linewidth.

for all resonator frequencies higher than 2.5 GHz (to omit those that enter the AFM phase). A few effects become apparent right away; (i) at low temperatures the g factor increases with increasing magnetic field, (ii) the value of g stays constant in the Fermi-liquid regime, (iii) at ‘high’ temperatures (here at around 1 K) g is basically field independent at around 3.4 and (iv) there is no change at the T^* crossover region.

At the high temperature edge of the displayed data the measured g -factors can be well extrapolated to those observed in other measurements at even higher temperatures and fields [88]. The changes of g with decreasing temperature are quite grave, especially as the magnetic resonance approaches the QCP.

Finally, the temperature dependent linewidth ΔH is plotted for the same resonator modes as displayed in Figure 7.11. The additional dashed green line indicates the temperature for which $T_{\text{th}} = g\mu_B H_{\text{ext}}/k_B = hf_{\text{res}}/k_B$. Above this temperature thermally activated processes can also lead to an increase of the linewidth.

As already mentioned before the linewidth increases drastically upon entering the AFM phase. In fact, an increase of ΔH can already be observed for temperatures slightly above T_N . This is again owed to the fact, that spectra which show a minimum (H_0) at fields indicating to be located in the non-Fermi-liquid regime, exhibit a low field behavior similar to those in the AFM phase.

All resonances share the same behavior of increasing linewidth with increasing temperature. For temperatures above T_{crit} spin lattice relaxation gets thermally assisted, intuitively explaining an increase of ΔH . However, no distinct changes are observed at that particular temperature.

Theory predicts a quadratic T -dependence within the Fermi-liquid regime and a linear dependence for $T \gg T_{\text{FL}}$. The red lines show quadratic model fits to the linewidth data in the Fermi-liquid regime. On the other hand, the T^2 prefactor should also display a H^2 dependence which cannot be observed. Quite to the contrary, one could argue that with increasing magnetic field the linewidth flattens out in the Fermi-liquid regime and only starts to increase close to the crossover temperature.

However, these results have to be treated with care since the linewidth fitting parameter is highly susceptible to the background subtraction of the original $Q(H)$ data which is also reflected in the rather strong noise observable for some spectra.

8 Sensitivity or Why Size Does Matter

So far, this work has demonstrated the working principle of this novel, unconventional way of performing ESR experiments and pointed out its numerous advantages. Obviously, as for any experimental technique, there exist also general limitations as well as preconditions for the samples to be investigated. Therefore this section will address the important point of sensitivity and will discuss the influence of geometrical parameters on the expected strength of the ESR signal.

The sensitivity, or the minimum number of spins that can be detected using the described broadband ESR technique can be estimated from the lowest frequency for which a signal is distinctly visible. Contemplating the results obtained from measurements of the NITPhOMe compound the low-limit frequency is about 500 MHz. From the total mass of sample material transferred onto the chip and the known molecular mass of each radical the total number of spins can be determined to be $\approx 10^{18}$. In section 5 it was already mentioned that the microwave fields are considered to be too weak at a distance greater than $S + W$ from the center conductor to drive ESR transitions that will show up above the noise. Taking also the special geometry of the waveguide which was utilized for this experiment into account the effective interaction volume is significantly smaller than the whole sample volume. The total length of the waveguide is approximately 1.9 cm and S and W are given with 60 and 25 μm , respectively. The half circle area above the waveguide thus covers a surface of $\approx 0.0113 \text{ mm}^2$ and elongated along the length of the waveguide an effective interaction volume of $\approx 0.22 \text{ mm}^3$ is formed. Since the waveguide structure of this particular waveguide is oriented in a way that only the z -component of the rf field can drive spin transitions (because $H_y \parallel H_{\text{ext}}$ for almost the whole waveguide length) it is justified to reduce the interaction volume by a factor of two. The whole sample area has a diameter of 2 mm and a thickness of roughly 500 μm resulting in a sample volume of $\approx 6.28 \text{ mm}^3$. The number of spins within the effective interaction volume can then be estimated to be around 10^{16} . This is the estimated minimum spin number to observe ESR signatures at 500 MHz for temperatures around 1.6 K. If above made assumptions reflect the actual situation remains questionable. The following paragraph, however, gives expressions for the frequency and temperature dependence of the minimum number of spins as a function of the total number. Once the actual rf field limit is established absolute values for the sensitivity can be derived.

To quantitatively describe the frequency and temperature dependence of the minimum required spin number one has to use the thermal occupancy of the initial and final

spin states which is given as

$$N_i(f, T) = N_{\text{tot}} e^{-\frac{h0}{k_B T}} / Z(f, T) \quad (8.1)$$

$$N_f(f, T) = N_{\text{tot}} e^{-\frac{hf}{k_B T}} / Z(f, T) \quad (8.2)$$

with the partition function

$$Z(f, T) = e^{-\frac{h0}{k_B T}} + e^{-\frac{hf}{k_B T}}.$$

Here, the initial state $|m_i\rangle$ was set to zero energy and the final state $|m_f\rangle$ is separated by a transition frequency f . With a total number of spins $N_{\text{tot}} = 10^{16}$ as stated above, the absolute difference of occupancy at a level separation frequency of $f^* = 500$ MHz and a temperature of $T^* = 1.6$ K is given as

$$\begin{aligned} \Delta N_{if}(f^*, T^*) &= N_i(f^*, T^*) - N_f(f^*, T^*) = \frac{N_{\text{tot}}}{1 + e^{-\frac{hf^*}{k_B T^*}}} \left(1 - e^{-\frac{hf^*}{k_B T^*}}\right) \quad (8.3) \\ &\approx 7.5 \cdot 10^{13}. \end{aligned}$$

This difference determines the intensity of the ESR signal. With this information one can define a minimum total number of spins $N_{\text{tot}}^{\text{min}}$ as a function of frequency and temperature for which the absorption peak is of the same magnitude as for the distinguished set of (f^*, T^*) . The quantity $N_{\text{tot}}^{\text{min}}$ is defined as

$$N_{\text{tot}}^{\text{min}}(f, T) = N_i(f, T) + N_f(f, T)$$

with the condition

$$N_i(f, T) - N_f(f, T) \stackrel{!}{=} N_i(f^*, T^*) - N_f(f^*, T^*).$$

With Equation (8.1) through Equation (8.3), $N_{\text{tot}}^{\text{min}}(f, T)$ can be expressed by

$$N_{\text{tot}}^{\text{min}}(f, T) = \frac{\frac{N_{\text{tot}}}{1 + e^{-\frac{hf^*}{k_B T^*}}} \left(1 - e^{-\frac{hf^*}{k_B T^*}}\right)}{\frac{1}{1 + e^{-\frac{hf}{k_B T}}} \left(1 - e^{-\frac{hf}{k_B T}}\right)} = \frac{\Delta N_{if}(f^*, T^*)}{\frac{1}{1 + e^{-\frac{hf}{k_B T}}} \left(1 - e^{-\frac{hf}{k_B T}}\right)} \quad (8.4)$$

Figure 8.1 shows $N_{\text{tot}}^{\text{min}}(f, T)$ on a log-log-log scale for frequencies between 10 MHz and 10 GHz and temperatures ranging from 1 mK up to 10 K. As expected, the



minimum required number of spins increases with increasing temperature for a fixed frequency and decreases with increasing frequency for a fixed temperature. For high frequencies and low temperatures $N_{\text{tot}}^{\text{min}}(f, T)$ levels off at a constant value which is just $\Delta N_{if}(f^*, T^*)$ since the denominator in Equation (8.4) quickly approaches unity for high frequencies or low temperatures with

$$\lim_{\frac{hf}{k_B T} \rightarrow \infty} \frac{\Delta N_{if}(f^*, T^*)}{\frac{1}{1 + e^{-\frac{hf}{k_B T}}} \left(1 - e^{-\frac{hf}{k_B T}}\right)} = \Delta N_{if}(f^*, T^*)$$

indicating that all spins are in the ground state for sufficiently low temperatures and/or high frequencies. That means the total minimum number of spins cannot decrease below $\Delta N_{if}(f^*, T^*) \approx 7.5 \cdot 10^{13}$ for this geometry and a total number of effectively coupled spins of $N_{\text{tot}} = 10^{16}$.

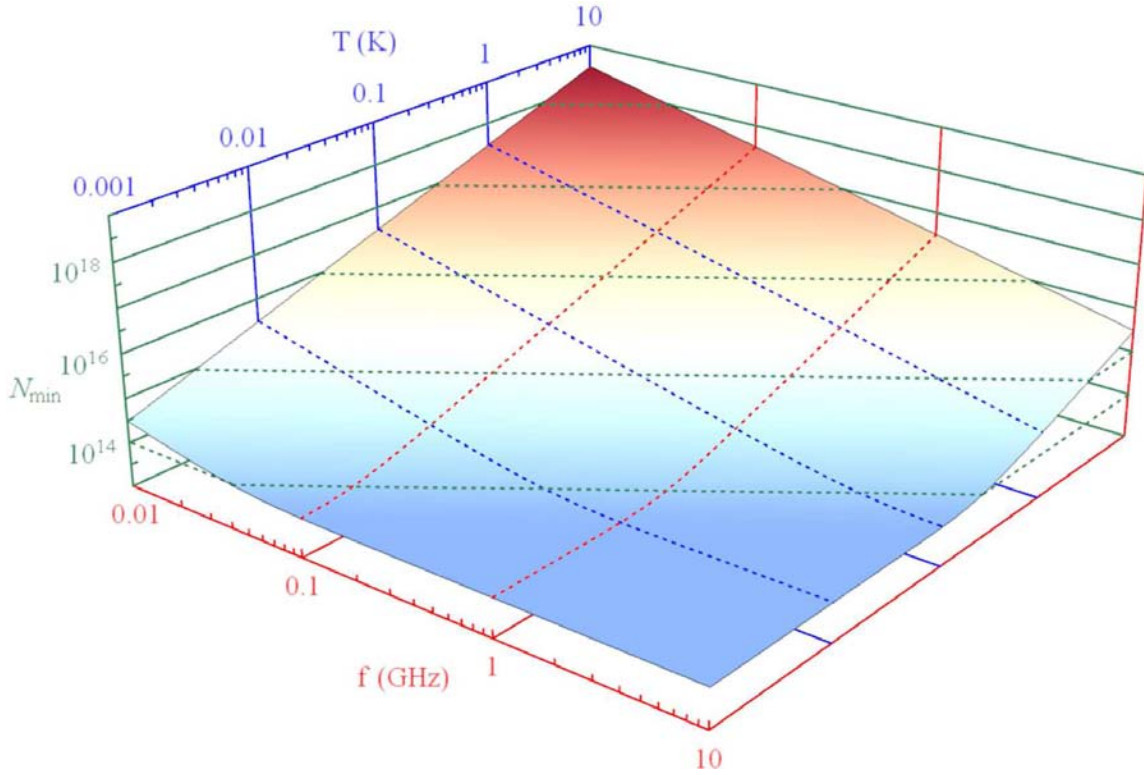


Figure 8.1: Minimum number of spins to detect an ESR signal as a function of frequency and temperature. At low temperatures and high frequencies the surface levels at ΔN_{if} (see text).

All sensitivity considerations made above were based on the measurements on NIT-PhOMe with a waveguide structure composed of a 60 μm wide center conductor and

a center strip-ground plane separation of $25 \mu\text{m}$. However, since different structural parameters lead to different rf field strengths as well as different spatial field expansions the effect of geometrical modifications on the sensitivity will be discussed in the following.

To quantitatively compare the different structures it is again assumed that rf fields for $d > S + W$ (for $60 \mu\text{m}$ center conductor width) do not contribute to observable ESR transitions. Although, theoretically, any non-vanishing microwave field can drive spin transitions the actual signal intensity scales with H_{rf}^2 [14] (also see below) which supports the definition of a low rf field limit. For a direct comparison of different geometries the absolute value of the field limit is of no concern and can be chosen arbitrarily. For an input power of 1 W the average absolute field ($\sqrt{H_y^2[y, z] + H_z^2[y, z]}$) along the half-circle with radius $S + W$ around the center of the structure is $H_{\text{lim}}^{\text{avg}} \approx 169 \text{ A/m}$. With this field limit, the area for which $|H(y, z)|$ is greater than $H_{\text{lim}}^{\text{avg}}$ can be determined. The resulting regions are shown for different structures (different center conductor widths S) in Figure 8.2 with the center of the structure located at $y = 0$. It becomes clearly apparent that the area $A|_{H(y,z) \geq H_{\text{lim}}^{\text{avg}}}$

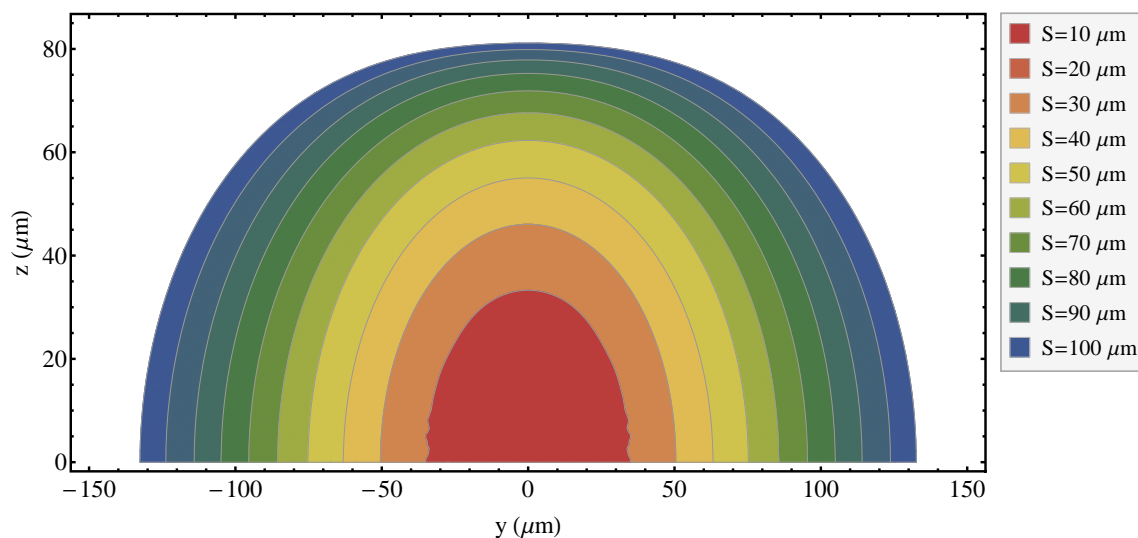


Figure 8.2: Spatial regions for which the microwave magnetic field amplitude is greater than the low field limit $H_{\text{lim}}^{\text{avg}}$ for different center conductor widths S . Different colors are used to distinguish the areas from one another.

increases with increasing center conductor width. Assuming a homogeneous sample which expands far beyond the typical waveguide geometries (S, W) larger structures effectively couple to a larger number of spins which should result in a stronger absorption signal. This rash reasoning, however, might lead to wrong conclusions

since not only does the number of effectively coupled spins matter but so does the absolute microwave field strength within the area of interaction. Figure 8.3 shows isosurfaces of different rf field strengths as a function of the center conductor width S (center strip to ground plane distance W is always chosen to create structures with 50Ω impedance matching). As already displayed in Figure 8.2, the effective area

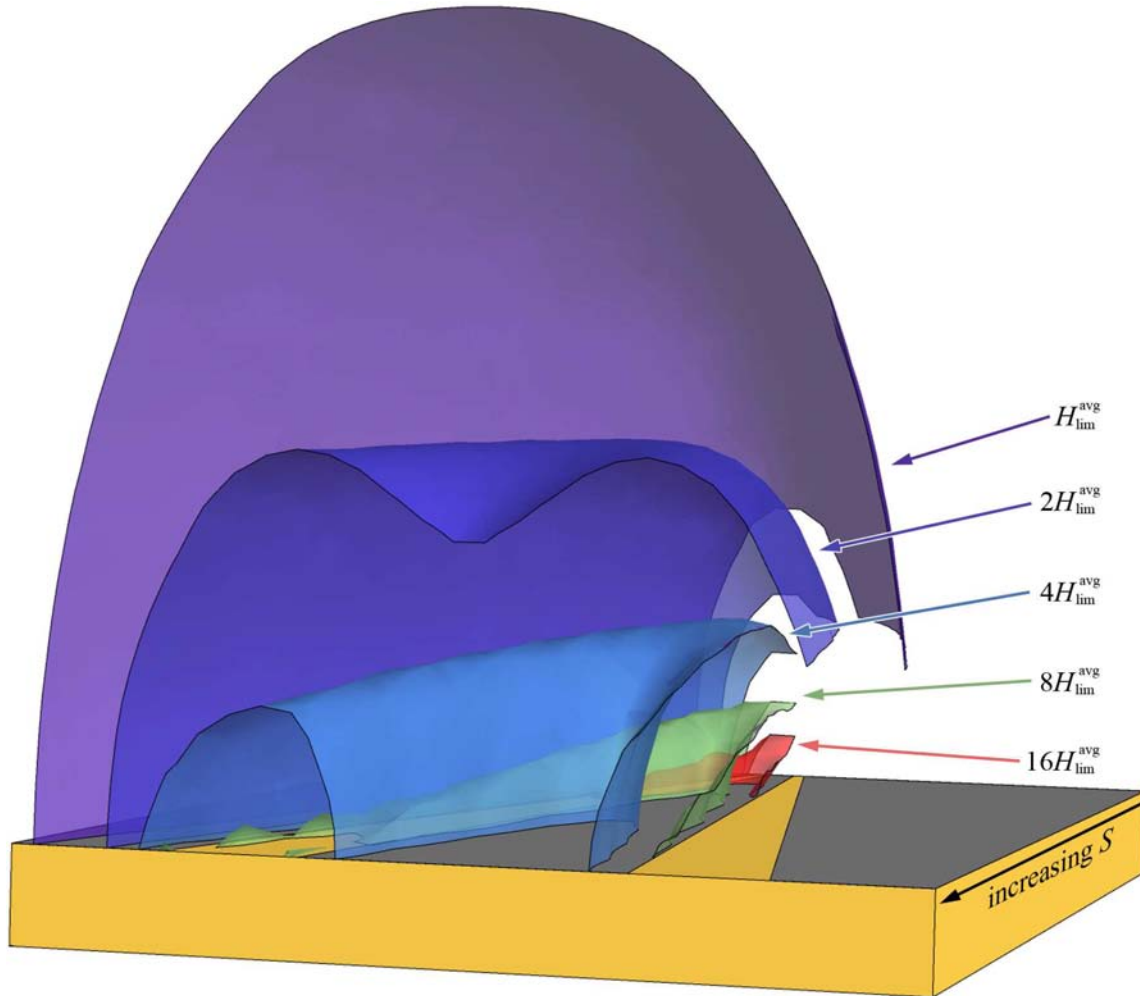


Figure 8.3: Cut open isosurfaces of the microwave field amplitudes at $|H(y, z)| = 2^n H_{\text{lim}}^{\text{avg}}$ ($n = 0, 1, 2, 3, 4$) as a function of center conductor width. Although the interaction area increases with increasing S , the field amplitudes are strongly enhanced for smaller structures.

increases with increasing size of the structures. On the other hand, however, the absolute rf field strength close to the waveguide strongly increases with decreasing structural dimensions. The differences of the field strengths are quite significant as can be seen in Figure 8.4 as a plot of the maximum microwave field amplitude at

the edge of the center conductor. Shown are the absolute field amplitudes (left axis) as well as the field amplitudes as multiples of the low field limit $H_{\text{lim}}^{\text{avg}}$ (right axis). For center conductor widths ranging from 10 to 100 μm the maximum field strength varies around one order of magnitude. Therefore, to accurately compare different geometrical sizes this effect has to be taken into account.

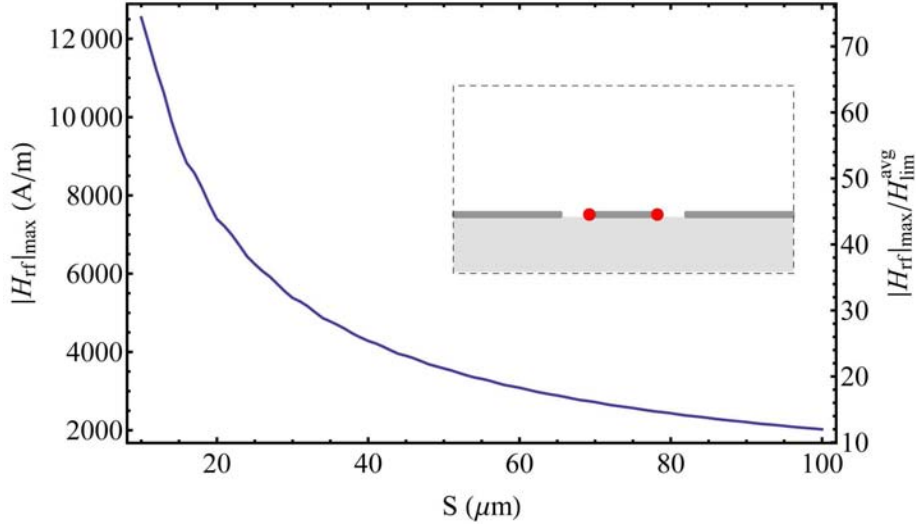


Figure 8.4: Maximum field amplitude at the edges of the center conductor (marked in the inset) as a function of center conductor width. The amplitude is maximized for narrow structures and decreases fast with increasing width.

According to Abragam and Bleaney [14] the power absorbed in a transition between spin states $|m_i\rangle$ and $|m_f\rangle$ (intensity of the ESR line) is given by the expression

$$\frac{dW}{dt} = N_i \frac{\pi\omega^2}{2k_B T} H_{\text{rf}}^2 |\mu_{if}|^2 \quad (8.5)$$

for the case that $(\hbar\omega/k_B T) \ll 1$. Here, N_i is the number of spins in the initial state and μ_{if} is the generalized matrix element describing the transition probability including a normalized line shape function $f(\omega)$ (which is ignored here since $\int f(\omega) d\omega \stackrel{!}{=} 1$). As can be seen from expression (8.5), the line intensity therefore shows a quadratic dependence of the microwave magnetic field H_{rf} . Equation (8.5), however, does not distinguish between $|m_i\rangle$ being the upper or the lower state in energy and both transitions (up and down) happen with equal probability. There will, at least close to thermal equilibrium, be a net absorption since the population of the lower state is than that of the upper one.

Equation (8.5) works very well for cavities with small filling factors, meaning the

amplitude of the microwave field strength can be considered constant over the sample volume. For coplanar structures with the sample basically covering the whole chip this presumption is no longer valid since the rf fields show a very strong spatial dependence and one has to integrate the square of the microwave magnetic field over the sample volume. To compare waveguides with different center conductor widths it suffices to integrate over the area above the waveguide within which the magnetic field is larger than the low limit field $H_{\text{lim}}^{\text{avg}}$ (colored areas in Figure 8.2), leading to

$$\frac{dW}{dt} \propto \left[\int_A H_{\text{rf}}^2 dA \right]_{H_{\text{rf}} > H_{\text{lim}}^{\text{avg}}} = \left[\int_0^\infty \int_{-\infty}^\infty H_{\text{rf}}^2[y, z] dy dz \right]_{H_{\text{rf}} > H_{\text{lim}}^{\text{avg}}}. \quad (8.6)$$

This integral is directly proportional to the line intensity expressed in Equation (8.5) since the area above the waveguide is proportional to the number of spins N_i , assuming a large enough sample with a homogeneous spin density. The result of this surface integral is plotted in Figure 8.5 as a function of center conductor width (from 10 μm to 100 μm) for different z -offsets. The majority of samples are single crystals or magnetic particles diluted in a non-magnetic matrix which are placed on top of the waveguide structure and fixed with vacuum grease. Consequently, a thin layer

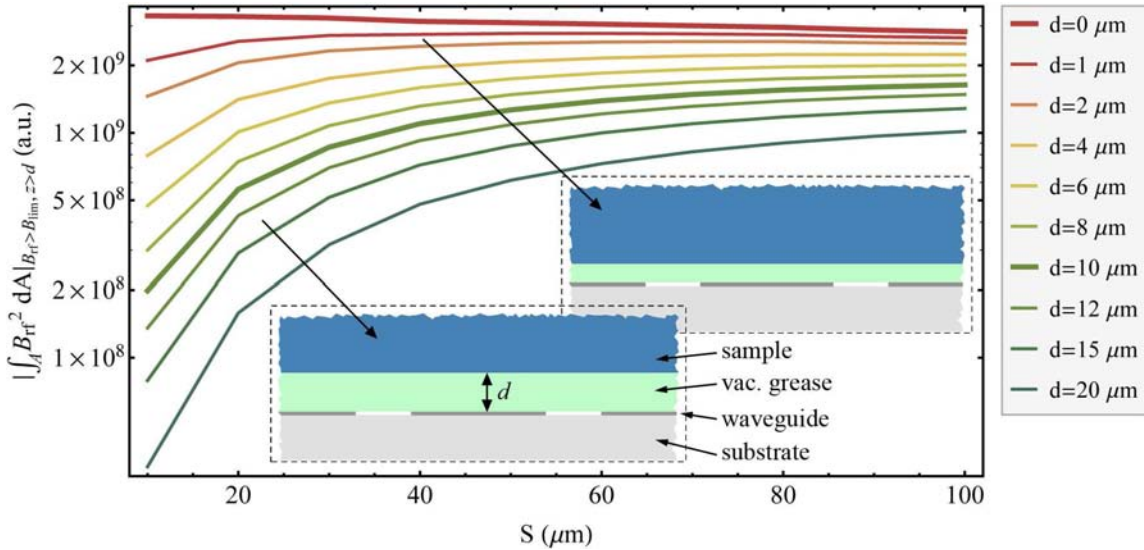


Figure 8.5: ESR absorption intensity for a given transition frequency as a function of center conductor width for different distances between sample and waveguide structure. Further information see text.

of grease remains between the waveguide and the sample material. The thickness of this separation layer strongly depends on the amount of vacuum grease and the force used to press the sample onto the chip and is typically around 10 μm . For such a dis-

tance, the wider structures are better suited as they lead to an absorption intensity roughly one order of magnitude higher than that of the narrow ones. Is the sample, however, like in the case of NITPhOMe crystalized directly onto the chip (without any separation layer) the ESR intensity is maximized for smaller center conductor widths, profiting from the highly enhanced field strengths at the conductor edges.

note

It is to note that the considerations made above do not take the length of the waveguide ℓ into account! They are absolutely valid for waveguides of equal length but for varying lengths the amplitude profile along the waveguide has to be included into the integration, resulting in a volume integral over the whole half-space region above the resonator. A more general description is given below.

Taking a snapshot at any given time t_0 , the microwave magnetic fields show a sinusoidal profile along x -direction. With Equation (8.5) and (8.6) a general formulation of the line intensity can be given as

$$\frac{dW}{dt} = \frac{\pi\omega^2}{2k_B T} |\mu_{if}|^2 \int_0^\infty \int_{-\infty}^\infty \int_{-\ell/2}^{\ell/2} H_{\text{rf}}^2[x, y, z] dx dy dz \quad (8.7)$$

$$= \frac{\pi\omega^2}{2k_B T} |\mu_{if}|^2 \int_0^\infty \int_{-\infty}^\infty \int_{-\ell/2}^{\ell/2} H_{\text{rf}}^2[y, z] \left| \cos\left(\frac{2\pi}{\lambda_{\text{wg}}}x\right) \right| dx dy dz. \quad (8.8)$$

Above, the cosine function describes the amplitude profile along the waveguide, centered at its midpoint at $x = 0$. The wavelength is given by λ_{wg} (waveguide wavelength, not vacuum). In contrast to Equation (8.6), in this general formulation, the integrand is now integrated over the whole half-space region above the waveguide. This is legitimate as long as the integrals converge well inside the sample volume. (The limit field strength $H_{\text{lim}}^{\text{avg}}$ was introduced above to better compare different geometries since a numerical computation of the integrals over very large areas with high resolution is extremely time consuming.) Considering a propagating wave the time averaged amplitude (along x) can be obtained with (equivalent to $\ell \gg \lambda_{\text{wg}}$)

$$\left\langle \int_{-\ell/2}^{\ell/2} \left| \cos\left(\frac{2\pi}{\lambda_{\text{wg}}}x\right) \right| dx \right\rangle_{\text{avg}} = \frac{2\ell}{\lambda_{\text{wg}}} \int_{-\lambda_{\text{wg}}/4}^{\lambda_{\text{wg}}/4} \cos\left(\frac{2\pi}{\lambda_{\text{wg}}}x\right) dx = \frac{2\ell}{\pi}. \quad (8.9)$$

Using this relation Equation (8.8) simplifies to the generalized waveguide line intensity expression

$$\frac{dW}{dt} = \frac{\ell \omega^2}{k_B T} |\mu_{if}|^2 \int_0^\infty \int_{-\infty}^\infty H_{\text{rf}}^2[y, z] dy dz. \quad (8.10)$$

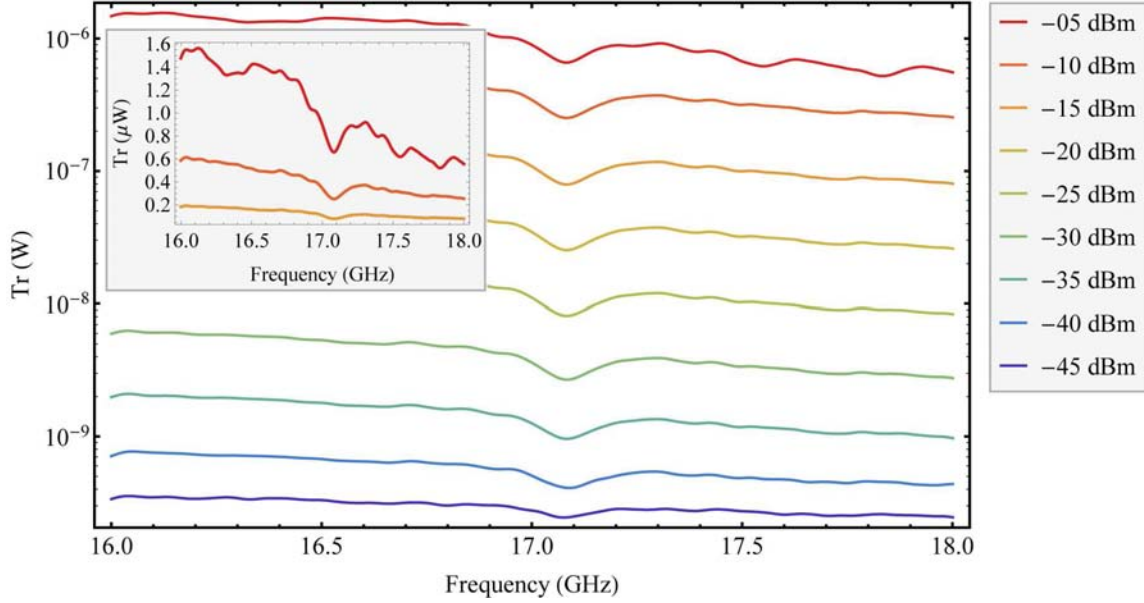


Figure 8.6: Frequency-swept transmission spectra of an ESR absorption of NITPhOMe at $B = 600$ mT for different microwave input powers. On the logarithmic scale the intensities appear to be equal while on a linear scale (inset) the differences become apparent.

For signal to noise (SNR) considerations of this technique as well as to verify the H_{rf}^2 -dependence shown above, input power dependent spectra were taken with the NITPhOMe sample at an external magnetic field of $H_{\text{ext}} = 600$ mT for input powers ranging from -45 dBm (≈ 32 nW) to -5 dBm (≈ 0.32 mW) in steps of 5 dBm. The results are plotted in Figure 8.6 on a logarithmic scale in the main panel and on a linear scale in the inset. The spectra are raw transmission data treated with a low pass filter to eliminate high frequency noise (with cut-off frequency of $\pi/37 \approx 0.085$).

note

It is important to compare the raw transmission data of different input powers since the rf field dependence would be cancelled out if the data was treated with the moving normalization scheme. For identical input powers at any given frequency, the microwave magnetic

fields at the waveguide are identical and when divided by each other the rf field dependence vanishes.

On a logarithmic scale, the intensities appear to be independent of the input power. This, however, is just an elusive effect due to scaling. On the linear scale it becomes apparent that the depth of the absorption peak in fact strongly depends on the input power. To quantitatively compare the peak intensities the spectra were subtracted from the baseline of each individual transmission spectrum (just a straight line for this small frequency window). The resulting spectra show a rather straight baseline at zero and a clear absorption peak centered around 17.08 GHz. Spectra for the five highest input powers are shown in Figure 8.7. To get the peak intensity, the spectra are integrated within the limits drawn as lines in Figure 8.7 (see also upper left panel in Figure 8.8).

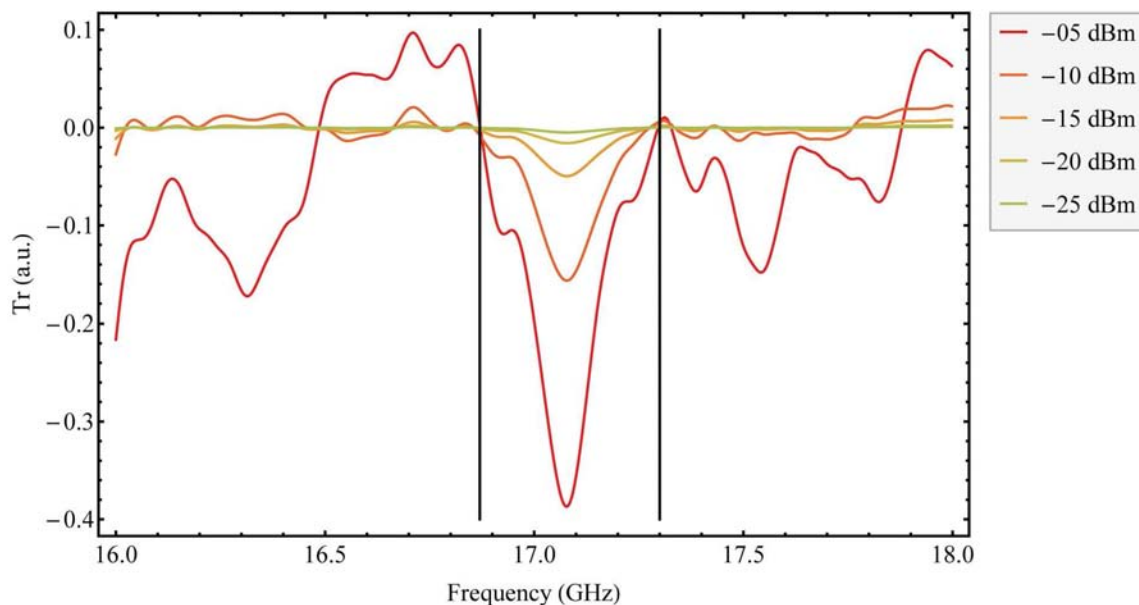


Figure 8.7: Spectra for the five highest input powers leveled by baseline subtraction. The intensity of the ESR absorption is given by the area below the peak (between the integration limits marked with vertical lines).

Figure 8.8 shows the linear relation between peak intensity and microwave input power on a double logarithmic scale. Since the microwave magnetic field scales with $\sqrt{P_{\text{in}}}$, a linear dependence of the intensity on the input power directly confirms the H_{rf}^2 dependence expressed in Equation (8.5). This is further supported by the fact,

that the spectrum taken with $P_{\text{in}} = -10$ dBm can be reproduced nicely by the spectrum taken with -40 dBm multiplied with the factor of 1000 (see lower right panel in Figure 8.8). From these results one could conclude that the higher the input power the better and stronger the signal. This, however, might be a little premature since not only does the strength of the signal play an important role but so does the strength of the noise. As a quantitative measure of the overall signal quality the ratio of signal to noise is the appropriate quantity.

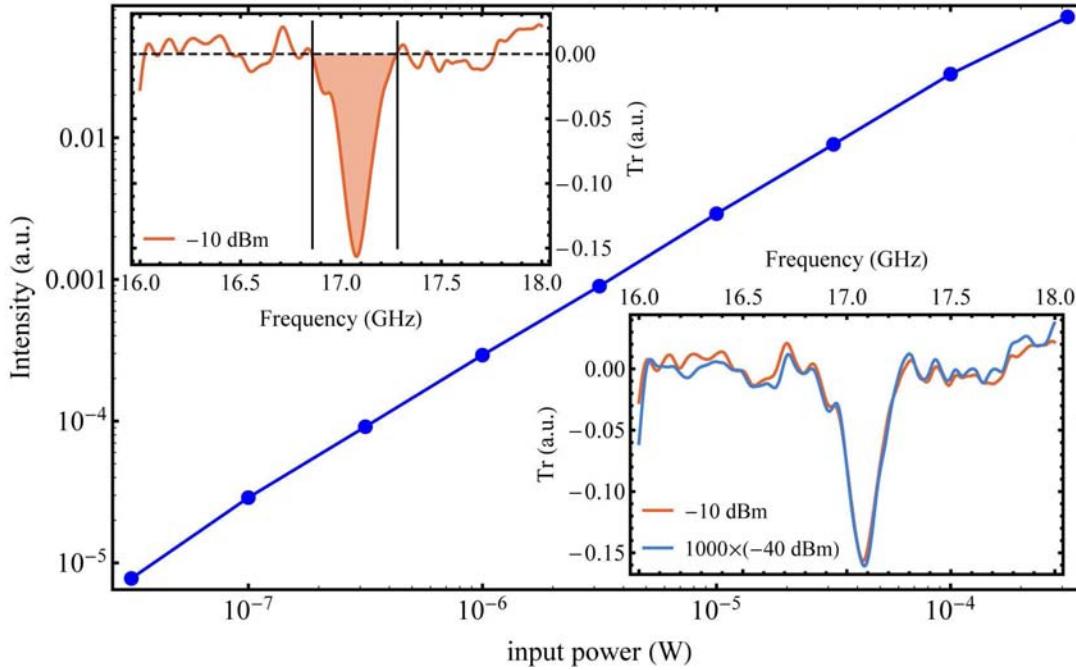


Figure 8.8: Peak intensity as a function of input power plotted on a double logarithmic scale. The intensity scales linearly with input power, confirming the H_{rf}^2 dependence. Upper left panel illustrates that the intensity is determined as the area between the frequency axis and the transmission spectrum. The lower right panel additionally demonstrates the rf field square dependence by reproducing the -10 dBm spectrum by 10^3 times the -40 dBm one ($\Rightarrow P_{\text{in}} \propto H_{\text{rf}}^2$).

Here, the signal to noise ratio is defined as the ratio of the peak amplitude to the standard deviation of the noise of the unfiltered normalized transmission spectra. For very low input powers, the spectra are rather noisy since the transmitted power is close to the detection limit and therefore the detector noise leads to a poor SNR. With increasing input power the baseline transmission escapes the detector noise and, at the same time, the signal gains intensity due to ever increasing microwave magnetic fields. As a result the signal to noise ratio increases roughly linearly with

increasing input power by about one order of magnitude over the whole investigated power range. The SNR at the highest input power of ~ 0.2 mW is approximately 35. This value is comparable to the achievable signal to noise ratio of early cavity based EPR spectrometers [116]. Since the NITPhOMe sample, however, is not a standard to test spectrometer performance (like the ‘weak pith sample’) a direct comparison is not possible. The result holds high prospects for the future development of the technique, nevertheless.

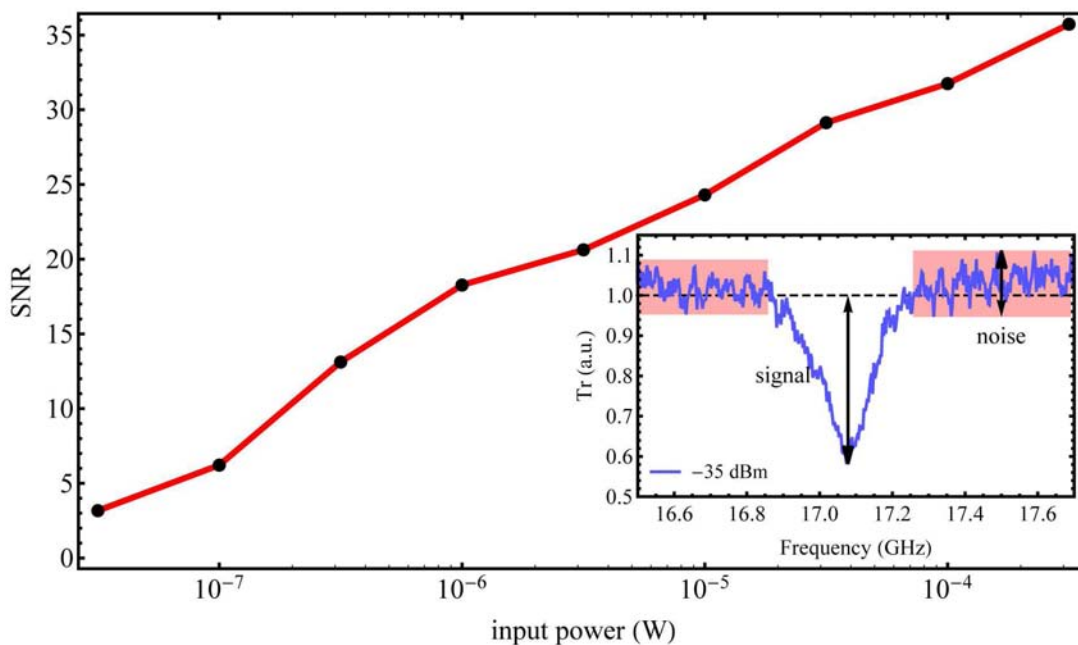


Figure 8.9: Signal to noise ratio as a function of input power. At low powers the detector noise is dominant, leading to a poor SNR and at very high input powers the filling factor reduces as the microwave field exceeds the sample volume. For intermediate input powers there exists a broad range with higher SNR.

important note

This input power dependent signal to noise ratio was obtained from measurements at 600 mT at a frequency around 17 GHz. At this frequency, the input power displayed on the abscissa axis of plots shown in Figs 8.8 and 8.9 does not represent the power at the waveguide input! As can be noticed from the frequency-dependent transmis-

sion (see Figure 6.2 in section 6.1.1 on page 64), at that frequency the transmitted power has already decreased by about two orders of magnitude compared to the transmitted power close to zero frequency (which is the input power assigned to the abscissa axis). To maintain a constant and high signal to noise ratio the input power has to be increased with increasing frequency as it was done for the broadband measurements on the Gd single ion magnet system (see section 6.3).

So far, only the broadband technique using coplanar waveguides was considered. However, similar contemplations can be made concerning ESR studies utilizing coplanar waveguide resonators. For simple waveguide structures the ESR line intensity is given by Equation (8.10). For identical geometrical parameters the maximum field strength amplitude of a resonator relates to that of a waveguide in the way

$$H_{\text{rf, res}} = \sqrt{Q_n} H_{\text{rf, wg}} \quad (8.11)$$

with $H_{\text{rf, res}}$ and $H_{\text{rf, wg}}$ being the rf field amplitudes in a coplanar waveguide resonator and a simple coplanar waveguide, respectively, and Q_n the quality factor of the n -th mode of the resonator ($n = 1, 2, \dots$). The mode profile for a resonator of length ℓ (going from 0 to ℓ) can be written as

$$H_{\text{rf, res}}[x, y, z] = H_{\text{rf, res}}[y, z] \sin\left(\frac{n\pi}{\ell}x\right). \quad (8.12)$$

Substituting the expression for the magnetic field in Equation (8.7) with those of Equation (8.11) and (8.12) and only considering absolute values of the amplitude leads to the general term for the absorption intensity of resonant coplanar structures as

$$\frac{dW}{dt} = \frac{\pi\omega_n^2}{2k_B T} |\mu_{if}|^2 \int_0^\infty \int_{-\infty}^\infty \int_0^\ell H_{\text{rf, wg}}^2[y, z] Q_n \left| \sin\left(\frac{n\pi}{\ell}x\right) \right| dx dy dz. \quad (8.13)$$

Executing the x -integration while taking into account that $\ell = n\lambda/2$ leads to

$$\frac{dW}{dt} = \frac{\ell\omega_n^2}{k_B T} |\mu_{if}|^2 Q_n \int_0^\infty \int_{-\infty}^\infty H_{\text{rf, wg}}^2[y, z] dy dz \quad (8.14)$$

which is identical to Equation (8.10) for $Q_n = 1$. This result demonstrates nicely that the absorption intensity linearly scales with the quality factor.

The remaining integrand in Equation (8.14) solely depends on geometrical parameters and the resulting integral can be maximized for the appropriate sample according

to Figure 8.5. To further increase the absorption intensity, the quality factor should be as high as possible and the length of the resonator should be maximized. The quality factor of superconducting coplanar resonators can be controlled to some extent by the coupling to the in and output feeds. Reducing the coupling leads to higher quality factors but on the other hand decreases the power injected into the resonator. Additionally, as an increasing length also enhances the absorption intensity it might be useful to use the higher harmonics of a low frequency resonator for the actual experiment, just to increase the effective interaction volume. However, this strongly depends on the sample since the quality factor of an unperturbed superconducting coplanar resonator decreases with higher harmonics with $Q_n = \frac{1}{n}Q_0$ and the length increases for lower frequencies also with $\frac{1}{\omega}$ leading to no net enhancement of the absorption intensity. Often, however, the sample itself acts as a strong additional loss channel (dielectric or Ohmic losses) that dominates the quality factor for at least the first few harmonics (leading to relatively constant or even erratic values of Q as a function of n , far from the $1/n$ dependence).

To get an impression of how the fields are distributed for such a resonant structure, sections of isosurfaces of the magnetic field amplitudes are drawn as shells on top of an exemplary resonant structure with a quality factor of $Q = 10^3$ in Figure 8.10. For comparison, the isosurfaces are again chosen to be multiples of the limit field strength $H_{\text{lim}}^{\text{avg}}$. Even for a relatively small quality factor of only 1000, the fields reach quite far into the half-space region above the resonator. In y and z -direction, the region within which H exceeds $H_{\text{lim}}^{\text{avg}}$ extends almost as far as 500 μm . The real structures used in this work, however, are no straight resonators as schematically depicted in Figure 8.10 but in fact meandering structures (to save space while keeping the chip size small and to push potential box modes to high frequencies). Neighboring lines are typically 350 or 400 μm apart (depending on design). As a consequence, the different microwave field components generated at different points along the length of the resonator add up (z -components) or cancel each other out (y -components) where the lines are running parallel. Figure 8.11 shows the microwave field amplitudes in a cut plane (red shaded plane in the inset on the top right) of the resonator design for ‘R04’ ($S = 60 \mu\text{m}$, $W = 25 \mu\text{m}$, $f_0 = 2.68 \text{ GHz}$). The inner five lines are separated by 350 μm from each other and the two outer lines are placed at a distance of 492 μm from their inner neighbors. The upper panel shows the microwave field amplitudes directly at the resonator-air (vacuum) interface at $z = 0$. As the resonant structure meanders along the chip, the amplitude is maximized at the midpoint of the resonator (with respect to its length ℓ). The sinusoidal mode profile leads to weaker

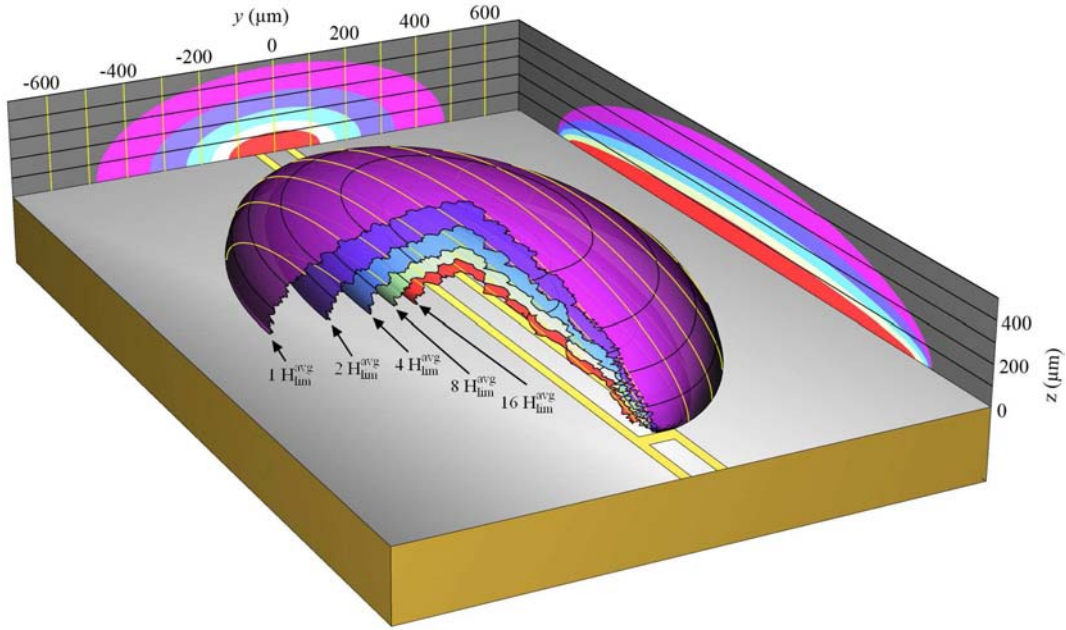


Figure 8.10: Microwave magnetic field amplitude profile of the fundamental mode of a coplanar waveguide resonator (with $S = 60 \mu\text{m}$ and $\ell = 4 \text{ mm}$) with a quality factor of $Q = 1000$. Isosurfaces enclose volumes for which $H_{\text{rf}} > 2^k H_{\text{lim}}^{\text{avg}}$ ($k = 0, 1, 2, 3, 4$). Yellow and black lines are drawn in $100 \mu\text{m}$ steps in y and z -direction, respectively.

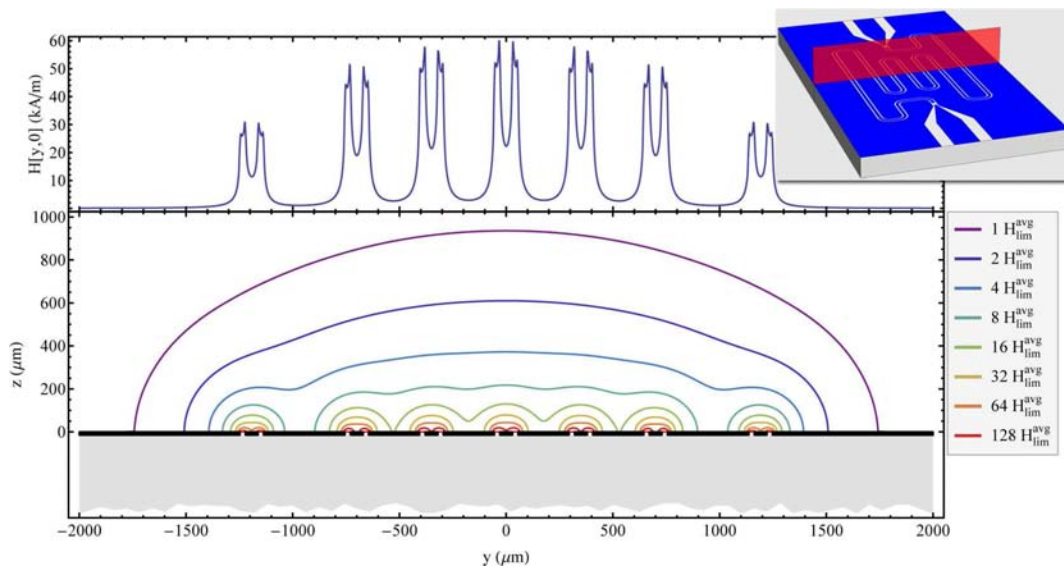


Figure 8.11: Microwave magnetic fields in the red shaded cut plane (inset) of resonator ‘R04’ ($\omega_{\text{res}} = 2.68 \text{ GHz}$, $Q = 1000$). The fields generated at neighboring lines add up, forming widespread regions of high field strength. The upper panel shows the actual field amplitudes at $z = 0$ (profile reflects the sinusoidal shape of the fundamental mode).

amplitudes for off-center lines (higher harmonics produce different amplitude profiles). Due to the proximity of the inner lines the fields add up between them, forming a large area with strong fields extending very far into the half-space region above the resonator structure. In this way, superconducting coplanar resonators represent a formidable tool to perform ESR measurements for a variety of (low) freely selectable frequencies due to the typical high achievable quality factors and the consequent high absorption intensity.

general note

The field distributions shown above were calculated for input powers of 1 W. In the actual experiments, much lower input powers of only -50 dBm to -20 dBm were used. However, since this is merely a scaling factor the results remain representative for comparisons of structures with different geometrical parameters.

Additionally, the nature of the sample was not taken into account. In fact, merely the field distributions above the waveguide or the resonator were calculated in the absence of any sample (treated as vacuum). Real samples will modify the field distributions depending on their permittivity. For samples with very high dielectric constants or even for metallic samples the field profiles will be modified to such an extent that above made considerations fail to describe the real situation properly.

9 Summary and Outlook

Since its first experimental realization in 1945 [19], electron paramagnetic resonance has not suffered from a loss of interest up to this date. Quite on the contrary, the range of studied materials was never wider spread and the obtained results never had so far reaching implications as today. Was it initially ‘only’ the investigation of simple paramagnetic compounds, the field of examined systems quickly broadened, spanning many different research areas and thus making EPR an interdisciplinary experimental tool.

The novel technique presented in this work combines quite a few experimental advantages which renders it into a powerful research instrument.

- (1) Both, the broadband and the resonant approach are very compact in design and can therefore easily be placed in a dilution refrigerator to study any material of choice at mK temperatures. In standard EPR devices the cavity is typically kept at room temperature and only the sample itself is cooled by a flow cryostat to the desired temperature. These systems, however, cannot reach temperatures below ~ 2 K. Although there are several realizations of EPR spectrometers at mK temperatures [107–111], these systems are extremely challenging due to various technical difficulties.

The devices presented in this work, on the other hand, are quite easy to handle and it poses no problem to combine them with standard dilution refrigerators. Also the heat load otherwise inserted via the rectangular waveguides [110, 111] or through the quartzglass shields [107, 108] is not present and the resulting base temperatures are lower.

- (2) Another consequence of the compact design is that also very small amounts of sample material can be studied at multiple frequencies or even continuously over a wide frequency range in one cool-down. This is especially advantageous for degrading samples which are otherwise to be studied in different spectrometers (for different frequencies) with waiting times between the measurements.

- (3) The broadband nature of the non-resonant/transmission line approach, however, is probably the most outstanding novelty of the presented work. As mentioned already in the introduction, previous broadband EPR spectrometers were either rather limited in their frequency range [28] or the system had to be warmed up and modified to cover the whole frequency span [29].

Performing EPR experiments at many different frequencies holds the ability to

study many different effects and phenomena [30] as already indicated in the introduction.

This work demonstrates the possibility to observe magnetic transitions over a wide range of frequencies by using superconducting coplanar waveguides to generate the necessary microwave magnetic fields. The first part of this thesis (after introducing the investigated systems; starting at section 4) is dedicated to the properties and geometrical aspects of coplanar waveguides and coplanar waveguide resonators. At the end of that section the fabrication steps are explained and the so-called microsphere lithography is introduced, as an additional step to efficiently produce large area arrays of sub- μm microholes (antidots). It is shown that the formation of antidot arrays significantly improves the performance of superconducting coplanar resonators in external magnetic fields owing to the fact that the antidots act as efficient traps for vortices and thus reduce the vortex associated losses. The improved performance in the presence of moderate external magnetic fields (up to several 100 mT) is essential for the usage of superconducting CPW resonators in EPR experiments. This result also holds strong prospects for the research field of quantum information processing, in particular circuit quantum electrodynamics with spin ensembles in which superconducting CPW resonators act as quantum buses to transfer quantum states between superconducting qubits and atomic (spin) ensembles.

The following section describes the electric and magnetic microwave field distribution in coplanar waveguide structures based on analytical calculations and 3D electromagnetic (EM) simulations (using CST Microwave Studio). In particular, EM simulations with a metallic sample placed at a distance d above a resonant structure revealed an optimum distance for which the microwave magnetic fields at the sample surface are maximized.

As proof of principle for the technique, two systems were investigated. One of them is so-called NITPhOMe, a member of the vast family of Nitronyl-Nitroxides which are often used as spin labels in investigations of structure and motion in biological/biomedical studies [18, 30]. It was demonstrated that a clear EPR signal is visible for frequencies up to 40 GHz and fields up to ~ 1.4 T. This section also introduced different ways of analyzing the raw data since the absorption lines are often not directly visible in the frequency-swept spectra as recorded (due to the large background of the frequency dependent damping of the coaxial lines).

Having successfully confirmed the operation of the device with a simple spin $1/2$ system the apparatus was further tested with the higher spin system ruby (basically Cr^{3+} in sapphire; $S = 3/2$). Since the field dependence of the transition frequencies

of ruby is more rich compared to that of NITPhOMe it represents an excellent model system to validate the performance of the technique. In addition, ruby is a very well studied material which allows for the verification of the obtained results by comparison with literature.

It is shown that the six visible transitions are in perfect agreement with theory and that their position as a function of field and frequency allowed for the determination of the crystal orientation with respect to the external magnetic field.

Following this, a single crystal of a newly synthesized single ion magnet based on the rare earth element of gadolinium was studied by broadband EPR at mK temperatures. At the lowest sample temperature of $T \approx 60$ mK a whole variety of transitions could be observed. The abundance of visible transitions can be explained by a strong mixing of the spin levels within the ground state multiplet which leads to a violation of the selection rules ($\Delta m_s = \pm 1$) and almost any transition is ‘allowed’ to a certain probability. The low symmetry of the system (monoclinic, C_2) leads to ten unknown parameters in the spin Hamiltonian (nine anisotropy terms plus one angle). Since the individual transition lines observed in the spectra can not be assigned to transitions between specific spin states, a determination of those parameters is not possible (at least not without further a priori information about the system).

Finally, the heavy fermion metal YbRh_2Si_2 was studied using both the broadband and the resonant approach. The results obtained from broadband EPR showed a very weak signal which could be enhanced by filtering and discrete derivation of the data. A signal could also only be observed in the Fermi-liquid and non-Fermi-liquid regime, not in the antiferromagnetic phase. At all measured temperatures the absorption frequency increases linearly with increasing external magnetic field. The g -factor determined from the slope of that line for the lowest measured temperature yields $g_{\text{slope}} \approx 3.4$. Is the g -factor, however, extracted from the absolute position in frequency and field (as in every resonant EPR experiment with a fixed resonator frequency) it displays a strong reduction close to the quantum critical point (down to $g_{\text{abs}} \approx 2.8$ at $H_{\text{ext}} \lesssim 70$ mT) and only approaches g_{slope} asymptotically for large external fields. It is shown that this difference can be attributed to some as of yet unclear low frequency/field behavior.

Concerning the results gained from resonant EPR, it was possible to study the system at 19 different frequencies ranging in total from 1.5 GHz to 13.4 GHz. The absorption line parameters show unique features in the three distinguishable regions of the phase diagram. Within the non-Fermi-liquid regime the resonance field shifts towards higher values and the linewidth decreases with decreasing temperature. Upon

entering the antiferromagnetic phase, at low fields, this shift is reversed and the resonance field decreases sharply. The linewidth, on the other hand, is increased drastically, indicating additional relaxation channels. At higher fields the system enters the Fermi-liquid regime and the resonance field remains constant. Within the Fermi-liquid region the linewidth follows the predicted T^2 behavior fairly well. The predicted additional H^2 dependence [95], however, could not be observed.

It is also shown that in the vicinity of the antiferromagnetic phase boundary the spectra exhibit features which might be related to the onset of antiferromagnetic fluctuations.

These results are, so far, the first experimental EPR studies that could probe the low temperature/field region in the vicinity of the quantum critical point. However, a full, unambiguous data interpretation is still pending. Especially the linewidth as a function of temperature and magnetic field (which also holds valuable information about the various coupling strengths in the system) needs to be examined with particular care since it is highly susceptible to the prior background subtraction.

The last section of this work deals with the minimum number of spins that can be detected with the broadband technique based on the results obtained with the NIT-PhOMe sample. In addition, a general model for the expected absorption strength as a function of waveguide or resonator (geometrical) parameters is derived and the importance of choosing the best possibly suited geometry for a given sample is discussed.

To summarize the work it can be said that it was clearly demonstrated that broadband (and multi-frequency resonant) EPR studies are possible utilizing superconducting coplanar waveguides. The accessible temperature range of this technique easily expands into the mK regime. Frequency coverage up to ~ 40 GHz is achievable.

Although these are already pretty impressive key features, the full potential of the technique has not been reached yet. Based on the pioneering work presented in this thesis the frequency as well as the temperature range could be extended to broaden the scope of applicability [117]. By replacing the sub-miniature A (SMA) coaxial connectors by 1.85 mm connectors the high-frequency limit could be pushed to 67 GHz. In addition, by fabricating the coplanar waveguides with normal conducting thin films (copper, silver, gold) instead of superconducting ones, an EPR signal could be observed up to room temperature (with a NITPhOMe sample). In this way, the waveguides also do not show any inconvenient magnetic field dependence of the

microwave transport properties.

As a possible way to increase sensitivity in future generations of this technique, a modulation of the external magnetic field and the use of lock-in detection, as done in standard cavity based EPR, could be envisioned.

To further increase the range of application a pulsed broadband EPR apparatus based on coplanar waveguides could be constructed. The realization of such a device would allow to study (frequency dependent) spin relaxation processes under a greatly extended set of conditions (ultra-low temperatures, arbitrarily close to interesting phenomena such as quantum critical points, at any frequency of choice, etc.).

Appendix

A Field Calculations for Coplanar Structures

The microwave field strengths used to plot the graphs Figure 5.1 and Figure 5.2 as well as for the sensitivity considerations discussed in section 8 were derived from a formalism stated in a work by Simons and Arora [106] which is an extension to the work by Cohn [105] and give analytical expressions for the electric and magnetic high frequency field components. The components are derived from a summation over the infinite TE and TM modes propagating in a rectangular waveguide model.

On the air or vacuum side of the waveguide ($z \leq 0$) the electric and magnetic field components are given by

$$E_y = \frac{2V_0}{b} \sum_{n>0} \left[\frac{\sin(n\pi\delta/2)}{n\pi\delta/2} \sin(n\pi\bar{\delta}/2) \right] \sin\left(\frac{n\pi y}{b}\right) e^{-\gamma_n|z|} \quad (\text{A.1})$$

$$E_z = -\frac{2V_0}{b} \sum_{n>0} \frac{1}{F_n} \left[\frac{\sin(n\pi\delta/2)}{n\pi\delta/2} \sin(n\pi\bar{\delta}/2) \right] \cos\left(\frac{n\pi y}{b}\right) e^{-\gamma_n|z|} \quad (\text{A.2})$$

$$H_y = \frac{2V_0}{\eta b} \frac{\lambda'}{\lambda} \sum_{n>0} \frac{1}{F_n} \left[\frac{\sin(n\pi\delta/2)}{n\pi\delta/2} \sin(n\pi\bar{\delta}/2) \right] \cos\left(\frac{n\pi y}{b}\right) e^{-\gamma_n|z|} \quad (\text{A.3})$$

$$H_z = \frac{2V_0}{\eta b} \frac{\lambda'}{\lambda} \sum_{n>0} \left[\frac{\sin(n\pi\delta/2)}{n\pi\delta/2} \sin(n\pi\bar{\delta}/2) \right] \sin\left(\frac{n\pi y}{b}\right) e^{-\gamma_n|z|} \quad (\text{A.4})$$

with the vacuum impedance $\eta \approx 376.7 \Omega$. $\pm b/2$ denotes the position of a magnetic wall in y -direction. λ and λ' are the wavelengths in vacuum and on the waveguide for any given frequency f , respectively. Electric walls are positioned at $x = 0$ and $x = \lambda'/2$. The constant V_0 is the voltage across the gap between center conductor and ground plane. The geometric parameters enter the equations via $\delta = w/b$ and $\bar{\delta} = (s + w)/b$ and the remaining quantities are given as

$$\begin{aligned}
F_n &= \frac{b\gamma_n}{n\pi} = \sqrt{1 + \left(\frac{2bv}{n\lambda}\right)^2} & F_{n1} &= \frac{b\gamma_{n1}}{n\pi} = \sqrt{1 - \left(\frac{2bu}{n\lambda}\right)^2} \\
v &= \sqrt{\left(\frac{\lambda}{\lambda'}\right)^2 - 1} & u &= \sqrt{\left(\varepsilon_r - \frac{\lambda}{\lambda'}\right)^2} \\
r_n &= \gamma_{n1}d + \tanh^{-1}\left(\frac{F_{n1}}{\varepsilon_r F_n}\right) & q_n &= \gamma_{n1}d + \coth^{-1}\left(\frac{F_n}{F_{n1}}\right).
\end{aligned}$$

Within the substrate ($0 \leq z \leq d$) with thickness d the field components are given by

$$\begin{aligned}
E_y &= \frac{2V_0}{b} \sum_{n>0}^{\infty} \left[\frac{\sin(n\pi\delta/2)}{n\pi\delta/2} \sin(n\pi\bar{\delta}/2) \right] \sin\left(\frac{n\pi y}{b}\right) \\
&\quad \cdot \left(\cosh(\gamma_{n1}z) - \left[\frac{\tanh r_n + (2b/n\lambda')^2 \coth q_n}{1 + (2b/n\lambda')^2} \right] \sinh(\gamma_{n1}z) \right) \quad (\text{A.5})
\end{aligned}$$

$$\begin{aligned}
E_z &= -\frac{2V_0}{b} \sum_{n>0}^{\infty} \frac{1}{F_{n1}} \left[\frac{\sin(n\pi\delta/2)}{n\pi\delta/2} \sin(n\pi\bar{\delta}/2) \right] \cos\left(\frac{n\pi y}{b}\right) \\
&\quad \cdot \left(\sinh(\gamma_{n1}z) - \tanh r_n \cosh(\gamma_{n1}z) \right) \quad (\text{A.6})
\end{aligned}$$

$$\begin{aligned}
H_y &= -\frac{2V_0}{\eta b} \frac{\lambda'}{\lambda} \sum_{n>0}^{\infty} \frac{1}{F_n} \left[\frac{\sin(n\pi\delta/2)}{n\pi\delta/2} \sin(n\pi\bar{\delta}/2) \right] \cos\left(\frac{n\pi y}{b}\right) \\
&\quad \cdot \left(\left[\frac{F_{n1}^2 \coth q_n + \varepsilon(2b/n\lambda)^2 \tanh r_n}{1 + (2b/n\lambda')^2} \right] \left(\cosh(\gamma_{n1}z) - \sinh(\gamma_{n1}z) \right) \right) \quad (\text{A.7})
\end{aligned}$$

$$\begin{aligned}
H_z &= \frac{2V_0}{\eta b} \frac{\lambda'}{\lambda} \sum_{n>0}^{\infty} \left[\frac{\sin(n\pi\delta/2)}{n\pi\delta/2} \sin(n\pi\bar{\delta}/2) \right] \sin\left(\frac{n\pi y}{b}\right) \\
&\quad \cdot \left(\cosh(\gamma_{n1}z) - \coth q_n \sinh(\gamma_{n1}z) \right). \quad (\text{A.8})
\end{aligned}$$

The red marked parentheses in Equation (A.7) are not included in the original work by Simons and Arora but are necessary for the sum to converge for large n .

On the air/vacuum side below the substrate ($z \geq d$) equations (A.5) through (A.8) can be used with $\gamma_{n1}z$ replaced by $\gamma_{n1}d$ and when multiplied with an additoinal factor of $\exp[-\gamma_n(z-d)]$.

To compute the infinite series, a termination criterion is introduced by $n_t = n_0/(1 + z/z_1)$ with n_0 and z_1 being constants. Here, n_0 was chosen to $n_0 = 10000$ and $z_1 = s$. The position of the magnetic walls at $y = \pm b/2$ is important and the results are good for sufficiently large b (typically $b > \lambda'$).

B AFM Phase Transition Spectra with adjusted Temperatures

As mentioned in the discussion about the magnetic resonance spectra close to the antiferromagnetic phase transition in section 7 the uncertainty about the actual sample temperature is a non-negligible issue. It was also already mentioned that the measured temperature is rather noisy (while the temperature at the mixing chamber is stable and fluctuates only in the order of $\Delta T_{MC} \approx \pm 0.1$ mK) and varies with time (and therefore magnetic fields since the data was obtained by performing field sweeps). To account for those changes while assuming a continuous temperature drift (no sudden jumps) one can approximate the sample temperature as a function of magnetic field as shown in Figure B.1. The plot shows the averaged sensor temperature at each measurement point (blue connected dots), the range between lowest and highest measured temperature within the averaging cycle (light blue shaded area) and a smoothed temperature drift approximated by a B-spline (red).

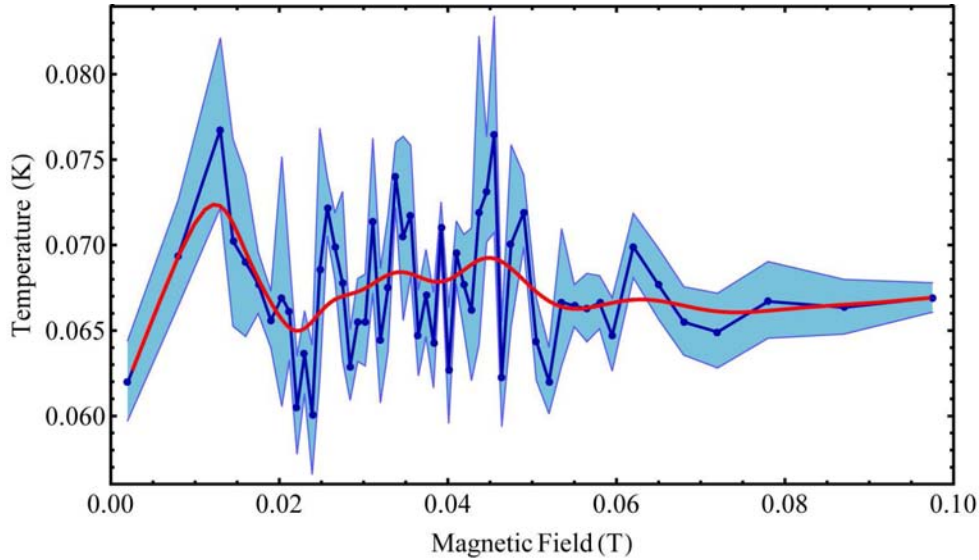


Figure B.1: Field dependent average sensor temperature (blue connected dots), range between lowest and highest measured temperature within one readout cycle (light blue area) and B-spline approximated continuous sample temperature (red).

Doing so for all the spectra shown in Figure 7.6 on page 103 and plotting the resulting spectra as a function of magnetic field and field dependent temperature the result naturally looks exactly as Figure 7.6 if the spectra are projected onto the Q - H_{ext} plane (see top panel of Figure B.2). If the viewing angle, however, is moved slightly

out of the plane it becomes apparent how the spectra ‘wind’ themselves through the diagram. Figure B.3 continues to tilt the viewing angle further. In this illustration

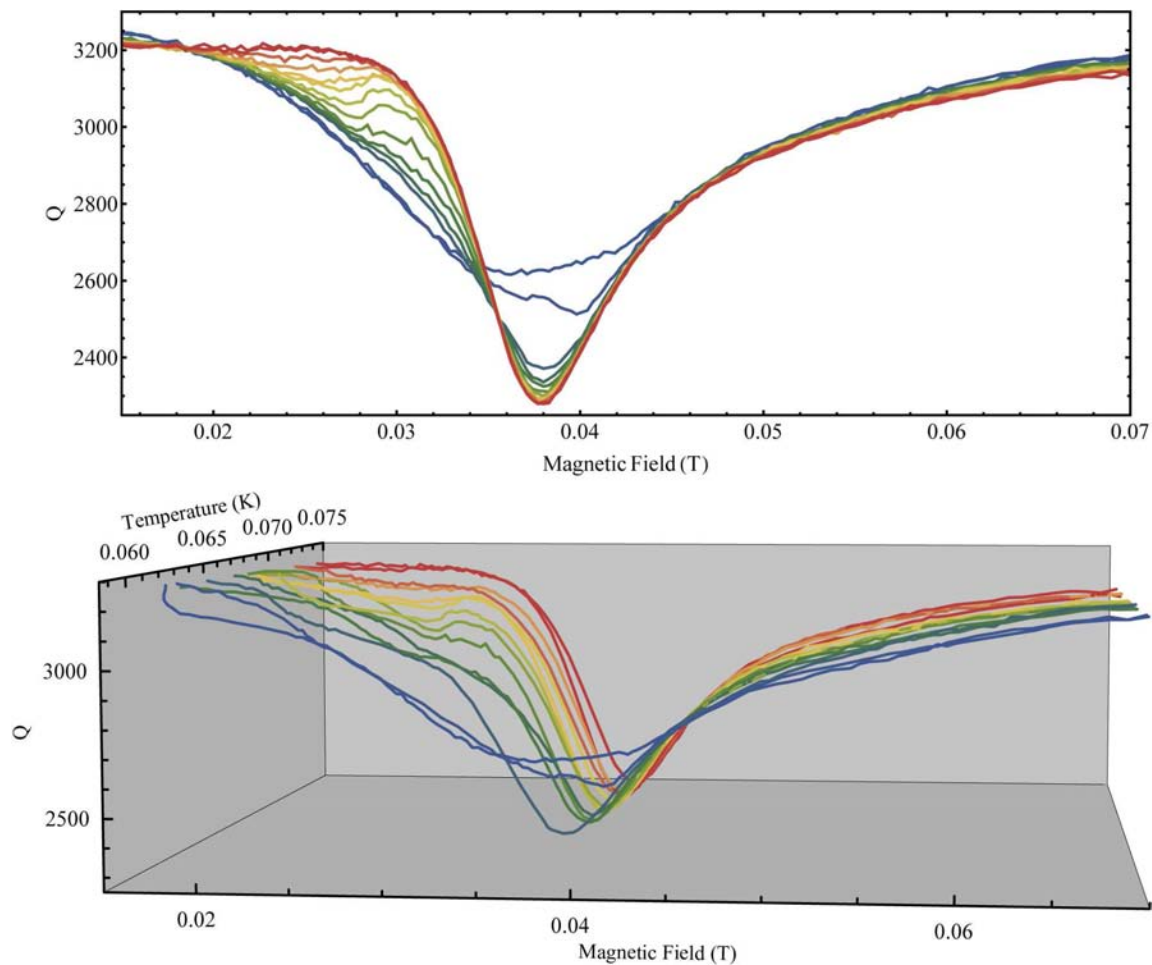


Figure B.2: Quality factor as a function of external field and temperature. The top panel shows a projection onto the Q - H_{ext} plane while for the bottom panel the viewing angle is slightly moved out-of-plane. The characteristic feature which marks the transition from antiferromagnetic order to paramagnetism is still discernible.

it is rather difficult to make out any specific features. The lower panel finally shows the data as a projection onto the temperature-field plane, thus depicting the approximated sample temperature as a function of external field.

To compare the different analysis methods, the combination of all $Q[H_{\text{ext}}, T(H_{\text{ext}})]$ spectra was again interpolated by a B-spline function and the resulting surface is shown in Figure B.4. The result looks surprisingly similar to that shown in Figure 7.8 thus legitimating the use of steady, field independent averaged sample temperatures as it was done in section 7.

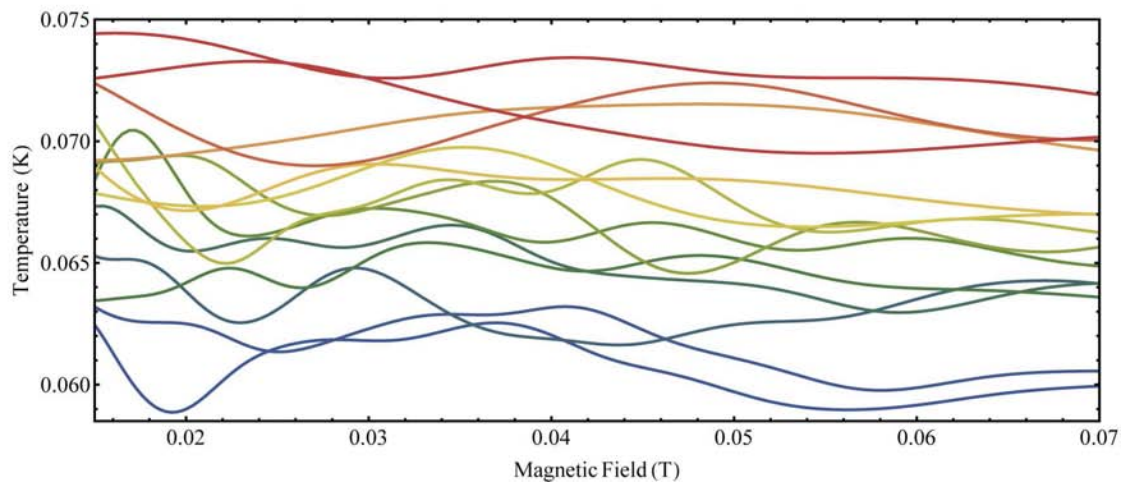
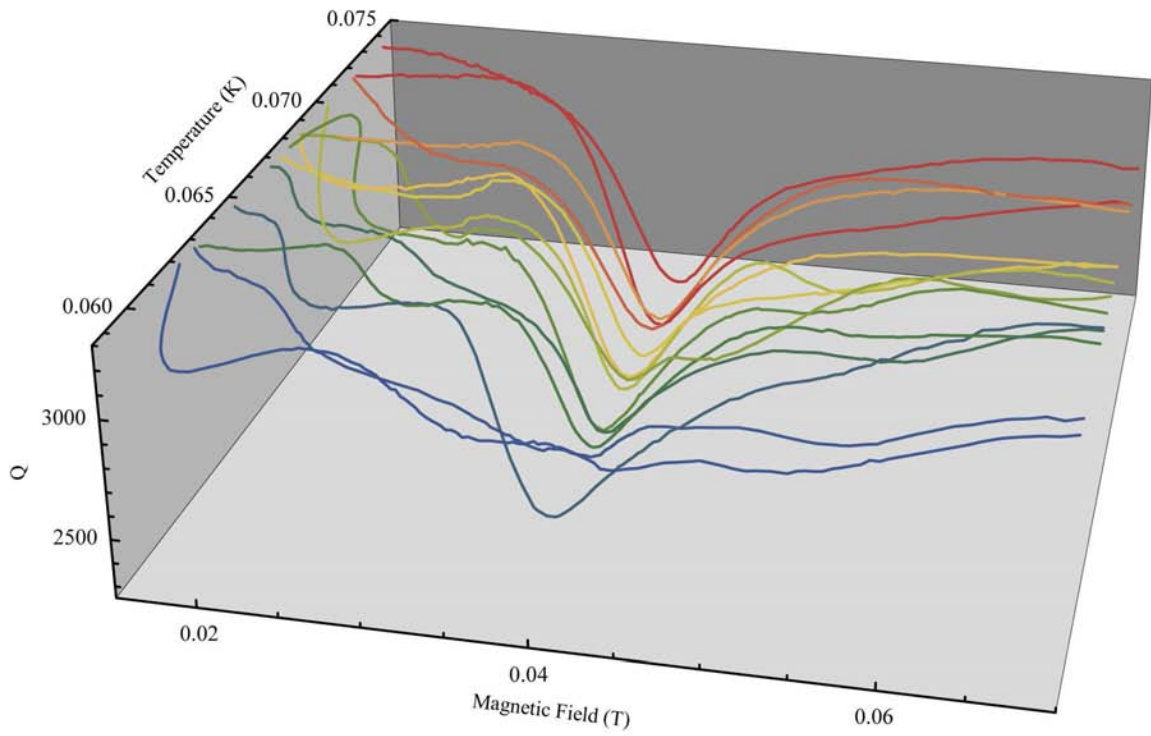


Figure B.3: Continuation of Figure B.2. Top panel has the viewing angle tilted further out-of-plane. The bottom panel shows a projection onto the $T-H_{\text{ext}}$ plane displaying the approximated sample temperature as a function of magnetic field.

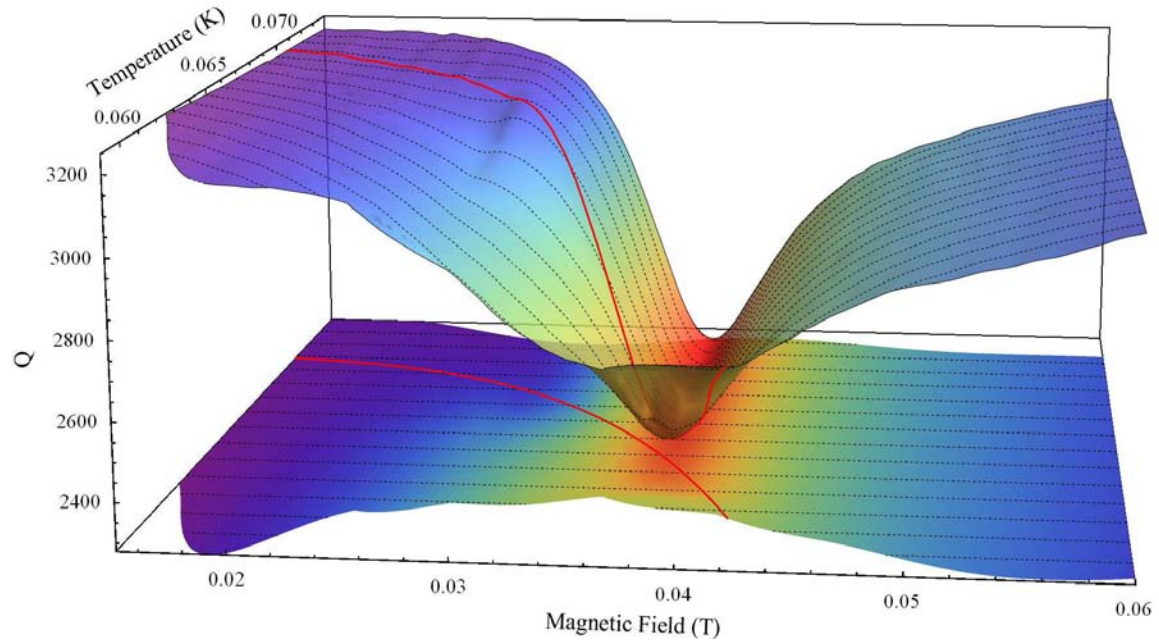


Figure B.4: Interpolated quality factor as a function of external field and temperature. The surface looks strikingly similar to that shown in Figure 7.8.

References

- [1] P. Dirac, ‘The quantum theory of the emission and absorption of radiation’, *Proc. R. Soc. Lond. A* **114**, 243 (1927).
- [2] E. Fermi, ‘Quantum theory of radiation’, *Rev. Mod. Phys.* **4**, 87 (1932).
- [3] C. Cohen-Tannoudji, J. Dupont-Roc, and G. Grynberg, ‘Photons and Atoms – Introduction to Quantum Electrodynamics’, *Wiley* (1989).
- [4] Serge Haroche and Jean-Michel Raimond, ‘Exploring the Quantum – Atoms, Cavities and Photons’, *Oxford University Press* (2006).
- [5] J. D. Jackson, ‘Classical Electrodynamics’, 2nd edn., *Wiley* (1975).
- [6] E. M. Purcell, ‘Spontaneous Emission Probabilities at Radio Frequencies’, *Phys. Rev.* **69**, 681 (1946).
- [7] A. Faist, E. Geneux, P. Meystre, and P. Quattropani, ‘Coherent radiation in interaction with two-level system’, *Helv. Phys. Acta* **45**, 956 (1972).
- [8] J. H. Eberly, N. B. Narozhny, and J. J. Sanchez-Mondragon, ‘Periodic Spontaneous Collapse and Revival in a Simple Quantum Model’, *Phys. Rev. Lett.* **44**, 1323 (1980).
- [9] Y. Kaluzny, P. Goy, M. Gross, J. M. Raimond, and S. Haroche, ‘Observation of Self-Induced Rabi Oscillations in Two-Level Atoms Excited Inside a Resonant Cavity: The Ringing Regime of Superradiance’, *Phys. Rev. Lett.* **51**, 1175 (1983).
- [10] G. Rempe, H. Walther, and N. Klein, ‘Observation of Quantum Collapse and Revival in a One-Atom Maser’, *Phys. Rev. Lett.* **58**, 353 (1987).
- [11] R. J. Brecha, L. A. Orozco, M. G. Raizen, Min Xiao, and H. J. Kimble, ‘Observation of oscillatory energy exchange in a coupled-atom-cavity system’, *J. Opt. Soc. Am. B* **12**, 2329 (1995).
- [12] Y. Kubo, I. Diniz, C. Grezes, T. Umeda, J. Isoya, H. Sumiya, T. Yamamoto, H. Abe, S. Onoda, T. Ohshima, V. Jacques, A. Dréau, J.-F. Roch, A. Auffeves, D. Vion, D. Esteve, and P. Bertet, ‘Electron spin resonance detected by a superconducting qubit’, *Phys. Rev. B* **86**, 064514 (2012).

- [13] C. Grezes, B. Julsgaard, Y. Kubo, M. Stern, T. Umeda, J. Isoya, H. Sumiya, H. Abe, S. Onoda, T. Ohshima, V. Jacques, J. Esteve, D. Vion, D. Esteve, K. Moelmer, and P. Bertet, ‘Multi-mode storage and retrieval of microwave fields in a spin ensemble’, *Phys. Rev. X* **4**, 021049 (2014).
- [14] A. Abragam and B. Bleaney, ‘Electron Paramagnetic Resonance of Transition Ions’, *Oxford University Press* (1970).
- [15] C. P. Poole, ‘Electron Spin Resonance – A Comprehensive Treatise on Experimental Techniques’, 2nd edn., *Wiley* (1983).
- [16] C. P. Schlichter, ‘Principles of Magnetic Resonance’, 3rd edn., *Springer* (1992).
- [17] G. A. Rinard, R. W. Quine, R. Song, G. R. Eaton, and S. S. Eaton, ‘Absolute EPR Spin Echo and Noise Intensities’, *J. Magn. Reson.* **140**, 69 (1999).
- [18] G. R. Eaton, S. S. Eaton, D. P. Barr, and R. T. Weber, ‘Quantitative EPR’, *Springer* (2010).
- [19] E. Zavoisky, ‘Spin-magnetic resonance in paramagnetics’, *J. Phys. USSR* **9**, 211 (1945).
- [20] R. L. Cumberow and D. Halliday, ‘Paramagnetic Losses in Two Manganous Salts’, *Phys. Rev.* **70**, 433 (1946).
- [21] B. Bleaney and R. P. Penrose, ‘Ammonia Spectrum in the 1 cm. Wave-length Region’, *Nature* **157**, 339 (1946).
- [22] G. Boero, M. Bouterfas, C. Massin, F. Vincent, P.-A. Besse, R. S. Popovic, and A. Schweiger, ‘Electron-spin resonance probe based on a 100 μm planar microcoil’, *Rev. Sci. Instrum.* **74**, 4794 (2003).
- [23] R. Narkowicz, D. Suter, and R. Stonies, ‘Planar microresonators for EPR experiments’, *J. Magn. Reson.* **175**, 275 (2005).
- [24] R. Narkowicz, D. Suter, and I. Niemeyer, ‘Scaling of sensitivity and efficiency in planar microresonators for electron spin resonance’, *Rev. Sci. Instrum.* **79**, 084702 (2008).
- [25] A. Blais, R.-S. Huang, A. Wallraff, S. M. Girvin, and R. J. Schoelkopf, ‘Cavity quantum electrodynamics for superconducting electrical circuits: An architecture for quantum computation’, *Phys. Rev. A* **69**, 062320 (2004).

-
- [26] J. R. Anderson, R. R. Mett, and J. S. Hyde, ‘Cavities with axially uniform fields for use in electron paramagnetic resonance. II. Free space generalization’, *Rev. Sci. Instrum.* **73**, 3027 (2002).
- [27] J. S. Hyde, R. R. Mett, and J. R. Anderson, ‘Cavities with axially uniform fields for use in electron paramagnetic resonance. III. Re-entrant geometries’, *Rev. Sci. Instrum.* **73**, 4003 (2002).
- [28] Z. H. Jang, B. J. Suh, M. Corti, L. Cattaneo, D. Hajny, F. Borsa, and M. Luban, ‘Broadband electron spin resonance at low frequency without resonant cavity’, *Rev. Sci. Instrum.* **79**, 046101 (2008).
- [29] C. Schlegel, M. Dressel, and J. van Slageren, ‘Broadband electron spin resonance at 4-40 GHz and magnetic fields up to 10 T’, *Rev. Sci. Instrum.* **81**, 093901 (2010).
- [30] S. K. Misra, ‘Multifrequency Electron Paramagnetic Resonance – Theory and Applications’, Wiley (2011).
- [31] A. T. Fiory, A. F. Hebard, and R. P. Minnich, ‘The rf Resistivity of a Perforated Superconducting Film in a Magnetic Field’, *J. Phys. Colloq.* **39**, 633 (1978).
- [32] J. I. Martín, M. Vélez, J. Nogués, and I. K. Schuller, ‘Flux Pinning in a Superconductor by an Array of Submicrometer Magnetic Dots’, *Phys. Rev. Lett.* **79**, 1929 (1997).
- [33] V. V. Moshchalkov, M. Baert, V. V. Metlushko, E. Rosseel, M. J. Van Bael, K. Temst, Y. Bruynseraede, and R. Jonckheere, ‘Pinning by an antidot lattice: The problem of the optimum antidot size’, *Phys. Rev. B* **57**, 3615 (1998).
- [34] P. Selders and R. Wördenweber, ‘Low-frequency noise reduction in $\text{YBa}_2\text{Cu}_3\text{O}_{7-\delta}$ superconducting quantum interference devices by antidots’, *Appl. Phys. Lett.* **76**, 3277 (2000).
- [35] R. Wördenweber, P. Dymashevski, and V. R. Misko, ‘Guidance of vortices and the vortex ratchet effect in high- T_c superconducting thin films obtained by arrangement of antidots’, *Phys. Rev. B* **69**, 184504 (2004).
- [36] M. Häffner, M. Kemmler, R. Löffler, B. Vega Gómez, M. Fleischer, R. Kleiner, D. Koelle, and D. P. Kern, ‘Controlling superconducting properties via vortex pinning by regular arrays of vertical carbon nanotubes’, *Microelectron. Eng.* **86**, 147003 (2009).

- [37] D. Bothner, C. Clauss, E. Koroknay, M. Kemmler, T. Gaber, M. Jetter, M. Scheffler, P. Michler, M. Dressel, D. Koelle, and R. Kleiner, ‘The phase boundary of superconducting niobium thin films with antidot arrays fabricated with microsphere photolithography’, *Supercond. Sci. Technol.* **25**, 065020 (2012).
- [38] C. Song, M. P. DeFeo, K. Yu, and B. L. T. Plourde, ‘Reducing microwave loss in superconducting resonators due to trapped vortices’, *Appl. Phys. Lett.* **95**, 232501 (2009).
- [39] D. Bothner, T. Gaber, M. Kemmler, D. Koelle, and R. Kleiner, ‘Improving the performance of superconducting microwave resonators in magnetic fields’, *Appl. Phys. Lett.* **98**, 102504 (2011).
- [40] D. Bothner, C. Clauss, E. Koroknay, M. Kemmler, T. Gaber, M. Jetter, M. Scheffler, P. Michler, M. Dressel, D. Koelle, and R. Kleiner, ‘Reducing vortex losses in superconducting microwave resonators with microsphere patterned antidot arrays’, *Appl. Phys. Lett.* **100**, 012601 (2012).
- [41] D. Bothner, ‘Micropatterned superconducting film for operation in hybrid quantum devices’, *PhD Thesis*, Universität Tübingen (2013).
- [42] H. K. Onnes, ‘The resistance of pure mercury at helium temperatures’, *Commun. Ohys. Lab. Univ. Leiden* **12**, 120 (1911).
- [43] W. Meissner and R. Ochsenfeld, ‘Ein neuer Effekt bei Eintritt der Supraleitfähigkeit’, *Naturwissenschaften* **21**, 787 (1933).
- [44] F. London and H. London, ‘The Electromagnetic Equations of the Supraconductor’, *Proc. Roy. Soc. (London) A* **149**, 866 (1935).
- [45] L. W. Shubnikov, V. I. Chotkewitsch, J. D. Schepelew, and J. N. Rjabinin, ‘Magnetische Eigenschaften supraleitender Metalle und Legierungen’, *Phys. Z. Sowiet.* **10**, 165 (1936).
- [46] L. W. Shubnikov, V. I. Khotkewitsch, Yu. D. Schepelev, and Yu. N. Rjabinin, ‘Magnetic properties of superconducting metals and alloys’, *Zh. Eksp. Teor. Fiz.* **7**, 221 (1937).
- [47] N. Zavaritskii, ‘Superconducting properties of thallium and tin films condensed at low temperatures’, *Doklady Akad. Nauk. SSSR* **86**, 501 (1952).

-
- [48] A. A. Abrikosov, ‘On the Magnetic Properties of Superconductors of the Second Group’, *Zh. Eksp. Teor. Fiz.* **32**, 1442 (1957).
- [49] V. L. Ginzburg and L. D. Landau, ‘On the theory of superconductivity’, *Zh. Eksp. Teor. Fiz.* **20**, 1064 (1950).
- [50] J. Bardeen, L. N. Cooper, and J. R. Schrieffer, ‘Theory of Superconductivity’, *Phys. Rev.* **108**, 1175 (1957).
- [51] M. Tinkham, ‘Introduction to Superconductivity’, *McGraw-Hill* (1996).
- [52] V. V. Schmidt, ‘The Physics of Superconductors’, *Springer* (1997).
- [53] J. R. Clem, ‘Inductances and attenuation constant for a thin-film superconducting coplanar waveguide resonator’, *J. Appl. Phys.* **113**, 013910 (2013).
- [54] C. P. Bean, ‘Magnetization of Hard Superconductors’, *Phys. Rev. Lett.* **8**, 250 (1962).
- [55] C. P. Bean, ‘Magnetization of High-Field Superconductors’, *Rev. Mod. Phys.* **36**, 31 (1964).
- [56] W. T. Norris, ‘Calculation of hysteresis losses in hard superconductors carrying ac: isolated conductors and edges of thin sheets’, *J. Phys. D: Appl. Phys.* **3**, 489 (1970).
- [57] E. H. Brandt and M. Indenbom, ‘Type-II-superconductor strip with current in a perpendicular magnetic field’, *Phys. Rev. B* **48**, 12893 (1993).
- [58] T. H. Johansen, M. Baziljevich, H. Bratsberg, Y. Galperin, P. E. Lindelof, Y. Shen, and P. Vase, ‘Direct observation of the current distribution in thin superconducting strips using magneto-optic imaging’, *Phys. Rev. B* **54**, 16264 (1996).
- [59] Ch. Jooss, J. Albrecht, H. Kuhn, S. Leonhardt, and H. Kronmüller, ‘Magneto-optical studies of current distributions in high- T_c superconductors’, *Rep. Prog. Phys.* **65**, 651 (2002).
- [60] D. Bothner, T. Gaber, M. Kemmler, D. Koelle, and R. Kleiner, ‘Magnetic hysteresis effects in superconducting coplanar microwave resonators’, *Phys. Rev. B* **86**, 014517 (2012).

- [61] H. Jäger, A. Koch, V. Maus, H. W. Spiess, and G. Jeschke, ‘Relaxation-based distance measurements between a nitroxide and a lanthanide spin label’, *J. Magn. Reson.* **194**, 254 (2008).
- [62] L. Bogani, ‘A perspective on slow-relaxing molecular magnets built from rare-earths and nitronyl-nitroxide building blocks’, *J. APP. PHYS.* **109**, 07B115 (2011).
- [63] E. Heintze, F. El Hallak, C. Clauss, A. Rettori, M. G. Pini, F. Totti, M. Dressel, and L. Bogani, ‘Dynamic control of magnetic nanowires by light-induced domain-wall kickoffs’, *Nature Materials* **12**, 202 (2013).
- [64] P. L. Gentili, L. Bussotti, R. Righini, A. Beni, L. Bogani, and A. Dei, ‘Time-resolved spectroscopic characterization of photo-induced valence tautomerism for a cobalt-dioxolene complex’, *CHEM. PHYS.* **314**, 9 (2008).
- [65] G. Makhov, C. Kikuchi, J. Lambe, and R. W. Terhune, ‘Maser Action in Ruby’, *Phys. Rev.* **109**, 1399 (1958).
- [66] A. A. Manenkov and A. M. Prokhorov, *J. Exp. Theor. Phys. (U.S.S.R.)* **28**, 762 (1955).
- [67] J. E. Geusic, *Phys. Rev.* **102**, 1252 (1956).
- [68] M. Zaripov and I. J. Shamonin, *J. Exp. Theor. Phys. (U.S.S.R.)* **30**, 291 (1956).
- [69] E. O. Schulz-DuBois, ‘Paramagnetic Spectra of Substituted Sapphires-Part I: Ruby’, *Bell System Techn. J.* **38**, 271 (1959).
- [70] J. Weber, ‘Masers’, *Rev. Mod. Phys.* **31**, 681 (1959).
- [71] H. Klein, U. Scherz, M. Schulz, H. Setyono, and K. Wiszniewski, ‘Temperature Dependence of the EPR Spectrum of Ruby’, *Z. Physik B* **28**, 149 (1977).
- [72] M. Blume, R. Orbach, A. Kiel, and S. Geschwind, *Phys. Rev.* **139**, A314 (1965).
- [73] D. Gatteschi, R. Sessoli, and J. Villain, ‘Molecular Nanomagnets’, *Oxford University Press* (2006).
- [74] R. Winpenny, ‘Single-Molecule Magnets and Related Phenomena’, *Springer* (2006).
- [75] O. Kahn, ‘Molecular Magnetism’, *VCH Publishers* (1993).

- [76] C. Cervetti, E. Heintze, and L. Bogani, ‘Interweaving spins with their environment: novel inorganic nanohybrids with controllable magnetic properties’, *Dalton Trans.* **43**, 4220 (2014).
- [77] F. El Hallak, ‘Magnetic Anisotropy of Molecular Nanomagnets’, *PhD Thesis*, Universität Stuttgart (2009).
- [78] A. Paretzki, S. Hohloch, W. Kröner, P. Müller, S. Rauschenbach, M. Dressel, K. Kern, and L. Bogani, *in preparation*.
- [79] P. Gegenwart, Q. Si, and F. Steglich, ‘Quantum criticality in heavy-fermion metals’, *Nat. Phys.* **4**, 186 (2008).
- [80] V. A. Ivanshin, L. K. Aminov, I. N. Kurkin, J. Sichelschmidt, O. Stockert, J. Ferstl, and C. Geibel, ‘Electron paramagnetic resonance of Yb^{3+} ions in a concentrated YbRh_2Si_2 compound with heavy fermions’, *JETP Lett.* **77**, 625 (2003).
- [81] J. Sichelschmidt, V. A. Ivanshin, J. Ferstl, C. Geibel, and F. Steglich, ‘Low Temperature Electron Spin Resonance of the Kondo Ion in a Heavy Fermion Metal: YbRh_2Si_2 ’, *Phys. Rev. Lett.* **91**, 156401 (2003).
- [82] V. A. Ivanshin and D. G. Zverev, ‘ESR Study of the Undoped Heavy-Fermion Compound YbRh_2Si_2 ’, *Appl. Magn. Reson.* **27**, 87 (2004).
- [83] G. I. Mironov and V. A. Ivanshin, ‘Spin dynamics in YbRh_2Si_2 probed by ESR’, *Physica B* **47-49**, 359 (2005).
- [84] J. Wykhoff, J. Sichelschmidt, J. Ferstl, C. Krellner, C. Geibel, F. Steglich, I. Fazlishanov, and H.-A. Krug von Nidda, ‘Electron spin resonance in YbRh_2Si_2 : The role of the residual linewidth’, *Physica C* **460-462**, 686 (2007).
- [85] J. Wykhoff, J. Sichelschmidt, G. Lapertot, G. Knebel, J. Flouquet, I. Fazlishanov, H.-A. Krug von Nidda, C. Krellner, C. Geibel, and F. Steglich, ‘On the local and itinerant properties of the ESR in YbRh_2Si_2 ’, *Sci. Technol. Adv. Mater.* **8**, 389 (2007).
- [86] J. Sichelschmidt, J. Wykhoff, H.-A. Krug von Nidda, J. Ferstl, C. Geibel, and F. Steglich, ‘Spin dynamics of YbRh_2Si_2 observed by electron spin resonance’, *J. Phys.: Condens. Matter* **19**, 116204 (2007).

- [87] C. Krellner, T. Förster, H. Jeevan, C. Geibel, and J. Sichelschmidt, ‘Relevance of Ferromagnetic Correlations for the Electron Spin Resonance in Kondo Lattice Systems’, *Phys. Rev. Lett.* **100**, 066401 (2008).
- [88] U. Schaufuss, V. Kataev, A. A. Zvyagin, B. Büchner, J. Sichelschmidt, J. Wykhoff, C. Krellner, C. Geibel, and F. Steglich, ‘Evolution of the Kondo State of YbRh_2Si_2 Probed by High-Field ESR’, *Phys. Rev. Lett.* **102**, 076405 (2009).
- [89] J. G. S. Duque, E. M. Bitter, C. Adriano, C. Giles, L. M. Holanda, R. Lora-Serrano, P. G. Pagliuso, C. Rettori, C. A. Pérez, Rongwei Hu, C. Petrovic, S. Maquilon, Z. Fisk, D. L. Huber, and S. B. Oseroff, ‘Magnetic field dependence and bottleneck behavior of the ESR spectra in YbRh_2Si_2 ’, *Phys. Rev. B* **79**, 035122 (2009).
- [90] V. Kataev, U. Schaufuß, B. Büchner, A. A. Zvyagin, J. Sichelschmidt, J. Wykhoff, C. Krellner, C. Geibel, and F. Steglich, ‘High-Field ESR study of the Kondo lattice system YbRh_2Si_2 ’, *J. Phys.: Conf. Ser.* **150**, 042085 (2009).
- [91] J. Sichelschmidt, J. Wykhoff, T. Gruner, C. Krellner, C. Klingner, C. Geibel, F. Steglich, H.-A. Krug von Nidda, D. V. Zakharov, A. Loidl, and I. Fazlizhanov, ‘Effect of pressure on the electron spin resonance of a heavy-fermion metal’, *Phys. Rev. B* **81**, 205116 (2010).
- [92] J. Sichelschmidt, T. Kambe, I. Fazlizhanov, D. V. Zakharov, H.-A. Krug von Nidda, J. Wykhoff, A. Skvortsova, S. Belov, A. Kutuzov, B. I. Kochelaev, V. Pashchenko, M. Lang, C. Krellner, C. Geibel, and F. Steglich, ‘Low temperature properties of the electron spin resonance in YbRh_2Si_2 .’, *Phys. Status Solidi B* **247**, 747 (2010).
- [93] V. A. Ivanshin, T. O. Litvinova, N. A. Ivanshin, A. Pöpl, D. A. Sokolov, and M. C. Aronson, ‘Evolution of the $4f$ Electron Localization from YbRh_2Si_2 to YbRh_2Pb Studied by Electron Spin Resonance’, *JETP* **118**, 760 (2014).
- [94] E. Abrahams and P. Wölfle, ‘Electron spin resonance in Kondo systems’, *Phys. Rev. B* **78**, 104423 (2008).
- [95] Peter Wölfle and Elihu Abrahams, ‘Phenomenology of ESR in heavy-fermion systems: Fermi-liquid and non-Fermi-liquid regimes’, *Phys. Rev. B* **80**, 235112 (2009).

-
- [96] A. A. Zvyagin, V. Kataev, and B. Büchner, ‘Theory of electron spin resonance in heavy fermion systems with non-Fermi-liquid behavior’, *Phys. Rev. B* **80**, 024412 (2009).
- [97] D. L. Huber, ‘The effects of anisotropy and Yb-Yb interactions on the low-field electron spin resonance in YbRh_2Si_2 and YbIr_2Si_2 ’, *J. Phys.: Condens. Matter* **21**, 322203 (2009).
- [98] P. Schlottmann, ‘Electron spin resonance in heavy-fermion systems’, *Phys. Rev. B* **79**, 045104 (2009).
- [99] B. I. Kochelaev, S. I. Belov, A. M. Skvortsova, A. S. Kutuzov, J. Sichelschmidt, J. Wykhoff, C. Geibel, and F. Steglich, ‘Why could electron spin resonance be observed in a heavy fermion Kondo lattice?’, *Eur. Phys. J. B* **72**, 485 (2009).
- [100] N. Oeschler, S. Hartmann, A. P. Pikul, C. Krellner, C. Geibel, and F. Steglich, ‘Low-temperature specific heat of YbRh_2Si_2 ’, *Physica B: Condensed Matter* **403**, 1254 (2008).
- [101] R. N. Simons, ‘Coplanar Waveguide Circuits, Components, and Systems’, *Wiley* (2001).
- [102] K. B. Blodgett and I. Langmuir, ‘Built-Up Films of Barium Stearate and Their Optical Properties’, *Phys. Rev.* **51**, 964 (1937).
- [103] E. Koroknay, U. Rengstl, M. Bommer, M. Jetter, and P. Michler, ‘Site-controlled growth of InP/GaInP islands on periodic hole patterns in GaAs substrates produced by microsphere photolithography’, *Journal of Crystal Growth* **370**, 146 (2013).
- [104] M. S. Ebrahimi, ‘Planar Superconducting Microwave Resonators’, *Master Thesis*, Universität Stuttgart (2013).
- [105] S. B. Cohn, ‘Slot-Line Field Components’, *IEEE Trans. Microw. Theory Techn.* **20**, 172 (1972).
- [106] R. N. Simons and R. K. Arora, ‘Coupled Slot Line Field Components’, *IEEE Trans. Microw. Theory Techn.* **30**, 1094 (1982).
- [107] J. Nagel, K. Baberschke, and E. Tsang, ‘ESR of Er^{3+} and Yb^{3+} in Gold between 100 mK and 1 K’, *Journal of Magnetism and Magnetic Materials* **15-18**, 3292 (1980).

- [108] Y. von Spalden and K. Baberschke, ‘Combination of a $^3\text{He}/^4\text{He}$ dilution refrigerator and an ESR spectrometer’, *Physica B+C* **107**, 599 (1981).
- [109] J. Sanny and W. G. Clark, ‘Microwave electron spin resonance spectrometer with operation to 54 mK in a dilution refrigerator’, *Rev. Sci. Instrum.* **52**, 539 (1981).
- [110] T. Sakon, H. Nojiri, K. Koyama, T. Asano, Y. Ajiro, and M. Motokawa, ‘ESR measurements at ultra-low temperatures using a dilution refrigerator’, *J. Phys. Soc. Jpn.* **72**, 140 (2003).
- [111] M. Hagiwara, T. Kashiwagi, H. Yashiro, T. Umeno, T. Ito, and T. Sano, ‘Development of an Ultra-Low Temperature Multi-Frequency ESR Apparatus’, *J. Phys.: Conf. Ser.* **150**, 012015 (2009).
- [112] K. Ishida, D. E. MacLaughlin, B.-L. Young, K. Okamoto, Y. Kawasaki, Y. Kitaoka, G. J. Nieuwenhuys, R. H. Heffner, O. O. Bernal, W. Higemoto, A. Koda, R. Kadono, O. Trovarelli, C. Geibel, and F. Steglich, ‘Low-temperature magnetic order and spin dynamics in YbRh_2Si_2 ’, *Phys. Rev. B* **68**, 184401 (2003).
- [113] J. P. Joshi and S. V. Bhat, ‘On the analysis of broad Dysonian electron paramagnetic resonance spectra’, *J. Magn. Reson.* **168**, 284 (2004).
- [114] V. A. Ivanshin, J. Deisenhofer, H.-A. Krug von Nidda, A. Loidl, A. A. Mukhin, A. M. Balbashov, and M. V. Eremin, ‘ESR study in lightly doped $\text{La}_{1-x}\text{Sr}_x\text{MnO}_3$ ’, *Phys. Rev. B* **61**, 6213 (2000).
- [115] S. E. Barnes, ‘Theory of electron spin resonance of magnetic ions in metals’, *Adv. Phys.* **30**, 801 (1981).
- [116] S. S. Eaton and G. R. Eaton, ‘Quality Assurance in EPR’, *Bull. Magn. Reson.* **13**, 83 (1992).
- [117] Y. Wiemann, J. Simmendinger, C. Clauss, L. Bogani, D. Bothner, D. Koelle, R. Kleiner, M. Dressel, and M. Scheffler, ‘Broadband electron spin resonance measurements up to 67 GHz using metallic coplanar waveguides’, *submitted to Appl. Phys. Lett.* (2014).

Acknowledgements

Just as any experimental research study this work would not have been possible without the steady and outright support of others. In order to duly acknowledge this support I would like to candidly express my gratitude in the following.

First of all, I would like to thank Prof. Martin Dressel for the opportunity to perform my PhD work at the 1. Physikalisches Institut. I am especially grateful for his patience regarding the duration of my work, which took quite a bit longer than expected. Although he was regularly teasing me about my seemingly never-ending task, he also constantly encouraged me and gave me the freedom to pursue different projects of my own.

I thank my direct supervisor Dr. Marc Scheffler for his support throughout the whole time of my PhD work. He was always eager to help should problems arise and I gained a substantial amount of knowledge from his expertise spanning a vast variety of research fields and experimental techniques.

I sincerely thank Prof. Jörg Wrachtrup who kindly accepted to co-referee my Thesis.

Many thanks to Dr. Lapo Bogani who not only provided top-notch samples but also extremely helpful theoretical assistance. He was also the first one to realize the great potential of the broadband EPR technique presented in this work. Without his constant support and great ideas about how to push things forward this work would not have advanced the way it did. He always expressed his confidence in my work which was great backing in times of slow progress.

Since my work involved heavy usage of a dilution refrigerator and low temperature equipment in general, a constant supply of liquid helium was of essential importance. In that regard I want to express my deepest gratitude to our low temperature department, namely Joachim Lefèvre, Bernd Schobel, Andreas Manz and Florian Münzenmayer for their outstanding work. The supply of freshly tapped helium was always guaranteed and I could invariably rely on their quick and unbureaucratic support. Amongst many other things, I am especially thankful for the repair of a ^3He pump (which was running better afterwards than ever before) and the super fast repair of a He transfer pipe. All members of the low temperature department quickly became highly valued colleagues and I always enjoyed the friendly atmosphere. Last

but not least, I am also very grateful for the countless technical facts and details I learned concerning low temperatures and low pressures.

At this point I would also like to thank all members of the mechanical workshop. The fabrication of my sample holder boxes required challenging accuracy – which nevertheless was always met to my full satisfaction.

This work would not have been possible without the great collaboration with the Physikalisches Institut in Tübingen. I am very grateful for the help the group around Dieter Koelle and Reinhold Kleiner provided. The major part of the work was carried out by Daniel Bothner with whom I spent many long days in the clean room fabricating the micro-structured devices. Although sometimes a whole day's work was ruined in the evening by the DISCO Bitch we still managed to fabricate more devices than I was able to measure.

Many thanks are also in order to the IHFG run by Peter Michler in Stuttgart. Thanks to a fruitful collaboration with the group of Michael Jetter, in particular with Elisabeth Koroknay, we could fabricate devices that efficiently hamper the movement of vortices in rf microwave fields to significantly improve the performance.

When it comes to sample preparation and delicate operations under the microscope I am very happy that I had two wonderful teachers. One being Tomislav Ivek whom I first met already during my Diploma work on a visit to the Institut za Fiziku in Zagreb and the other one is Gabriele Untereiner, one of the most important persons at the institute. They showed me how to apply itsy bitsy tiny contacts to very small samples and taught me the high arts of perfect sample preparation. Based on that knowledge I was later on able to refine these techniques according to my needs and develop schemes for reliable and reproducible signal injection into my microwave devices.

Special thanks to Sabrina Haas, a highly valued colleague and dear friend. She is a wonderful person and she often cheered me up when things weren't going well. Although she is quite scary of electricity, she is a very diligent and conscientious worker in the lab and she outshines everyone else concerning far-infrared magneto-optical measurements. I have always enjoyed our conversations over a beer or two and I am very much looking forward to see her again soon.

Many thanks and a big hooray to the THz Sidewinders subdivision, namely Eric Heintze and Uwe Unschuld who are great colleagues and quickly became dear friends. Thanks for admitting me into your illustrious circle. I hope the prime number research as well as the highly praised Pracht Design will advance further to undreamt-of heights. I very much enjoyed our countless (scientific) meetings and I look forward to the continuation of that tradition.

Thanks also to all the former and current members of Pi1, especially Stefan Kaiser and Eva Rose who provided great help in my early days at the institute. Thanks to Sina Zapf, Tobias Peterseim, Rebecca Beyer, David Neubauer, Christian Cervetti, Stefano De Zuani, Ralph Hübner, Mojtaba Javaheri, Anja Löhle and Michael Slota who are all great company and make the everyday work life more pleasant. Also thanks to Bruno Gompf and Helga Kumrić who are always nice to talk to and always eager to help on any matter. Helga, many thanks for the support with CST Microwave Studio.

Many thanks to my dear friends from schooldays and from the Hohenheim Bauern Bootcamp connection. Your friendship is very important to me and you always set me back straight when times are bad. Thanks!

Many thanks also to my parents for any type of support they provided when the need arised.

Last but definitely not least, I want to thank the woman of my heart for all the backing and cheering-up. You make me whole. Thanks a lot!

